



Bělin, Jakub (2020) *Optics of polyhedra: from invisibility cloaks to curved spaces*. PhD thesis.

<http://theses.gla.ac.uk/81559/>

Copyright and moral rights for this work are retained by the author

A copy can be downloaded for personal non-commercial research or study, without prior permission or charge

This work cannot be reproduced or quoted extensively from without first obtaining permission in writing from the author

The content must not be changed in any way or sold commercially in any format or medium without the formal permission of the author

When referring to this work, full bibliographic details including the author, title, awarding institution and date of the thesis must be given

Enlighten: Theses

<https://theses.gla.ac.uk/>
research-enlighten@glasgow.ac.uk

Optics of Polyhedra: from Invisibility Cloaks to Curved Spaces

Jakub Bělin

A thesis submitted in fulfilment of the requirements for the degree of
Doctor of Philosophy

School of Physics and Astronomy
College of Science and Engineering
University of Glasgow

May 2020

Abstract

Transformation optics is a new and highly active field of research, which employs the mathematics of differential geometry to design optical materials and devices with unusual properties. Probably the most exciting device proposed by transformation optics is the invisibility cloak. However, transformation optics can be employed in many other cases, for example when designing a setup mimicking a curved space-time phenomena in a lab. The purpose of this thesis is to establish a new concept of transformation optics: instead of designing complicated materials, we will design our devices using standard optical elements such as lenses or optical wedges. We will stretch the possibilities of geometrical optics by providing a novel description of imaging due to combinations of tilted lenses and the theory of invisibility with ideal thin lenses. This theory will be then applied to design novel transformation optics devices, namely the omnidirectional lens and a number of ideal-lens invisibility cloaks.

We also present a new approach of building optical systems that simulate light-field propagation in both 2D and 3D curved spaces. Instead of building the actual curved space, the light field is regarded to travel in the respective unfolded net, whose edges are optically identified, using the so-called space-cancelling wedges. By deriving a full analytical solution of the Schrödinger equation, we will also investigate a quantum motion in a number of two-dimensional compact surfaces including the Klein bottle, Möbius strip and projective plane. We will show that the wavefunction exhibits perfect revivals on these surfaces and that quantum mechanics on many seemingly unphysical surfaces can be realised as simple diffraction experiments. Our work therefore offers a new concept of optical simulation of curved spaces, and potentially represents a new avenue for research of physics in curved spaces and simulating otherwise inaccessible phenomena in non-Euclidean geometries.

We conclude with a summary of potential future projects which lead naturally from the results of this thesis.

Contents

| | |
|---|--------------|
| Abstract | i |
| List of Figures | v |
| List of Tables | xv |
| Acknowledgements | xvi |
| Declaration of Authorship | xvii |
| Publications | xviii |
| Introduction | 1 |
| 1 Geometrical optics and first-order optics | 3 |
| 1.1 Basic concepts of geometrical optics | 4 |
| 1.1.1 Refractive index | 4 |
| 1.1.2 Optical path length and Fermat's principle | 4 |
| 1.1.3 Law of reflection | 4 |
| 1.1.4 Snell's law of refraction | 4 |
| 1.2 Imaging systems | 5 |
| 1.3 Spherical interface as an imaging system | 6 |
| 1.3.1 Cardinal points of a spherical interface | 7 |
| 1.3.2 Imaging equations due to a curved interface | 8 |
| 1.4 Lens-imaging equations | 9 |
| 1.4.1 Thick lens | 10 |
| 1.4.2 Ideal thin lens | 11 |
| 1.5 Generalised lens-glens | 12 |
| 1.6 Projective space and Central Collineation | 14 |
| 2 Lens-imaging coordinates and imaging with unusual combinations of ideal lenses | 15 |
| 2.1 Introduction | 15 |
| 2.1.1 Contributions | 16 |
| 2.2 Lens-imaging coordinates | 16 |
| 2.3 Motivation for lens-imaging coordinates | 17 |
| 2.3.1 Two coaxial lenses | 18 |
| 2.3.2 Two coplanar non-coaxial lenses | 18 |
| 2.3.3 Lens-imaging coordinates for an ideal thin lens | 19 |
| 2.3.4 Two-lens optical axis | 21 |
| 2.3.5 Example: Parallel, but non-coaxial lenses | 22 |
| 2.3.6 Transverse planes of two skew lenses | 23 |

| | | |
|----------|---|-----------|
| 2.3.7 | Focal planes | 24 |
| 2.3.8 | Principal planes | 25 |
| 2.4 | Deriving the Lens-imaging coordinates for two skew lenses | 26 |
| 2.5 | Applying lens-imaging coordinates: Two skew lenses with coinciding principal points | 29 |
| 2.6 | Applying lens-imaging coordinates: Image rotation with three skew lenses | 29 |
| 2.6.1 | Image rotation with three lenses mathematically | 32 |
| 2.7 | Discussion | 33 |
| 2.7.1 | Comparison of lens-imaging-coordinate systems | 33 |
| 2.7.2 | Combinations of skew physical lenses | 34 |
| 2.7.3 | Applications of the three-lens image rotator | 35 |
| 3 | Transformation optics with ideal lenses | 36 |
| 3.1 | Transformation optics and transformation optics devices | 36 |
| 3.1.1 | Contributions | 37 |
| 3.2 | Mapping conditions in TO devices | 37 |
| 3.3 | Conditions on the principal points | 40 |
| 3.4 | Lens combinations that satisfy the edge-imaging condition | 41 |
| 3.4.1 | 2 lenses | 42 |
| 3.4.2 | 3 lenses | 43 |
| 3.4.3 | 4 lenses | 44 |
| 3.4.4 | Mirror-symmetric four-lens intersection | 44 |
| 3.4.5 | Asymmetric four-lens intersection | 44 |
| 3.5 | Building TO devices using the edge-imaging condition | 45 |
| 3.6 | Structure S as an Omnidirectional lens | 47 |
| 3.7 | Structure S as an almost-invisibility cloak | 49 |
| 3.8 | Structure S as an abyss cloak | 49 |
| 3.9 | Bi-abyss cloak: an ultimate invisibility | 49 |
| 3.10 | Discussion | 50 |
| 3.11 | Potential applications | 51 |
| 4 | Optical simulations of curved spaces | 52 |
| 4.1 | Introduction | 52 |
| 4.1.1 | Contributions | 53 |
| 4.2 | Loop-imaging condition as a “flat-space condition” | 53 |
| 4.3 | Angular deficit, parallel transport and curvature | 55 |
| 4.4 | Geodesics | 57 |
| 4.5 | Topology, Triangulation and ε -cones | 58 |
| 4.6 | Optical removal of space, the space-cancelling wedges | 59 |
| 4.6.1 | SC wedge using negative refraction | 60 |
| 4.6.2 | SC wedges using absolute instruments | 61 |
| 4.6.3 | SC-wedge using ideal lenses | 63 |
| 4.6.4 | SC-wedge by transferring the light field | 63 |
| 4.7 | Simulating curved 2D spaces | 65 |
| 4.8 | Simulating curved 3D spaces | 66 |
| 4.9 | Discussion | 68 |
| 4.9.1 | Non-euclidean Transformation Optics | 68 |
| 4.9.2 | Negative refraction | 68 |
| 4.9.3 | General relativity | 70 |
| 4.9.4 | Wave optics | 71 |

| | | |
|----------|--|------------|
| 4.9.5 | Negative curvature | 71 |
| 4.10 | Conclusions | 72 |
| 5 | Wave optics and quantum motion on compact manifolds | 73 |
| 5.1 | Introduction | 73 |
| 5.1.1 | Contributions | 74 |
| 5.2 | Solving the Helmholtz equation on a manifold and on its quotient space . . | 74 |
| 5.3 | Tessellating the plane with copies of quotient space | 75 |
| 5.3.1 | Manifolds without hard boundaries | 75 |
| 5.3.2 | Manifolds with hard boundaries | 76 |
| 5.3.3 | Transiting from the quotient space to the entire plane | 76 |
| 5.4 | The mode structure of the quotient space | 77 |
| 5.5 | Connection to the diffraction theory | 79 |
| 5.6 | Eigenmodes and eigenvalues on different manifolds | 80 |
| 5.6.1 | Torus | 80 |
| 5.6.2 | Infinite potential well | 81 |
| 5.6.3 | Cylinder with hard edges | 82 |
| 5.6.4 | Möbius Strip | 82 |
| 5.6.5 | Klein Bottle | 83 |
| 5.6.6 | Real projective plane | 85 |
| 5.6.7 | Tetrahedron | 86 |
| 5.6.8 | Double-sided square | 86 |
| 5.6.9 | Double-sided triangle | 88 |
| 5.7 | Obtaining the topology of the manifold from its modes | 88 |
| 5.8 | Simulations | 90 |
| 5.9 | Discussion and conclusions | 90 |
| 6 | Conclusions and future work | 94 |
| A | Derivation of the formula for intersection point w_i | 97 |
| B | Derivation of the formulas for slopes $\cot \alpha$ and $\cot \alpha'$ of two-lens object-sided and image-sided transverse planes | 98 |
| C | Parameters of the three-lens image-rotation system | 99 |
| D | Calculation leading to focal lengths of an asymmetric four-lens intersection, which satisfies the edge-imaging condition | 101 |
| E | Derivation of the formula for Talbot length | 104 |
| F | Derivation of the formula for the fractional Talbot effect | 106 |
| | Bibliography | 108 |

List of Figures

| | | |
|-----|---|----|
| 1.1 | (a) Law of reflection and (b) Law of refraction; (a) Angle α_r the refracted ray makes with a normal to the surface equals minus the angle α_i the incident ray makes with the normal; (b) When traveling from a medium with refractive index n_1 to a medium with refractive medium n_2 , a light ray is refracted according to Snell's law of refraction (1.4). | 5 |
| 1.2 | A Gaussian imaging system is fully described by its focal planes \mathcal{F} and \mathcal{F}' , principal planes \mathcal{P} and \mathcal{P}' and the cardinal points, located on the optical axis z : focal points F and F' , the principal points P and P' , and the nodal points N and N' . Nodal points coincide with the principal points if the optical medium on both sides of the optical system is the same. The imaging system (cyan box) redirects the light rays emerging from an object position \mathbf{Q} to an image position \mathbf{Q}' as if all of the refraction happened at the principal planes \mathcal{P} and \mathcal{P}' | 7 |
| 1.3 | Cardinal points of a spherical interface; (a) rays (red lines) from an object-sided focal point F will form a parallel bundle after a transmission through the interface; (b) Rays which are all parallel to the optical axis will be transformed into rays which intersect in an image-sided focal point F' . Principal points P and P' coincide with an intersection of the surface with an optical axis, whereas the nodal points N and N' are situated at point R of the centre of curvature of the interface. | 8 |
| 1.4 | Mapping due to a spherical interface with a radius r between two optical media with refractive indices n_1 (white area) and n_2 (cyan area). | 9 |
| 1.5 | A thick lens consists of two spherical interfaces: the first interface intersects the z -axis at point $(0, 0, 0)$ and the second interface intersects the z -axis at point $(0, 0, d)$. The principal planes \mathcal{P} and \mathcal{P}' intersect the optical axis at points P and P' respectively, given by Eqs. (1.21) and (1.22). A thick lens maps a point \mathbf{Q} in an object space to a position \mathbf{Q}' in an image space, following the imaging equations (1.24) and (1.25). | 11 |
| 1.6 | (a) Convex lens, (b) concave lens, (c) notation of an ideal thin lens used in this thesis. (d) Imaging due to a lens with a general principal point position \mathbf{P} and orientation of an optical axis $\hat{\mathbf{z}}$ | 12 |

| | | |
|-----|---|----|
| 1.7 | (a) Location of the nodal point of a glens. Two parallel light rays are incident on the glens: one of them passes through the negative focal point, F^- , and intersects the glens at position S. the other ray passes through the nodal point N and intersects the first light ray at position I. Clearly, the triangles F^-SP and NIF^+ (shaded green areas) are congruent. (b) Imaging due to a glens. Again, two light rays, emerging from a point O , are incident on the glens: one of them passes through the object-sided focal point, F^- , whereas the other light ray passes through an image-sided focal point, F^+ . Both light rays intersect at point I after transmission through the glens. Similarity of triangles OqF^- and $h'PF^-$ (yellow shaded areas) implies Eq. (1.30). Analogously, similarity triangles hPF^+ and $Iq'F^+$ (green shaded areas) implies Eq. (1.31). | 13 |
| 1.8 | (a) Visualisation of a projective space $\mathbf{P}(\mathbb{R}^3)$: vectors $\mathbf{u}, \mathbf{v} \in \mathbb{R}^3$ are “projected” to points $P_{\mathbf{u}}$ and $P_{\mathbf{v}}$ in $\mathbf{P}(\mathbb{R}^3)$ and plane M through the origin is mapped to line m in $\mathbf{P}(\mathbb{R}^3)$. (b) Imaging due to an ideal thin lens is an example of elation. | 14 |
| 2.1 | Telescope-like behaviour of a combination of two skew lenses, L_1 and L_2 . An array of parallel light rays (red lines) is incident on lens L_1 with a direction such that the light rays are focused to a point on the intersection line I between the image-sided focal plane of lens L_1 , \mathcal{F}'_1 , and the object-sided focal plane of lens L_2 , \mathcal{F}_2 (black dashed lines). Because I lies in the object-sided focal plane of L_2 , the light rays become parallel again when emerging lens L_2 . Points P_1 and P_2 are the principal points of the respective lenses. | 16 |
| 2.2 | (a) A system of two coaxial lenses, marked L_1 and L_2 , provides the same mapping of an object-space point Q to an image-space point Q' as a single thick lens, of focal length f (given by Eq. (2.6)); focal planes of the combination of lenses L_1 and L_2 are labelled \mathcal{F} and \mathcal{F}' , whereas \mathcal{P} and \mathcal{P}' are the corresponding principal planes; (b) Two coplanar non-coaxial lenses: lens L_2 is offset by h with respect to lens L_1 . This two-lens system can also be regarded as a single ideal lens, of focal length f , given by Eq. (2.10). To find the principal point P of this optical system, we employ a light ray (red arrow), which travels parallel to the z -axis and remains undeviated after the transmission through both lenses L_1 and L_2 | 19 |
| 2.3 | Coordinates for single-lens imaging. A pair of conjugate positions O and I is shown. In a Cartesian (x, y, z) coordinate system, placed such that the lens is in the $z = 0$ plane and the position of the principal point, P , coincides with the origin, the relationships between the coordinates of O and I have the standard form, given by Eqs. (2.13). The object and image positions can alternatively be expressed in skew coordinates with basis vectors $\hat{\mathbf{u}}, \hat{\mathbf{v}}$, and $\hat{\mathbf{w}}$, with the imaging equations retaining their standard form. The figure shows a cross section in the $y = v = 0$ plane. | 20 |
| 2.4 | System of two tilted lenses L_1 and L_2 (cyan lines). We chose the optical axis for this two-lens system to coincide with a line passing through both principal points P_1 and P_2 . Angles, formed by the normals of the respective lenses and the two-lens optical axis, are denoted φ_1 and φ_2 | 21 |
| 2.5 | System of two parallel, non-coaxial lenses L_1 and L_2 . The black dashed lines represent the focal planes of this system, whereas the green dashed lines correspond to its principal planes with principal points $P = (P_z \tan \alpha, 0, P_z)$ and $P' = (P'_z \tan \alpha, 0, P'_z)$, when expressed in Cartesian coordinates (x, y, z) | 22 |

| | | |
|-----|--|----|
| 2.6 | Construction of the image-sided (a) and object-sided (b) two-lens focal planes, \mathcal{F}' and \mathcal{F} . The respective focal points, F' and F , coincide with the intersections of the focal planes with the optical axis. | 24 |
| 2.7 | Construction of the skew-lens principal planes, \mathcal{P} and \mathcal{P}' . The object-sided principal plane \mathcal{P} coincides with the object-sided skew-lens transverse plane through V (the line of intersection of both lenses L_1 and L_2). Analogously, the image-sided transverse skew-lens plane through V coincides with the image-sided principal plane \mathcal{P}' . Consequently, the principal points P and P' can be found as the intersections of the respective principal planes with the optical axis w . Both principal planes \mathcal{P} and \mathcal{P}' are linked together by the plane through both lines V and I : \mathcal{P} is imaged due to lens L_1 to that plane and \mathcal{P}' is an image of that plane due to a lens L_2 . This intermediate plane intersects the optical axis at point w_{im} | 26 |
| 2.8 | Definition of the object- and image-space lens-imaging coordinates. Positions in object and image space are expressed in skew coordinate systems with basis vectors \mathbf{u} , $\hat{\mathbf{v}}$, $\hat{\mathbf{w}}$ (object space) and \mathbf{u}' , $\hat{\mathbf{v}}'$, $\hat{\mathbf{w}}'$ (image space). Basis vectors in the u and u' directions are not normalised; their lengths are chosen such that the x components of these vectors is equal to one. We define \mathbf{u} by the intersection of the object-sided principal plane, \mathcal{P} , and the median plane, \mathcal{M} , which is through the two-lens optical axis w and perpendicular to the (v, w) plane. Similarly, vector \mathbf{u}' lies on the intersection of the image-sided principal plane, \mathcal{P}' , and plane \mathcal{M} . Origins of the object- and image-sided lens-imaging coordinates coincide with the object- and image-sided principal points, P and P' respectively. | 27 |
| 2.9 | (a) The construction of the three-lens image rotator starts with a system D of two skew lenses, L_1 and L_2 , characterised by its effective focal length, f_D , the two-lens optical axis, which coincides with the w and w' axes of the lens-imaging coordinate systems, the object- and image-sided focal planes \mathcal{F} and \mathcal{F}' , and the object- and image-sided principal planes \mathcal{P} and \mathcal{P}' . A bundle of parallel light rays (red lines) is incident on D from a direction that is perpendicular to the object-sided principal planes, \mathcal{P} . Lens L_3 is placed in the image-sided principal plane \mathcal{P}' of the two-lens system D , such that its object-sided focal point coincides with the point X , where the bundle of rays intersects the image-sided two-lens focal plane, \mathcal{F}' . (b) The same system of three lenses in lens-imaging coordinates (u, w) acts like a combination of two coplanar lenses of opposite focal lengths, f_D and $-f_D$, offset in the transverse direction. The mapping due to this lens combination — a pure shearing — exactly cancels the shearing of the lens-imaging coordinate system, so that the mapping in the global Cartesian coordinates is a pure rotation. | 30 |

| | | |
|------|---|----|
| 2.10 | Demonstration of image rotation with three lenses. A square lattice is placed behind three-lens image rotator T, whose lenses are framed with red, green and blue rings respectively. The actual field of view through all three included lenses is circumscribed by a green ellipsoid inside the red-framed lens (which is actually an image of the frame of the middle lens due to the red-framed one). The lattice, as seen through all three lenses, appears rotated by an angle $\Delta\alpha = -15^\circ$ around a vertical axis. (c) For comparison, the simulation was performed without the lenses but with the camera physically rotated by 15° around the same axis. Chosen parameters are (a) $\varphi_1 = 2.5^\circ$, $\varphi_2 = -2.5^\circ$ and $d = 0.5$ and (b) $\varphi_1 = 0.5^\circ$, $\varphi_2 = -0.5^\circ$ and $d = 0.1$. The remaining values have been calculated using formulas presented in the Appendix C. One can see that the field of view increases when the inclination $\varphi_2 - \varphi_1$ between first two lenses of rotator T (red and green-framed) becomes smaller, which appears to be the case generally. The simulations were performed using an extended version of our custom raytracer Dr TIM [1]. | 31 |
| 3.1 | Examples of transformation optics devices: (a) Invisibility cloak proposed by John Pendry, David Schurig and David R. Smith [2]: the optical medium between two concentric spheres is such that the light rays (black lines) circumvent the inner sphere – the cloaked volume – and then continue in their original trajectories; (b) non-euclidean invisibility cloak by Tomáš Tyc and Ulf Leonhardt [3]: The cloaked volume, which the light rays (red lines) are never incident on, is depicted as a lentil shape; (c) Rochester cloak, first proposed by Joseph S. Choi and John C. Howell [4]: this device consists of four lenses, arranged such that the incident and emerging parts of light rays passing through are in line. In a space between the lenses, there are regions which are omitted by the light rays passing through all four lenses. Any object in such a region (for example, a human eye) is therefore invisible from a region close to the optical axis. | 37 |
| 3.2 | Diagram of part of a transformation-optics device formed by lenses (cyan lines). The lenses divide the inside of the device into cells, five of them are marked g to k; cell 0 is the outside of the device. Lens L_{uv} then separates cells u and v. Light rays (red lines), starting from a point Q_i , located in cell i, form an image Q_0 in the outside space, regardless whether they travel through cells j and k or cells h and g. Dotted red arrows show the trivial loops, containing none or only one lens. | 38 |
| 3.3 | Application of the loop-imaging condition to TO devices, built of spatially-varying optical materials. Panel (a) shows several light rays (red lines), intersecting at point O and passing through an invisibility cloak, similar to one proposed in Ref. [5]. The light rays travel along their original trajectories after being transmitted through the device and thus the device satisfies the loop-imaging condition since the image I of point O due to the device coincides with O . Panel (b) shows an area within a TO device and a light ray intersecting itself at point O . As a consequence of the loop-imaging condition, the trajectory of such ray coincides with a closed loop. | 39 |

| | | |
|-----|---|----|
| 3.4 | Diagrams used when deriving the conditions on the principal-point positions in combinations of two (a), three (b), four (c), and seven (d) lenses (which in fact can be combined to a six-lens system) that satisfy the identity-mapping condition. The red lines show the trajectories of light rays that pass through the principal point P_1 of lens L_1 and, in panel (c), also through the principal point P_2 of lens L_2 . In (d), the combination of lenses L_1 - L_4 itself satisfies the identity-mapping condition, as well as the combination of lenses L_5 - L_7 | 40 |
| 3.5 | Intersections of (a) two, (b) three, and (c)-(d) four lenses, which potentially satisfy the edge-imaging condition. Lenses are labelled L_i , and P_i are their principal points. | 42 |
| 3.6 | Building TO devices from lenses. Structures presented in panels (a) and (b) do not satisfy the conditions on principal-point positions, discussed in Sec. 3.3. The simplest two-dimensional lens structure, satisfying all those conditions, is presented in panel (c). Three-dimensional version is shown in panel (d); wherever blue cylinders form a triangle, there is a lens with an aperture circumscribed by that triangle. $P_{ij\dots}$ denotes a common principal point of lenses L_i, L_j, \dots | 46 |
| 3.7 | Lenses included in the structure S , highlighted as blue surfaces. Lenses are labelled L_A, \dots, L_F , with corresponding principal point positions P_A, \dots, P_F (black dots). | 47 |
| 3.8 | (a) Structure S without lenses; blue cylinders represent common edges of lenses included in the structure. If an object (patterned sphere) is placed in cell 1 (green semi-transparent area), it is imaged to the outside as due to a base lens L_A (b). That is why we sometimes call it an omnidirectional lens; (c) if the focal lengths of included lenses are chosen such that the cell 1 is imaged to the outside space with a magnification approaching zero, the omnidirectional lens can be regarded as an almost-invisibility cloak; panels (d)-(f) demonstrate the abyss cloak: object P is imaged to a position P' outside the cloak; (f) If camera is placed in a position such that both image of the object (patterned sphere) and the cloak are seen in the same direction (red shaded area in panel (d)), that image is visible for the camera; (e) otherwise the image is invisible. Panels (g)-(i) present the bi-abyss cloak: the final object P''_i due to both cloaks I and O can be visible from the outside only if there are lines (like the black dotted one in panel (g)) such that all O, I' (the purple structure in panel (h)) and P''_i are located on that line. This is shown in raytracing simulations, presented in panels (h) and (i): panel (h) shows the geometries of the outer cloak O (blue structure), inner cloak I (red structure) and its image I' due to O (purple structure) and positions of the cloaked object P_1 (patterned sphere) and its corresponding images P'_1 and P''_1 ; (i) as (h) but blue, red and purple structures indicating the geometries of O, I and I' are removed and all ideal lenses are in place. The zoomed view of the image P'_1 is provided in the top right corner of both panels. | 48 |

| | | |
|-----|---|----|
| 3.9 | Raytracing simulations of a phase-hologram realisation of the Structure S. When seen from the intended viewing position (a), the device does not distort the scene seen through it, exactly as with the corresponding ideal-thin-lens device. This is not the case for any other viewing position; an example is shown in (b). All simulations assumed perfect dispersion compensation for all visible light and were performed with an extended version of our custom raytracer Dr TIM [1]. | 51 |
| 4.1 | Similarities between the algebraic topology and TO devices; (a) the structure S can be regarded as a simplicial complex, a structure composed of 2D simplices (triangles); (b) simplicial complexes are commonly used for modelling curved surfaces, for example a surface of a bunny [6]. | 54 |
| 4.2 | In two dimensions, the tangent spaces $T_{x_1}M$ and $T_{x_2}M$ to the manifold M can be visualised as tangent planes to the surface M at points x_1 and x_2 respectively. A parallel transport of a vector (black arrow) from x_1 to x_2 is then defined by an affine connection between $T_{x_1}M$ and $T_{x_2}M$ | 56 |
| 4.3 | Parallel transport and curvature; (a) the parallel transport of vector \mathbf{v} in a Euclidean space corresponds to moving the vector along a curve (red dotted line), keeping its components constant; (b) in a curved space, the parallel transport depends on the path: vector \mathbf{a} corresponds to \mathbf{v} parallel transported along the blue solid line, whereas \mathbf{b} coincides with \mathbf{v} parallel transported along the red solid line. | 57 |
| 4.4 | The shortest path between two points on the globe — the geodesic— usually does not map to a straight line between the corresponding points on the map. Picture taken from [7]. | 58 |
| 4.5 | A smooth manifold (a) (a sphere) can be approximated by a complex of simplices (b). The curvature is then concentrated to the vertices: this can be visualised by cutting the surface around a vertex (for example V) and unfolding it into a plane. A wedge of “missing space” of angle ε will appear (c). | 60 |
| 4.6 | The space cancelling wedge between half-planes 1 and 1' using negative refraction. (a) Half-plane 1, the outer face of the wedge of $n = -1$ medium (of angle $\varepsilon/2$), gets mapped due to the wedge to half-plane 1', such that 1' coincides with 1 rotated around the wedge edge V by an angle ε . Although ray A (solid red line) is refracted as desired, ray B (dashed red line) is refracted such that it diverges from half-plane 2 and gets “lost” in the wedge. (b) This can be treated by building a fan of N (here $N = 3$) wedges, each of angle $\varepsilon/2N$ or (c) one can insert mirrors M and M' at the end of the $n = -1$ wedge, symmetrically with respect to half-plane 2. This requires the angle μ to be chosen to lie in the range $\pi/2 \leq \mu \leq \pi - \varepsilon$ | 61 |
| 4.7 | The space-cancelling wedge using absolute instruments (a) The half planes ρ and σ , making an angle ε around the line a in a physical space and (b) the corresponding half-planes ρ' and σ' in virtual space, lying in the plane XY. Points A and B are mapped to each other by a medium with refractive index N. | 62 |

| | | |
|------|--|----|
| 4.8 | The space-cancelling wedge using ideal thin lenses. (a) An orthogonal lattice consisting of green and blue cylinders is placed behind a three-lens image rotator. Only the closest lens (red-framed) is seen directly. When seen through all three lenses, the lattice appears rotated by 15 degrees around a vertical axis. (b) This is confirmed by a simulation without the lenses, but with the camera rotated by -15 degrees around the same axis; The scene seen through all three lenses in (a) is identical to the corresponding part in (b). Both simulations were performed with an extended version of our raytracing software Dr TIM [1]. | 63 |
| 4.9 | The space-cancelling wedge using light-field transfer. (a) Two lenslet arrays (cyan) fill the optically identified faces. The array of optical fibres (yellow) then connects the “inner” focal planes (dotted lines) of the two lenslet arrays; baffles (solid black lines) eliminates the cross-talking between neighbouring lenslets. Then, each fibre represents one particular combination of a position (given by the position of the corresponding lenslet) and direction with which light rays (solid red lines) are incident on the faces. (b) To employ a coherent fibre bundle, further optical components, e.g. a combination of two identical lenslet arrays, needs to be added. The faces of the SC wedge are then formed by the outermost arrays. | 65 |
| 4.10 | Optical simulations of the surface of a regular tetrahedron (a) and a cube (d). The simulations are performed on the respective nets of both tetrahedron and a cube; panels (b) and (e) show intermediate stages of unfolding. The corresponding gluing instructions are represented by numbers: edges labelled with the same number are identified; in panels (b) and (e), the black arrows indicate how the original edges of the folded surface split into two edges in the equivalent net and thus need to be identified optically in the simulations. V labels the fourth vertex of the tetrahedron, which appears as three separate vertices in the (partially) unfolded net. The surface of the cube has been unfolded symmetrically, at the cost of dividing one of its faces into four right triangles; C is the centre of that face. Panels (g,j) then show the nets of the tetrahedron and the cube, fitted with the space-cancelling wedges. Rays represent the geodesics on both (optically glued) surfaces; three rays (red, green, blue) are shown in each case. The continuity of the light-ray trajectories can be confirmed by mechanical folding and gluing of the nets, shown in panels (h) and (k). Finally, we present a simulation of the view of a scene (a white sphere) as seen from within the surface, with an added third, Euclidean, dimension perpendicular to the surface. The cyan lines show the edges of the respective nets of the tetrahedron and the cube. The raytracing simulations were performed using Dr TIM [1]. | 67 |

| | | |
|------|--|----|
| 4.11 | Raytracing simulations of the 3D hypersurface of (a) a 5-cell and (c) of a hypercube. The gluing instructions are represented with numbers: faces with the same numbers are identified (e.g. faces 1 and 1' are identified, some faces are unnumbered since the identified face is not visible.) (a) After unfolding, the fifth vertex of the 5-cell V splits into the 4 outermost vertices. On the other hand, the four outermost vertices of the net of the hypercube (c), all labelled C , represent the centre of the eighth cubic cell of the hypercube. Panel (b) shows one light-ray trajectory as seen from the outside of the net of a 5-cell. The view from the inside of such hypersurface is shown in (e), where a white sphere has been placed into the net as shown in the bottom left corner of panel (e). (d, f) Similar simulations, performed in Dr TIM [1], have also been performed for the hypercube. | 69 |
| 5.1 | (a) A torus is an example of a manifold without hard boundaries; (b) The quotient space of a torus is equivalent to a rectangle of sides a and b , with the opposite sides being identified by relations $(0, y) \sim (a, y)$ and $(x, 0) \sim (x, b)$, indicated with red and blue arrows. The Tessellation rule no. 1 then yields a periodic function $\phi(x, y)$, whose unit cell (red-shaded area) coincides with the function $\psi_0(x, y)$, defined on the quotient space. . | 76 |
| 5.2 | (a) An infinite potential well is an example of a manifold with hard boundaries. (b) Employing the Tessellation rule no. 2 leads to the periodic function $\phi(x, y)$, whose unit cell consists of four copies of the function $\psi_0(x, y)$; black lines represent the hard boundaries of the quotient space σ and blue spots represent the “negative” tiles. | 77 |
| 5.3 | (a) Cylinder, when cut and unfolded to a plane, is equivalent to a rectangle of sides a and b , with hard boundaries on sides b , whereas the sides a are identified according to gluing instruction $(x, 0) \sim (x, b)$. (b) Tessellation of the plane with copies of $\psi_0(x, y)$ defined on the quotient space σ yields a periodic function $\phi(x, y)$, whose unit cell consists of two copies of $\psi_0(x, y)$ | 83 |
| 5.4 | (a) Möbius strip, when cut and unfolded to a plane, is equivalent to a rectangle of sides a and b , with hard boundaries on sides b and with a gluing instruction $(x, 0) \sim (a - x, b)$ on sides a . (b) The tessellation $\phi(x, y)$ with copies of a function $\psi_0(x, y)$ defined on the quotient space σ . A unit cell of $\phi(x, y)$ consists of four copies of $\psi_0(x, y)$ | 84 |
| 5.5 | (a) A two-dimensional representation of the Klein bottle immersed in three-dimensional space; (b) (b) the quotient space σ of Klein bottle is a rectangle of sides a and b with identification $(0, y) \sim (a, y)$ and $(x, 0) \sim (a - x, b)$. Applying the tessellation rule no. 1 then yields a function $\phi(x, y)$, whose unit cell consists of two copies of function $\psi_0(x, y)$ defined on σ | 84 |
| 5.6 | (a) Cross-capped disk, a two-dimensional visualization of a real projective plane embedded in a three-dimensional flat space. (b) Tessellation $\phi(x, y)$ of a plane with copies of a function $\psi_0(x, y)$ defined on the quotient space σ . The quotient space σ corresponds to a rectangle of sides a and b , whose opposite sides are identified by gluing instructions $(x, 0) \sim (a - x, b)$ and $(0, y) \sim (a, b - y)$. The unit cell of the function $\phi(x, y)$ then consists of four copies of σ | 85 |

| | | |
|------|---|----|
| 5.7 | (a) A regular tetrahedron of side length a ; (b) To obtain a corresponding quotient space, edges 1, 2, 3 depicted in panel (a) need to be cut and then equipped with appropriate gluing instructions, i.e. edges labelled with the same colour (e.g. 1 and 1') are identified. The tessellation rule no. 1 then yields a periodic function $\phi(x, y)$, with a structure analogous to one presented in panel (b) (red shaded area represents the unit cell). | 87 |
| 5.8 | (a) A folded square of a side $a/\sqrt{2}$, where a is a length of its diagonal; (b) The quotient space is equivalent to square of side a , created by cutting the diagonals on one of its sides (e.g., the upper side as indicated in panel (a)). The sides of the original folded square are indicated with black dashed lines and black dots indicate its corners. Panel (b) shows a function $\phi(x, y)$, created by the tessellation with copies of $\psi_0(x, y)$ defined solely on σ | 87 |
| 5.9 | (a) A both-sided regular triangle of a side a ; (b) The quotient space is equivalent to a regular hexagon, created by cutting one of the faces from the centre of mass towards the corners of the triangle (e.g., the upper side as indicated in panel (a)). The unit cell (red-shaded rectangle) consists of six copies of the quotient space. One copy is just shifted by vector $(3a/2, a\sqrt{3}/2)$ with respect to the original quotient space. Two other copies are shifted by vectors $(a, 0)$ and $(0, a\sqrt{3}/2)$ respectively and rotated by angle $2\pi/3$ with respect to the original quotient space. The two remaining copies are then rotated by angle $4\pi/3$ and shifted by vectors $(2a, 0)$ and $(a/2, a\sqrt{3}/2)$ respectively. The gluing instructions are visualised with red, green and blue colours of identified edges, e.g. blue edges labelled 1 and 1' are identified. | 89 |
| 5.10 | (a) Torus with the mode $\psi = \phi_{1,1} + \phi_{-1,1} + \phi_{1,-1} + \phi_{-1,-1}$. (b) Klein bottle with $\psi = \phi_{1,1} + \phi_{1,-1}$. (c) Real projective plane with the mode $\psi = \phi_{1,1}$. (d) Tetrahedron with $\psi = \phi_{1,1} + \phi_{1,-1} + \phi_{0,2}$ (e) Double-sided square with $\psi = \phi_{1,1} + \phi_{1,-1}$. (f) Double-sided triangle with $\psi = \phi_{1,1} + \phi_{-1,-1}$. Maxima/minima are labelled with dark-yellow dots, whereas saddle points are marked with grey dots. Some critical points on the edges are actually identified due to the gluing instructions (e.g. all three maxima in the corners of the quotient space of a tetrahedron in panel (d) actually correspond to a single point on the folded surface). Their indices are therefore multiplied by a factor (1/3 in the case of a tetrahedron), so their sum yields the correct single-point index value on the respective folded surface. | 91 |
| 5.11 | Evolution of the state on the Klein bottle shown at (a) $t = 0$ (initial state), (b) $t = T/8$ and (c) $t = T/6$. Note that in (b) the probability density exhibits a rectangular symmetry while in (c) its symmetry is almost hexagonal. | 91 |
| 5.12 | Evolution of the state on the Möbius strip shown at (a) $t = 0$ (initial state), (b) $t = T/4$ and (c) $t = 5T/13$. In (a) the signs of the initial wavefunction at different copies of the quotient space are marked. | 92 |
| 5.13 | “Quantum motion of the continents” – evolution of the state on the double-sided square shown at (a) $t = 0$ (initial state in the form of the Earth surface conformally projected on the square quotient space, using Peirce quincuncial projection), (b) at $t = T/4$, we see four overlapping copies of the original map of the world. | 92 |

| | | |
|------|--|-----|
| 5.14 | “Quantum motion of the continents”, projected on the surface of a tetrahedron – the initial state in the form of the map of the Earth conformally projected on a tetrahedron; evolution of this state is presented at time (a) $t = 0$, (b) $t = T/128$, (c) $t = T/6$, and (d) $t = T/3$ | 93 |
| D.1 | To explain the calculations of focal lengths of lenses included in an asymmetric four-lens intersection. | 101 |

List of Tables

| | | |
|-----|--|----|
| 5.1 | Euler characteristics χ for different manifolds S , obtained by summing the indices of zero points of a vector field $\mathbf{v} = \text{grad } \phi$ (scalar function ϕ is presented in Fig. 5.10 for each manifold) defined on the respective quotient spaces σ | 90 |
|-----|--|----|

Acknowledgements

My research would not have been made possible without the help and guidance of others. In particular I would like to thank my supervisor Dr Johannes Courtial for being an enthusiastic, helpful, funny and patient PhD supervisor and for giving me the opportunity to participate in such an adorable research, meet new people and grow my scientific career. I truly appreciate our daily discussions, which made me feel to be his equal partner rather than a student. This thesis would not have been possible without his guidance and support throughout my PhD.

I would also like to thank Prof. Tomáš Tyc and Dr Simon Horsley for their invaluable expertise, inspiration, enthusiasm and for being a thorough and patient collaborators. I always enjoyed my visits in Brno and Exeter where we always had a good time together, which resulted in a wonderful collaboration. I also value Tomáš' patience when writing papers with me – I realise he sometimes had a hard work with editing my drafts.

I would also like to thank Prof. Miguel Alonso for giving me the opportunity to visit his research group in Rochester in 2017 and the University of Glasgow College of Science and Engineering for the funds that supported this experience. The visit to Rochester gave me the opportunity to work with great people and widely expand my physics knowledge.

I would like to thank all members of the optics group for making the optics department a place I enjoyed going to every day. Especially, I would like to thank Sara Restuccia, Stephen Oxburgh, Euan Cowie and Gergely Ferenczi for being such friendly and helpful pals: I truly appreciate your support and friendship! I would also like to thank Thomas Gregory for joining me in the gym and his patient proof-reading of my thesis drafts.

Most importantly, I want to thank my girlfriend Zuzana Vrabcová for her love, patience and support when writing this thesis. I truly value that she has always been there with love and encouragement, even when I was looking for a motivation to write. *Miluju Tě Zuzko a jsem moc rád že Tě mám!* Last but not least, I would like to thank my family and friends for being so encouraging and supporting me throughout my PhD.

Finally, this work was supported by the Engineering and Physical Sciences Research Council (grant number EP/N/509668/1).

Declaration of Authorship

I hereby declare that this thesis is the result of my own work, except where explicit reference is made to the work of others, and has not been presented in any previous application for a degree at this or any other institution.

Jakub Bělín

Publications

What follows is a list of papers written during my PhD which have either been published, or submitted.

1. Courtial, J., Tyc, T., Bělin, J., Oxburgh, S., Ferenczi, G., Cowie, E. N., & White, C. D. (2018). Ray-optical transformation optics with ideal thin lenses makes omnidirectional lenses. *Optics express*, 26(14), 17872-17888.
2. Bělin, J., & Tyc, T. (2018). Talbot effect for gratings with diagonal symmetry. *Journal of Optics*, 20(2), 025604.
3. Bělin, J., & Courtial, J. (2019). Imaging with two skew ideal lenses. *JOSA A*, 36(1), 132-141.
4. Bělin, J., Lembessis, V. E., Lyras, A., Aldossary, O., & Courtial, J. (2019). Arrays of dark optical traps on a toroidal surface. *Physical Review A*, 99(1), 013841.
5. Bělin, J., Horsley, S. A. R., & Tyc, T. (2019). Quantum mechanics and Talbot revivals on a tetrahedron. *Physical Review A*, 100(3), 033806.
6. Bělin, J., Tyc, T., Grunwald, M., Oxburgh, S., Cowie, E. N., White, C. D., & Courtial, J. (2019). Ideal-lens cloaks and new cloaking strategies. *Optics Express* 27(26), 37327-37336.
7. Tyc, T., Bělin, J., Oxburgh, S., White, C. D., Cowie, E. N., & Courtial, J. (2020). Glens combinations that satisfy the edge-imaging condition of transformation optics. *JOSA A* 37(2), 305-315.
8. Garcia, D. G., Chaplain, G. J., Bělin, J., Tyc, T., Englert, Ch., & Courtial, J. (2020). Optical triangulations of curved spaces. *Optica* 7(2), 142-147.
9. Bělin, J., Tyc, T., & Horsley, S. A. R. (2020). Quantum mechanics on the Möbius strip, Klein bottle, and other manifolds. Submitted to *Physical Review A*.
10. Chen, H., Tao, S., Bělin, J., Courtial, J. & and Miao, R. X. (2020). Transformation cosmology. Accepted for publishing in *Physical Review A*.

Sign conventions

To formulate imaging equations due to considered optical systems, we are using the following set of sign conventions throughout this thesis:

- All distances are measured in a Cartesian sense: directed distances above or to the right from the origin of the coordinate system are positive; below or to the left are negative.
- Counterclockwise angles are positive, whereas clockwise angles are negative.
- The radius of curvature of a surface is defined to be the directed distance from its vertex to its center of curvature.
- Light rays travel from left to right.

In our diagrams, the sign conventions defined above are visualised by arrows, pointing out of a reference point, line, or plane.

Introduction

One can rarely find a natural phenomenon as exciting and at the same time ordinary as light. Although most people use light as the primary source of information in their everyday life, a number of breakthrough theories (including the electromagnetism, the special theory of relativity and quantum field theory) had been developed in order to answer the question of what light is. Optics is the branch of physics that describes the behaviour and properties of light, including its interactions with matter and the construction of instruments that either process the light field to enhance an image for viewing, or to analyze and determine its properties. Particularly interesting materials and devices can be proposed by applying the mathematics of differential geometry and coordinate transforms; the science of designing optical devices and materials in this way is called *transformation optics* (TO). One could say that TO is the science of using a material structure to distort light-ray trajectories within the said structure, thereby changing the apparent shape and/or size of any object inside it. The actual structure is said to be in physical space, whereas the apparent structure as seen from the outside is said to be in a virtual space. TO [5, 8] is a relatively new, and highly active, research field and the ideas of TO have even been applied to other branches of physics, resulting, for example, in transformation thermodynamics [9, 10], acoustic cloaking [11], elastic cloaking [12], and seismic cloaking [13].

Practical realisations of the devices proposed by TO usually require highly advanced materials engineering and some designs can not be realised at all [14]. Due to these limitations, several research groups [15, 16] started thinking about building TO devices using sheets which produce a certain transformation of a ray bundle passing through them. As an example of what may be considered as a “beam-transforming” sheet, ideal thin lenses, generalised confocal lenslet arrays [17] or ray-rotation sheets [18] may all be regarded as such. The branch of TO regarding ray-transformation surfaces is sometimes called transformation optics with metasurfaces.

Since TO utilises the mathematics of differential geometry, the theory of curved spaces is very closely related. Curved spaces play an essential role in General Relativity, where gravity is regarded as a consequence of a curvature of space-time around a massive body. The beauty of General Relativity is that it provides fantastic and well-tested predictions at the same time, for example space-time singularities from which even light cannot escape – black holes. Many predictions of General Relativity have been astronomically observed, but some effects remain to be confirmed by observations. However, creating tabletop optical analogues of black holes is a new and promising approach [19, 20] that may hold the key to the elucidation of phenomena that are extremely difficult to study through direct astronomical observations. Indeed, transformation optics represents a highly promising tool for both designing and building setups which could mimic curved spaces and, in principle, space-times.

This thesis aims to propose new methods of designing omnidirectional optical devices, including invisibility cloaks and setups simulating the optics in curved spaces, using simple and well-known optical elements such as ideal lenses or optical wedges. We start briefly by reviewing the relevant concepts of geometrical optics in Chapter 1. These include Fermat’s principle of the stationary optical path length, Snell’s law of refraction, and the theory of classical optical imaging.

Applying these concepts, we will then investigate the imaging properties of systems of tilted lenses in Chapter 2. We will generalize the concept of the optical axis of an ideal thin lens and show that the imaging due to a system of two skew lenses can be regarded as that due to a single ideal lens when expressed in an appropriate object-sided and image-sided coordinate system. Our picture of imaging due to a pair of tilted lenses will be then employed to design a three-lens device, which performs an image rotation by an arbitrary angle $\Delta\alpha$ around the axis V of common intersection of all three included lenses.

In Chapter 3, we will then push the limits of geometrical optics even further when we develop a theory of building omnidirectional transformation optics devices using ideal thin lenses. Applying this theory, we will then propose several optical devices, including the omnidirectional lens and the invisibility cloak. The experimental feasibility of these devices is also presented in Chapter 3.

In Chapter 4, we will define a new method of building optical systems that simulate light-field propagation in both 2D and 3D curved spaces. Our method employs the equivalency of light-ray propagation in a curved space and in its respective unfolded net, equipped with “gluing instructions”, i.e. the rules defining how the edges of the unfolded net are identified. This “gluing” can be performed optically, using the so-called space-cancelling wedges, which are also presented in Chapter 4.

In Chapter 5, we will then investigate the wave mechanics on two-dimensional compact surfaces including the Klein bottle, Möbius strip and projective plane. For each manifold discussed, we will derive a full analytical solution of the Helmholtz equation, which is indeed equivalent to the stationary Schrödinger equation. This correspondence is then applied to study the quantum motion on the presented manifolds: we will show that the wavefunction exhibits perfect revivals on these surfaces and that quantum mechanics on them can be realised as simple diffraction experiments with a periodic grating with an appropriate structure of the unit cell.

Finally in Chapter 6, we summarise the results of this thesis and briefly describe future work that could be undertaken to advance the research already presented.

Chapter 1

Geometrical optics and first-order optics

In this chapter, we will provide the fundamentals of geometrical optics, first-order optics and the Gaussian imaging systems. All the provided concepts can be found in any textbook of optics, for example in Refs [21–24]. **Geometrical optics**, or ray optics, is a widely used concept in optics, where the propagation of light is described with geometric light rays. The ray in geometrical optics is an abstraction useful for approximating the paths along which light propagates. The assumptions on the light rays are:

- They have a zero thickness.
- They are straight lines in homogeneous optical materials.
- They can be reflected or refracted at smooth optical interfaces, with certain laws determining the outgoing ray directions.
- They can be absorbed, e.g. when hitting some optical aperture.
- Light rays can cross without influencing each other.

Although ray optics is widely used concept, geometrical rays are related to physical light beams only partially. There are similarities between geometrical light rays and real light beams: for example, a laser beam can be relatively narrow and propagates along a straight line in a homogeneous medium. However, real light beams always have a non-zero cross-section and exhibit the wave-optical phenomena, e.g. a diffraction. These wave-optical aspects can be suppressed if an incoherent light source is considered. Therefore, geometrical rays are only a rather abstract representation of actual, incoherent light rays. Their behavior can be derived from wave optics in the limiting case when the wavelength λ of a considered beam is much smaller than the dimensions of the optical system.

First-order optics is the study of ideal optical systems, i.e. optical systems without aberrations. It aims to analyse the imaging properties of the system, namely the image location and magnification. Throughout this thesis, we will mostly study the first-order optics of novel and unconventional optical systems.

1.1 Basic concepts of geometrical optics

1.1.1 Refractive index

The refractive index n is defined as a ratio of the velocity of light in vacuum c and the velocity of light v in a considered medium

$$n := \frac{c}{v}. \quad (1.1)$$

Of course, refractive index n is a constant in a homogeneous medium, whereas in an inhomogeneous medium the refractive index $n(\mathbf{x})$ is position-dependent.

1.1.2 Optical path length and Fermat's principle

Given an optical medium with refractive index $n(\mathbf{x})$, in which the light travels along a curve $\mathbf{x}(s) = (x_1(s), x_2(s), x_3(s))$ parametrized by a parameter s . Then, the optical path length OPL between points $\mathbf{Q} = \mathbf{x}(s_1)$ and $\mathbf{Q}' = \mathbf{x}(s_2)$ is given by the time required for light to travel between these two points

$$\text{OPL} = \int_{s_1}^{s_2} n(\mathbf{x}) dl, \quad (1.2)$$

where $dl = \sqrt{(dx_1/ds)^2 + (dx_2/ds)^2 + (dx_3/ds)^2} ds$ is a line element of a curve $\mathbf{x}(s)$. The optical path length lies in the core of probably the most important principle of optics — the Fermat's principle. Fermat's principle states that the path taken by a ray between two given points is the path with a stationary (maximal or minimal) optical path length. Among others, two important laws of ray optics can be derived from this principle: the law of reflection and the Snell's law of refraction. Both laws are depicted in Fig. 1.1.

1.1.3 Law of reflection

On a mirror-like surface, a light ray is reflected such that the angle α_r of the reflected ray equals minus the angle α_i of the incident ray (both measured from a normal to the surface)

$$\alpha_r = -\alpha_i \quad (1.3)$$

All normal, incident, and reflected rays are *coplanar*, i.e. they lie in the same plane.

1.1.4 Snell's law of refraction

When light rays are incident on an interface between two different transparent media with refractive indices n_1 and n_2 , some of the light rays are reflected, and some of them are transmitted. The propagation direction of the transmitted rays is modified according to the Snell's law of refraction

$$n_1 \sin \alpha_1 = n_2 \sin \alpha_2, \quad (1.4)$$

where angle α_1 is an angle formed by the incident ray with respect to the normal to the interface and α_2 is an angle between the transmitted ray and the normal. When propagating through a series of parallel interfaces, the quantity $n_i \sin \alpha_i$ is conserved.

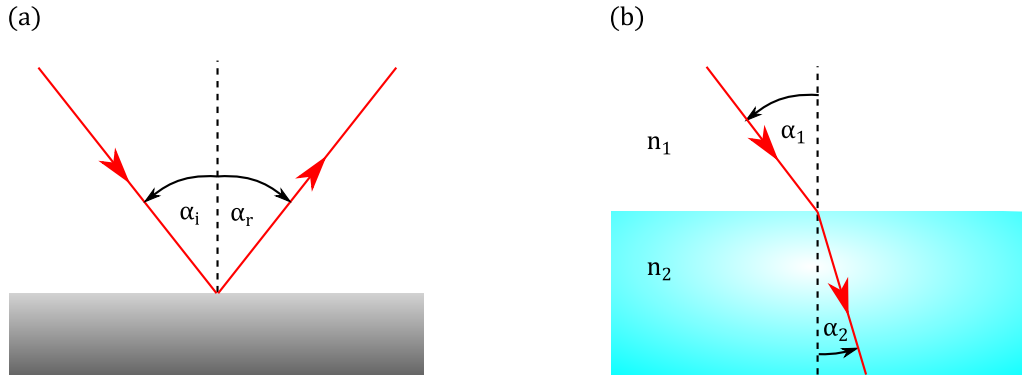


Figure 1.1: (a) Law of reflection and (b) Law of refraction; (a) Angle α_r the refracted ray makes with a normal to the surface equals minus the angle α_i the incident ray makes with the normal; (b) When traveling from a medium with refractive index n_1 to a medium with refractive medium n_2 , a light ray is refracted according to Snell’s law of refraction (1.4).

1.2 Imaging systems

Ray-optically speaking, an imaging system is any device, which changes the directions of light rays passing through such that all light rays emerging from a point \mathbf{Q} intersect again at point \mathbf{Q}' . Point \mathbf{Q} — an object — is said to be in an *object space* and point \mathbf{Q}' — an image — is said to be in an *image space*. Throughout this thesis, we will use the notation that unprimed entities refer to object space and primed entities to image space. The images are divided into two groups: real and virtual. Real images are created at the actual light-ray intersection, whereas the virtual image is created at an intersection of backward elongations of the light rays that otherwise do not intersect.

In this thesis, we will focus on *Gaussian* imaging systems, through which points are imaged to points, lines to lines and planes to planes. Such imaging corresponds to a *collinear transformation* of an object space. The object and image space are then called *conjugate spaces* and the corresponding object and image elements *conjugate elements*.

For a mathematical description of imaging due to the Gaussian imaging system, a **paraxial approximation** is commonly used. In this approximation, the light rays make small angles with the optical axis and consequently trigonometric functions can be expressed as linear functions of the angles, e.g. $\tan \alpha \approx \alpha$ and $\sin \alpha \approx \alpha$. Additionally, Gaussian imaging systems have these properties:

- They are rotationally symmetric and the axis of symmetry of the system is called *optical axis* or *z-axis*. Planes perpendicular to this axis are then called *transverse planes*.
- Transverse planes in an object space are imaged to transverse planes in an image space.
- Lines parallel to the optical axis in an object space map to conjugate lines in the image space such that they either intersect the axis at a common point (focal system), or are also parallel to the axis (afocal system). We will consider mostly focal systems throughout this thesis.
- In a focal system, lines parallel to the optical axis in an object space are imaged to lines that intersect at a common point F' — *image-sided focal point* — in an image

space. Similarly, lines intersecting at an *object-sided focal point* F in an object space are imaged to a set of lines parallel with the optical axis in an image space.

- We will define the *transverse magnification* m as a ratio of the image point transverse position h' to the corresponding object position h :

$$m := h'/h \quad (1.5)$$

A complete description of a Gaussian imaging system is given by the focal planes, principal planes and the *cardinal points*, located on the optical axis: the *principal points*, *focal points* (defined above) and the *nodal points*, all shown in Fig. 1.2.

Principal planes form a pair of conjugated planes such that an object-sided principal plane \mathcal{P} is imaged to an image-sided principal plane \mathcal{P}' with a magnification $m = +1$ in an image space. Object- and image-sided principal points P and P' are then the intersections of the object- and image-sided principal planes respectively with the optical axis. According to this definition, any light ray incident on the object-sided principal plane emerges the image-sided principal plane at the same transverse coordinates. This means that the imaging system can be treated as if all the refraction happened at the principal planes (see Fig. 1.2).

Object- and image-sided **focal planes**, \mathcal{F} and \mathcal{F}' , are simply the transverse planes containing the object- and image-sided focal points respectively. Object and image-sided **Focal lengths**, f^- and f^+ respectively, can be then defined as oriented distances from object and image-sided principal points to the respective focal points

$$f^+ = F' - P', \quad (1.6)$$

$$f^- = P - F. \quad (1.7)$$

Note that in a case $f^+ = -f^-$ (this applies, for example, to an ideal thin lens), the optical system is usually described by an effective focal length $f \equiv f^+$. Light rays intersecting at any point on the object-sided focal plane are imaged to a set of parallel lines in an image space. Analogously, a set of parallel lines in an object space is imaged to a set of lines intersecting at a point on an image-sided focal plane.

The object- and image-sided **nodal points** N and N' have the property that a ray incident on the object-sided nodal point will be refracted by the system such that it emerges from the image-sided nodal point, and with the same angle with respect to the optical axis. If the medium on both sides of the optical system is the same, then the nodal points coincide with the principal points.

1.3 Spherical interface as an imaging system

In this thesis, several non-conventional imaging systems are discussed. However, most of these systems are composed of lenses and it is therefore essential to understand imaging due to a lens. The following sections aim to bring the necessary insight to lens imaging. Since a conventional lens consists of two spherical interfaces, we will first show that a spherical interface between two media with refractive indices n_1 and n_2 is a Gaussian imaging system and derive the imaging equations due to such an interface. Then, we will apply the obtained results to describe an imaging due to a combination of two curved interfaces — a lens.

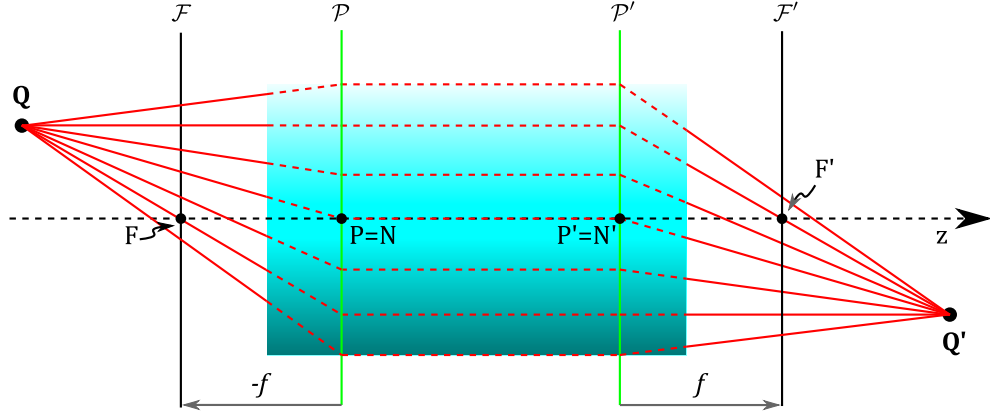


Figure 1.2: A Gaussian imaging system is fully described by its focal planes \mathcal{F} and \mathcal{F}' , principal planes \mathcal{P} and \mathcal{P}' and the cardinal points, located on the optical axis z : focal points F and F' , the principal points P and P' , and the nodal points N and N' . Nodal points coincide with the principal points if the optical medium on both sides of the optical system is the same. The imaging system (cyan box) redirects the light rays emerging from an object position Q to an image position Q' as if all of the refraction happened at the principal planes \mathcal{P} and \mathcal{P}' .

1.3.1 Cardinal points of a spherical interface

As mentioned before, a Gaussian imaging system is fully described by focal and principal planes and the cardinal points. Therefore, if a spherical interface of a radius r between two media with refractive indices n_1 and n_2 is a Gaussian imaging system, we should be able to find its cardinal points, located on its optical axis. We first find the focal points F and F' as shown in Fig. 1.3. Following the definition of focal points, the object-sided focal point F is found such that all the light rays from this point will become parallel after being refracted on the interface (see Fig. 1.3(a)). In a paraxial regime, the light rays are refracted according to a paraxial Snell's law

$$n_1\alpha = n_2\beta \quad (1.8)$$

If the light ray from the object-sided focal point F intersects the spherical interface at height y above the optical axis, from Fig. 1.3(a) one can deduce that $\beta \approx y/R$ and $\alpha = \beta + \delta$, where $\delta \approx -y/F$ in a paraxial approximation. Inserting these expressions to Eq. (1.8) yields

$$-\frac{n_1}{F} = \frac{n_2 - n_1}{R}. \quad (1.9)$$

Similarly, a position F' of an image-sided focal point can be found. Fig. 1.3(b) implies that $\alpha \approx y/R$ and $\beta \approx \alpha - \delta$, where $\delta \approx y/F'$. When these expressions are inserted to Eq. (1.8), the image-sided focal-point position F' can be found

$$\frac{n_2}{F'} = \frac{n_2 - n_1}{R}. \quad (1.10)$$

Comparing equations (1.9) and (1.10) yields $F/F' = -n_1/n_2$. We will use this relation later when we derive the imaging equations due to a spherical interface.

Following the definition, principal points P and P' can be found easily: Since the refraction happens only on the interface itself, both P and P' coincide with an intersection of the interface with the optical axis.

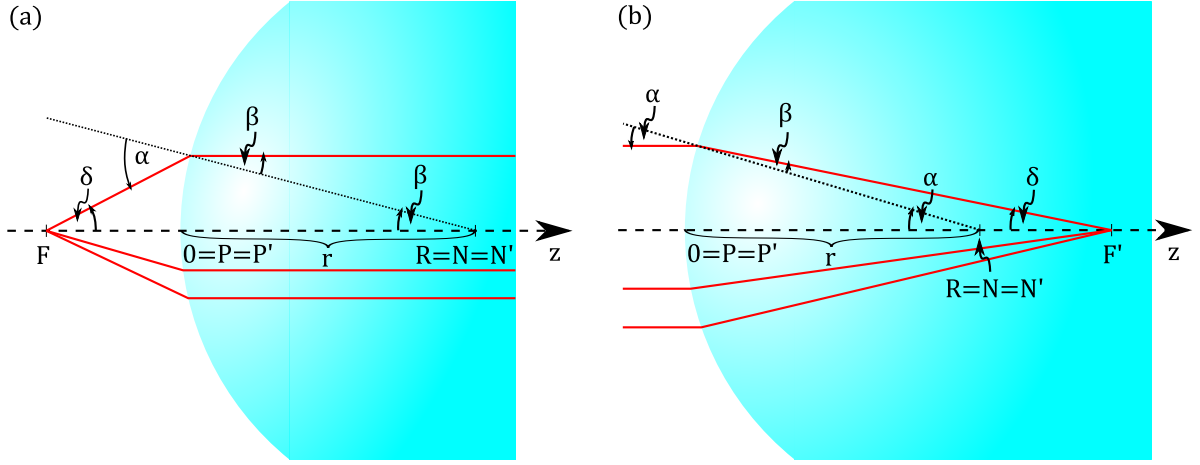


Figure 1.3: Cardinal points of a spherical interface; (a) rays (red lines) from an object-sided focal point F will form a parallel bundle after a transmission through the interface; (b) Rays which are all parallel to the optical axis will be transformed into rays which intersect in an image-sided focal point F' . Principal points P and P' coincide with an intersection of the surface with an optical axis, whereas the nodal points N and N' are situated at point R of the centre of curvature of the interface.

Similarly, one can find the positions of nodal points N and N' : any light ray pointing at position R of the centre of curvature is normal to the interface. Therefore, its direction remains unchanged after the transition through the interface. This follows the definition of nodal points and thus both object-sided and image-sided nodal points coincide with a point R of the centre of curvature of the interface (see Fig. 1.3).

1.3.2 Imaging equations due to a curved interface

After we have found the cardinal points of a spherical interface, we can derive the imaging equations due to such an interface. A diagram is presented in Fig. 1.4. Cartesian coordinate system is chosen such that z -axis coincides with the optical axis of the interface and the origin is placed at the intersection of the interface with z -axis. Consider an object at position $(0, h, q)$. To find the image position $(0, h', q')$, we employ two light rays: the first ray, labelled 1, passes through focal point F , whereas the second ray, labelled 2, travels parallel to the z -axis. Light ray 1 is refracted on the interface such that it becomes parallel with z -axis. Light ray 2, initially parallel to the z -axis, passes through the image-sided focal point F' after being refracted on the interface. Both light rays intersect at point $(0, h', q')$. From Fig. 1.4 one can deduce by similar triangles that

$$\frac{h - h'}{q'} = \frac{h}{F'} \quad (1.11)$$

$$\frac{h - h'}{q} = -\frac{h'}{F} \quad (1.12)$$

These two equations yield the first imaging equation

$$\frac{h'}{h} = -\frac{F}{F'} \frac{q'}{q} = \frac{n_1}{n_2} \frac{q'}{q}, \quad (1.13)$$

where we used the relation $F/F' = -n_1/n_2$, derived above. To find the relationship between positions q and q' , we will employ one more light ray, labelled 3, emerging the

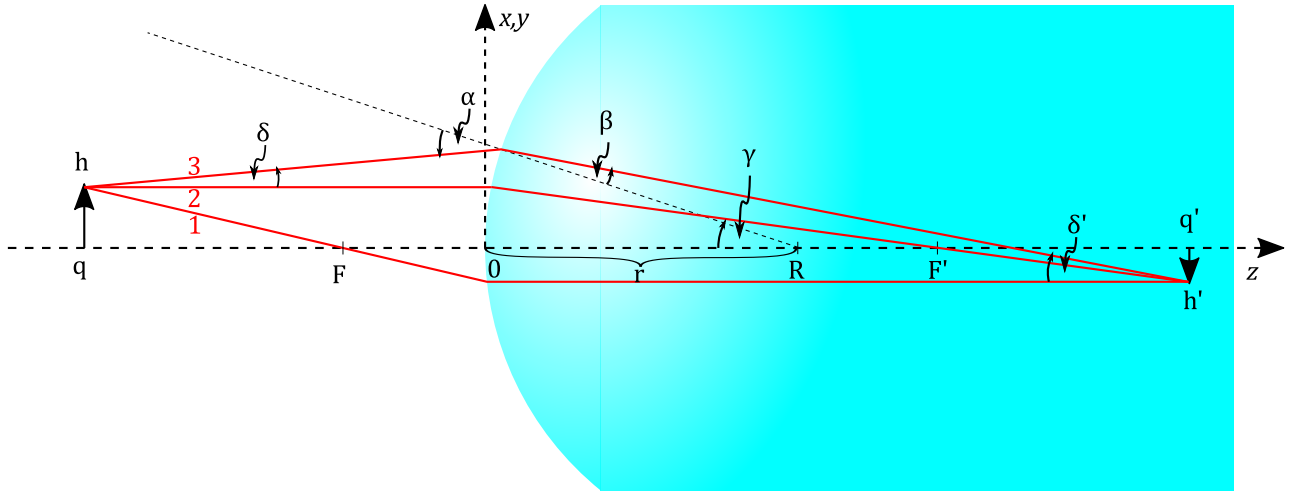


Figure 1.4: Mapping due to a spherical interface with a radius r between two optical media with refractive indices n_1 (white area) and n_2 (cyan area).

object at an angle δ with z -axis. This light ray intersects the interface at height y and makes angle $\alpha = \delta + \gamma$ with a normal to the interface (see Fig. 1.4). In a paraxial approximation, this ray is refracted on the interface according to a paraxial Snell's law, Eq. (1.8). The refracted part of the light ray makes an angle $\delta' = \gamma - \beta$ with the z -axis. In a paraxial approximation, $\delta \approx -(y - h)/q$, $\gamma \approx y/R$ and $\delta' \approx (y - h')/q'$. Inserting these expressions into Eq. (1.8) yields

$$n_1 \left(-\frac{y-h}{q} + \frac{y}{R} \right) = n_2 \left(\frac{y}{R} - \frac{y-h'}{q'} \right), \quad (1.14)$$

when re-arranged

$$-y \frac{n_1}{q} + y \frac{n_2}{q'} + \left(n_1 \frac{h}{q} - n_2 \frac{h'}{q'} \right) = y \frac{n_2 - n_1}{R}. \quad (1.15)$$

The term inside the bracket equals zero according to Eq. (1.13). Using this fact, we finally obtain a simple equation

$$-\frac{n_1}{q} + \frac{n_2}{q'} = \frac{n_2 - n_1}{R} \equiv \frac{1}{f}, \quad (1.16)$$

where we denoted $f \equiv R/(n_2 - n_1)$ the focal length of the interface. Together with Eq. (1.13), Eq. (1.16) is a general imaging equation for a curved interface, where the object is placed in a medium with refractive index n_1 and the image is created in a medium with refractive index n_2 . Note that R is not a radius but a position of the centre of curvature and thus can be both positive and negative.

1.4 Lens-imaging equations

We already showed that a single curved interface can be regarded as a Gaussian imaging device. In this section, we derive the imaging equations for a combination of two curved interfaces: a lens. To achieve this, we first employ Eq. (1.16) to find a z -position of an intermediate image $\mathbf{Q}'' = (0, h'', q'')$ of an object $\mathbf{Q} = (0, h, q)$ due to the first interface. Eq. (1.16) is then applied again to find the z -position of the final image is denoted $\mathbf{Q}' = (0, h', q')$, which is actually an image of \mathbf{Q}'' due to the second interface. Finally, the formula for a transverse magnification will be derived.

1.4.1 Thick lens

The choice of a coordinate system is depicted in Fig. 1.5. The first interface with a focal length f_1 maps a point \mathbf{Q} in an object space with refractive index n_1 to a point \mathbf{Q}'' in an image space with refractive index n_2 . The z -coordinates q and q'' respectively satisfy the Eq. (1.16)

$$-\frac{n_1}{q} + \frac{n_2}{q''} = \frac{1}{f_1}. \quad (1.17)$$

The second interface, of focal length f_2 and intersecting the z -axis at point d , then re-images \mathbf{Q}'' back from space with refractive index n_2 to space with refractive index n_1 . The z -position q' of the final image can be found using the following equation

$$-\frac{n_2}{q'' - d} + \frac{n_1}{q' - d} = \frac{1}{f_2}, \quad (1.18)$$

where d is a distance at which the second interface intersects the z -axis. If one combines Eqs. (1.17) and (1.18), the following complicated formula for an image position q' will be obtained

$$q' = d - \frac{n_1 f_2 (-f_1 n_2 q + d(f_1 n_1 + q))}{f_1 f_2 n_1 n_2 + (f_1 + f_2) n_2 q - d(f_1 n_1 + q)}. \quad (1.19)$$

However, if one denotes

$$f \equiv \frac{n_2 f_1 f_2}{n_2(f_1 + f_2) - d} \quad (1.20)$$

$$P \equiv \frac{n_1 d f_1}{n_2(f_1 + f_2) - d} = n_1 \frac{d f}{n_2 f_2} \quad (1.21)$$

$$P' \equiv d - \frac{n_1 d f_2}{n_2(f_1 + f_2) - d} = d - n_1 \frac{d f}{n_2 f_1}, \quad (1.22)$$

it can be easily shown that expression (1.19) can be rewritten to a form

$$q' = P' + \frac{n_1 f (q - P)}{n_1 f + q - P}, \quad (1.23)$$

or equivalently

$$-\frac{n_1}{q - P} + \frac{n_1}{q' - P'} = \frac{1}{f}, \quad (1.24)$$

which is a thick-lens-imaging equation. This equation reveals that the entity f , defined by Eq. (1.20), is the focal length of a thick lens. The meaning of P and P' will become clear when a formula for the transverse magnification h'/h is derived

$$\frac{h'}{h} = \frac{h' h''}{h'' h} = \frac{q' - d}{q'' - d} \frac{q''}{q} = \frac{n_1 n_2 f_1 f_2}{n_1 n_2 f_1 f_2 + [n_2(f_1 + f_2) - d]q - d n_1 f_1} = \frac{n_1 F}{n_1 F + q - P} = \frac{q' - P'}{q - P}. \quad (1.25)$$

We employed Eqs. (1.13), (1.20), (1.21), (1.22), (1.23) and (1.24) in our manipulations. Using Eqs. (1.24) and (1.25), one can see that point P is imaged to a point P' with a transverse magnification equal to +1. Therefore, points P and P' are the principal points of a thick lens.

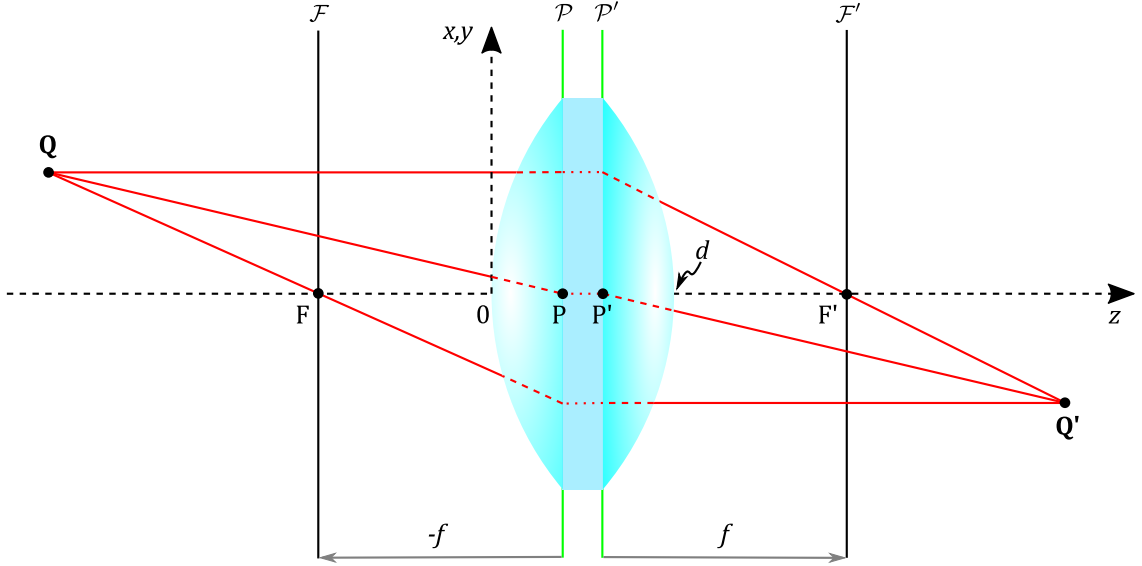


Figure 1.5: A thick lens consists of two spherical interfaces: the first interface intersects the z -axis at point $(0, 0, 0)$ and the second interface intersects the z -axis at point $(0, 0, d)$. The principal planes \mathcal{P} and \mathcal{P}' intersect the optical axis at points P and P' respectively, given by Eqs. (1.21) and (1.22). A thick lens maps a point \mathbf{Q} in an object space to a position \mathbf{Q}' in an image space, following the imaging equations (1.24) and (1.25).

1.4.2 Ideal thin lens

Probably the most commonly used mathematical model in geometrical optics is an ideal thin lens, which is a lens thin enough to assume that light rays bend only once, i.e. $d \rightarrow 0$. Assuming that the ideal thin lens is situated in a plane $z = 0$ and its centre coincides with the origin of the coordinate system, both principal points P and P' , given by Eqs. (1.21) and (1.22), equal zero at the limit $d \rightarrow 0$. The formula (1.20) for a focal length f then becomes $f = f_1 f_2 / (f_1 + f_2)$ and finally the imaging equations (1.24) and (1.25) are simplified to well-known imaging equations due to an ideal thin lens (given $n_1 = 1$)

$$-\frac{1}{q} + \frac{1}{q'} = \frac{1}{f}, \quad (1.26)$$

$$\frac{h'}{h} = \frac{q'}{q} = \frac{f}{q + f}. \quad (1.27)$$

Fig. 1.6(a) and (b) shows a standard graphical notation of a convex and concave thin lens respectively: a lens is *convex* when its both surfaces are of a positive curvature, which results in a positive focal length. On the other hand, surfaces of a *concave* lens are of a negative curvature and consequently the focal length of a concave lens is negative. However, we will treat lenses in a more general way; according to a chosen parameter regime, the same lens can be of both positive and negative focal length in systems discussed in this thesis. For this reason, we will depict thin lenses as cyan lines, without any arrows on the ends (see Fig. 1.6(c)).

For numerical simulations, it is convenient to formulate a vector form of an imaging equation between object position \mathbf{Q} and image position \mathbf{Q}' , due to an ideal thin lens with a principal point position $\mathbf{P} = (P_x, P_y, P_z)$ and the optical-axis orientation given by a unit vector $\hat{\mathbf{z}}$. Such an equation can be deduced from Fig. 1.6(d). Using a light ray (red line) passing through the principal point \mathbf{P} , it is easy to see that $\mathbf{Q}' - \mathbf{P} = (q'/q)(\mathbf{Q} - \mathbf{P})$,

where $q = (\mathbf{Q} - \mathbf{P}) \cdot \hat{\mathbf{z}}$ and $q' = (\mathbf{Q}' - \mathbf{P}') \cdot \hat{\mathbf{z}}$ are projections of vectors $(\mathbf{Q} - \mathbf{P})$ and $(\mathbf{Q}' - \mathbf{P}')$ respectively in the direction of the optical axis $\hat{\mathbf{z}}$. The magnifying factor therefore equals $q'/q = f/(q + f) = f/((\mathbf{Q} - \mathbf{P}) \cdot \hat{\mathbf{z}} + f)$ (using Eq. (1.27)) and the resulting imaging equation is finally of the form

$$\mathbf{Q}' - \mathbf{P}' = \frac{f}{(\mathbf{Q} - \mathbf{P}) \cdot \hat{\mathbf{z}} + f} (\mathbf{Q} - \mathbf{P}). \quad (1.28)$$

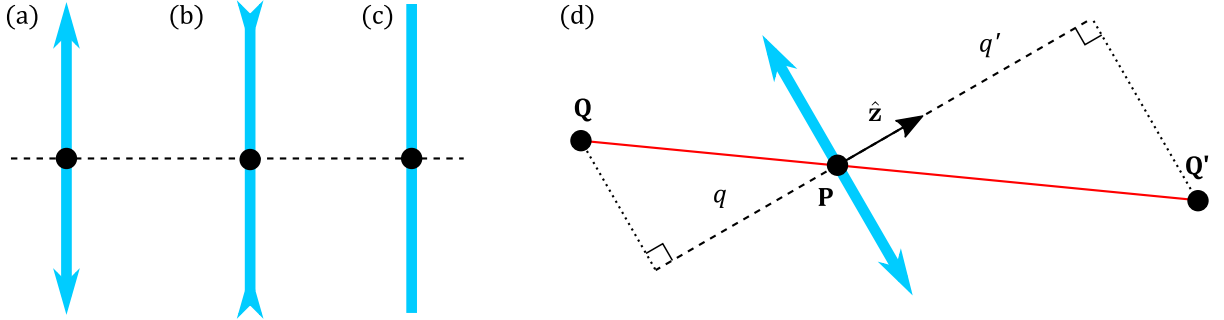


Figure 1.6: (a) Convex lens, (b) concave lens, (c) notation of an ideal thin lens used in this thesis. (d) Imaging due to a lens with a general principal point position \mathbf{P} and orientation of an optical axis $\hat{\mathbf{z}}$.

1.5 Generalised lens-glens

We have generalised the concept of ideal thin lenses such that the object and image-sided focal lengths may be different from each other. We name such a device a glens, a generalised lens [25].

To describe imaging due to a glens, consider a coordinate system such that the z -axis coincides with an optical axis of the discussed glens and the glens itself lies in $z = 0$ plane. The focal lengths are then identified by the a coordinate of the corresponding focal point, whereby the object-sided focal length is called f^- , whereas the image-sided focal length is called f^+ . By this convention, an ideal lens of focal length f is a glens with focal lengths $f^+ = f$ and $f^- = -f$. In contrast with an ideal thin lens, where principal and nodal point coincide and lie in a plane of the lens, the nodal point N does not coincide with the principal point in a glens. The z coordinate of N , the nodal distance ν , can be deduced from Fig. 1.7(a). Because of the congruence of the triangles F^-SP and NIF^+ , the nodal distance ν equals

$$\nu = f^+ + f^-. \quad (1.29)$$

To obtain the imaging equations, we will employ Fig. 1.7(b). Again, using the congruences of triangles, one can see that

$$\frac{h}{q - f^-} = -\frac{h'}{f^-}, \quad (1.30)$$

$$\frac{h}{f^+} = -\frac{h'}{q' - f^+}, \quad (1.31)$$

when h and h' are eliminated

$$f^+ f^- = (q - f^-)(q' - f^+), \quad (1.32)$$

can be finally rearranged to a following form

$$\frac{f^-}{q} + \frac{f^+}{q'} = 1. \quad (1.33)$$

The formula for a transverse magnification h'/h can be derived from Eq. (1.30)

$$\frac{h'}{h} = -\frac{f^-}{q - f^-} = -\frac{f^- q'}{f^+ q}. \quad (1.34)$$

Note that Eqs. (1.33) and (1.34) are exactly of the form of the imaging equations due to a spherical interface for $f^- = -n_1 R / (n_2 - n_1)$ and $f^+ = n_2 R / (n_2 - n_1)$. One can check easily that $f^- + f^+ = R$ in this case, which is indeed the nodal point position for a spherical interface.

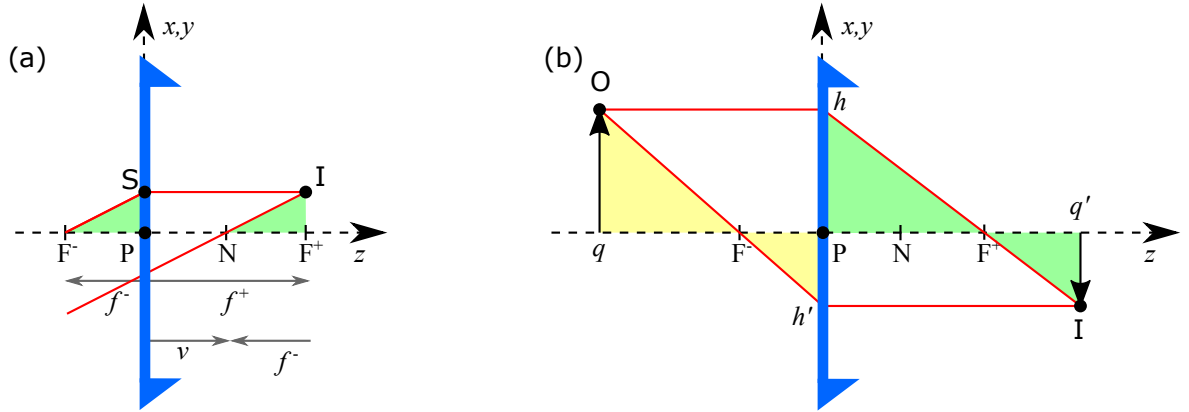


Figure 1.7: (a) Location of the nodal point of a lens. Two parallel light rays are incident on the lens: one of them passes through the negative focal point, F^- , and intersects the lens at position S . The other ray passes through the nodal point N and intersects the first light ray at position I . Clearly, the triangles F^-SP and NIF^+ (shaded green areas) are congruent. (b) Imaging due to a lens. Again, two light rays, emerging from a point O , are incident on the lens: one of them passes through the object-sided focal point, F^- , whereas the other light ray passes through an image-sided focal point, F^+ . Both light rays intersect at point I after transmission through the lens. Similarity of triangles OqF^- and $h'PF^-$ (yellow shaded areas) implies Eq. (1.30). Analogously, similarity triangles hPF^+ and $Iq'F^+$ (green shaded areas) implies Eq. (1.31).

1.6 Projective space and Central Collineation

Imaging due to all spherical interface, ideal thin lens and glens are examples of a *central collineation*. In this section, we will discuss the properties of collineations, which are relevant for the following chapters. Before doing so, the *projective space* needs to be defined: given a vector space V over a field K , the projective space $\mathbf{P}(V)$ induced by V is the set $(V - \{0\}) / \sim$ of equivalence classes of nonzero vectors in V under the equivalence relation \sim defined such that for all vectors $\mathbf{u}, \mathbf{v} \in V - \{0\}$, $\mathbf{u} \sim \mathbf{v}$ if $\mathbf{v} = \lambda \mathbf{u}$, for some $\lambda \in K - \{0\}$ [26]. If V has some finite dimension $\dim(V) = n \geq 1$, the dimension of projective space $\mathbf{P}(V)$ has a dimension $\dim(\mathbf{P}(V)) = n - 1$. An example of the projective space $\mathbf{P}(\mathbb{R}^3)$ is depicted in Fig. 1.8(a).

A *collineation* is a bijective map (a map $\varphi : A \rightarrow B$ from set A to set B such that (i) preimages are unique, i.e. $(a_i \neq a_j) \rightarrow (\varphi(a_i) \neq \varphi(a_j))$ for each $a_i, a_j \in A$, and (ii) each point $b \in B$ has a preimage [27]) from one projective space to another, or from a projective space to itself, such that the images of collinear points are collinear (i.e. points are mapped to points and lines are mapped to lines again) [28]. It follows immediately from this definition that the line segment between points X and Y must be mapped to the line between the respective images X' and Y' (see Fig. 1.8(b)). Another observation is that the set of all collineations of the projective space form a group under the binary operation of composition of maps, called the *collineation group*. One obvious consequence of the group structure of collineations is that a combined imaging due to several lenses is a collineation again.

A collineation of projective space is called a *central collineation* if there exists a hyperplane H (called the axis of the collineation) and a point C (called the center of the collineation) such that:

- Each point of H is a fixed point, i.e. it is mapped back to itself
- Each line through C is a fixed line, i.e. it is mapped back to itself.

If the center of collineation C lies on the axis of collineation H , then we call the collineation an *elation*, and when it doesn't we call the collineation a *homology*.

Translating to the language of collineations, imaging due to a thin lens is an elation since the axis of collineation is the plane of the lens and the center of collineation is a principal point of the lens (see Fig. 1.8(b)). On the other hand, imaging due to a glens (and the spherical interface in a paraxial approximation) corresponds to a homology as the center of collineation coincides with a center of curvature of the interface.

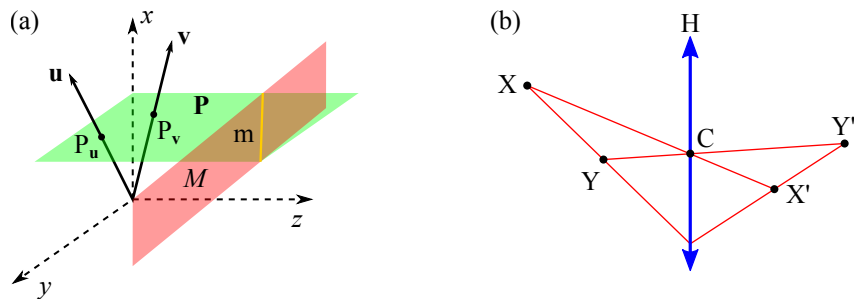


Figure 1.8: (a) Visualisation of a projective space $\mathbf{P}(\mathbb{R}^3)$: vectors $\mathbf{u}, \mathbf{v} \in \mathbb{R}^3$ are “projected” to points $P_{\mathbf{u}}$ and $P_{\mathbf{v}}$ in $\mathbf{P}(\mathbb{R}^3)$ and plane M through the origin is mapped to line m in $\mathbf{P}(\mathbb{R}^3)$. (b) Imaging due to an ideal thin lens is an example of elation.

Chapter 2

Lens-imaging coordinates and imaging with unusual combinations of ideal lenses

2.1 Introduction

In the first chapter, we have presented the basic principles of geometrical optics and studied simple first-order imaging systems. In the following chapters, we will employ these concepts and present unusual combinations of lenses with unprecedented imaging properties.

We showed that ideal-lens imaging corresponds to a central collineation and therefore has a group structure, i.e. combining two collineations yields collineation again. The combined image due to a system of two lenses therefore coincides with a collineation of the object-space structure.

At this point, a question might arise: does an image due to a combination of two lenses compare to an image due to a single lens? The answer might sound trivial since lens imaging corresponds to a collineation and therefore has a group structure. However, collineation is a more general concept than lens imaging and thus combined imaging due to a combination of lenses may result in a mapping, corresponding to a collineation other than lens-imaging.

It is well known that a coaxial combination of lenses can be elegantly described as a single thick lens, i.e. object- and image-sided principal planes, in general, neither coincide with each other, nor do they coincide with the principal planes of the individual lenses. This is done by describing object- and image-space positions in a specific coordinate system, constructed such that the imaging equations due to the two-lens combination have the same form as the standard ideal-lens equations.

Inspired by this approach, we will investigate various geometries of two lenses in this chapter. We will reveal some of the potential applications of systems of lenses, which are not restricted to a paraxial regime; although standard lenses are optimised for a paraxial regime, the current progress in metalenses makes researchers to believe that even closer approximations of ideal thin lenses will be built in the near future (see Sec. 2.7.2). We will show that it is possible to find the “*lens-imaging coordinates*”, in which the mapping between object and image space is exactly of the form of ideal-lens imaging. Such coordinates can be found even for a system which appears unlikely to be described as a single lens: two lenses making an angle. Later, we will apply the lens-imaging coordinates of two skew lenses to design an image rotator, composed of three ideal lenses.

2.1.1 Contributions

The work in this chapter was carried out by myself with help from Dr Johannes Courtial and Dr Gergely Ferenczi, who helped me with programming the simulations.

2.2 Lens-imaging coordinates

Throughout this chapter, we will discuss imaging properties of numerous combinations of two lenses. The key ingredient of our description is a coordinate system (u, v, w) , in which the imaging equations are of the form of ideal-lens imaging equations. We will call such coordinates “*lens-imaging coordinates*”. In case of two coaxial lenses (sharing their optical axis), lens-imaging coordinates can be easily constructed from the optical axis and the principal planes of an optical system.

For a combination of skew lenses, however, the desired single-lens description becomes more complicated since the standard definitions of the optical axis, transverse planes, cardinal points etc. lose their meaning. For example, the definition of the optical axis, provided in Sec. 1.2, “the axis of symmetry of the system is called the optical axis”, can no longer be applied as there is no axis of symmetry of a system of two skew lenses. The requirements of the transverse planes, i.e. planes perpendicular to the optical axis which are imaged due to the optical system to planes perpendicular to the optical axis 1.2, need to be scrutinised. Perhaps worse, Fig. 2.1 shows that a combination of skew lenses exhibits telescope-like behaviour for certain ray bundles, which seems to be even incompatible with a description as a single lens.

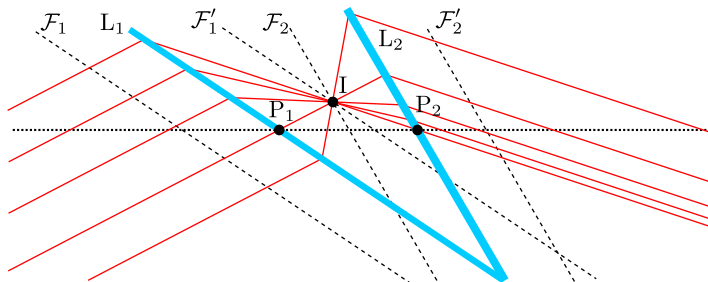


Figure 2.1: Telescope-like behaviour of a combination of two skew lenses, L_1 and L_2 . An array of parallel light rays (red lines) is incident on lens L_1 with a direction such that the light rays are focused to a point on the intersection line I between the image-sided focal plane of lens L_1 , \mathcal{F}'_1 , and the object-sided focal plane of lens L_2 , \mathcal{F}_2 (black dashed lines). Because I lies in the object-sided focal plane of L_2 , the light rays become parallel again when emerging from lens L_2 . Points P_1 and P_2 are the principal points of the respective lenses.

In light of the observations in the previous paragraph, it seems to be very challenging to find the corresponding lens-imaging coordinates, in which the imaging due to a pair of skew lenses can be described as a standard single-lens imaging. One attempt at construction of lens-imaging coordinates for a general optical system has been presented in an earlier work performed by Buchroeder on a choice of coordinate systems that simplifies any collinear mapping between object and image space [29]. In his thesis, Buchroeder starts from a general collinear mapping, which can be written in the form (Eqn (2.1) in

Ref. [29])

$$x' = \frac{a_1x + b_1y + c_1z + d_1}{a_0x + b_0y + c_0z + d_0}, \quad (2.1)$$

$$y' = \frac{a_2x + b_2y + c_2z + d_2}{a_0x + b_0y + c_0z + d_0}, \quad (2.2)$$

$$z' = \frac{a_3x + b_3y + c_3z + d_3}{a_0x + b_0y + c_0z + d_0}, \quad (2.3)$$

where a_i, b_i, c_i and d_i ($i = 0, \dots, 3$) are constants, and x, y, z and x', y', z' are the coordinates of the object and image positions, measured in the same Cartesian coordinate system. Then, Buchroeder showed that these equations simplify significantly if object and image space are described by different Cartesian coordinate systems. Namely, the object-sided coordinate system (x, y, z) was chosen such that the z -axis is perpendicular to the object-space focal plane (plane such that $a_0x + b_0y + c_0z + d_0 = 0$) and the z -axis coincides with a line which is imaged due to the optical system to a line Z' , perpendicular to the image-sided focal plane. The image-sided coordinate system (x', y', z') is then chosen such that the z' coincides with line Z' and plane $x'y'$ is parallel to an image-sided focal plane. If the origins of both systems (x, y, z) and (x', y', z') are conjugate to each other (object-image), one can obtain following equations (Eqn (2.7) in Ref. [29])

$$x' = \frac{ax}{z+d}, \quad y' = \frac{by}{z+d}, \quad z' = \frac{cz}{z+d}, \quad (2.4)$$

where a, b, c and d are constants. Let us call these coordinates *Buchroeder coordinates*. One can see easily that Eqs. (2.4) can be transformed to a form of ideal-lens imaging equations by scaling $x' \rightarrow dx'/a, y' \rightarrow dy'/b, z' \rightarrow dz'/c$, which yields

$$x' = \frac{fx}{z+f}, \quad y' = \frac{fy}{z+f}, \quad z' = \frac{fz}{z+f}, \quad (2.5)$$

where the focal length f is given by the constant d . We call these coordinates *scaled Buchroeder coordinates*.

In the following lines, we will present an alternative set of lens-imaging coordinates for a pair of two skew lenses. We will consider ideal thin lenses; the implementation of real lenses will be discussed in section 2.7.2. Our construction starts with a generalised concept of the optical axis: in our lens-imaging coordinates, optical axes in both object and image space are identified with a single straight line. Later, we will find the transverse planes and the cardinal points and formulate the corresponding coordinate transformations between Cartesian and the lens-imaging coordinates.

We first review the standard description of coaxial pairs of lenses as a single lens (section 2.3.1). In Sec. 2.3.2, we will show that even two coplanar lenses with offset principal points can be regarded as a single lens. We then motivate our construction of lens-imaging coordinates for single-lens imaging (section 2.3) and show, in section 2.4, that it works. We then employ the obtained lens-imaging coordinates for imaging due to a combination two lenses with coinciding principal points 2.5 and for an image rotation with three skew lenses 2.6. Finally, we discuss several aspects not mentioned elsewhere in section 2.7.

2.3 Motivation for lens-imaging coordinates

The aim is to describe imaging due to a pair of (in general) tilted lenses as that of a single ideal lens, in suitable coordinates. We require symmetric and affine coordinates (so

parallel lines remain parallel and ratios between points on a straight line are preserved) in which the imaging equations have the form of ideal-lens imaging equations. To achieve this goal, we will generalise some concepts, e.g. the optical axis of the general two-lens system will no longer coincide with the axis of symmetry of the system (since there is none).

2.3.1 Two coaxial lenses

We start with well-understood system of two coaxial lenses, i.e. lenses whose optical axes coincide. Example of such a system is shown in Fig. 2.2(a). Lens L_1 , of focal length f_1 , is placed at $z = 0$ plane and its optical axis coincides with z -axis. Lens L_2 , of focal length f_2 , is then located in $z = d$ plane and its principal point lies at position $(0, 0, d)$. To obtain imaging equations due to a pair of coaxial lenses, we can successively apply the thin-lens imaging equation first due to L_1 and then due to L_2 to get an image position \mathbf{Q}' of an object \mathbf{Q} . We have performed a very similar procedure in Sec. 1.4, where the thick-lens equation was derived. Indeed, given $n_1 = n_2 = 1$, one can see that a pair of coaxial lenses of focal lengths f_1 and f_2 , separated by d , is equivalent to a single thick lens with focal length f and principal-point positions given by the following formulas

$$f \equiv \frac{f_1 f_2}{f_1 + f_2 - d}, \quad (2.6)$$

$$P \equiv \frac{d f_1}{f_1 + f_2 - d} = \frac{d f}{f_2}, \quad (2.7)$$

$$P' \equiv d - \frac{d f_2}{f_1 + f_2 - d} = d - \frac{d f}{f_1}. \quad (2.8)$$

Therefore, the imaging equations due to a pair of coaxial lenses are the same as for a thick lens (see Sec. 1.4) with a focal length and principal points, given by Eqs. (2.6), (2.7) and (2.8), i.e.

$$-\frac{1}{z - P} + \frac{1}{z' - P'} = \frac{1}{f}, \quad \frac{x'}{x} = \frac{y'}{y} = \frac{z' - P'}{z - P}. \quad (2.9)$$

In the language of collineations, imaging due to a pair of coaxial lenses is obviously a collineation. However, it is not a central collineation as there is no axis of collineation H and no center of collineation C in this case.

2.3.2 Two coplanar non-coaxial lenses

A more exotic system is a pair of coplanar lenses, i.e. lying in the same plane, e.g. $z = 0$. A principal point of a lens L_1 (of focal length f_1) is situated at the origin of a coordinate system, whereas the principal point of lens L_2 (of focal length f_2) is offset by h in a transverse direction (see Fig. 2.2(b)).

Now we will derive an imaging equation due to such a two-lens system. Since the combined focal length f , given by Eq. (2.6), does not depend on the transverse offset of the principal points of included lenses, we can simply use Eq. (2.6) to find the combined focal length f (given $d = 0$)

$$f = \frac{f_1 f_2}{f_1 + f_2}. \quad (2.10)$$

and the z coordinates of the principal points, given by Eqs. (2.7) and (2.8), both equal to zero. Since both object and image-sided principal points of a considered two-lens system lie in the same transverse plane, these two principal points must coincide. To find the

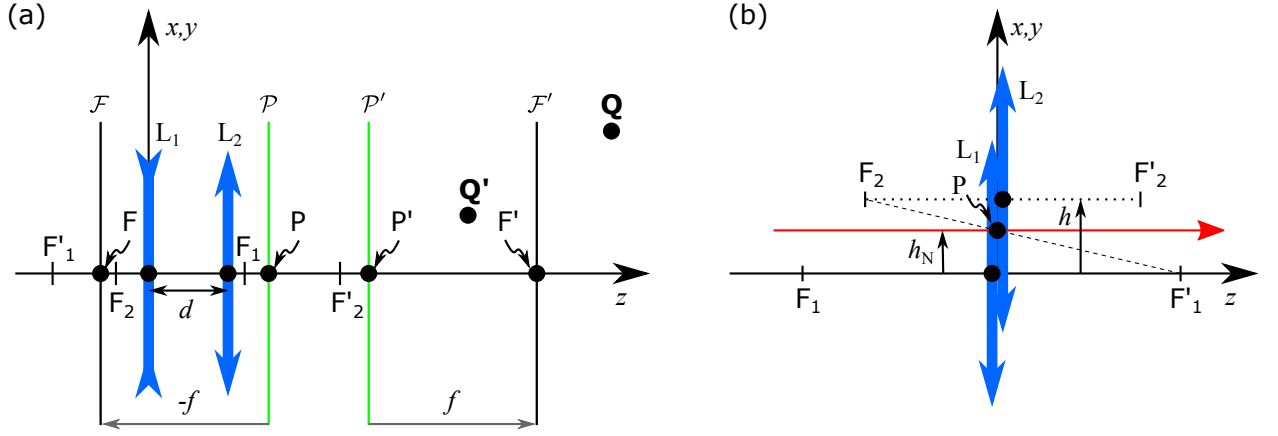


Figure 2.2: (a) A system of two coaxial lenses, marked L_1 and L_2 , provides the same mapping of an object-space point Q to an image-space point Q' as a single thick lens, of focal length f (given by Eq. (2.6)); focal planes of the combination of lenses L_1 and L_2 are labelled \mathcal{F} and \mathcal{F}' , whereas \mathcal{P} and \mathcal{P}' are the corresponding principal planes; (b) Two coplanar non-coaxial lenses: lens L_2 is offset by h with respect to lens L_1 . This two-lens system can also be regarded as a single ideal lens, of focal length f , given by Eq. (2.10). To find the principal point P of this optical system, we employ a light ray (red arrow), which travels parallel to the z -axis and remains undeviated after the transmission through both lenses L_1 and L_2 .

transverse position of this combined principal point, we employ the fact that any light ray passes through the principal point undeviated.

Fig. 2.2(b) shows one example of such a light ray, travelling parallel to z -axis at height h_N above that axis. This ray is first incident on lens L_1 at point P . L_1 then redirects the ray towards its image-sided focal point F'_1 in a direction which is exactly a direction from object-sided focal point F_2 of lens L_2 to the point P . According to a definition of an object-sided focal point (all light rays intersecting in an object-sided focal point propagate parallel to an optical axis after transition through an imaging system), the light ray propagates parallel with z -axis again after transmission through both lenses L_1 and L_2 . Using a similarity of triangles, one can see that

$$\frac{h_N}{f_1} = \frac{h - h_N}{f_2}, \quad (2.11)$$

when solved for h_N

$$h_N = h \frac{f_1}{f_1 + f_2}. \quad (2.12)$$

Indeed, one can check easily that imaging equation due to a pair of coplanar non-coaxial lenses (of focal lengths f_1 and f_2) is of a form of an ideal-lens imaging equation due to a lens of focal length f , given by Eq. (2.10), with a principal point offset by h_N (given by Eq. (2.12)) in a transverse direction.

2.3.3 Lens-imaging coordinates for an ideal thin lens

Before we find the lens-imaging coordinates for a pair of tilted lenses, it is instructive to first show a generalised concept of an optical axis to the particularly simple example of a single lens.

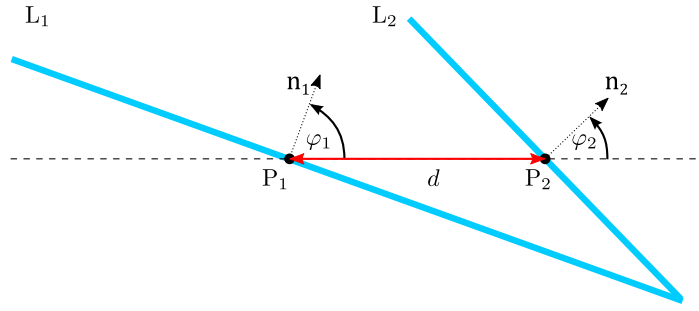


Figure 2.4: System of two tilted lenses L_1 and L_2 (cyan lines). We chose the optical axis for this two-lens system to coincide with a line passing through both principal points P_1 and P_2 . Angles, formed by the normals of the respective lenses and the two-lens optical axis, are denoted φ_1 and φ_2 .

2.3.4 Two-lens optical axis

We just showed that any straight line through the principal point of an ideal thin lens is a perfectly good choice of an optical axis for that lens. Now we will apply this observation to find a common optical axis of a pair of tilted lenses, L_1 and L_2 . We will use one special property of the optical axis of a standard, rotationally symmetric Gaussian system, namely that the optical axis is imaged back to the same line due to the system. It is easy to find such a line even for a case of two skew lenses: a straight line through the principal points P_1 and P_2 . This line is therefore an excellent candidate for the optical axis of the combination. We will refer to it as *two-lens optical axis*.

For an object lying on such two-lens optical axis, it is easy to derive an imaging equation due to a two-lens combination. Similar to sec. 2.3.3, let us denote w the coordinate along the two-lens optical axis, with the origin at principal point P_1 of lens L_1 . The projected focal lengths g_1 and g_2 of lenses L_1 and L_2 can be calculated using Eqn. (2.14)

$$g_1 = \frac{f_1}{\hat{\mathbf{w}} \cdot \hat{\mathbf{n}}_1}, \quad g_2 = \frac{f_2}{\hat{\mathbf{w}} \cdot \hat{\mathbf{n}}_2}, \quad (2.17)$$

where $\hat{\mathbf{n}}_1$ and $\hat{\mathbf{n}}_2$ are the normals to the respective lenses (see Fig. 2.4). Since the two-lens optical axis is one of the lens-imaging coordinates, imaging on this axis follows the standard ideal-lens imaging equation. Therefore, the effective focal length f , the *two-lens focal length*, can be calculated using Eqn. (2.6),

$$f = \frac{g_1 g_2}{g_1 + g_2 - d}, \quad (2.18)$$

and use the standard formulas in Eqs. (2.7) and (2.8) to calculate the values P_w and P'_w of the w coordinate of the object and image-sided two-lens principal points, P and P' , as

$$P_w = \frac{df}{g_2}, \quad (2.19)$$

$$P'_w = d - \frac{df}{g_1}. \quad (2.20)$$

Finally, the imaging equation between object position w and the respective image position w' is of the desired standard form

$$-\frac{1}{w - P_w} + \frac{1}{w' - P'_w} = \frac{1}{f}. \quad (2.21)$$

So far, our choice of two-lens optical axis seems to be a highly suitable pick.

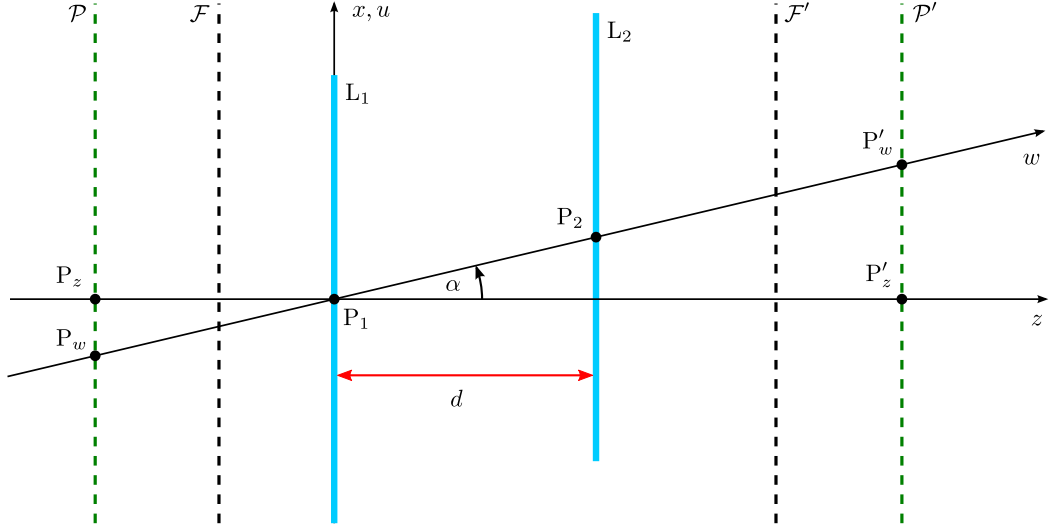


Figure 2.5: System of two parallel, non-coaxial lenses L_1 and L_2 . The black dashed lines represent the focal planes of this system, whereas the green dashed lines correspond to its principal planes with principal points $P = (P_z \tan \alpha, 0, P_z)$ and $P' = (P'_z \tan \alpha, 0, P'_z)$, when expressed in Cartesian coordinates (x, y, z) .

2.3.5 Example: Parallel, but non-coaxial lenses

Our search for lens-imaging coordinates of two skew lenses yielded a promising candidate for an optical axis, or w -axis. In the following sections, we will complete the set of lens-imaging coordinates with transverse planes. First, it is instructive to do this to completion for a simple but non-trivial example: a system of two parallel lenses. Unlike in section 2.3.1, this time the lenses are offset relative to each other in the x direction (Fig. 2.5).

The coordinate system is chosen in a following way: the w coordinate coincides with the two-lens optical axis, passing through the principal points P_1 and P_2 . The remaining two coordinates, marked u and v , are set to be parallel to x and y , respectively. The coordinate transformation between the coordinates (u, v, w) and Cartesian coordinates (x, y, z) is then given by formula

$$u = x - z \tan \alpha, \quad v = y, \quad w = \frac{z}{\cos \alpha}. \quad (2.22)$$

We will show that (u, v, w) are indeed lens-imaging coordinates by comparing the standard imaging equations (2.9), with a substitution $(x, y, z) \rightarrow (u, v, w)$, with those obtained by successive applying an ideal-thin lens imaging equation: first due to lenses L_1 and then due to lens L_2 . The standard thick-lens equations, with a substitution (u, v, w) for (x, y, z) , are of the form

$$-\frac{1}{w - P_w} + \frac{1}{w' - P'_w} = \frac{1}{F}, \quad \frac{u'}{u} = \frac{v'}{v} = \frac{w' - P'_w}{w - P_w}, \quad (2.23)$$

where $P_w = P_z / \cos \alpha$, $P'_w = P'_z / \cos \alpha$ (P_z and P'_z are given by Eqs. (2.7) and (2.8)), and $F = f / \cos \alpha$, where f is given by the Eqn (2.6). One can apply the transformation (2.22) to express these imaging equations in Cartesian coordinates. Inserting the expressions for the parameters P_w, P'_w and F finally yields

$$-\frac{1}{z - P_z} + \frac{1}{z' - P'_z} = \frac{1}{f}, \quad \frac{x' - P'_z \tan \alpha}{x - P_z \tan \alpha} = \frac{y'}{y} = \frac{z' - P'_z}{z - P_z}. \quad (2.24)$$

It is easy to see the effect of the transverse offset of lens L_2 : it simply causes a transverse shift of the resulting image by a quantity $(P'_z - P_z) \tan \alpha$ in the direction of the lens displacement (x -direction in this case).

Note that equations (2.24) can be transformed into the standard form of Eqs. (2.13), simply by moving the origins of the coordinate systems in such that $(x, y, z) \rightarrow (x - P_z \tan \alpha, y, z - P_z)$ in an object space and $(x', y', z') \rightarrow (x' - P'_z \tan \alpha, y', z' - P'_z)$ in an image space. The coordinates $(x - P_z \tan \alpha, y, z - P_z)$ and $(x' - P'_z \tan \alpha, y', z' - P'_z)$ are thus lens-imaging coordinates as well, actually the scaled Buchroeder coordinates for this combination.

Eqs. (2.24) can be indeed obtained by successive applying the ideal-thin-lens imaging equations due to lenses L_1 and L_2 . This proves that coordinates (u, v, w) are the lens-imaging coordinates for a system of two parallel, but non-coaxial lenses. At the same time, it makes our concept of the two-lens optical axis stronger since it is possible to match it with other two coordinates to form the lens-imaging coordinates. For this particularly simple example, the remaining two coordinates point in the transverse directions. But what are the transverse coordinates in the general case?

2.3.6 Transverse planes of two skew lenses

As defined in Sec. 1.2, transverse planes of a standard Gaussian imaging system are planes perpendicular to the optical axis and have the property that transverse planes in an object space are mapped to transverse planes in an image space due to the system. One could also say that transverse planes form a set of parallel planes in an object space (since they are perpendicular to the optical axis), which is imaged due to the optical system to another set of parallel planes in an image space. In this section, we will find two sets of parallel planes that are imaged into each other: one set in an object space and the other in an image space. Later, we will show that, although they are not perpendicular to the two-lens optical axis, these two conjugated sets are good candidates for the two-lens transverse planes.

To find such conjugated sets of parallel planes, we will use (maybe unexpectedly) the curious telescope-like behaviour of a system of two skew lenses, which at first seems not to have a match in the case of an ideal thin lens. This telescope-like behaviour happens when a parallel bundle of light rays is incident on lens L_1 with a direction such that it is focused to a point lying on the intersection line I of the image-sided focal plane \mathcal{F}'_1 of lens L_1 and the object-sided focal plane \mathcal{F}_2 of lens L_2 . Now we will consider one subset of these “telescope rays”, intersecting an arbitrarily chosen point W in an object space. The object-space segments of those rays form a plane (call it \mathcal{O}), which is parallel to the plane through the principal point P_1 of lens L_1 and the line I . Similarly, the image-space segments of those rays form a plane (call it \mathcal{I}), which is parallel to the plane through the intersection line I and the principal point P_2 of lens L_2 . In this way, we have constructed a conjugated pair of planes since any point lying in \mathcal{O} is imaged to a point lying in the plane \mathcal{I} . Repeating this procedure, for other choices of the point where telescope rays intersect, leads to a set of conjugated planes such that all the object-sided planes are parallel to each other, as are the image-space ones. These planes clearly satisfy our requirements for transverse planes, i.e. that they form two conjugated sets of parallel planes, and therefore we will refer to them as object- and image-sided skew-lens transverse planes.

Note that our construction can be applied even in the case of parallel lenses: the line I lies at an infinite distance from the optical axis and thus we would obtain the standard transverse planes, perpendicular to the optical axis.

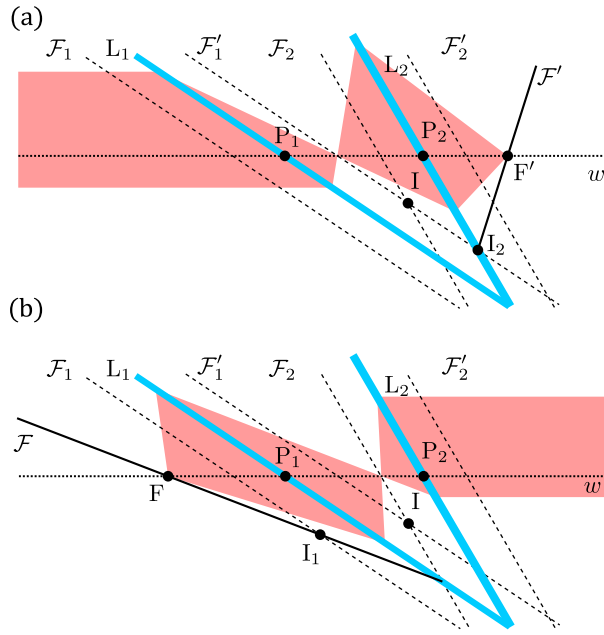


Figure 2.6: Construction of the image-sided (a) and object-sided (b) two-lens focal planes, \mathcal{F}' and \mathcal{F} . The respective focal points, F' and F , coincide with the intersections of the focal planes with the optical axis.

2.3.7 Focal planes

Now we will make our concept of transverse planes (presented above) even stronger by showing that the focal planes of a system of two lenses belong to those transverse planes. To achieve this goal, we will employ the standard definitions of focal planes, provided for example in [30] “Rays which are parallel in the object space will be transformed into rays which intersect in a point on the [image-space] focal plane [...]. Similarly rays from a point in the [object-space] focal plane [...] will transform into a pencil of parallel rays.” Then the focal points can be found as the intersections of the focal planes with the optical axis.

Fig. 2.6 shows our construction of the two-lens focal planes, which fully follows the above definitions: panel (a) shows a parallel bundle of rays incident on the two-lens system. Lens L_1 focuses the light rays to a point in its image-sided focal plane of \mathcal{F}'_1 . Lens L_2 then provides a final image of this point. All the light rays from the original parallel bundle therefore intersect in this final image point, which means that final image point lies in an image-sided focal plane of the two-lens combination. This construction implies that the two-lens image-sided focal plane coincides with an image of the image-sided focal plane \mathcal{F}'_1 due to lens L_2 . Since lenses L_1 and L_2 form, in general, a non-zero angle, plane \mathcal{F}'_1 intersects the lens L_2 in a line, labelled I_2 in Fig. 2.6(a). This line, I_2 , must also lie in the two-lens image-sided focal plane because line I_2 is imaged back to itself due to lens L_2 .

Now because the image-sided focal plane \mathcal{F}'_1 of lens L_1 also contains the intersection line I , its image due to lens L_2 (the two-lens image-sided focal plane) is an image-sided skew-lens transverse plane as suggested by the construction presented in section 2.3.6. This proves that the image-sided focal plane \mathcal{F}' of a general two-lens combination coincides with an image-sided skew-lens transverse plane.

The two-lens object-sided focal plane, \mathcal{F} , can be constructed in a similar way. Fig. 2.6(b) shows that \mathcal{F} is imaged by a lens L_1 to the object-sided focal plane \mathcal{F}_2 of lens L_2 . However, the object-sided focal plane \mathcal{F}_2 of lens L_2 passes through the line I and thus \mathcal{F}_2 must be an

image of an object-sided skew-lens transverse plane due to lens L_1 . This shows that the object-sided two-lens focal plane \mathcal{F} is indeed an object-sided skew-lens transverse plane.

Finally, we will show that the intersections of these focal planes with the optical axis, call them F_w and F'_w , are consistent with the w coordinates of the focal points

$$F_w = P_w - f, \quad (2.25)$$

$$F'_w = P'_w + f, \quad (2.26)$$

where f is the two-lens focal length (given by Eqn. (2.18)) and P_w and P'_w are the two-lens principal points (given by Eqs. (2.19) and (2.20)). Fig. 2.6(b) shows that the intersection F_w of the object-sided skew-lens focal plane can be found using the following imaging equation

$$-\frac{1}{F_w} + \frac{1}{d - g_2} = \frac{1}{g_1}, \quad (2.27)$$

when solved for F_w

$$F_w = \frac{g_1 d - g_1 g_2}{g_1 + g_2 - d}. \quad (2.28)$$

If the RHS of this equation is expressed in terms of the w coordinate of the object-sided two-lens principal point P_w and the two-lens focal length f , defined in Eqn (2.18), one will obtain Eqn (2.25).

Analogously, one can deduce from Fig 2.6(a) that

$$F'_w = d + \frac{g_1 g_2 - g_2 d}{g_1 + g_2 - d}. \quad (2.29)$$

Expressing the RHS in terms of f and P'_w then yields Eqn (2.26). So far, everything is consistent.

2.3.8 Principal planes

In Sec. 1.2, we have defined the object and image-sided principal planes, \mathcal{P} and \mathcal{P}' , as conjugate transverse planes which are imaged to each other due to a considered imaging system with a transverse magnification equal to unity. In the case of two skew lenses, one can spot a set of points with such a property immediately: the intersection line V of the planes of the lenses L_1 and L_2 (Fig. 2.7). That is because an ideal thin lens images any point lying in a plane of the lens back to itself; consequently, any point lying on the intersection line of two ideal lenses is imaged back to itself (and thus with magnification equal to unity) due to both lenses. Line V is therefore a sensible candidate for the line where object and image-sided skew-lens principal planes intersect.

With this choice, the skew-lens principal planes can be found easily: they coincide with object and image-sided skew-lens transverse planes, passing through the line V. Following the definition in Sec. 1.2, the skew-lens principal points, P and P', are the intersection points of the respective skew-lens principal planes with the skew-lens optical axis. Our construction is depicted in Fig. 2.7.

Now we will show the consistency of this definition of skew-lens principal points, P and P', with the w coordinates of principal point positions P_w and P'_w , given by Eqs. (2.19) and (2.20). For this goal, we will use a fact, which arises from our construction of skew-lens transverse planes: the intermediate image of the object-sided principal plane \mathcal{P} due to lens L_1 lies in a plane through both lines V (as each lens images V to itself) and I. This plane intersects the w -axis at point w_{im} . Provided that the origin of the w -axis coincides

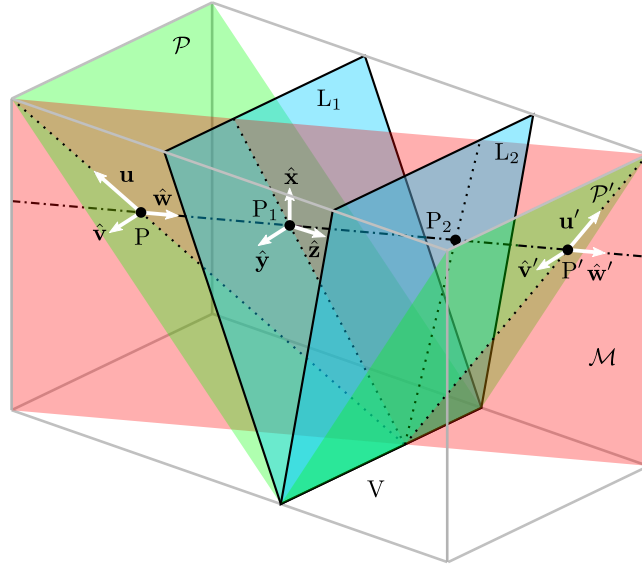


Figure 2.8: Definition of the object- and image-space lens-imaging coordinates. Positions in object and image space are expressed in skew coordinate systems with basis vectors \mathbf{u} , $\hat{\mathbf{v}}$, $\hat{\mathbf{w}}$ (object space) and \mathbf{u}' , $\hat{\mathbf{v}}'$, $\hat{\mathbf{w}}'$ (image space). Basis vectors in the u and u' directions are not normalised; their lengths are chosen such that the x components of these vectors is equal to one. We define \mathbf{u} by the intersection of the object-sided principal plane, \mathcal{P} , and the median plane, \mathcal{M} , which is through the two-lens optical axis w and perpendicular to the (v, w) plane. Similarly, vector \mathbf{u}' lies on the intersection of the image-sided principal plane, \mathcal{P}' , and plane \mathcal{M} . Origins of the object- and image-sided lens-imaging coordinates coincide with the object- and image-sided principal points, P and P' respectively.

coordinate system (u, v, w) , with the origin at object-sided skew-lens principal point P . The w axis coincides with the two-lens optical axis, which is a line passing through both principal points P_1 and P_2 of lenses L_1 and L_2 . Any position in the object-sided principal plane \mathcal{P} is then uniquely described by the other axes, u and v . An analogous coordinate system with its origin at point P' , (u', v', w') , is then employed to express the positions in an image space.

The corresponding basis vectors, \mathbf{u} , $\hat{\mathbf{v}}$, $\hat{\mathbf{w}}$ in an object space and \mathbf{u}' , $\hat{\mathbf{v}}'$, $\hat{\mathbf{w}}'$ in an image space, are presented in Fig. 2.8. Both w and w' axes coincide with the skew-lens optical axis, i.e. a line passing through both principal points P_1 and P_2 of the respective lenses. Axes v and v' are chosen to be parallel with an intersection line V . Finally, u and u' axes are given by intersections of the respective transverse planes with a plane \mathcal{M} , through w and perpendicular to (v, w) plane. Apart from \mathbf{u} and \mathbf{u}' , all the basis vectors are normalised. The lengths of vectors \mathbf{u} and \mathbf{u}' are chosen such that their components perpendicular to the optical axis are both equal to 1. This choice ensures that any light ray, incident on the skew-lens system, intersects both object and image-sided skew-lens principal planes, \mathcal{P} and \mathcal{P}' , at the same transverse coordinates.

We will show that (u, v, w) and (u', v', w') coordinates defined in Fig. 2.8 are object- and image-sided lens-imaging coordinates in a following way: we will consider an object position $\mathbf{Q} = x\hat{\mathbf{x}} + y\hat{\mathbf{y}} + z\hat{\mathbf{z}} = u\mathbf{u} + v\hat{\mathbf{v}} + w\hat{\mathbf{w}}$. Then, we will compare image positions $\mathbf{Q}'' = x'\hat{\mathbf{x}} + y'\hat{\mathbf{y}} + z'\hat{\mathbf{z}}$, obtained by a successive imaging due to lenses L_1 and L_2 , and

$\mathbf{Q}' = u'\mathbf{u}' + v'\hat{\mathbf{v}}' + w'\hat{\mathbf{w}}'$, obtained by the standard imaging equations (2.5),

$$\begin{pmatrix} u' \\ v' \\ w' \end{pmatrix} = \frac{f}{w+f} \begin{pmatrix} u \\ v \\ w \end{pmatrix}, \quad (2.34)$$

where f is the two-lens focal length, given by Eq. (2.18). At the end, we will show that \mathbf{Q}' and \mathbf{Q}'' coincide. The comparison will be done by transforming the position vector \mathbf{Q}' into Cartesian coordinates, chosen as follows: the y -axis is parallel to the line V, the x direction is given by the cross product $\hat{\mathbf{y}} \times \hat{\mathbf{w}}$, and the unit vector in the z direction is $\hat{\mathbf{z}} = \hat{\mathbf{x}} \times \hat{\mathbf{y}}$. The origin of this system lies at the principal point \mathbf{P}_1 of lens L_1 .

The following vectors can be expressed immediately in such coordinate system: $\mathbf{P}_1 = (0, 0, 0)$, $\mathbf{P}_2 = (0, d \sin \beta, d \cos \beta)$, $\mathbf{P} = (0, P_w \sin \beta, P_w \cos \beta)$, $\mathbf{P}' = (0, P'_w \sin \beta, P'_w \cos \beta)$ (where P_w and P'_w are given by Eqs. (2.19) and (2.20)), $\hat{\mathbf{n}}_1 = (\sin \varphi_1, 0, \cos \varphi_1)$ and $\hat{\mathbf{n}}_2 = (\sin \varphi_2, 0, \cos \varphi_2)$. Furthermore, one can parametrize the skew-lens principal planes, \mathcal{P} , \mathcal{P}' and the median plane \mathcal{M} as follows

$$\begin{aligned} \mathcal{P} : \quad x &= -(z - P_w \cos \beta) \cot \alpha \\ \mathcal{P}' : \quad x &= -(z - P'_w \cos \beta) \cot \alpha' \\ \mathcal{M} : \quad y &= z \tan \beta, \end{aligned}$$

where α and α' are angles between the x axis and the respective principal planes, given by the equations (full derivation is provided in Appendix B)

$$\cot \alpha = \cot \varphi_1 \frac{d - g_1 - g_2}{d - g_2 - g_1 \cot \varphi_1 / \cot \varphi_2}, \quad (2.35)$$

$$\cot \alpha' = \cot \varphi_2 \frac{d - g_1 - g_2}{d - g_1 - g_2 \cot \varphi_2 / \cot \varphi_1}. \quad (2.36)$$

Finally, the basis vectors \mathbf{u} , \mathbf{u}' , $\hat{\mathbf{v}}$, $\hat{\mathbf{v}}'$, $\hat{\mathbf{w}}$ and $\hat{\mathbf{w}}'$ can be expressed in the considered Cartesian coordinate system:

$$\begin{aligned} \hat{\mathbf{w}} &= \hat{\mathbf{w}}' = (\mathbf{P}_2 - \mathbf{P}_1)/d = (0, \sin \beta, \cos \beta), \\ \hat{\mathbf{v}} &= \hat{\mathbf{v}}' = \hat{\mathbf{y}} = (0, 1, 0), \\ \mathbf{u} &= (1, -\tan \beta \tan \alpha, -\tan \alpha), \\ \mathbf{u}' &= (1, -\tan \beta \tan \alpha', -\tan \alpha'). \end{aligned} \quad (2.37)$$

Note that vectors \mathbf{u} and \mathbf{u}' coincide with intersections of \mathcal{M} with \mathcal{P} and \mathcal{P}' respectively, with x -component equal to 1. The matrix describing the image-space transformation $((x', y', z') - (P'_w \sin \beta, 0, P'_w \cos \beta))^T = T_i^{-1}(u', v', w')^T$, is then of form

$$T_i^{-1} = \begin{pmatrix} 1 & 0 & 0 \\ -\tan \beta \tan \alpha' & 1 & \sin \beta \\ -\tan \alpha' & 0 & \cos \beta \end{pmatrix}. \quad (2.38)$$

The matrix describing the object-space transformation

$(u, v, w)^T = T_o((x, y, z) - (P_w \sin \beta, 0, P_w \cos \beta))^T$ is then the inverse of T_i^{-1} with the image-space slope $-\cot \alpha'$ replaced by the object-space slope $-\cot \alpha$, which can be expressed in the form

$$T_o = \begin{pmatrix} 1 & 0 & 0 \\ 0 & 1 & -\tan \beta \\ 0 & \frac{\tan \alpha}{\cos \beta} & \frac{1}{\cos \beta} \end{pmatrix}. \quad (2.39)$$

Now we have everything needed to transform the Eqn (2.34), and thus the image position $\mathbf{Q}' = (u', v', w')$, to Cartesian coordinates

$$\mathbf{Q}' - \mathbf{P}' = T_i^{-1} \begin{pmatrix} u' \\ v' \\ w' \end{pmatrix} = T_i^{-1} \frac{f}{w+f} T_o (\mathbf{Q} - \mathbf{P}), \quad (2.40)$$

or explicitly,

$$\begin{pmatrix} x' \\ y' - P'_w \sin \beta \\ z' - P'_w \cos \beta \end{pmatrix} = \frac{f}{w+f} \begin{pmatrix} 1 & 0 & 0 \\ (\tan \alpha - \tan \alpha') \tan \beta & 1 & 0 \\ \tan \alpha - \tan \alpha' & 0 & 1 \end{pmatrix} \begin{pmatrix} x \\ y - P_w \sin \beta \\ z - P_w \cos \beta \end{pmatrix}. \quad (2.41)$$

We compared this result to that due to successive application of the equations describing imaging due to the individual lenses. We performed this calculation in the *Mathematica* notebook `TwoLensProof.nb` [31], finding that the resulting image positions are identical. Our choice of lens-imaging coordinates is therefore correct.

2.5 Applying lens-imaging coordinates: Two skew lenses with coinciding principal points

After presenting the lens-imaging coordinates of a system of two skew lenses, we will apply those to a couple of examples.

The first example we will discuss is a combination, let us call it C, of two tilted lenses, with coinciding principal points, i.e. $P_1 = P_2 = P$. As previously defined, the two-lens optical axis of such combination can be any line through P. More interestingly, object and image-sided two-lens transverse planes are parallel to each other. This arises from the construction of the two-lens transverse planes, presented in Sec. 2.3.6: object-sided two-lens transverse planes are planes parallel to one through P_1 and the line I (which is the intersection line of image-sided focal plane of L_1 and the object-sided focal plane of L_2) and, similarly, image-sided two-lens transverse planes are planes parallel to a plane through P_2 and the line I. But points P_1 and P_2 coincide for the combination C, which means that object and image-sided two-lens transverse planes must be parallel to each other.

These observations imply that if one chooses the two-lens optical axis to be perpendicular to the two-lens transverse planes, the lens-imaging coordinates for the combination C will be simple Cartesian coordinates, with the origin at P. Therefore, two tilted lenses sharing a principal point can be regarded as an ideal thin lens of focal length $f = g_1 g_2 / (g_1 + g_2)$.

2.6 Applying lens-imaging coordinates: Image rotation with three skew lenses

The lens-imaging coordinates of two skew lenses L_1 and L_2 can be even employed to build a combination of three lenses, which provides an image rotation around the common intersection line V, by an arbitrary angle $\Delta\alpha$. The idea of how to obtain image rotation with a combination of three lenses is shown in Fig. 2.9 (a). Consider a system D of two skew lenses, with principal planes \mathcal{P} , \mathcal{P}' and effective focal length f_D . A collimated ray bundle, perpendicular to the object-sided principal plane \mathcal{P} , is incident on D, which

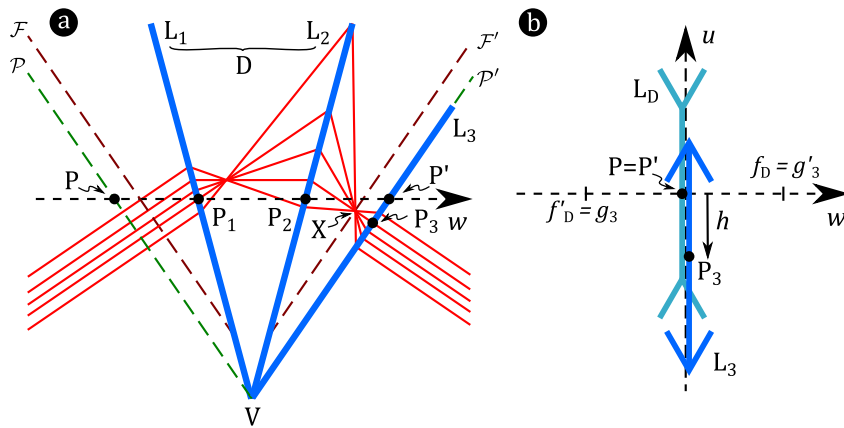


Figure 2.9: (a) The construction of the three-lens image rotator starts with a system D of two skew lenses, L_1 and L_2 , characterised by its effective focal length, f_D , the two-lens optical axis, which coincides with the w and w' axes of the lens-imaging coordinate systems, the object- and image-sided focal planes \mathcal{F} and \mathcal{F}' , and the object- and image-sided principal planes \mathcal{P} and \mathcal{P}' . A bundle of parallel light rays (red lines) is incident on D from a direction that is perpendicular to the object-sided principal planes, \mathcal{P} . Lens L_3 is placed in the image-sided principal plane \mathcal{P}' of the two-lens system D , such that its object-sided focal point coincides with the point X , where the bundle of rays intersects the image-sided two-lens focal plane, \mathcal{F}' . (b) The same system of three lenses in lens-imaging coordinates (u, w) acts like a combination of two coplanar lenses of opposite focal lengths, f_D and $-f_D$, offset in the transverse direction. The mapping due to this lens combination — a pure shearing — exactly cancels the shearing of the lens-imaging coordinate system, so that the mapping in the global Cartesian coordinates is a pure rotation.

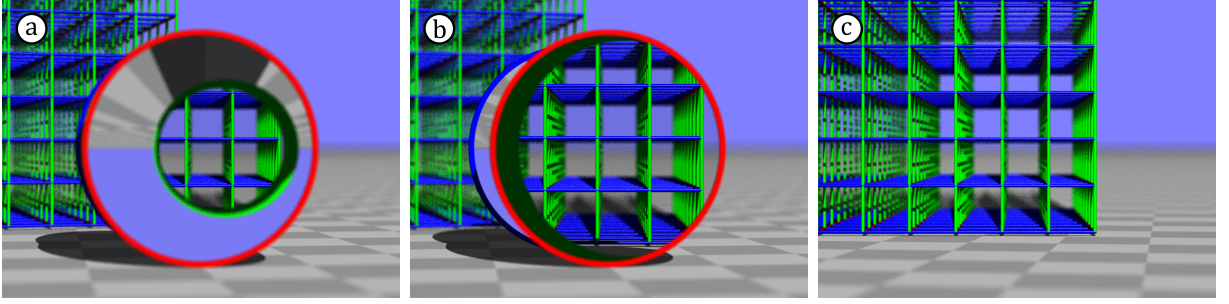


Figure 2.10: Demonstration of image rotation with three lenses. A square lattice is placed behind three-lens image rotator T, whose lenses are framed with red, green and blue rings respectively. The actual field of view through all three included lenses is circumscribed by a green ellipsoid inside the red-framed lens (which is actually an image of the frame of the middle lens due to the red-framed one). The lattice, as seen through all three lenses, appears rotated by an angle $\Delta\alpha = -15^\circ$ around a vertical axis. (c) For comparison, the simulation was performed without the lenses but with the camera physically rotated by 15° around the same axis. Chosen parameters are (a) $\varphi_1 = 2.5^\circ$, $\varphi_2 = -2.5^\circ$ and $d = 0.5$ and (b) $\varphi_1 = 0.5^\circ$, $\varphi_2 = -0.5^\circ$ and $d = 0.1$. The remaining values have been calculated using formulas presented in the Appendix C. One can see that the field of view increases when the inclination $\varphi_2 - \varphi_1$ between first two lenses of rotator T (red and green-framed) becomes smaller, which appears to be the case generally. The simulations were performed using an extended version of our custom raytracer Dr TIM [1].

focusses it to a point X in the image-sided focal plane \mathcal{F}' . If one inserts a third lens L_3 such that the plane of this lens coincides with the image-sided principal plane \mathcal{P}' of D and the object-sided focal point of L_3 coincides with point X, the ray bundle will be collimated again and perpendicular to the image-sided principal plane \mathcal{P}' after transmission through the lens L_3 (see Fig. 2.9 (a)).

One can see that the projected focal length g_3 of lens L_3 is exactly opposite to the effective focal length f_D of the two-lens system D, i.e. $g_3 = -f_D$. Consequently, since the plane of L_3 coincides with the image-sided principal plane \mathcal{P}' of the system D, all object-sided transverse planes of D are mapped to image-sided transverse planes, with magnification equal to unity. There is no shearing of the image due to three-lens system $D + L_3$: the parallel ray bundle considered above was chosen to be perpendicular to the transverse planes both in object and image space; as object-space points on one such ray are imaged to image-space points on the same ray, lines that are perpendicular to the object-sided transverse planes are therefore re-imaged to lines that are perpendicular to the image-sided transverse planes again. This means that the mapping due to a three-lens system $T = D + L_3$ is a pure rotation by an angle $\Delta\alpha = \alpha' - \alpha$ formed by the object and image-sided transverse planes.

This is demonstrated by the ray-tracing simulations shown in Fig. 2.10. Fig. 2.10(a,b) show views through two different three-lens combinations that are designed to rotate the image seen through all three lenses by an angle $\Delta\alpha = -15^\circ$ around an axis V; Fig. 2.10(c) shows the same scene but without the lenses and with the camera instead rotated around V by $-\Delta\alpha$. The part of the image in which the scene is seen through all three lenses in (a,b) is identical to the corresponding part of the image shown in (c), as expected. A comparison of Figs. 2.10(a) and (b) shows that the size of the field of view, that is the angular size of the image seen through all three lenses, depends on the parameters of the three lenses. Specifically, the field of view can be increased, if the inclination $\varphi_2 - \varphi_1$

between the first two lenses is reduced.

2.6.1 Image rotation with three lenses mathematically

We will see below that it is convenient to work in the lens-imaging coordinates of the two-lens system D. In these lens-imaging coordinates, the three-lens system T is equivalent to a system of two coplanar lenses like the one presented in Fig. 2.9 (b): the two-lens system D acts like a lens L_D of focal length f_D and with its principal points coinciding (i.e. $P=P'$) at the origin of the coordinate system. The other lens, L_3 , is of focal length $g_3 = -f_D$ and its principal point P_3 is offset in the (transverse) u -direction. The offset has to be chosen such that the image shearing due to the combination $L_D + L_3$ exactly cancels the shearing of the lens-imaging coordinate system, so that the mapping in the global Cartesian coordinates is a pure rotation.

This formulation enables a simple description of the imaging due to the system T in lens-imaging coordinates: first, an intermediate image (u', w') due to lens L_D is created:

$$\begin{pmatrix} u' \\ v' \\ w' \end{pmatrix} = \frac{f_D}{f_D + w} \begin{pmatrix} u \\ v \\ w \end{pmatrix}. \quad (2.42)$$

Then, the intermediate image (u', w') is re-imaged by lens L_3 (with principal-point position $(h, 0, 0)$ and focal length $g_3 = -f_D$) as follows:

$$\begin{pmatrix} u'' - h \\ v'' \\ w'' \end{pmatrix} = \frac{-f_D}{-f_D + w'} \begin{pmatrix} u' - h \\ v' \\ w' \end{pmatrix}. \quad (2.43)$$

Combining these two equations together yields the imaging equation due to the three-lens system T in lens-imaging coordinates, which can be written in the matrix form

$$\begin{pmatrix} u'' \\ v'' \\ w'' \end{pmatrix} = \begin{pmatrix} 1 & 0 & -\frac{h}{f_D} \\ 0 & 1 & 0 \\ 0 & 0 & 1 \end{pmatrix} \begin{pmatrix} u \\ v \\ w \end{pmatrix}. \quad (2.44)$$

To transform this imaging equation into global Cartesian coordinates, we simply replace the factor describing the effect of a thin lens in Eq. (2.40) (i.e., the term $f/(w+f)$) by the matrix describing the effect of the three-lens system T (Eq. (2.44)). Given $\beta = 0$, this yields the equation

$$\begin{pmatrix} x' \\ y' \\ z' - P'_w \end{pmatrix} = \begin{pmatrix} 1 & 0 & 0 \\ 0 & 1 & 0 \\ -\tan \alpha' & 0 & 1 \end{pmatrix} \begin{pmatrix} 1 & 0 & -\frac{h}{f_D} \\ 0 & 1 & 0 \\ 0 & 0 & 1 \end{pmatrix} \begin{pmatrix} 1 & 0 & 0 \\ 0 & 1 & 0 \\ \tan \alpha & 0 & 1 \end{pmatrix} \begin{pmatrix} x \\ y \\ z - P_w \end{pmatrix}. \quad (2.45)$$

Performing the matrix multiplication yields

$$\begin{pmatrix} x' \\ y' \\ z' - P'_w \end{pmatrix} = \begin{pmatrix} 1 - \frac{h}{f_D} \tan \alpha & 0 & -\frac{h}{f_D} \\ 0 & 1 & 0 \\ -\tan \alpha' + \tan \alpha + \frac{h}{f_D} \tan \alpha' \tan \alpha & 0 & 1 + \frac{h}{f_D} \tan \alpha' \end{pmatrix} \begin{pmatrix} x \\ y \\ z - P_w \end{pmatrix}. \quad (2.46)$$

For Eq. (2.46) to describe a rotation, the 3×3 matrix on the right-hand side must be anti-symmetric. That yields the condition

$$-\tan \alpha' + \tan \alpha + \frac{h}{f_D} \tan \alpha' \tan \alpha = \frac{h}{f_D}, \quad (2.47)$$

which can be solved for h/f_D to give

$$\frac{h}{f_D} = \frac{\sin(\alpha - \alpha')}{\cos(\alpha' + \alpha)}. \quad (2.48)$$

We are required to set $\alpha = -\alpha'$ in order to ensure that the denominator is equal to 1 and hence the matrix presented in Eq. (2.46) can be a pure rotation matrix. With our earlier definition $\Delta\alpha \equiv \alpha' - \alpha$, the condition on the fraction h/f_D simplifies to

$$\frac{h}{f_D} = -\sin \Delta\alpha, \quad (2.49)$$

and it is easy to show that the diagonal terms in the 3×3 matrix in Eq. (2.46) are both equal to $\cos \Delta\alpha$. Therefore, Eq. (2.46) can be written in the form

$$\begin{pmatrix} x' \\ y' \\ z' - P'_w \end{pmatrix} = \begin{pmatrix} \cos \Delta\alpha & 0 & \sin \Delta\alpha \\ 0 & 1 & 0 \\ -\sin \Delta\alpha & 0 & \cos \Delta\alpha \end{pmatrix} \begin{pmatrix} x \\ y \\ z - P_w \end{pmatrix}. \quad (2.50)$$

From Fig. 2.9(a) one can see that the point P' is the point P , rotated around V by an angle $\Delta\alpha = \alpha' - \alpha$, and therefore satisfies the equation

$$\begin{pmatrix} -V_x \\ -V_y \\ P'_w - V_z \end{pmatrix} = \begin{pmatrix} \cos \Delta\alpha & 0 & \sin \Delta\alpha \\ 0 & 1 & 0 \\ -\sin \Delta\alpha & 0 & \cos \Delta\alpha \end{pmatrix} \begin{pmatrix} -V_x \\ -V_y \\ P_w - V_z \end{pmatrix}, \quad (2.51)$$

where V_x , V_y and V_z are coordinates of an arbitrary point on line V where all three lenses intersect. Note that line V is perpendicular to xz plane for angle $\beta = 0$. Summing Eqs. (2.50) and (2.51) gives

$$\begin{pmatrix} x' - V_x \\ y' - V_y \\ z' - V_z \end{pmatrix} = \begin{pmatrix} \cos \Delta\alpha & 0 & \sin \Delta\alpha \\ 0 & 1 & 0 \\ -\sin \Delta\alpha & 0 & \cos \Delta\alpha \end{pmatrix} \begin{pmatrix} x - V_x \\ y - V_y \\ z - V_z \end{pmatrix}. \quad (2.52)$$

This equation states that the mapping between object space and image space is a pure rotation by an angle $\Delta\alpha = \alpha' - \alpha = 2\alpha'$ around V .

2.7 Discussion

2.7.1 Comparison of lens-imaging-coordinate systems

It is instructive to compare the lens-imaging coordinates defined in section 2.4 with the scaled Buchroeder coordinates (see Eqs. (2.5)), presented in [29]. Scaled Buchroeder coordinates consist of two Cartesian coordinate systems, whereas our sheared lens-imaging coordinates is composed of two skew, non-normalised coordinate systems. Below we will point out both the similarities and the differences between these descriptions.

Due to their very specific physical meaning, the focal planes must be the same in both coordinate systems. The definition of the transverse planes (called ‘‘normal planes’’ in [29]) is also the same in both descriptions; as shown in Sec. 2.3.6, there is only one set of parallel planes in an object space, which is imaged to a set of parallel planes again in an image space. Consequently, the principal planes are also the same in both descriptions.

Buchroeder and the sheared lens-imaging coordinates differ, however, in their choice of the optical axis, and therefore the positions of the cardinal points also differ. Note

that cardinal points lie at the intersections between the optical axis and the focal planes and principal planes. In our description, the two-lens optical axis is defined as a straight line through the principal points of the two lenses. On the other hand, the optical axis is defined by the trajectory of the *one* light ray that is perpendicular to the both object and image-sided transverse planes in the Buchroeder description. Our choice of the optical axis coincides with the “Buchroeder optical axis” if and only if the two lenses are coaxial, i.e. they share their (standard) optical axes.

Due to their nature, Buchroeder and the sheared lens-imaging coordinates, presented in Sec. 2.4 are complementary since there are applications for which one description suits better than the other one. For example, the image-sided Buchroeder coordinates are rotated relative to the object-sided ones and thus the Buchroeder coordinates are appropriate for studying the rotations between object and image space. Analogously, our sheared lens-imaging coordinates are suitable for a description of shearing between object and image space.

2.7.2 Combinations of skew physical lenses

In our calculations, we have considered ideal thin lenses so far. Therefore, a natural question arises: how do our results change if real lenses are implemented?

Lenses are commonly used and well understood optical elements, but designing and manufacturing novel types of lenses is a highly active field of research and is capable of yielding impressive outcomes, e.g. metalenses [32–34]. The reason for this research is the limited functionality of conventional lenses, which are well-optimised for imaging of object lying on its optical axis. Images of off-axis objects suffer from several aberrations, e.g. barrel distortion (when straight lines are imaged to curved lines in a shape of a barrel) or coma (when an off-axis point appears to have a tail), chromatic aberration etc. All these aberrations degrade the image quality beyond the paraxial regime, in which the light rays form small angles with the optical axis. However, lenses in form of metasurfaces might become real-life implementations of ideal thin lenses as they seem to have a potential to overcome these aberrations [32–34].

In our combinations of skew lenses, at least one of the lenses is used non-paraxially, which means that images due to a combination of skew conventional lenses are likely to be degraded by aberrations. This is possibly the reason why combinations of tilted lenses are infrequently employed (one example can be found in [35]). However, this limitation can be overcome by optimising the lenses (or metalenses) to create stigmatic (ray-optically perfect) images of non-paraxial points. For example, one can consider a lens comprising two surfaces, which are optimised for two pairs of conjugate (object-image) positions [36]. Such a non-paraxial lens can be applied if either point light sources or point-like observers are located in the optimised positions.

Finally, combinations of two skew lenses can be realised experimentally using metalenses [33, 34, 37, 38]: metasurface phase holograms [39–44] which aim to approximate ideal thin lenses. The key feature of metasurfaces is the option of tuning their properties in many different ways. This freedom enabled, for example, the development of low-dispersion metalenses [34, 45, 46]. The rapid progress in developing and fabricating metalenses makes researchers to believe that even closer approximations of ideal thin lenses with reduced aberrations such as coma will be built in the near future [47].

2.7.3 Applications of the three-lens image rotator

In Sec. 2.6, we showed that an appropriate combination of three skew lenses can provide a rotation of an image with magnification equal to one. If the lenses are replaced with corresponding omni-directional lenses (presented in the following chapter), this rotation can be seen in any direction. Finally, we demonstrated our theoretical predictions with ray-tracing simulations.

Our lens combinations can be seen as *space-cancelling wedges* that make a wedge of space disappear. In Chapter 4, we will use combinations of space-cancelling wedges to construct, theoretically, optical simulations of curved three-dimensional spaces that correspond to the surface of a 4-tetrahedron and of a hypercube. However, to open up this and other applications of our lens combinations, they first need to be realised with physical lenses.

Chapter 3

Transformation optics with ideal lenses

3.1 Transformation optics and transformation optics devices

Transformation optics (TO) is a relatively novel and highly active field of research, proposed by works of Ulf Leonhardt and John Pendry [2, 48]. It employs mathematics of differential geometry to design optical materials and devices with unprecedented properties. In this thesis, we provide just a brief overview of the fundamentals of transformation optics. Further details and a more rigorous treatment can be found in [24].

The fundamental idea of transformation optics lies in an equivalence of light-ray propagation in two spaces: *physical* space [with coordinates (x, y, z)], filled with a spatially varying refractive index, and *virtual* space [with coordinates (u, v, w)], with a homogeneous optical medium [49]. Since the optical medium is homogeneous in a virtual space, light rays are travelling along straight lines in this space. The structure of a physical space is then given by mapping $\varphi : (u, v, w) \rightarrow (x, y, z)$, applied to the virtual space. The physical space relative permittivity and permeability tensors ε and μ are calculated from the corresponding virtual-space tensors using the well-known formula [2]

$$\varepsilon = \mu = \frac{JJ^T}{\det(J)}, \quad (3.1)$$

where $J = \partial(u, v, w)/\partial(x, y, z)$ is the Jacobian matrix.

A *Transformation optics (TO) device* is an optical system, that provides the mapping φ between the virtual space – the apparent structure, i.e. how it is seen from the outside of the device – and the physical space – the actual structure. Since the mapping φ is unique, the distortion of a physical-space structure in the TO device is the same for each outside viewing position. We therefore define a TO device by unique mapping between physical and virtual space. Probably the most publicised example of a TO device is the invisibility cloak, where the physical-space inside the cloak is shrunk to a point; the virtual-space structure then corresponds to an empty space. The most famous designs of invisibility cloaks are shown in Fig. 3.1.

Building TO devices requires advanced material engineering, typically using metamaterials. One can imagine a metamaterial as an assembly of microfabricated elements, typically made of metal or plastic [50]. Although the science and the theory of metamaterials progresses rapidly, fabrication of metamaterials with desired properties still needs to overcome several serious difficulties. This motivated several research groups [15, 16] to

develop alternative approaches of designing TO devices. In this chapter, we will present a theory of building TO devices using well-known and common optical elements, namely ideal thin lenses. We first derive the imaging conditions on such devices: loop and edge-imaging condition. Later, we apply the edge-imaging condition on simple intersections of several lenses to get the conditions on their principal-point positions and their focal lengths. After this, we will use these lens combinations as building blocks of a TO device, which we call the Structure S. Finally, we discuss the imaging properties, experimental realisation and potential applications of our TO device, built purely of ideal thin lenses.

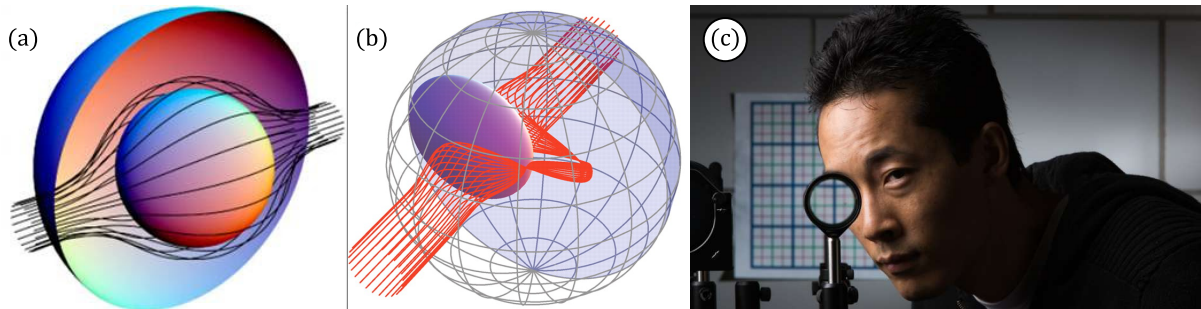


Figure 3.1: Examples of transformation optics devices: (a) Invisibility cloak proposed by John Pendry, David Schurig and David R. Smith [2]: the optical medium between two concentric spheres is such that the light rays (black lines) circumvent the inner sphere – the cloaked volume – and then continue in their original trajectories; (b) non-Euclidean invisibility cloak by Tomáš Tyc and Ulf Leonhardt [3]: The cloaked volume, which the light rays (red lines) are never incident on, is depicted as a lenticular shape; (c) Rochester cloak, first proposed by Joseph S. Choi and John C. Howell [4]: this device consists of four lenses, arranged such that the incident and emerging parts of light rays passing through are in line. In a space between the lenses, there are regions which are omitted by the light rays passing through all four lenses. Any object in such a region (for example, a human eye) is therefore invisible from a region close to the optical axis.

3.1.1 Contributions

The work carried out in this chapter stems from a collaboration between Dr Johannes Courtial, Prof. Tomáš Tyc, Dr Stephen Oxburgh, Dr Euan Cowie, Dr Chris White, and myself.

3.2 Mapping conditions in TO devices

Consider a TO device constructed from ideal lenses. The inner region of such device is divided into cells by the lenses as depicted in Fig. 3.2. For the sake of clarity, here it is drawn in 2D, but our considerations equally apply in 3D. In Fig. 3.2, intersecting lenses meet at the vertices of the polygonal cells (in 3D, they intersect in the edges of the polyhedral cells). The lens separating cells i and j provides an imaging c_{ji} , corresponding to a collineation from the space of cell i to the space of cell j . We introduced a notation, in which the index of an image cell is followed by an index of an object cell. An obvious observation is that the mapping c_{ij} , i.e. from the space of cell j to the space of cell i , is the inverse of c_{ji} , i.e. $c_{ij} = c_{ji}^{-1}$. Now consider an object at position Q_i in the space of cell i (we allow this object position to be either real or virtual). The light rays intersecting

at Q_i then propagate to the outside, which we call cell 0, via two intermediate cells j and k (the generalisation to a different number of intermediate cells is obvious). Mapping of Q_i from the space of cell i to the outside space (cell 0) is then described by the following combination of the mappings: first from the space of cell i to the space of cell j , followed by a mapping from the space of cell j to the space of cell k , and finally the mapping from the space of cell k to the space of cell 0. If we describe the position Q_i by the vector \mathbf{Q}_i , then the position vector \mathbf{Q}_0 of its image in the space of cell 0, is given by equation

$$\mathbf{Q}_0 = c_{0k}c_{kj}c_{ji}\mathbf{Q}_i. \quad (3.2)$$

The expression $c_{0k}c_{kj}c_{ji}$ therefore describes the mapping of any object-space position in the space of cell i through the spaces of cells j and k to the image position in the outside space (cell 0). Since the TO device is defined by a unique mapping of the physical space

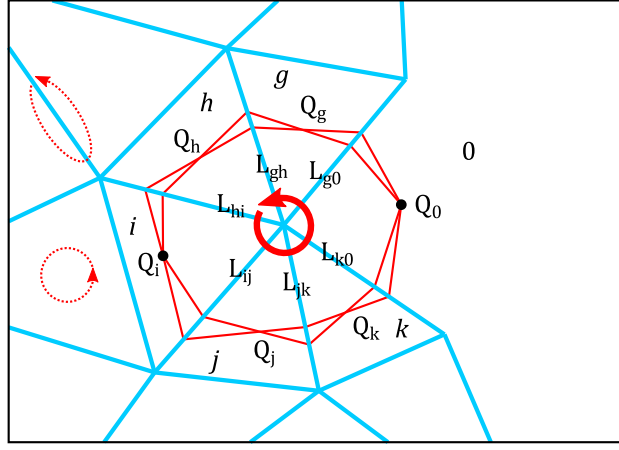


Figure 3.2: Diagram of part of a transformation-optics device formed by lenses (cyan lines). The lenses divide the inside of the device into cells, five of them are marked g to k ; cell 0 is the outside of the device. Lens L_{uv} then separates cells u and v . Light rays (red lines), starting from a point Q_i , located in cell i , form an image Q_0 in the outside space, regardless whether they travel through cells j and k or cells h and g . Dotted red arrows show the trivial loops, containing none or only one lens.

to the virtual space, the image Q_0 of the object Q_i must be independent of precisely which cells the light rays pass through on their way from cell i to the outside. This means that if the light rays emerging from Q_i are travelling from the space of cell i to the space of cell 0 via cells h and g (instead of cells j and k), they (or their backward elongations) must intersect at the same image position Q_0 in the space of cell 0 as the light rays travelling via cells j and k . Therefore, mapping $c_{0g}c_{gh}c_{hi}$ through cells g and h must be the same as mapping $c_{0k}c_{kj}c_{ji}$ discussed above, i.e.

$$c_{0g}c_{gh}c_{hi} = c_{0k}c_{kj}c_{ji}. \quad (3.3)$$

Multiplying both sides of this equation by $(c_{0k}c_{kj}c_{ji})^{-1} = c_{ij}c_{jk}c_{k0}$ from the left yields

$$I = c_{0k}c_{kj}c_{ji}c_{ih}c_{hg}c_{g0}, \quad (3.4)$$

where I is the identity mapping. The right-hand side corresponds to a mapping encountered along a closed loop $0 \rightarrow g \rightarrow h \rightarrow i \rightarrow j \rightarrow k \rightarrow 0$. We call this result the *loop-imaging condition*: the combination of all lenses encountered along the closed loop images every position back to itself. Of course, we can consider loops that start in any

cell within the device, encountering any number of lenses, which leads us to formulate the **loop-imaging theorem**: *the loop-imaging condition is satisfied for any closed loop in a TO device.*

The loop-imaging condition is a very powerful tool for building TO devices. However, one can consider infinitely many closed loops in the device, including “trivial” loops for which the loop-imaging condition is satisfied trivially: loops circumnavigating no lenses or only one lens. Therefore, we will concentrate on loops that contain one edge (point in 2D); from now, we will use only terms appropriate for a 3D case. This leads to a stronger condition, which we call *the edge-imaging condition*: for a particular edge, the combination of all lenses that meet at that particular edge images every point to itself. Later, we will show that the lens structure is a TO device if the edge-imaging condition is satisfied for all edges in the structure. This is what we called **the edge-imaging theorem**: the requirement that the edge-imaging conditions for all edges in a structure are satisfied is a sufficient condition for the structure to be a TO device.

Note that the requirement for a system of lenses to image every object position back to itself is equivalent to the requirement for a combination of lenses to restore every light ray to its original trajectory. This can easily be seen by considering two different object positions lying on the same light ray before it is incident on the first lens. As an imaging device, the lens combination must redirect all light rays intersecting in the object position such that they (or their backward elongations) intersect again at the corresponding image position. But the object and the image positions coincide to satisfy the loop-imaging condition and thus the light ray must pass through both object positions again after being transmitted through the lens combination. This means that the outgoing and the incoming parts of the same light ray coincide in a TO device.

This equivalent formulation of the loop-imaging condition can be applied to standard TO devices, built of materials with spatially-varying optical properties: after passing through any closed loop in a TO device, a light ray has to have its initial direction (see Fig. 3.3). Note that this requirement is not satisfied in the invisible lens [51, 52] since light-ray trajectories can intersect themselves at an angle in it. Therefore, the invisible lens is not a TO device.

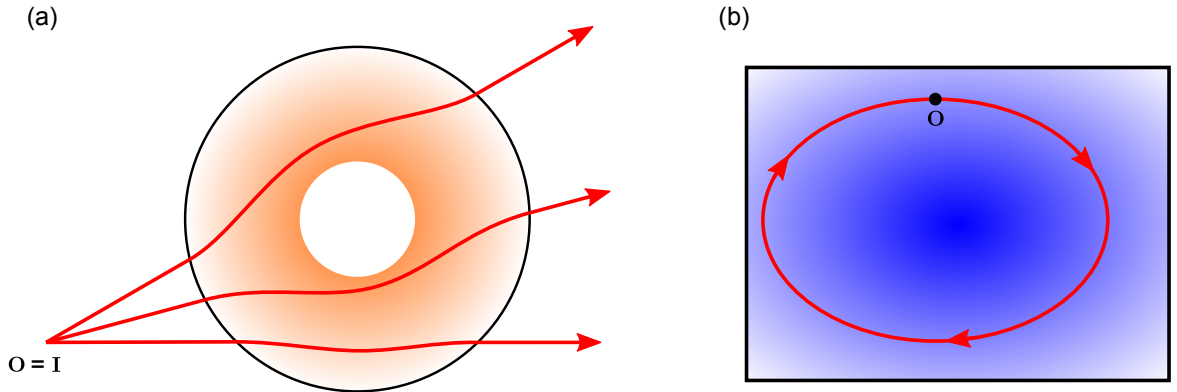


Figure 3.3: Application of the loop-imaging condition to TO devices, built of spatially-varying optical materials. Panel (a) shows several light rays (red lines), intersecting at point O and passing through an invisibility cloak, similar to one proposed in Ref. [5]. The light rays travel along their original trajectories after being transmitted through the device and thus the device satisfies the loop-imaging condition since the image I of point O due to the device coincides with O . Panel (b) shows an area within a TO device and a light ray intersecting itself at point O . As a consequence of the loop-imaging condition, the trajectory of such ray coincides with a closed loop.

3.3 Conditions on the principal points

In this section, we will use the edge-imaging condition to derive general conditions on principal-point positions of different combinations of lenses. Later, we will use these conditions to test whether or not a given combination of lenses can be a TO device. We discuss only combinations in which no two lenses are co-planar since such a pair of lenses can be regarded as a single lens of focal length $f = f_1 f_2 / (f_1 + f_2)$. We will see that these conditions on principal-point positions become more relaxed as the number of lenses increases.

It is instructive to start with a combination of two lenses, such as that presented in Fig. 3.4(a). Consider a light ray (ray 1 in Fig. 3.4(a)) incident on a lens L_1 at any point other than the line where lenses L_1 and L_2 intersect. To satisfy the edge-imaging condition, this light ray should restore its original trajectory when emerging the lens L_2 . This is possible only if L_1 and L_2 do not alter the light-ray direction. However, only light rays passing through the principal point of a lens do not change their direction after being transmitted through the lens. This means that only a light ray passing through both principal points P_1 and P_2 restores its original trajectory after passing through both lenses L_1 and L_2 ; trajectories of all other light rays will be changed by the lens combination. Consequently, **two lenses can not satisfy the edge-imaging condition until they lie in the same plane**, which we will show later in section 3.4.1.

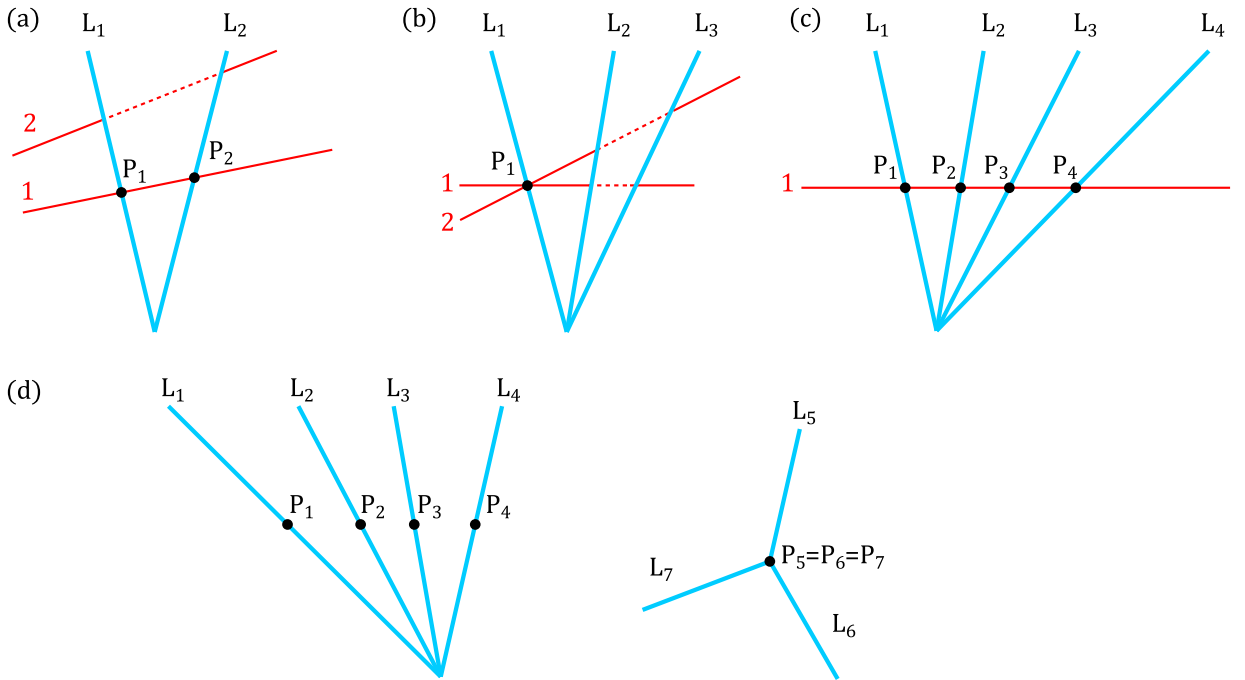


Figure 3.4: Diagrams used when deriving the conditions on the principal-point positions in combinations of two (a), three (b), four (c), and seven (d) lenses (which in fact can be combined to a six-lens system) that satisfy the identity-mapping condition. The red lines show the trajectories of light rays that pass through the principal point P_1 of lens L_1 and, in panel (c), also through the principal point P_2 of lens L_2 . In (d), the combination of lenses L_1 - L_4 itself satisfies the identity-mapping condition, as well as the combination of lenses L_5 - L_7 .

More interesting is a combination of three lenses, depicted in Fig. 3.4(b). Again, consider a light ray, labelled 1, passing through a principal point P_1 of lens L_1 and thus the trajectory of this light ray is not altered by L_1 . To satisfy the edge-imaging condition,

the light ray must be restored to its original trajectory after being transmitted through L_2 and L_3 . This is possible only if ray 1 passes through principal points P_2 and P_3 of both lenses L_2 and L_3 . Repeating the same argument with ray 2, passing through principal point P_1 but in a different direction than the ray 1, leads to a conclusion that principal points P_2 and P_3 must lie on ray 2 as well. Since P_2 and P_3 must lie on ray 1 and 2 at the same time, they must lie at the intersection of rays 1 and 2, which is the principal point P_1 of lens L_1 . Therefore, **the combination of three lenses satisfies the edge-imaging condition only if their principal points coincide.**

Now we will fearlessly add one more lens to our considerations and derive a condition of principal-point positions for a combination of four lenses, satisfying the edge-imaging condition (Fig. 3.4(c)). Similarly to the previous cases, consider a light ray, labelled 1, passing through both principal points P_1 and P_2 of lenses L_1 and L_2 . The trajectory of ray 1 thus remains undeviated by L_1 and L_2 . Using the same argument as in the previous cases, ray 1 should be restored to its original trajectory after passing through lenses L_3 and L_4 , which is possible only if ray 1 passes through their principal points, P_3 and P_4 . Because ray 1 passes also through principal points P_1 and P_2 of lenses L_1 and L_2 , **principal points of a four-lens combination must lie on the same straight line** to satisfy the edge-imaging condition. Later in section 3.4.3, we will show that this is a sufficient condition of principal-point position of four-lens combination. Note that we assumed that no two principal points coincide; any two lenses, whose principal points coincide, can be considered as a single lens (see Sec. 2.5) and thus the problem would reduce to a three-lens combination, which has been already discussed.

From the cases discussed already, one can notice the following pattern: the conditions on principal-point positions are becoming less restrictive when the number of lenses increases. As a reminder, the principal points must intersect for a three-lens combination, whereas principal points of a four-lens system only have to lie on a straight line to satisfy the edge-imaging condition. Following this pattern, the principal points do not even have to lie on a straight line any longer if the number of lenses is greater than some minimum number. One might wonder what this minimum number is. It can be easily shown that this number is 6 as will be shown in the following: consider two systems of lenses, each individually satisfying the edge-imaging condition (shown in Fig. 3.4(d)). One of them contains four lenses L_1 - L_4 (with principal points lying on a straight line) and the other one consists of three lenses L_5 - L_7 (with coinciding principal points). Now, we can arrange these two systems such that one lens forms the four-lens combination, e.g. L_4 , is co-planar with a lens from the three-lens group, e.g. L_5 . However, these two lenses can be replaced by a single equivalent lens (as explained in Sec. 2.3.2). As a result, we have a system of 6 lenses satisfying the edge-imaging condition, but the principal points do not lie on a straight line. Note that a similar construction can be done for two groups of three lenses, resulting in a combination of 5 lenses, whose principal points lie on a straight line.

3.4 Lens combinations that satisfy the edge-imaging condition

In this section, we will derive formulas for focal lengths of lenses, meeting at a common edge, which together satisfy the edge-imaging condition for their intersection edge. We start with a combination of two lenses, then we will discuss a system of three lenses sharing a common edge and finally we will investigate two intersections of four lenses: first one which is mirror-symmetric with respect to a common plane of two of the included lenses, then another four-lens intersection which is asymmetric.

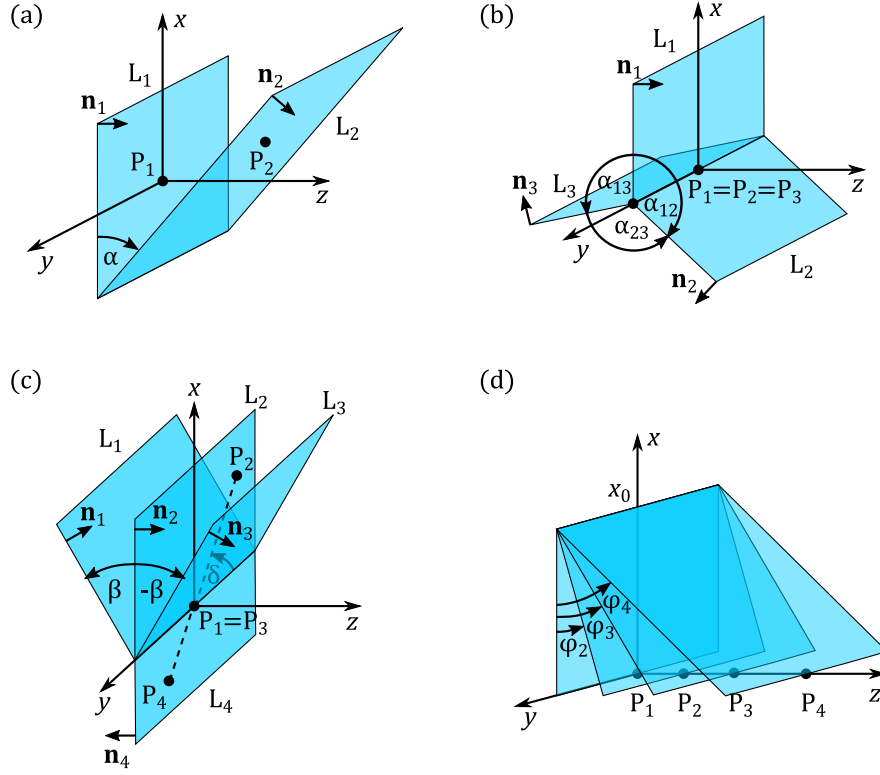


Figure 3.5: Intersections of (a) two, (b) three, and (c)-(d) four lenses, which potentially satisfy the edge-imaging condition. Lenses are labelled L_i , and P_i are their principal points.

3.4.1 2 lenses

It is instructive first to discuss briefly two two-lens systems that obviously satisfy the loop-imaging condition. In the first arrangement, one lens cancels the effect of the other one. This will happen if the two-lens system consists of two co-planar and coaxial lenses, whose focal lengths are of the same magnitude but opposite signs. The loop-imaging condition is also trivially satisfied in the case when the loop (along which the lenses are encountered) intersects a single lens twice. This can be regarded as a special case of two lenses, call them L_1 and L_2 , intersecting along a line threading the loop: they are actually two parts of one lens L divided along the threading-the-loop line.

The following calculation shows that there are no other arrangements of two lenses that satisfy the identity-mapping condition. Fig. 3.5(a) shows the geometry of lenses, L_1 and L_2 . Without loss of generality, we can choose a coordinate system such that the origin coincides with the principal point P_1 of lens L_1 and the z -axis coincides with an optical axis of L_1 and the y -axis is parallel with a line I along which the lenses intersect. The principal point P_1 is then located at position $\mathbf{P}_1 = (0, 0, 0)$ and its optical axis is given by a unit vector $\hat{\mathbf{n}}_1 = (0, 0, 1)$. The remaining lens L_2 is rotated by an angle α about the y -axis with respect to L_1 . Optical axis of L_2 then points in a direction $\hat{\mathbf{n}}_2 = (\sin \alpha, 0, \cos \alpha)$ and the principal point P_2 of L_2 is then placed at point $\mathbf{P}_2 = (P_{2x}, P_{2y}, P_{2z})$. We then choose an arbitrary object position $\mathbf{Q} = (x, y, z)$, which gets successively imaged first by lens L_1 to an intermediate position \mathbf{Q}' , then by lens L_2 to the position \mathbf{Q}'' . We calculate this position by applying Eqn. 1.28 twice, once for each imaging event. If the identity-mapping

condition is satisfied, then $\mathbf{Q}'' = \mathbf{Q}$ or explicitly written

$$\begin{aligned} P_{2x} + \frac{f_1 f_2 x - f_2 P_{2x} (f_1 + z)}{f_1 (f_2 - P_{2x} \sin \alpha - P_{2z} \cos \alpha) + z [f_2 + (f_1 - P_{2z}) \cos \alpha - P_{2x} \sin \alpha] + x f_1 \sin \alpha} &= x, \\ P_{2y} + \frac{f_1 f_2 y - f_2 P_{2y} (f_1 + z)}{f_1 (f_2 - P_{2x} \sin \alpha - P_{2z} \cos \alpha) + z [f_2 + (f_1 - P_{2z}) \cos \alpha - P_{2x} \sin \alpha] + x f_1 \sin \alpha} &= y, \\ P_{2z} + \frac{f_1 f_2 z - f_2 P_{2z} (f_1 + z)}{f_1 (f_2 - P_{2x} \sin \alpha - P_{2z} \cos \alpha) + z [f_2 + (f_1 - P_{2z}) \cos \alpha - P_{2x} \sin \alpha] + x f_1 \sin \alpha} &= z. \end{aligned}$$

To satisfy the edge-imaging condition, these equations must be satisfied for any combination (x, y, z) . This implies the following conditions on principal-point position $\mathbf{P}_2 = (P_{2x}, P_{2y}, P_{2z})$ of lens L_2 (principal point \mathbf{P}_1 of lens L_1 is located at the origin of the coordinate system), focal lengths f_1 and f_2 and the angle α between lenses L_1 and L_2

$$\alpha = N\pi, \quad N \in \mathbb{Z} \quad (3.5)$$

$$P_{2x} = P_{2y} = P_{2z} = 0, \quad (3.6)$$

$$f_2 = -f_1 \cos N\pi. \quad (3.7)$$

This calculation shows that only the two arrangements of lenses L_1 and L_2 mentioned above satisfy the edge-imaging condition as L_1 and L_2 must be co-planar ($\alpha = N\pi$), their principal points coincide, and their focal lengths are either equal or opposite to each other.

3.4.2 3 lenses

To calculate the relationship between the focal lengths in a three-lens combination satisfying an edge-imaging condition, we consider 3 lenses intersecting along the z -axis such that their principal points all coincide with the origin of the coordinate system, as presented in Fig. 3.5(b). We will perform this calculation in an analogous fashion to that used in the case of the two-lens combination, namely by taking an arbitrary object position $\mathbf{Q} = (x, y, z)$, image this successively through all 3 lenses, and then require the resulting image position \mathbf{Q}''' to equal the original object position. Given the directions of optical axes of individual lenses $\hat{\mathbf{n}}_1 = (0, 0, 1)$, $\hat{\mathbf{n}}_2 = (\sin \alpha_{12}, 0, \cos \alpha_{12})$ and $\hat{\mathbf{n}}_3 = (\sin \alpha_{13}, 0, \cos \alpha_{13})$, one can obtain the following set of equations for focal lengths f_1, f_2, f_3

$$\begin{aligned} \frac{f_1 f_2 f_3 x}{f_1 f_2 f_3 + z (f_2 f_3 + f_1 f_3 \cos \alpha_{12} + f_1 f_2 \cos \alpha_{13}) + x f_1 (f_3 \sin \alpha_{12} + f_2 \sin \alpha_{13})} &= x, \\ \frac{f_1 f_2 f_3 y}{f_1 f_2 f_3 + z (f_2 f_3 + f_1 f_3 \cos \alpha_{12} + f_1 f_2 \cos \alpha_{13}) + x f_1 (f_3 \sin \alpha_{12} + f_2 \sin \alpha_{13})} &= y, \\ \frac{f_1 f_2 f_3 z}{f_1 f_2 f_3 + z (f_2 f_3 + f_1 f_3 \cos \alpha_{12} + f_1 f_2 \cos \alpha_{13}) + x f_1 (f_3 \sin \alpha_{12} + f_2 \sin \alpha_{13})} &= z. \end{aligned}$$

To be satisfied for any combination (x, y, z) , both terms in brackets in the denominators must equal zero, i.e.

$$\begin{aligned} f_2 f_3 + f_1 f_3 \cos \alpha_{12} + f_1 f_2 \cos \alpha_{13} &= 0, \\ f_3 \sin \alpha_{12} + f_2 \sin \alpha_{13} &= 0, \end{aligned}$$

with a solution

$$\frac{f_3}{\sin \alpha_{13}} = -\frac{f_2}{\sin \alpha_{12}}, \quad \frac{f_2}{\sin \alpha_{23}} = -\frac{f_1}{\sin \alpha_{13}}, \quad \frac{f_3}{\sin \alpha_{23}} = \frac{f_1}{\sin \alpha_{12}}, \quad (3.8)$$

where we have denoted $\alpha_{23} = 2\pi - (\alpha_{12} - \alpha_{13})$. It is easy to see that one focal length, for example f_1 , can be chosen arbitrarily and the remaining two focal lengths f_2 and f_3 are then given by Eqs. (3.8). Note that in a case when $\alpha_{12} = -\alpha_{13} = -2\pi/3$ all focal lengths f_1, f_2, f_3 equal to each other.

3.4.3 4 lenses

In this section, we will present two arrangements of four lenses, satisfying the edge-imaging condition.

3.4.4 Mirror-symmetric four-lens intersection

The system of four lenses mapping any object back to itself that will be discussed first is that depicted in Fig. 3.5(c). The structure is mirror-symmetric with respect to the common plane of lenses L_2 and L_4 . Additionally, all principal points lie on a straight line through the origin in the (x, y) plane at an angle δ to the y axis; principal points P_1 and P_3 of lenses L_1 and L_3 lie on the origin, P_2 and P_4 respectively lie at points $\mathbf{P}_1 = h_2(\sin \delta, \cos \delta, 0)$ and $\mathbf{P}_2 = h_4(\sin \delta, \cos \delta, 0)$.

Given the normals $\hat{\mathbf{n}}_1 = (\sin \beta, 0, \cos \beta)$, $\hat{\mathbf{n}}_2 = (0, 0, 1)$, $\hat{\mathbf{n}}_3 = (-\sin \beta, 0, \cos \beta)$ and $\hat{\mathbf{n}}_4 = (0, 0, -1)$ and using the same approach as above, we obtain following equations

$$\begin{aligned} \frac{f_1 f_2 f_3 f_4 x + f_1 f_3 (f_4 h_2 - f_2 h_4) z \sin \delta}{d} &= x, \\ \frac{f_1 f_2 f_3 f_4 y + f_1 f_3 (f_4 h_2 - f_2 h_4) z \cos \delta}{d} &= y, \\ \frac{f_1 f_2 f_3 f_4 z}{d} &= z, \end{aligned}$$

where

$$d = f_1 f_2 f_3 f_4 - x(f_1 - f_3) f_2 f_4 \sin \beta + z(f_1 f_3 (f_4 - f_2) + f_2 (f_1 + f_3) f_4 \cos \beta - f_1 f_4 h_2 \sin \beta \sin \delta)$$

For these equations to be satisfied for any combination (x, y, z) yields following conditions on focal lengths f_1, f_2, f_3 and f_4

$$f_4 h_2 = f_2 h_4, \quad (3.9)$$

$$f_1 = f_3 = \frac{f_4 (2f_2 \cos \beta - h_2 \sin \beta \sin \delta)}{f_2 - f_4}, \quad (3.10)$$

and in a limit case $h_2 = h_4 \neq 0$

$$f_2 = \frac{h_2}{2} \tan \beta \sin \delta. \quad (3.11)$$

3.4.5 Asymmetric four-lens intersection

Finally, we will study an asymmetric system of four lenses, L_1 to L_4 , depicted in Fig. 3.5(d). The coordinate system is chosen such that lens L_1 lies in the $z = 0$ plane and the principal points P_1, P_2, P_3 and P_4 of all included lenses lie on z -axis. The line, where all four lenses intersect, is parallel to y -axis and intersects the x -axis at point x_0 . The principal point of lens L_i is then located at position $(0, 0, P_i)$. Let us denote φ_i the angle between lens L_i and the xy -plane; it holds $P_i = x_0 \tan \varphi_i$.

Using the same approach as that used in the previous cases would lead to a complicated set of non-linear equations for focal lengths f_1, f_2, f_3 and f_4 . Therefore, we will use an alternative approach, presented in the Appendix D. Thorough calculations then lead to

following formulas

$$\begin{aligned}
f_2 &= f_1 \frac{s_1 \Delta P_{4,2} \Delta P_{3,2}}{s_2 \Delta P_{4,1} \Delta P_{1,3}} - \frac{x_0 \Delta P_{2,3} \Delta P_{2,1}}{s_2 \Delta P_{3,1}}, \\
f_3 &= -f_1 \frac{s_1 \Delta P_{4,3} \Delta P_{3,2}}{s_3 \Delta P_{4,1} \Delta P_{1,2}}, \\
f_4 &= f_1 \frac{s_1 \Delta P_{4,3} \Delta P_{4,2}}{s_4 \Delta P_{3,1} \Delta P_{1,2}} + \frac{x_0 \Delta P_{4,3} \Delta P_{4,1}}{s_4 \Delta P_{3,1}},
\end{aligned} \tag{3.12}$$

where $\Delta P_{i,j} = P_i - P_j$ and $s_i = \sqrt{x_0^2 + P_i^2}$.

In a limit case when $x_0 \rightarrow \infty$ (and consequently $s_i \rightarrow x_0$), i.e. all four lenses are parallel and coaxial, the discussed four-lens intersection becomes a generalisation of the famous Rochester cloak [15]. We will show that by picking $f_1 = f_A$, $P_1 = 0$, $P_2 = t_1$, $P_3 = t_1 + t_2$ and $P_4 = 2t_1 + t_2$. In such a symmetric case, Eqs. (3.12) simplify to the following form:

$$\begin{aligned}
f_2 &= \frac{t_1 t_2}{t_1 + t_2} - f_A \frac{t_2}{2t_1 + t_2}, \\
f_3 &= f_A \frac{t_2}{2t_1 + t_2}, \\
f_4 &= -f_A + t_1 + \frac{t_1^2}{t_1 + t_2}.
\end{aligned}$$

If we require $f_4 = f_1$ and $f_2 = f_3 = f_B$, we will obtain $t_1 = f_A + f_B$ and $t_2 = 2f_B(f_A + f_B)/(f_A - f_B)$, which are indeed the formulas presented in [15]. This shows that the edge-imaging condition could have been employed to build the Rochester cloak.

3.5 Building TO devices using the edge-imaging condition

So far, we have derived conditions on principal-point positions and focal lengths of lenses intersecting at a common edge, for which the edge-imaging condition is satisfied. According to the edge-imaging theorem (A lens structure is a TO device if and only if every edge in the device satisfies the edge-imaging condition), such groups of lenses might be regarded as a building blocks of a TO device. In this section, we will present a guide on how to build a TO device using the conditions on focal lengths and principal point positions derived above.

Let us start with a structure depicted in Fig. 3.6(a), composed of three lenses arranged in a triangle. This structure clearly can not satisfy the edge-imaging condition since there is no common intersection of all three lenses. Moreover, two lenses, which do not lie in the same plane, can not satisfy the edge-imaging condition.

However, one can insert three more lenses to the structure as shown in Fig. 3.6(b). Now we have a system consisting of four edges. In each edge, three lenses are intersecting and thus their principal points must coincide at these edges to satisfy the edge-imaging condition. This requirement leads to a contradiction again: in this arrangement, each of the included lenses $L_1 - L_6$ contributes to two intersection edges at the same time, which means that they should have two principal points. Since an ideal thin lens has only one principal point, structure in Fig. 3.6(b) can not be a TO device.

Fearlessly, we insert three more lenses as presented in Fig. 3.6(c). The notation is chosen such that $P_{ij\dots}$ denotes a common principal point of lenses L_i, L_j, \dots . One can check easily that this structure satisfies all conditions on principal-point position, implied by the edge-imaging condition.

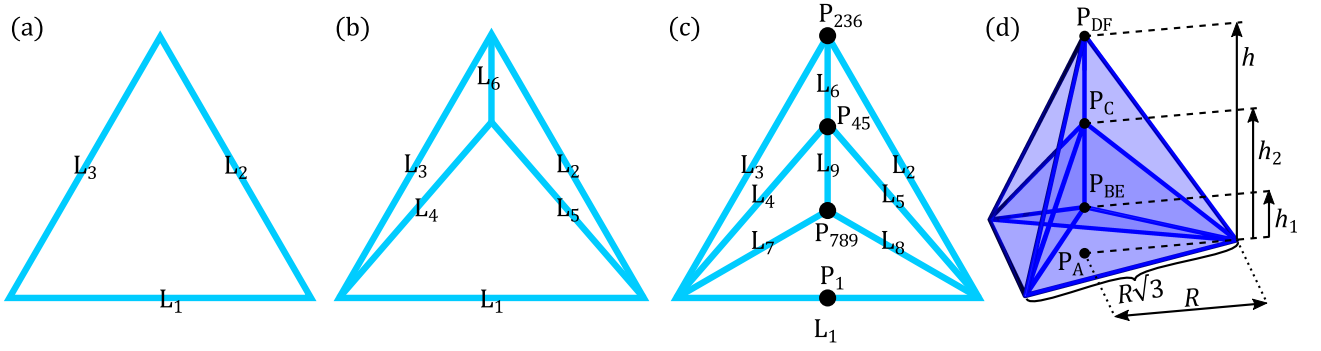


Figure 3.6: Building TO devices from lenses. Structures presented in panels (a) and (b) do not satisfy the conditions on principal-point positions, discussed in Sec. 3.3. The simplest two-dimensional lens structure, satisfying all those conditions, is presented in panel (c). Three-dimensional version is shown in panel (d); wherever blue cylinders form a triangle, there is a lens with an aperture circumscribed by that triangle. $P_{ij\dots}$ denotes a common principal point of lenses L_i, L_j, \dots

Encouraged by the success in two dimensions, we will extend the structure shown in Fig. 3.6(c), let us call it for a moment S_{2D} , to three dimensions. One common practice of extension to a third dimension is making the originally two-dimensional structure rotationally symmetric along a chosen axis. We will do this with the structure S_{2D} and make it regular and three-fold symmetric around the axis where all principal points are located. The resulting structure, let us call it S , can be seen in Fig. 3.6(d); wherever three blue cylinders form a triangle, there is an ideal thin lens fenced by the triangle. Similar to the two-dimensional case, $P_{ij\dots}$ denotes a common principal point of lenses L_i, L_j, \dots . For the sake of clarity, the individual lenses of structure S are presented in a separate figure, namely Fig. 3.7. Although structure S consists of 16 lenses in total, there are only 6 different types of lenses ($L_A - L_F$ in Fig. 3.7) due to the three-fold rotational symmetry of structure S ; there are three lenses of all types other than type A , of which there is only one lens.

One can check easily that all edges in structure S can potentially satisfy the edge-imaging condition, i.e. three intersecting lenses (e.g. L_D, L_F and another L_D) share a principal point (P_{DF} in this case) and principal points of four intersecting lenses (e.g. L_A, L_B, L_C and L_D) lie on a straight line (in this case, line through all P_A, P_{BE}, P_C and P_{DF}). Focal lengths of the included lenses can be calculated using Eqs. (3.12), (3.9) and (3.8). Namely, lenses L_A, L_B, L_C and L_D together form an asymmetric four-lens intersection. Therefore, their focal lengths can be calculated by Eqs. (3.12) with substitutions $f_1 \rightarrow f_A, f_2 \rightarrow f_B, f_3 \rightarrow f_C, f_4 \rightarrow f_D$ and $x_0 \rightarrow R/2, P_1 = 0, P_2 = h_1, P_3 = h_2$ and $P_4 = h$

$$\begin{aligned}
 f_B &= -f_A \frac{R(h-h_1)(h_2-h_1)}{h h_2 \sqrt{R^2 + 4h_1^2}} + R \frac{h_1(h_2-h_1)}{h_2 \sqrt{R^2 + 4h_1^2}}, \\
 f_C &= f_A \frac{R(h-h_2)(h_2-h_1)}{h h_1 \sqrt{R^2 + 4h_2^2}}, \\
 f_D &= -f_A \frac{R(h-h_1)(h-h_2)}{h_1 h_2 \sqrt{R^2 + 4h^2}} + R \frac{h(h-h_2)}{h_2 \sqrt{R^2 + 4h^2}}.
 \end{aligned} \tag{3.13}$$

Then, lenses L_D, L_F and one more L_D form a symmetric intersection of three lenses and thus the focal length f_F of lens L_F can be calculated using Eqn. (3.8) with substitutions

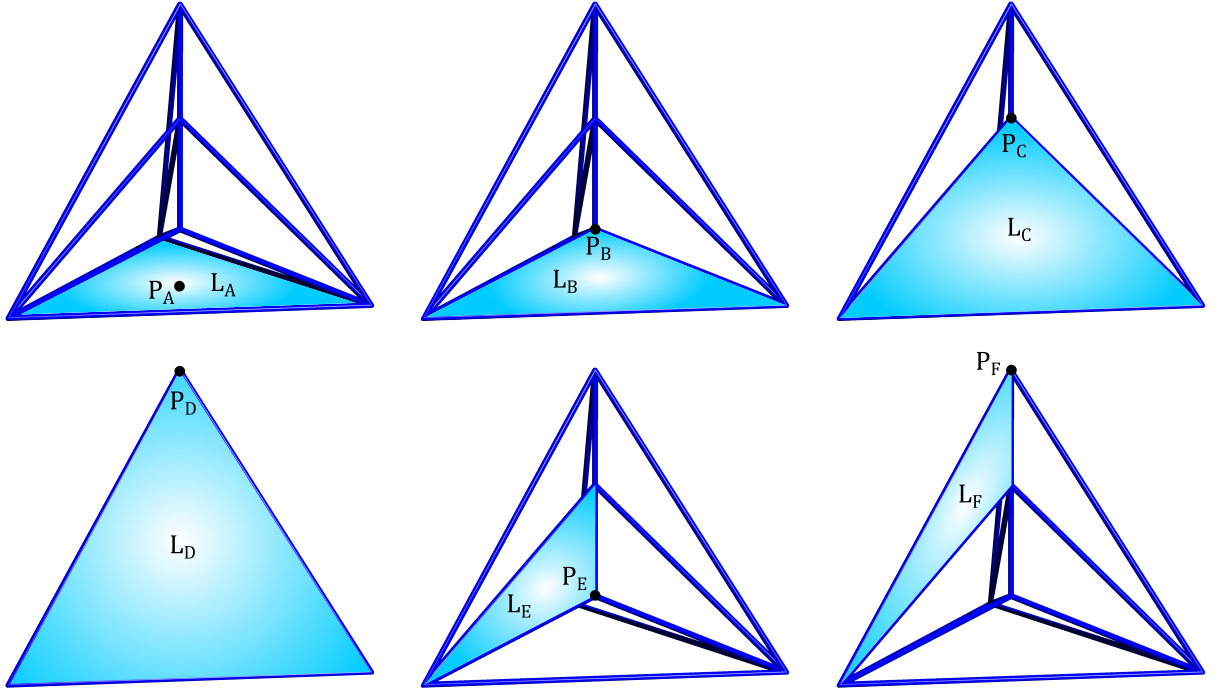


Figure 3.7: Lenses included in the structure S, highlighted as blue surfaces. Lenses are labelled L_A, \dots, L_F , with corresponding principal point positions P_A, \dots, P_F (black dots).

$f_1 \rightarrow f_F, f_2 \rightarrow f_D, f_3 \rightarrow f_D$ and $\alpha_{13} = -\alpha_{12} = \arctan \sqrt{3}h/\sqrt{R^2 + h^2}$

$$f_F = \frac{R(h - h_2)(f_A(h - h_1) - h h_1)}{2\sqrt{3} h h_1 h_2}. \quad (3.14)$$

Finally, lenses L_E, L_F and two lenses L_C form a symmetric four-lens intersection and therefore the focal length f_E of lens L_E can be obtained employing Eqn. (3.9) with substitutions $f_4 \rightarrow f_F, f_2 \rightarrow f_E, h_4 \rightarrow h - h_2$ and $h_2 \rightarrow h_1 - h_2$

$$f_E = \frac{R(h_1 - h_2)(f_A(h - h_1) - h h_1)}{2\sqrt{3} h h_1 h_2}. \quad (3.15)$$

3.6 Structure S as an Omnidirectional lens

So far, we have shown how to build a TO device, using ideal lenses only. As a result, we obtained the structure presented in Fig. 3.6(d), which we call Structure S. In this section, we will focus on the imaging properties of Structure S. Consider a cell separated from the outside by lens L_A . Let us call this cell, surrounded by lenses L_A and other three lenses of type L_B , cell 1. Clearly, cell 1 can be imaged to the outside space (cell 0) by the lens L_A . Since structure S is a TO device, the same mapping is achieved by any other combination of lenses, separating cell 1 from the outside. In other words, structure S provides a mapping of any physical-space structure in cell 1 like due to lens L_A in all directions. This observation leads us to call structure S an *omnidirectional lens*. Fig. 3.8(b) supports our arguments: a patterned sphere is placed in cell 1. When seen from the outside, the sphere appears magnified and stretched in the vertical direction. This is because, when imaged due to a lens, the longitudinal image magnification $m_L := dz'/dz$ actually equals the square of the transverse magnification $m_T = z'/z$.

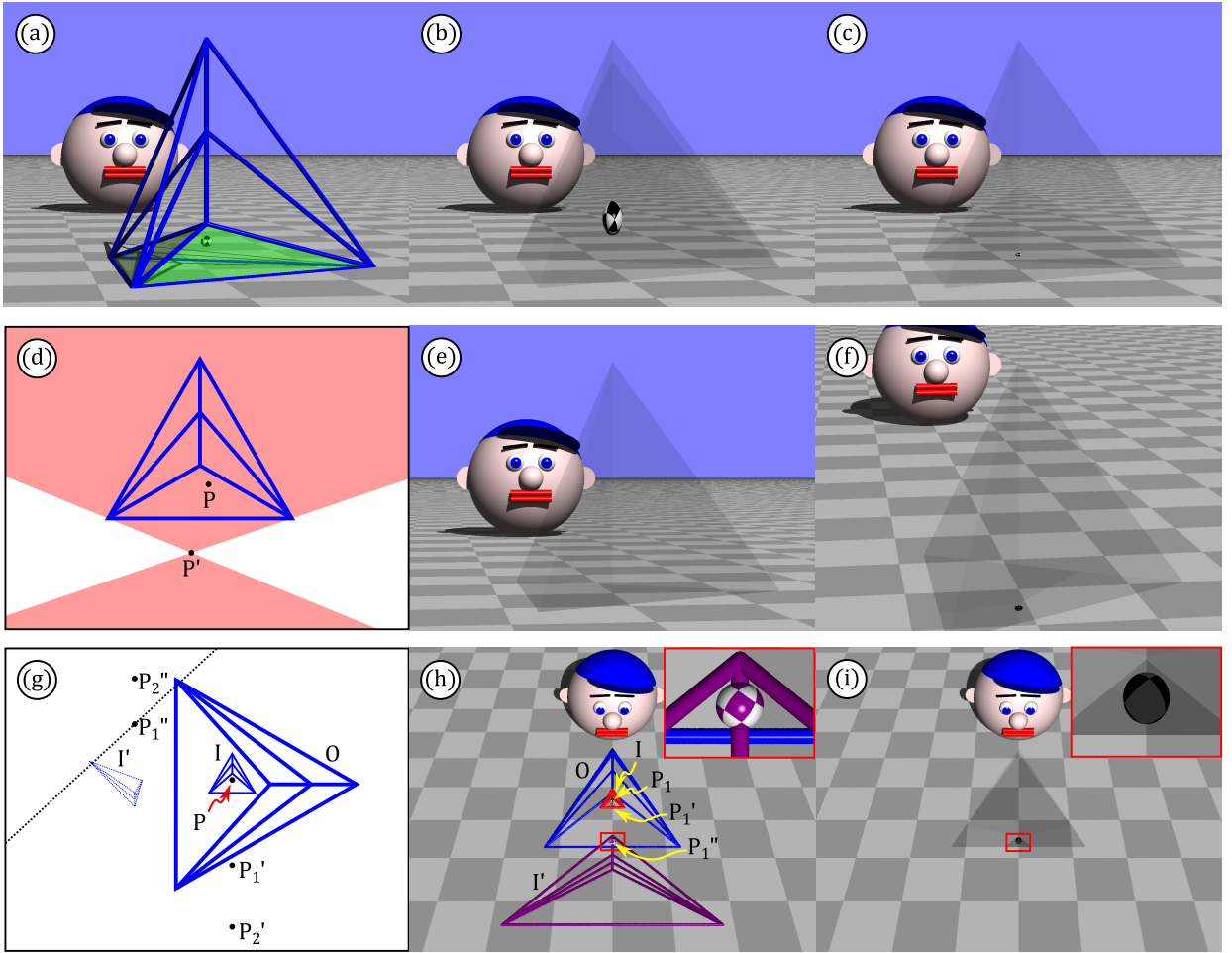


Figure 3.8: (a) Structure S without lenses; blue cylinders represent common edges of lenses included in the structure. If an object (patterned sphere) is placed in cell 1 (green semi-transparent area), it is imaged to the outside as due to a base lens L_A (b). That is why we sometimes call it an omnidirectional lens; (c) if the focal lengths of included lenses are chosen such that the cell 1 is imaged to the outside space with a magnification approaching zero, the omnidirectional lens can be regarded as an almost-invisibility cloak; panels (d)-(f) demonstrate the abyss cloak: object P is imaged to a position P' outside the cloak; (f) If camera is placed in a position such that both image of the object (patterned sphere) and the cloak are seen in the same direction (red shaded area in panel (d)), that image is visible for the camera; (e) otherwise the image is invisible. Panels (g)-(i) present the bi-abys cloak: the final object P''_i due to both cloaks I and O can be visible from the outside only if there are lines (like the black dotted one in panel (g)) such that all O , I' (the purple structure in panel (h)) and P''_i are located on that line. This is shown in raytracing simulations, presented in panels (h) and (i): panel (h) shows the geometries of the outer cloak O (blue structure), inner cloak I (red structure) and its image I' due to O (purple structure) and positions of the cloaked object P_1 (patterned sphere) and its corresponding images P'_1 and P''_1 ; (i) as (h) but blue, red and purple structures indicating the geometries of O , I and I' are removed and all ideal lenses are in place. The zoomed view of the image P'_1 is provided in the top right corner of both panels.

3.7 Structure S as an almost-invisibility cloak

As mentioned in the introduction, probably the most famous example of a TO device is an invisibility cloak. In the following sections, we will show three setups when our ideal-lens structure S can be regarded as an invisibility cloak, too.

In the first setup, we employ the fact that structure S is actually an omnidirectional lens, providing mapping of the inside space (cell 1) like due to a base lens L_A , in all directions. Therefore the physical-space structure (the object) inside S appears either magnified or de-magnified when seen from the outside. Now if the physical-space structure is de-magnified to a size approaching zero, it will become hardly recognizable when seen from the outside and therefore almost invisible. Structure S indeed provides, in certain parameter regimes, such de-magnification in all directions as demonstrated in Fig. 3.8(c). At the same time, any outside object seen through the cloak appears undistorted, as required for a structure S to be an invisibility cloak. Note that de-magnification equal to zero can be only achieved in a limit when the focal length of lens L_A equals zero, which is impossible even with ideal thin lenses.

3.8 Structure S as an abyss cloak

Because it seems that we can not achieve a perfectly zero de-magnification with the structure S, we will present two alternative cloaking strategies. The first one employs the fact that physical-space structure inside the cloak can be imaged to an area *outside* of the cloak. This idea is depicted in Fig. 3.8(d): a point P inside the cloak is imaged to a position P' below lens L_A . The image P' can be visible only from such viewing positions, from which P' is seen in the same direction as a part of the cloak. In the other cases, the observer either cannot see the cloak itself (and therefore cannot see the image due to that cloak) or the image is located outside the field of view due to the cloak. From all such positions, image P' (and thus object P itself) is invisible.

Figs 3.8(e) and (f) show raytracing simulations of a structure S, with the focal lengths of the included lenses chosen such that the physical-space structure inside S (a patterned sphere) is imaged below the cloak. In Fig. 3.8(e) the camera is positioned such that no part of the image of the sphere can be seen in the same direction as any part of the cloak, and thus it is invisible. However, when the camera is moved to a position such that a part of the image of the sphere lines up with the cloak (as in Fig. 3.8(f)), those parts of the image of the sphere become visible. Since the sphere appears to be located inside a bottomless cavity – an abyss – we call this configuration an *abyss cloak*.

3.9 Bi-abyss cloak: an ultimate invisibility

The final ideal-lens cloak consists of two nested abyss cloaks. Again, consider an object at position P. The inner abyss cloak, I, images P to a position P' lying outside of I. The outer abyss cloak, O, then creates two images, both external to O: an image P'' of P' and also image I' of the inner cloak I. As discussed above, P' can be visible only from positions such that both P' and a part of I are in line. At the same time, the outer cloak O images both I and P' to the outside space, and P'', the image of P', is visible only in the same direction as I', the image of I. But I' itself is visible only from directions from which a part of the outer cloak O can be seen, and so P'' is visible only if it is seen in the same direction as both I' and O. If this is not satisfied, object P becomes completely invisible.

Fig. 3.8(g) illustrates that there are indeed configurations in which P'' , I' and O can not be seen in the same line. The figure is sketched for two different values of the focal length f_{A-I} of the base lens (type L_A) of the inner cloak I : in the first case, the image of object P due to I is denoted P'_1 and the image of P due to both cloaks I and O is then P''_1 . For the other choice of the focal length of a base lens of cloak I , those images are denoted P'_2 and P''_2 respectively. In the first case, the focal length f_{A-I} is chosen such that P''_1 lines up with I' and O ; P''_1 can therefore be visible along such lines of sight, which is also confirmed by raytracing simulations, presented in Fig. 3.8(i). The second case is chosen such that P''_2 does not line up with I' and O . P''_2 will therefore be invisible from anywhere outside O . We confirmed this with numerous raytracing simulation, not shown for lack of anything to see. The resulting structure is therefore a perfect omnidirectional invisibility cloak; we call it *bi-abyss cloak*.

3.10 Discussion

The Structure S is an unusual combination of ideal thin lenses, which is not constrained by paraxiality of individual lenses. Unfortunately, real lenses do not work well in a non-paraxial regime and thus execution of our TO devices with real lenses seems unlikely to be realised.

However, one can replace ideal lenses with corresponding phase holograms. The resulting device, in principle, works perfectly for light rays passing through one particular viewing position. Although such a device is no longer omnidirectional, we will later show that even with this limitation, our devices have a number of potential applications.

Of course, these holograms should not be paraxial but designed for a specific conjugated object-image pair: since Structure S is a TO device, there is a unique mapping between any cell within the device, call it i , and the outside of the device, cell 0 . This also works the other way round, i.e. any outside point V_0 is uniquely imaged to a point V_i in cell i ; point V_0 can be chosen, for example, to be the viewing position. To satisfy the edge-imaging condition, the ideal thin lens separating cells i and j provides, in principle perfect, imaging between points V_i and V_j . Consequently, all that is required is to design the phase hologram replacing that lens such that it provides the same unique imaging between points V_i and V_j . Designing all phase holograms in the device in this way then leads to a structure which works exactly like the ideal-thin-lens structure when seen from the position V_0 . Fig. 3.9 shows that such a lens-hologram device works well only for the position V_0 for which it was optimised.

The idea of designing lens holograms optimised for an arbitrary object-image pairs, for example V_i and V_j , is actually very simple: the hologram just shifts the phase of the incident light field such that the phase measured along straight lines, emerging from point V_i and intersecting again at point V_j after passing through the hologram, is independent of the position where the line hits the hologram.

Our proposed application for lens holograms coincides very well with a rapid progress in the development of efficient phase (and amplitude) holograms in the form of metasurfaces [43], and already has been used as novel lenses [44, 53] which can even provide a compensation of dispersion effects [54, 55]. Therefore, metasurfaces appear to be very promising real-life approximations of ideal thin lenses.

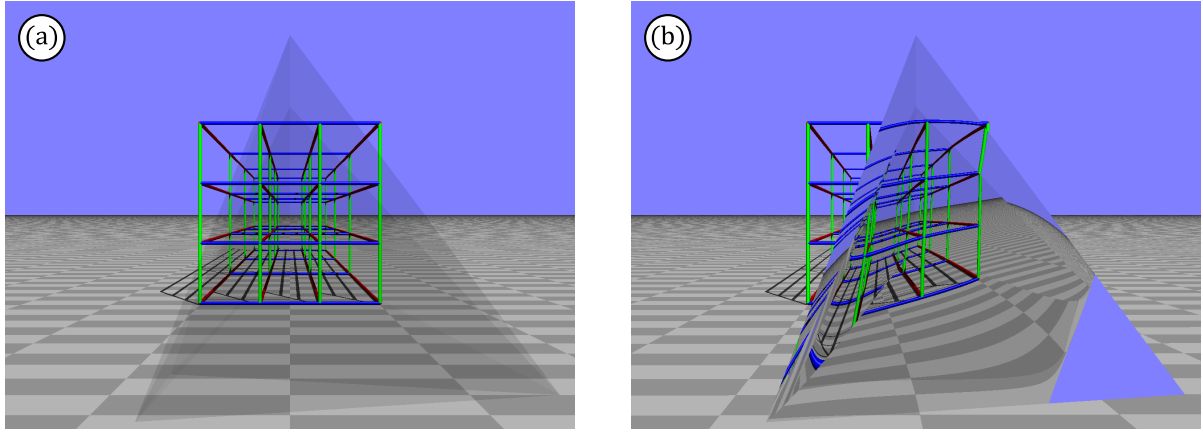


Figure 3.9: Raytracing simulations of a phase-hologram realisation of the Structure S. When seen from the intended viewing position (a), the device does not distort the scene seen through it, exactly as with the corresponding ideal-thin-lens device. This is not the case for any other viewing position; an example is shown in (b). All simulations assumed perfect dispersion compensation for all visible light and were performed with an extended version of our custom raytracer Dr TIM [1].

3.11 Potential applications

Without any doubt, lenses are widely used optical components. Improving their design then could therefore have wide-ranging applications. For example, our proposed omnidirectional lenses increase the field of view to the entire solid angle, i.e. 4π steradians and therefore may be used in any application, requiring a wide field of view (FOV). Below, we list few such applications, where the observation point is located in a close vicinity of a particular position, for which the real-life realizations of the proposed devices should be optimised.

Objective lens of a microscope is an obvious application for a lens with a large field of view and therefore for the omnidirectional lens. It is well known that the resolution of a microscope depends on the numerical aperture (NA) of its objective lens. Numerical aperture, as defined, is proportional to the solid angle from which the light is collected by the objective lens. That solid angle is usually limited to 2π , which corresponds to a case in which the objective lens is very close to the observed sample. To enlarge the solid angle, two objective lenses are sometimes employed. This strategy is used in a 4π microscopy [56]. Alternative, and perhaps better method of the collection of light over 4π solid angle can be achieved with our omnidirectional lens.

Omnidirectional lenses can be potentially used in virtual-reality (VR) headsets. Virtual reality is a growing market and VR headsets are a subject of a vast research and development [57–59]. However, VR headsets still suffer from several imperfections, e.g. a limited field of view, that prevent the user from a perfect immersion to a virtual world. Omnidirectional lenses get over the limited field of view: VR binoculars with omnidirectional lenses could, in principle, fill the observer’s entire visual field. Such “Omnidirectional binoculars” could therefore add to existing solutions (such as [60]).

Chapter 4

Optical simulations of curved spaces

4.1 Introduction

Physics in curved spaces and curved space-times are fascinating fields of research. In such a space, very unusual phenomena can be observed, e.g. the sum of the inner angles of a triangle can be different from 180 degrees or an observer travelling along a straight line can reappear at the point from which the journey started. Even more exciting predictions came along with the General theory of relativity [61], published in 1916. Although most of the theoretical predictions of curved space-time physics, e.g. gravitational lensing [62], black holes [63] or gravitational waves [64], have been observed already [65–67], there are still phenomena which remain unobserved, e.g. Hawking radiation [68] or the Unruh effect [69]. Consequently, several approaches had been made to simulate these inaccessible phenomena in the laboratory [19, 20, 70].

The concepts of curved spaces also appear very naturally in metamaterials [71]. These composite, sub-wavelength materials are defined by their ability to exhibit extraordinary properties not found naturally (such as negative refraction) and possess these abilities through their structuring, rather than chemical composition. Stemming from Ref. [72], the discovery that light propagation in an inhomogeneous anisotropic medium is equivalent to light propagation in a curved space has provided much motivation to design metamaterials that mimic such environments. The same idea lies in the background of the whole field of transformation optics [5, 8]. There, virtual space (or, equivalently, electromagnetic space) is mapped to physical space via a suitable mapping $\mathbf{R} = f(\mathbf{r})$. Physical space is filled with an optical medium such that the optical distances between points in physical space are the same as optical distances of the corresponding points in virtual space. A direct consequence (again due to Fermat’s principle) is that the function f also maps light rays themselves from virtual to physical space, so the rays are deformed along with the space. This has opened vast possibilities in designing devices such as invisibility cloaks [3, 5, 8], super-scatterers [73] and many other novel devices [74–78].

The extensive research highlighted above demonstrates that the optics of curved spaces is of a great interest and importance. In this chapter, we focus on a yet another aspect of optics of curved spaces and investigate light propagation on curved surfaces embedded in flat Euclidean spaces. The hallmark of curvature is *angular defect*: the angles completely surrounding a point in a 2D space add up *not* to 2π (as they would if the 2D space was flat, i.e. a plane), but to $2\pi - \varepsilon$, where ε is the so-called *deficit angle*. This happens, for example, at the tip of a cone, or at a polyhedron vertex. For smooth curved manifolds, e.g. the surface of a sphere, the angular defect is continuously distributed over the manifold. If such a surface is approximated by a manifold that is piecewise flat, the deficit angle as well as the curvature become concentrated to discrete points—vertices. This idea has been

formalised in Regge calculus [79], which enables an approximation of arbitrarily curved spaces of any dimension. Regge calculus is used as a unique way to numerically investigate aspects of general relativity, for instance black hole collisions [80] whose relevance is particularly timely after the recent discovery of gravitational waves [67]. In this thesis we adopt the technical framework of Regge calculus as a guiding principle to realise curvature, which this way links our research with some of the most pressing open questions of theoretical physics.

The angular deficit, e.g. of a tip of a cone, can be visualised when the manifold is unwrapped to a plane. The deficit angle then corresponds to a wedge of angle ε on 'non-existing space'. Because the unfolded manifold is flat, it might be easy to simulate it in a lab, which is also supposedly a flat space. Here the paradigm of simulating a curved space changes significantly: instead of building the actual curved space, one can equivalently build an unfolded net of the simulated manifold, containing wedges of 'non-existing space'. Of course, the edges of one single wedge must be identified to each other.

Clearly, the wedges of "non-existing space" can not be built mechanically. However, one can build them optically using the properties of negative refraction. Our design employs so-called Space-cancelling (SC) wedges, of which half of the wedge is composed of a simple empty space and the other half of the wedge is composed of material of the refractive index, which is negative to the surrounding space. These SC wedges, in principle, enable optical simulations both two and also three-dimensional curved spaces embedded in a flat Euclidean space.

4.1.1 Contributions

The work carried out in this chapter stems from the final-year projects of Gregory Chaplain and Dimitris Georgantzis Garcia, supervised by Dr Johannes Courtial and co-supervised by myself and Dr Christoph Englert. Dimitris' project was run in a collaboration with Prof. Tomáš Tyc.

4.2 Loop-imaging condition as a "flat-space condition"

In this section, we will present the connections between the main concepts of curved spaces and mapping in transformation-optics (TO) devices. In Chapter 3, we have formulated the crucial requirement for building TO devices, the loop-imaging condition. This condition states that any object is imaged back to itself due to elements of TO device encountered along any closed loop. This makes an intuitive connection to parallel transport mentioned above since one could say that any object-sided vector is retrieved in a TO device after being transported along a closed loop. Namely, it indicates that our TO devices are examples of flat spaces, which is actually an expected result: as mentioned in Chapter 3, the standard way of designing devices and tuning the material properties using transformation optics is based on distortions of a flat space. For example, the invisibility cloak proposed in [5] corresponds to the Euclidean space, in which one point is blown up to a finite volume. It was this analogy which actually motivated us to investigate the capabilities of building non-Euclidean transformation optics devices.

There is also a notable algebraic connection between the physics of curved spaces and our method of building TO devices using lenses. The loop-imaging condition can be formulated such that the image position is independent of the closed loop imaged through. This formulation implies the group structure of imaging due to TO device.

The proof is nearly trivial and well known. Mapping due to a lens corresponds to a central collineation. The important note is that collineation can be, in general, described by an $N \times N$ matrix [81] and the particular mappings we consider are also invertible. Therefore, collineations satisfy the axioms for a group. The group of invertible $N \times N$ matrices together with matrix multiplication forms the general linear group over \mathbb{R} , or $GL_N(\mathbb{R})$ [82]. At the same time, the mappings between loops on Riemannian manifolds (of N -dimensions), M_N , form a group - the fundamental group [79]. Taking this approach then allows a metric to be defined in M_N , which then leads to the curvature of such a space. This shows another connection between our theory of building TO devices and the mathematical tools of differential geometry, allowing us to extend our arsenal of TO devices.

Finally, one can notice similarities between our proposed TO structure, (see Fig. 4.1(a)) and the triangulation of Riemannian manifolds. In numerical calculations and computer physics, the common practice is to approximate a smooth manifold M_N by a piecewise flat complex of N -dimensional simplest flat elements — simplices. In two dimensions, these simplices coincide with triangles (that is why it is sometimes called a triangular approximation). The curvature is then concentrated to the *bones*, $(N - 2)$ -dimensional subsets where neighbouring simplices meet (in two dimensions, bones coincide with common vertices of neighbouring triangles). An example of a two-dimensional triangulation is depicted in Fig. 4.1(b). On the other hand, our transformation optics device, made entirely of lenses, can be seen as a complex of simplices: each lens included in the device has a triangular clear aperture. The triangular structure of this device therefore closely relates to simplicial complexes. This is a reason why we attempt to link the structure of the device to the abstract maths of algebraic topology.

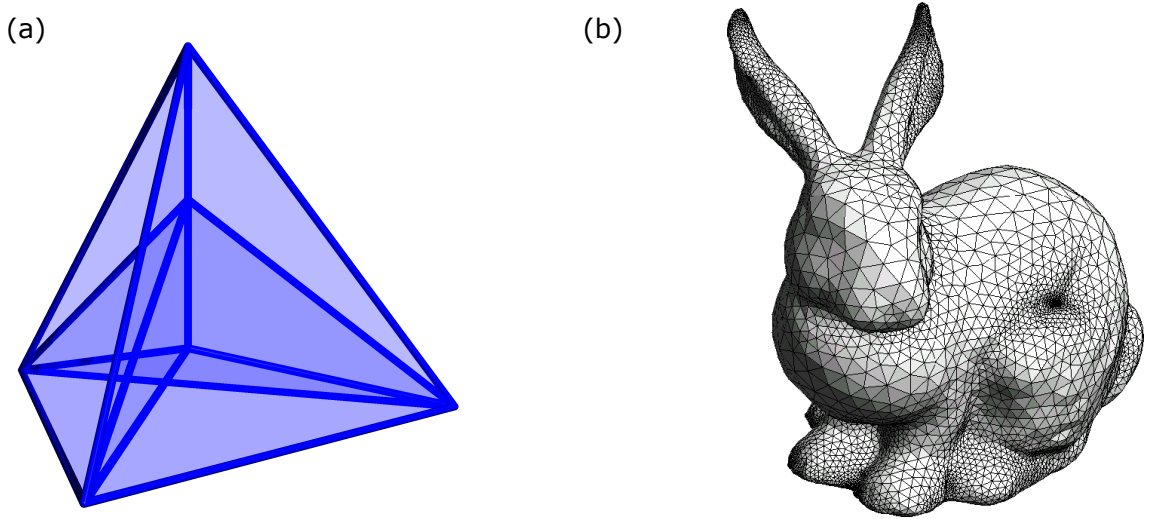


Figure 4.1: Similarities between the algebraic topology and TO devices; (a) the structure S can be regarded as a simplicial complex, a structure composed of 2D simplices (triangles); (b) simplicial complexes are commonly used for modelling curved surfaces, for example a surface of a bunny [6].

4.3 Angular deficit, parallel transport and curvature

Let us briefly discuss the key ingredients of description of the non-euclidean space and how they are connected. As mentioned in the introduction, very unusual phenomena can be observed in curved spaces. Let us call T some triangle embedded in a two-dimensional curved space; we denote ∂T the boundary of the triangle. Due to the curvature of the space, the sum α of the inner angles of T will differ from π . The *angular deficit* $\varepsilon = \alpha - \pi$, therefore seems to be an indicator of curvature. Indeed, this can be derived from the famous Gauss-Bonnet theorem [83]

$$\iint_T K dS + \int_{\partial T} k_g ds = \varepsilon, \quad (4.1)$$

where K is the Gauss curvature, k_g is a geodesic curvature, dS is the area measure and ds is the length measure.

The common practice to investigate curvature, however, is measuring the angle between a vector \mathbf{v}_i at point x , and vector \mathbf{v}_f , which corresponds to \mathbf{v}_i transported along a closed loop, keeping it constant all the while – “parallel transported”. The concept of parallel transport itself is interesting, and worth spending some time thinking about. In a flat space, it is natural to compare (add, subtract, take the dot product etc.) two vectors at different points since one can easily move a vector from one point to another, keeping its Cartesian components constant [84] (see Fig. 4.3(a)). Such a transport of a vector \mathbf{v} along a curve $x^\alpha(\lambda)$ with tangent $t^\alpha(\lambda) = dx^\alpha/d\lambda$ (where λ is an appropriate parameter) can be expressed mathematically in the following way

$$(t^\alpha \partial_\alpha) \mathbf{v} = 0, \quad (4.2)$$

where $\partial_\alpha = \partial/\partial x^\alpha$. Once both vectors are moved to the same point, the usual operations allowed in a vector space can be done. Note that in Eq. (4.2) and in the following calculations, the Einstein notation is employed, i.e. the summation is implied by index variable appearing twice in a single term, without being otherwise defined.

In N -dimensional manifold (that is a topological space that locally resembles Euclidean space near each point), let us call it M_N , the situation is more complicated. First, the Euclidean measure $ds^2 = dx^2 + dy^2 + dz^2$ is replaced by the Riemann measure

$$ds^2 = g_{ij} dx^i dx^j, \quad (4.3)$$

where g_{ij} is the *metric tensor*; the inverse tensor is then denoted g^{ij} , so $g_{ij} g^{jk} = \delta_i^k$. Since no global N -dimensional coordinates can be defined on M_N , the common practice is to define a *tangent space* $T_x M$ through a point $x \in M_N$ as a set of all tangent vectors to curves through x [85]. For a 2-manifold M , a tangent space $T_x M$ can be visualised as a tangent plane to M at point x (see Fig. 4.2). The parallel transport between two nearby points x_1 and x_2 is then defined by an *affine connection* [86]. Omitting the formal definition, the affine connection is equivalently specified by a *covariant derivative*

$$D_\nu v^\mu := \frac{\partial v^\mu}{\partial x^\nu} + \Gamma_{\nu\sigma}^\mu v^\sigma, \quad (4.4)$$

where $\Gamma_{\nu\sigma}^\mu$ is the connection coefficient. Provided the Levi-Civita connection, connection coefficients are the well-known Christoffel symbols, which can be calculated from the metric

$$\Gamma_{\nu\sigma}^\mu = \frac{1}{2} g^{\mu\rho} \left(\frac{\partial g_{\sigma\rho}}{\partial x^\nu} + \frac{\partial g_{\nu\rho}}{\partial x^\sigma} - \frac{\partial g_{\nu\sigma}}{\partial x^\rho} \right). \quad (4.5)$$

Eq. (4.2), describing the parallel transport in Euclidean space, then becomes [87]

$$t^\alpha D_\alpha v^\mu = 0. \quad (4.6)$$

Note that Eqs. (4.2) and (4.6) are equivalent since the connection vanishes in Euclidean space.

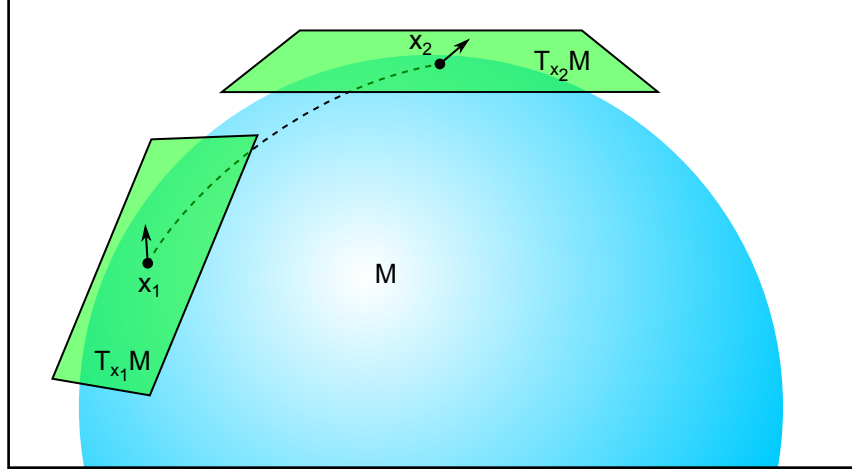


Figure 4.2: In two dimensions, the tangent spaces $T_{x_1}M$ and $T_{x_2}M$ to the manifold M can be visualised as tangent planes to the surface M at points x_1 and x_2 respectively. A parallel transport of a vector (black arrow) from x_1 to x_2 is then defined by an affine connection between $T_{x_1}M$ and $T_{x_2}M$.

It turns out that, in a curved space, the result of parallel transport of a vector from one point to another will depend on the path taken between the points [84]. This can be easily seen in the following example: given a vector v^μ at point $x \in M_N$. Now, parallel transport v^μ first along a curve with tangent t^α by a line element dt and then along the curve s^β by a line element ds (the blue solid line in Fig. 4.3(b)). Let us denote a^μ the vector created by such transport. Now we will compare a^μ with a vector b^μ , corresponding to the vector v^μ parallel transported first along the curve s^β by ds and then along curve t^α by dt (the red solid line in Fig. 4.3(b))

$$\begin{aligned} b^\mu - a^\mu &= (D_\alpha D_\beta - D_\beta D_\alpha) v^\mu t^\alpha s^\beta dt ds \\ &= \left[\frac{\partial}{\partial x^\alpha} \left(\frac{\partial v^\mu}{\partial x^\beta} + \Gamma_{\beta\sigma}^\mu v^\sigma \right) + \Gamma_{\alpha\nu}^\mu \left(\frac{\partial v^\nu}{\partial x^\beta} + \Gamma_{\beta\sigma}^\nu v^\sigma \right) - \frac{\partial}{\partial x^\beta} \left(\frac{\partial v^\mu}{\partial x^\alpha} + \Gamma_{\alpha\sigma}^\mu v^\sigma \right) \right. \\ &\quad \left. - \Gamma_{\beta\rho}^\mu \left(\frac{\partial v^\rho}{\partial x^\alpha} + \Gamma_{\alpha\sigma}^\rho v^\sigma \right) \right] t^\alpha s^\beta dt ds \\ &= \left[\frac{\partial \Gamma_{\beta\sigma}^\mu}{\partial x^\alpha} - \frac{\partial \Gamma_{\alpha\sigma}^\mu}{\partial x^\beta} + \Gamma_{\alpha\nu}^\mu \Gamma_{\beta\sigma}^\nu - \Gamma_{\beta\rho}^\mu \Gamma_{\alpha\sigma}^\rho \right] v^\sigma t^\alpha s^\beta dt ds \\ &= R_{\alpha\beta\sigma}^\mu v^\sigma t^\alpha s^\beta dt ds, \end{aligned} \quad (4.7)$$

where $R_{\alpha\beta\sigma}^\mu$ is the *Riemann curvature tensor*. From the definition, It is obvious that Riemann tensor vanishes in a flat space since the connection vanishes and the covariant derivatives become standard, commutative derivatives. Employing the contraction, one can easily obtain the *Ricci tensor*

$$R_{\alpha\beta} := R_{\alpha\mu\beta}^\mu = \frac{\partial \Gamma_{\alpha\beta}^\mu}{\partial x^\mu} - \frac{\partial \Gamma_{\alpha\mu}^\mu}{\partial x^\beta} + \Gamma_{\mu\nu}^\mu \Gamma_{\alpha\beta}^\nu - \Gamma_{\beta\rho}^\mu \Gamma_{\alpha\mu}^\rho, \quad (4.8)$$

from which we finally get the simplest curvature invariant of a Riemannian (smooth) manifold – the *scalar curvature* (or Ricci scalar)

$$R := g^{\alpha\beta} R_{\alpha\beta}. \quad (4.9)$$

This nicely shows the connection between parallel transport and curvature.

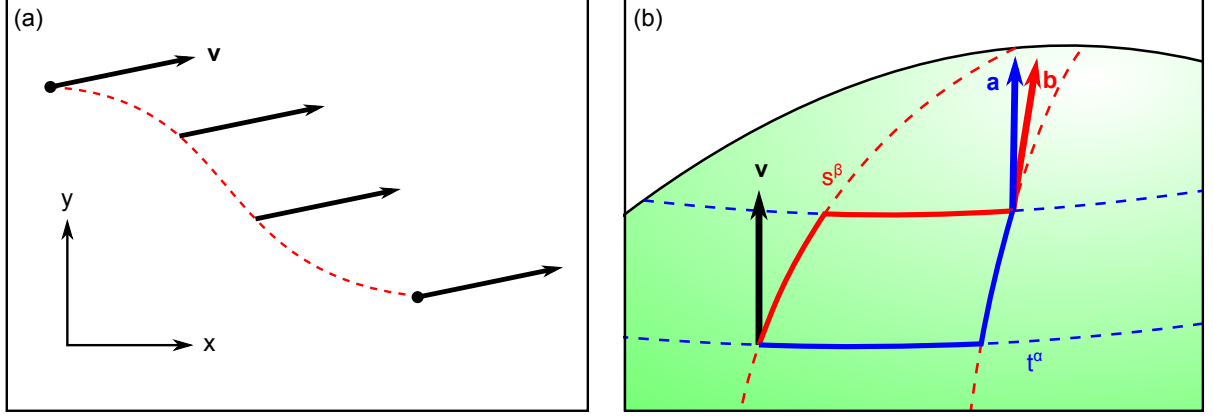


Figure 4.3: Parallel transport and curvature; (a) the parallel transport of vector \mathbf{v} in a Euclidean space corresponds to moving the vector along a curve (red dotted line), keeping its components constant; (b) in a curved space, the parallel transport depends on the path: vector \mathbf{a} corresponds to \mathbf{v} parallel transported along the blue solid line, whereas \mathbf{b} coincides with \mathbf{v} parallel transported along the red solid line.

4.4 Geodesics

One of the most important terms of curved-spaces physics is the geodesic. As defined, a geodesic is the shortest path between two points $x_1 = x(\lambda_1)$ and $x_2 = x(\lambda_2)$ in a manifold M (an example of a geodesic on the globe is shown in Fig. 4.4). This leads to the problem of minimizing the following functional [87]

$$\int_{x_1}^{x_2} ds = \int_{x_1}^{x_2} \sqrt{g_{\alpha\beta} dx^\alpha dx^\beta} = \int_{\lambda_1}^{\lambda_2} \sqrt{g_{\alpha\beta} \dot{x}^\alpha \dot{x}^\beta} d\lambda, \quad (4.10)$$

where $g_{\alpha\beta}$ is the metric tensor, $\dot{x}^\mu = dx^\mu/d\lambda$ and λ is a parameter describing the curve $x(\lambda)$. Recognizing Lagrangian $L = ds/d\lambda = \sqrt{g_{\alpha\beta} \dot{x}^\alpha \dot{x}^\beta}$, variation of Eq. (4.10) leads to the Lagrange equations

$$\frac{d}{d\lambda} \left[\frac{\partial \left(\sqrt{g_{\alpha\beta} \dot{x}^\alpha \dot{x}^\beta} \right)}{\partial \dot{x}^\mu} \right] = \frac{\partial \left(\sqrt{g_{\alpha\beta} \dot{x}^\alpha \dot{x}^\beta} \right)}{\partial x^\alpha}. \quad (4.11)$$

Now we transform this equation in terms of the line length s , using the definition of Lagrangian $L = ds/d\lambda$, which implies $d/d\lambda = L d/ds$. Denoting $v^\mu = dx^\mu/ds$, we finally get the geodesic equation

$$\frac{dv^\mu}{ds} + \frac{1}{2} g^{\mu\rho} \left(\frac{\partial g_{\sigma\rho}}{\partial x^\nu} + \frac{\partial g_{\nu\rho}}{\partial x^\sigma} - \frac{\partial g_{\nu\sigma}}{\partial x^\rho} \right) v^\nu v^\sigma = 0. \quad (4.12)$$

If Levi-Civita connection is considered, this equation can be written in the well-known form, using Christoffel symbols

$$\frac{dv^\mu}{ds} + \Gamma_{\nu\sigma}^\mu v^\nu v^\sigma = 0. \quad (4.13)$$

Note that the geodesic equation is equivalent to the equation of parallel transport (4.6) of vector v^μ along its own direction since

$$\frac{dv^\mu}{ds} + \Gamma_{\nu\sigma}^\mu v^\nu v^\sigma = \frac{dv^\mu}{dx^\sigma} \frac{dx^\sigma}{ds} + \Gamma_{\nu\sigma}^\mu v^\nu v^\sigma = v^\sigma \left(\frac{dv^\mu}{dx^\sigma} + \Gamma_{\nu\sigma}^\mu v^\nu \right) = v^\sigma D_\sigma v^\mu = 0. \quad (4.14)$$

A curve, which parallel transports its tangent vector, is called *autoparallel* [87]. Therefore, a geodesic is autoparallel if Levi-Civita connection is regarded. We will use this observation when we present our approach of simulating curved spaces, in which geodesics will be represented by light ray trajectories.



Figure 4.4: The shortest path between two points on the globe — the geodesic— usually does not map to a straight line between the corresponding points on the map. Picture taken from [7].

4.5 Topology, Triangulation and ε -cones

Our approach of optical simulation of curved spaces is inspired by the concept of a triangulation of topological spaces. Let us briefly present the fundamentals, which can be found in references [88–90].

The *topological space* is an ordered pair (X, τ) , where X is a set and τ is a collection of subsets of X , satisfying the following axioms:

- The empty set and X itself belong to τ .
- Any arbitrary (finite or infinite) union of members of τ still belongs to τ .

- The intersection of any finite number of members of τ still belongs to τ .

The elements of τ are called open sets and the collection τ is called a *topology* on X .

A *simplex*, or N -simplex, is the N -dimensional generalization of a tetrahedral region of space. Given a set of affinely independent points a_0, \dots, a_N (i.e. the vectors issuing from an arbitrarily chosen point to the rest of the points are linearly independent), a simplex σ can be defined as a set of all convex combinations $\lambda_0 a_0 + \dots + \lambda_N a_N$, where, $\lambda_0 + \dots + \lambda_N = 1$ and $0 \leq \lambda_i \leq 1$ for all $0 \leq i \leq N$. Points a_0, \dots, a_N are then *vertices* of σ . Given any subset $\{a_{i_0}, \dots, a_{i_k}\}$ (where $k < N$), the k -simplex generated by points a_{i_0}, \dots, a_{i_k} is then called the *face* of σ . For example, the 1-simplex is the line segment. Adding dimensions, the 2-simplex is a triangle and in three dimensions, the simplex coincides with the tetrahedron.

A *Euclidean simplicial complex* K in \mathbb{R}^N is a collection of k -simplices in \mathbb{R}^N ($0 \leq k \leq N$) such that (i) every face of a simplex of K is in K , (ii) the intersection of any two simplices of K is a face of each of them, and (iii) every point in a simplex of K has a neighborhood that intersects finitely many simplices of K . The union of all simplices in K is a topological space, called geometric representation of K and denoted $|K|$, with the subspace topology from \mathbb{R}^N . For example, a geometric representation of a closed euclidean simplicial complex of 2-simplices in \mathbb{R}^3 coincides with a surface of a polyhedron.

The *triangulation* of a topological space X is a particular homeomorphism (continuous function between topological spaces that has a continuous inverse function) between X and $|K|$. Very loosely speaking, triangulation corresponds to an approximation of a smooth manifold M_N by a similarly looking N -manifold $|K|$, composed of N -simplices. $|K|$ is therefore piecewise flat. It can be shown that any smooth N -manifold can be approximated by an appropriate geometric representation of a closed Euclidean simplicial complex $|K|$, composed of N -simplices.

The curvature of $|K|$ is then concentrated in $(N - 2)$ -dimensional intersections of simplices in $|K|$, sometimes called *bones* [79]. To see this, let us discuss a 2-dimensional case for a moment; the following ideas are readily extended into N dimensions, applying N -dimensional analogs [79]. In two dimensions, any triangulation $|K|$ can be regarded as a configuration of several tiny pyramids (without bases), which are topologically equivalent to a cone. Therefore, one such baseless pyramid can be characterised mathematically using the metric

$$ds^2 = dr^2 + r^2 d\phi^2, \quad (4.15)$$

where ds is the line element and r and ϕ are cylindrical coordinates. In a flat space, any two points with the same r and $\phi + 2N\pi$ with $N \in \mathbb{Z}$ are realised to be identical. To obtain a manifold with the topology of a cone, we can just replace 2π with $2\pi - \varepsilon$ [79]. This pyramid is then named the ε -cone, where ε gives us a notion of an angular deficit. This can be visualised when the ε -cone is cut along one of its edges and unfolded to a plane: a wedge of “missing space” of angle ε will appear. This concept is very important in linking the transformation optics devices to curved spaces.

4.6 Optical removal of space, the space-cancelling wedges

Before we present our simulations of more complex curved spaces, let us first discuss how a single ε -cone can be simulated optically. As mentioned in the previous section, the cone is topologically equivalent to the plane with a wedge of space being removed and the edges of the “non-existing space” are identified to each other. Such “gluing” is well-known in

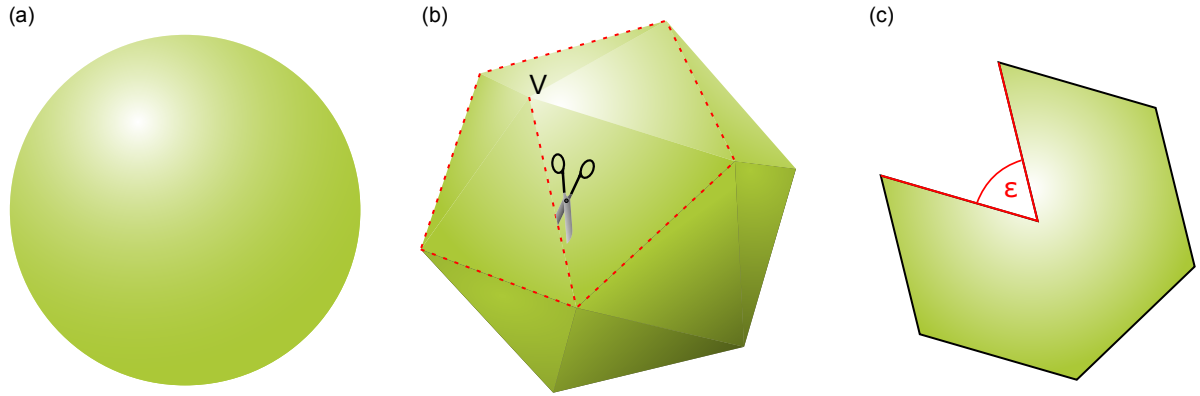


Figure 4.5: A smooth manifold (a) (a sphere) can be approximated by a complex of simplices (b). The curvature is then concentrated to the vertices: this can be visualised by cutting the surface around a vertex (for example V) and unfolding it into a plane. A wedge of “missing space” of angle ϵ will appear (c).

topology and defines an equivalence relation on the original surface: in addition to each point being identified to itself, pairs of points to be identified and declared equivalent. The new surface is then the set of equivalence classes with a suitable definition of distance between points based on the corresponding distances in the original surface [88]. Therefore, finding some wedge-like optical configuration that identifies one of its edges with the other, effectively removing a wedge of space, is central in optically simulating cone-like surfaces, such as the ϵ -cone. We call such a device the *space-cancelling wedge* or simply SC wedge. In the following sections, we will discuss several devices which have a potential to be space-cancelling wedges.

4.6.1 SC wedge using negative refraction

The principle of optical cancellation a wedge of space of angle ϵ is depicted in Fig. 4.6. Let us explain this in more detail: consider a wedge of apex angle $\epsilon/2$, built of material with refractive index $n = -1$, surrounded by a medium with $n = +1$ (vacuum). Using the Snell’s law, one can easily see that a light ray incident on point P at the interface 1 between media with $n = -1$ and $n = +1$ is refracted such that the light ray, after being refracted on both interfaces 1 and 2, passes through the point P’, which is actually the mirror image of P with respect to plane 2. Furthermore, the direction of the ray outgoing from P’ is rotated by ϵ around the wedge edge with respect to the direction of the of the same light ray, when incident on P (as shown for ray A in Fig. 4.6(a)). Together with the fact that the optical path length of any light ray in the space between half-planes 1 and 1’ equals zero, this space thus appears to be “non-existing” for a light ray passing through. Loosely speaking, the “negative space” (with $n = -1$) cancels out an equal portion of the “positive space” ($n = +1$), resulting in a “zero” or “non-existing space”, resulting in a 3D ϵ -cone. However, such an SC wedge suffers from the following limitation: consider a light ray, incident on interface 1, such that its projection to a plane perpendicular to the wedge edge makes an angle $\beta \leq \epsilon/2$ with the plane 1 (such as ray B in Fig. 4.6(a)). The light ray is then refracted at 1 such that it is either parallel or divergent from the interface 2 and thus “lost” in the wedge, instead of “transported” to the plane 1’. This effect can be eliminated by building a fan of SC wedges: the SC edge of angle ϵ is replaced by N consecutive wedges, each of angle ϵ/N , as shown in Fig. 4.6(b). Increasing the number of such wedges then eliminates the portion of light rays “lost” in the fan. Another solution

employs planar mirrors, symmetrically placed at the end of the wedge, as depicted in Fig. 4.6(c). The angle μ between each mirror and the face of the wedge, however, cannot be chosen arbitrarily: for $\mu < \pi/2$, some light rays might be reflected on the mirror to become divergent from plane 2. For $\mu > \pi - \varepsilon/2$, some light rays might become parallel with the mirror after being refracted on the interface 1. Therefore, μ should be chosen to lie in the range $\pi/2 \leq \mu \leq \pi - \varepsilon$. This is possible only if $\varepsilon/2 < \pi/2$; for $\varepsilon/2 \geq \pi/2$, a fan of wedges and mirrors can be employed.

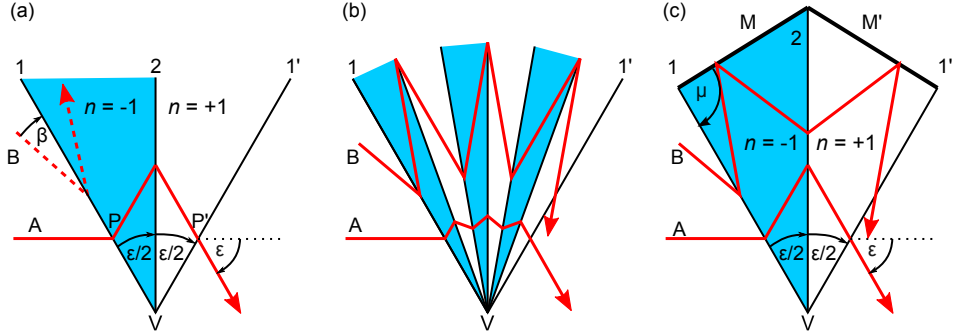


Figure 4.6: The space cancelling wedge between half-planes 1 and 1' using negative refraction. (a) Half-plane 1, the outer face of the wedge of $n = -1$ medium (of angle $\varepsilon/2$), gets mapped due to the wedge to half-plane 1', such that 1' coincides with 1 rotated around the wedge edge V by an angle ε . Although ray A (solid red line) is refracted as desired, ray B (dashed red line) is refracted such that it diverges from half-plane 2 and gets “lost” in the wedge. (b) This can be treated by building a fan of N (here $N = 3$) wedges, each of angle $\varepsilon/2N$ or (c) one can insert mirrors M and M' at the end of the $n = -1$ wedge, symmetrically with respect to half-plane 2. This requires the angle μ to be chosen to lie in the range $\pi/2 \leq \mu \leq \pi - \varepsilon$.

4.6.2 SC wedges using absolute instruments

The SC wedge can be also constructed using a combination of absolute optical instruments (i.e. a device, typically defined by a spatially varying refractive index, in which bound ray trajectories are closed [91]) and transformation optics. We will explain the idea in detail in this section. As mentioned above, the SC wedge aims to map optically two planes, ρ and σ , to each other, see Fig. 4.7(a). For this goal, we will apply transformation optics within the wedge between planes ρ and σ .

In the physical space, planes ρ and σ make an angle ε and their intersection line is denoted a . Now consider a virtual space, with Cartesian coordinates X, Y, Z , such that planes ρ and σ are mapped to planes ρ' and σ' in the virtual space, such that any functions ψ and ϕ defined on ρ and σ equal the respective functions ψ' and ϕ' , defined on ρ' and σ' . In the virtual space, however, ρ' and σ' make an angle π instead of ε . The half-plane $Z = 0; Y > 0$ then corresponds to the plane ρ , and similarly σ' lies in the half-plane $Z = 0; Y < 0$, see Fig. 4.7(b). The X -axis is then equivalent to the intersection line a , defined in the physical space. In such virtual space, we can construct the SC-wedge employing a suitable absolute instrument; the physical-space structure will be then obtained by an appropriate affine transformation.

The absolute instrument, that maps optically the planes ρ' and σ' to each other, is the Lissajous lens, a device in which all ray trajectories form Lissajous curves [92]. If the frequency of oscillations of the light ray in the X direction is chosen to be twice the

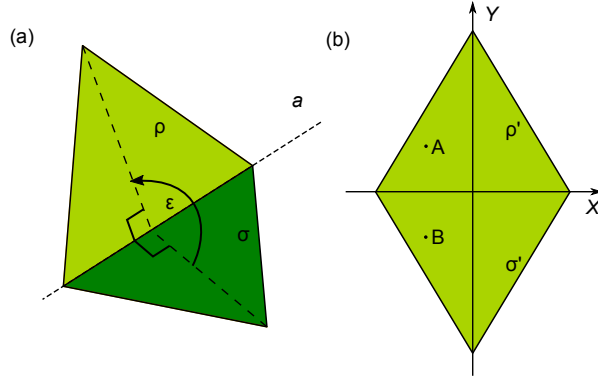


Figure 4.7: The space-cancelling wedge using absolute instruments (a) The half planes ρ and σ , making an angle ε around the line a in a physical space and (b) the corresponding half-planes ρ' and σ' in virtual space, lying in the plane XY . Points A and B are mapped to each other by a medium with refractive index N .

frequency in Y and Z directions, the light ray will make just half an oscillation in both Y and Z directions per one full oscillation in X direction. As a result, a light ray with the wavevector (K_X, K_Y, K_Z) , incident on the Lissajous lens at the point $A = (X, Y, 0)$, will leave the lens at the point $B = (X, -Y, 0)$ with the wavevector $(K_X, -K_Y, -K_Z)$. The corresponding refractive index in virtual space $N(\mathbf{R})$ is then given by the following formula, derived from the general formula presented in [92]

$$N(\mathbf{R}) = \alpha \sqrt{1 - \frac{4X^2 + Y^2 + Z^2}{b^2}} \quad (4.16)$$

where α and b are constants that can be chosen arbitrarily; b should be chosen large enough, so $4X^2 + Y^2 + Z^2 < b^2$ wherever within the SC wedge.

Now we will transform the refractive index $N(\mathbf{R})$ from the virtual space to the physical space. We will do it as follows: the X -axis is transformed to the axis a and the wedge of angle π between the half-planes ρ' and σ' in the virtual space is uniformly expanded into the wedge of angle ε between the half-planes ρ and σ in the physical space. In the cylindrical coordinates, such an expansion is equivalent to multiplying the azimuthal coordinate by the factor $\gamma \equiv \varepsilon/\pi$. This transformation finally yields the physical-space medium with the following permittivity and permeability tensors

$$\hat{\varepsilon}(\mathbf{r}) = N^2[\mathbf{R}(\mathbf{r})] \text{diag}(1/\gamma, \gamma, 1/\gamma), \quad \hat{\mu} = \text{diag}(1/\gamma, \gamma, 1/\gamma), \quad (4.17)$$

assuming that the refractive index $N(\mathbf{R})$ in virtual space is realized purely dielectrically. Remarkably, there is just a slight anisotropy in the medium, induced by the mapping from virtual to physical space.

SC wedges, built in this way, can be combined together to simulate a more complex triangulation of a curved space, containing several ε -cones. To avoid overlapping of multiple SC wedges, leading to multi-valued refractive indices, one has to choose the constant α large enough so that light rays will be refracted when leaving the net (where refractive index equals unity) and entering the SC wedge. By doing this, the light rays explore only a small portion of the “multivalued region”, which can then be divided into disjoint parts, each being “used” for one SC wedge. This yields the desired single-valued permittivity and permeability tensors $\hat{\varepsilon}(\mathbf{r})$ and $\hat{\mu}$.

4.6.3 SC-wedge using ideal lenses

The third approach for building the SC wedge is based on imaging properties of a combination of three skew ideal thin lenses. Although it cannot be realised physically, an ideal thin lens represents a very useful model for the initial design of instruments comprising physical lenses. In Chapter 2, we have presented a theory of imaging due to combinations of skew lenses and, in Chapter 3, we showed how to employ skew lenses to build novel transformation-optics devices, for example omnidirectional invisibility cloaks. In addition, we showed that an appropriate combination of three ideal lenses performs an image rotation: the image space coincides with the object space, but rotated by an arbitrary angle ε around the line where the planes of all three lenses intersect. Therefore, such a three-lens image rotator is equivalent to a space-cancelling wedge of wedge angle ε . We confirmed this idea with raytracing simulations, one of them is presented in Fig. 4.8, provided that the relevant light rays pass through all three lenses. However, not all the light rays entering the three-lens combination actually pass through all three lenses, which leads to a field-of-view limitation. This limitation can be overcome by improving the optical design, but is unlikely to be removed entirely.

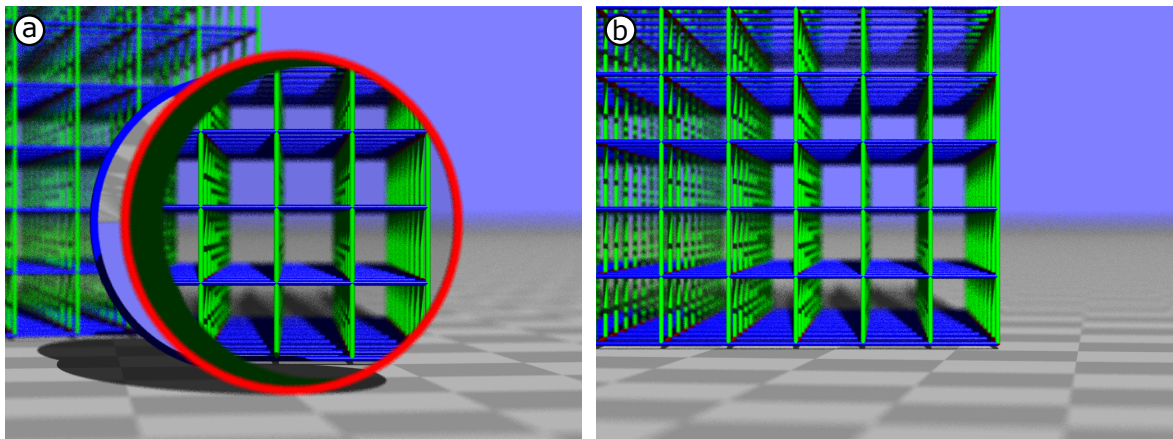


Figure 4.8: The space-cancelling wedge using ideal thin lenses. (a) An orthogonal lattice consisting of green and blue cylinders is placed behind a three-lens image rotator. Only the closest lens (red-framed) is seen directly. When seen through all three lenses, the lattice appears rotated by 15 degrees around a vertical axis. (b) This is confirmed by a simulation without the lenses, but with the camera rotated by -15 degrees around the same axis; The scene seen through all three lenses in (a) is identical to the corresponding part in (b). Both simulations were performed with an extended version of our raytracing software Dr TIM [1].

4.6.4 SC-wedge by transferring the light field

Probably the easiest to become practically realised, the final design of the SC wedge is inspired by light-field (or plenoptic) imaging based on arrays of very small lenses — lenslet (or microlens) arrays. Such arrays capture the information about both the position where light rays intersect a surface and the direction with which they do so [93]. This is exactly the information which needs to be recorded on the face of the SC wedge, before transportation to the other, optically identified, face of the wedge. The transfer of the optical field from one face to the other can be then realised using the optical fibres. Since the SC wedge is expected to transfer the light field without any distortion from one of its

wedges to another, an array of single-mode optical fibres is the most suitable choice as they can transfer the signal for long distances with low dispersion and, in principle, no degradation of the signal passing through.

The scheme of our device is shown in Fig. 4.9(a). Consider a parallel bundle of light rays incident on a lenslet L_1 located in one of the two optically identified faces of the SC wedge. L_1 then focuses these parallel light rays into the point in its back focal plane, where one end of a thin optical fiber is located. Obviously, light rays are focused to this fiber only if they pass through the clear aperture of lenslet L_1 in one particular direction. The fibre thus represents both the position and direction with which the light ray was incident on the face of the SC wedge; the accuracy of position is limited by the clear aperture of the lenslet and the accuracy of direction is limited by the spacing between the fibres.

In the respective position in other face of the SC wedge, an identical lenslet L_2 is placed. The optical fibre is, of course, located in the front focal plane of L_2 , so the light rays become collimated again when escaping the lenslet array. The direction of the light rays emerging at L_2 is given by the position of the end of the respective optical fibre in L_2 's front focal plane. Namely, one can place the fibre such that the direction of the light rays emerging from L_2 is rotated by the deficit angle ε with respect to the direction of the light rays incident on L_1 . If the two lenslet arrays (in which both L_1 and L_2 are included) cover both the optically identified faces of the SC-wedge, with the ‘‘inner’’ focal planes of these arrays being connected with a suitable array of optical fibres, the entire light field incident on plane of the first lenslet array is transferred to the plane of the second lenslet array. Note that the transfer works also in the other way round since the setup is symmetric. The optical field travelling through optical fibres of different lengths becomes phase-modulated when emerging the fibre array because of different optical path lengths gained in fibres of different lengths; however, this can be compensated by placing a suitable phase plate on the end of each fibre. To eliminate cross-talking between neighbouring ‘‘pixels’’ of optical fibres, corresponding to two neighbouring lenslets, an array of baffles between the lenslet arrays and their relevant focal planes (see Fig. 4.9(a)) can be inserted. However, this restricts the field of view of each lenslet. Furthermore, both the positions and directions are discretised in this space-cancelling wedge as the overall number of fibres equals the space-bandwidth product of the system [94].

To make the SC-wedge easier to fabricate, the relative position of the ends of each fibre should be the same at both sides of the fibre array. Such a fibre array is known as a coherent fibre bundle (which is not to be confused with fibre bundle known from differential geometry). However, the coherent fibre bundle, which simply connects the corresponding points in the inner focal planes of two lenslet arrays, does not provide the desired light-field transfer: the direction of emerging light rays is rotated by π around the normal of the second lenslet-array plane relative to the desired direction. To fix this problem, one can twist the ends of each individual sub-bundle of fibres, which connects the respective lenslets, by π (as is shown in Fig. 4.9(b)). Equivalently, further optical components (additional lenslet arrays in the case shown in Fig. 4.9(b)), providing the rotation of the light-ray direction by π , can be added to one end of the device. Note that these ideas are very closely related not only to many other fields of research and technology, including light-field capture [93], and display devices [95], Shack-Hartmann sensors [96], integral photography [97], integral imaging [98], generalised refraction using confocal lenslet arrays [99], Moiré magnifiers [100], Gabor superlenses [101], and digital integral cloaking [102].

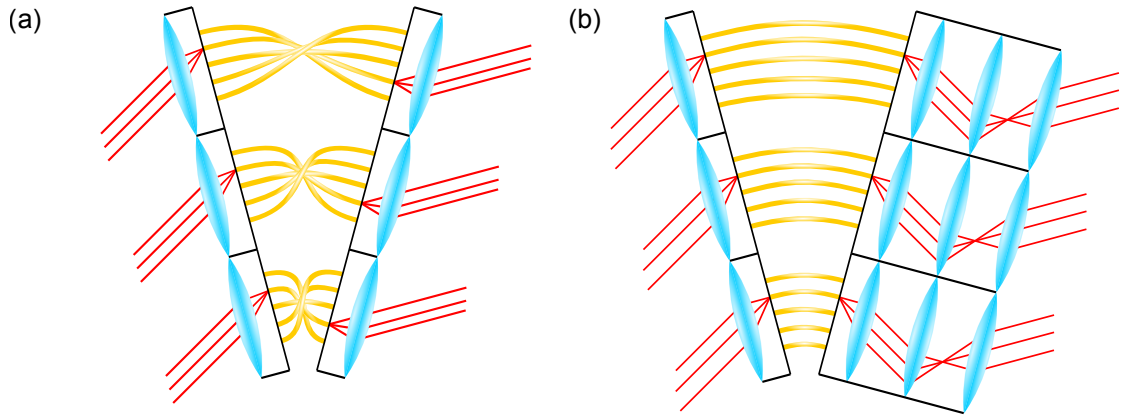


Figure 4.9: The space-cancelling wedge using light-field transfer. (a) Two lenslet arrays (cyan) fill the optically identified faces. The array of optical fibres (yellow) then connects the “inner” focal planes (dotted lines) of the two lenslet arrays; baffles (solid black lines) eliminates the cross-talking between neighbouring lenslets. Then, each fibre represents one particular combination of a position (given by the position of the corresponding lenslet) and direction with which light rays (solid red lines) are incident on the faces. (b) To employ a coherent fibre bundle, further optical components, e.g. a combination of two identical lenslet arrays, needs to be added. The faces of the SC wedge are then formed by the outermost arrays.

4.7 Simulating curved 2D spaces

Once we can build the SC-wedges, topologico-optical analogs of ε -cones, we will show how to build simplicial complexes from them. For the sake of clarity, we first present our concept for the two-dimensional (2D) curved spaces. After a general description, we will demonstrate our approach on specific examples, namely two simplest platonic bodies: the regular tetrahedron and the cube. Note that although square – a face of a cube – is not simplex, it can be seen as a complex containing two triangles. We will later extend our construction to one more dimension: we will build 3D hypersurfaces of 4D polyhedra.

Consider a two-dimensional surface S of a three-dimensional polyhedron P . Our method then employs the *net* N of the surface S , which is simply the surface S unfolded to a plane. Such unfolding of S to a plane includes “cutting” along some of the edges of S , e.g. edge 1 on the surface of the tetrahedron in Fig. 4.10(a) is split to edges 1 and 1’ after being unfolded to the net N . 1 and 1’ (and similarly all the other edges) need to be accompanied by appropriate gluing instructions, which identify them with one another. The net N fitted with appropriate gluing instructions is also called a quotient space [88]. The net N can then be folded and “glued” to become the surface S . A device providing the gluing instructions optically is the SC wedge presented above.

To make this procedure clearer, we will present some specific examples. Let us start with the surface of a tetrahedron 4.10(a). The tetrahedron can be unfolded to a plane, resulting in its net N , which coincides with an equilateral triangle. The gluing instructions on N are the following: each half of each edge of N is identified with the other half of the same edge. The midpoints of the edges then become three out of four vertices of S : the remaining vertex V is created by gluing the vertices of N together. The other polyhedra can be unfolded to their quotient spaces (nets with appropriate gluing instructions) in a similar way. Fig. 4.10(d-f) shows a symmetric unfolding of a cube.

Now we will employ the unfolded net N to simulate the light propagation on the surface of a polyhedron S . This is equivalent to light propagation in a free space, with

appropriate wedges of space being “removed”. Such space cancellation can be performed optically using the SC wedges. The net of a tetrahedron realised in this way is presented in Fig. 4.10(g). The outside of the net is filled with three SC wedges, each of deficit angle π . The vertices of the SC wedges coincide with midpoints of edges of the net N . Fig. 4.10(g) shows the ray-tracing simulation of the setup, with three different light ray trajectories (each labelled with a different colour). Similar simulation for the net of a cube is presented in Fig. 4.10(j,k).

The simulations of the scene (a grey ball in otherwise empty space) as seen by an observer respectively living on the surface of a tetrahedron and of a cube are presented in Figs 4.10(i,l). In these simulations, we have added a third dimension to demonstrate the features of the view; the resulting 3D space is a tensor product of the 2D surface and one-dimensional Euclidean space \mathbb{R} . We have added this extra dimension because keeping the original two dimensions would lead to one-dimensional simulations, with a limited information content. Both on the surface of a tetrahedron and the surface of a cube, the observer can see many copies of the scene (the ball). This because of the compactness of the surface, allowing many different rays from the ball to arrive at the observer’s eyes.

4.8 Simulating curved 3D spaces

We showed how the light-field propagation on 2D curved surfaces (namely tetrahedron and cube) can be simulated (and in principle demonstrated): the 2D, embedded in a 3D space, can be unfolded to a plane, with the gluing instructions being performed optically using the SC wedges. Now we will proceed one dimension higher.

Let us explain the idea of unfolding 3D hypersurfaces, embedded in 4D space, to the 3D flat space: consider a 3-manifold P , homeomorphic to a complex of 3-simplices (the tetrahedra). Analogously to the two-dimensional case discussed in the previous section, we can construct the net N of P , corresponding to a composition of 3-simplices with the appropriate gluing instructions. This time, however, pairs of 2D faces of the 3-simplices will be identified with one another. Provided that we can insert the appropriate SC wedges to the “non-existing” spaces between each such pair of 2D planes, the light propagation in this structure will be equivalent to a real 3D curved space.

Indeed, there are several examples of 3D hypersurfaces, which can be unfolded to a flat 3D space and fitted with SC wedges to simulate the light propagation in them. For example, this can be done for the hypersurface of 5-cell (or 4-simplex) or for a hypersurface of a hypercube. The net of a regular 5-cell consists of 5 regular tetrahedra: a central tetrahedron surrounded by 4 outer ones (note that each outer tetrahedron is stuck to a different face of the inner tetrahedron). Now, the gluing instructions, which tell us how this net should be folded into the 4th dimension, are represented by the numbers in Fig. 4.11(a).

The procedure of folding such 3D net into the 4th dimension is challenging since human brain usually experiences 3 spatial dimensions only. However, this folding can be performed optically using SC wedges: in total, 6 SC-wedges are needed, one for each edge of the central tetrahedron. Each SC-wedge has a bone (edge) which should lie on a different edge of the inner tetrahedron. Then, since the *dihedral angle* of a regular tetrahedron is $\alpha = \tan^{-1}(2\sqrt{2})$, each SC-wedge should cancel an angle $\varepsilon = 2\pi - 3\alpha \approx 2.59 \text{ rad} \approx 148^\circ$. Our ray-tracing simulation of this set-up is shown in Figs 4.11(b) and (e). The panel (b) shows the net from the outside with a light-ray trajectory within the hypersurface (similar to Fig. 4.10(g) which is a top view of the net of the tetrahedron) so we can see a geodesic on this space. Finally, in (e), we put a white sphere within the hypersurface of the 5-cell (as shown in in the bottom left corner of panel (e)) and observed

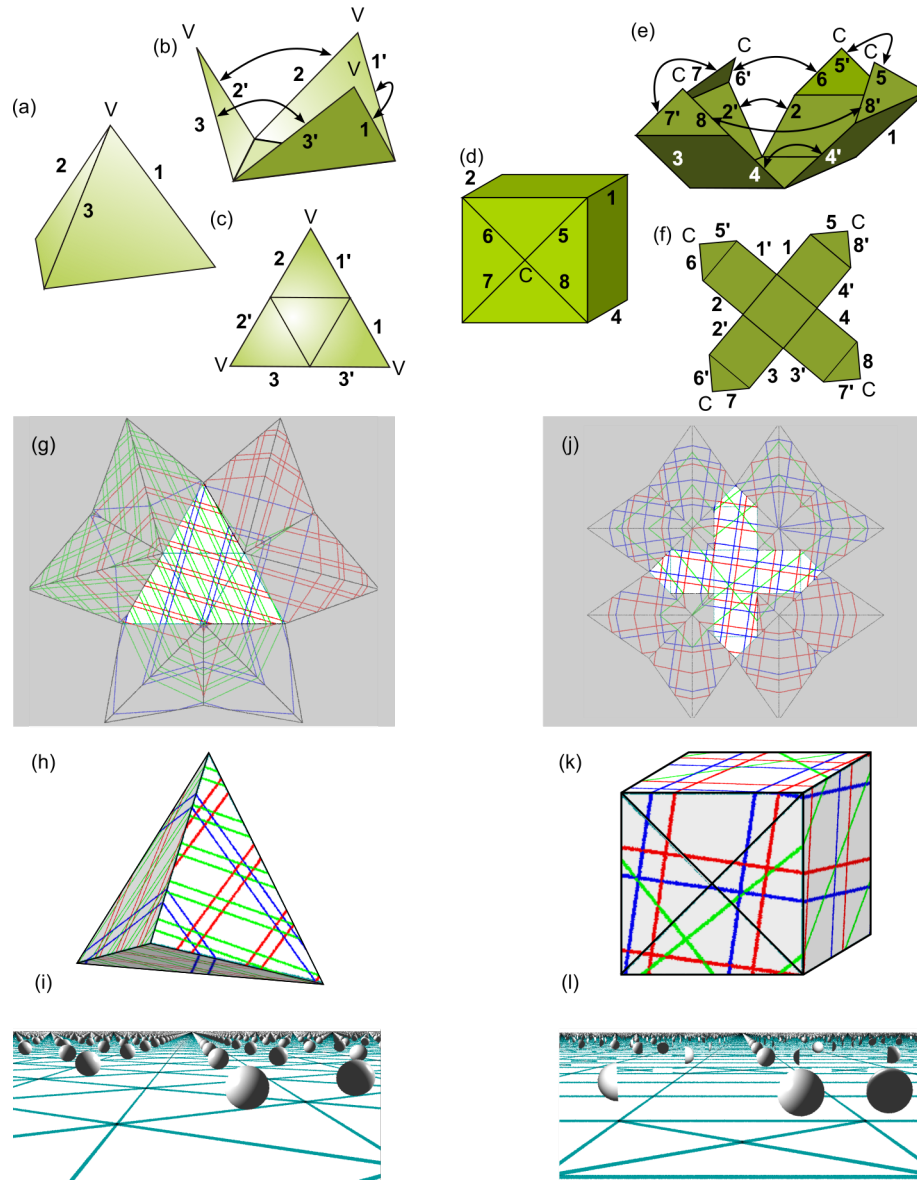


Figure 4.10: Optical simulations of the surface of a regular tetrahedron (a) and a cube (d). The simulations are performed on the respective nets of both tetrahedron and a cube; panels (b) and (e) show intermediate stages of unfolding. The corresponding gluing instructions are represented by numbers: edges labelled with the same number are identified; in panels (b) and (e), the black arrows indicate how the original edges of the folded surface split into two edges in the equivalent net and thus need to be identified optically in the simulations. V labels the fourth vertex of the tetrahedron, which appears as three separate vertices in the (partially) unfolded net. The surface of the cube has been unfolded symmetrically, at the cost of dividing one of its faces into four right triangles; C is the centre of that face. Panels (g,j) then show the nets of the tetrahedron and the cube, fitted with the space-cancelling wedges. Rays represent the geodesics on both (optically glued) surfaces; three rays (red, green, blue) are shown in each case. The continuity of the light-ray trajectories can be confirmed by mechanical folding and gluing of the nets, shown in panels (h) and (k). Finally, we present a simulation of the view of a scene (a white sphere) as seen from within the surface, with an added third, Euclidean, dimension perpendicular to the surface. The cyan lines show the edges of the respective nets of the tetrahedron and the cube. The raytracing simulations were performed using Dr TIM [1].

how the view of the sphere is altered due to the curvature of the space.

An analogous procedure can be done for the hypercube as well. The symmetric net of a hypercube, together with the respective gluing instructions, is presented in Fig. 4.11(c) (note that the cube, which acts as a 3D face of a hypercube, can be seen as a complex of five tetrahedra), and an example of a geodesic on the hypercube is simulated by a light-ray trajectory in Fig. 4.11(d). Again, a sphere is inserted to the net (bottom left corner in Fig. 4.11(f)), presenting the raytracing simulation of the view from the centre of the net.

4.9 Discussion

4.9.1 Non-euclidean Transformation Optics

Our method of simulating light propagation on both 2D and 3D simplicial complexes is closely related to the concept of non-Euclidean transformation optics [3], in which mapping between physical space and non-Euclidean virtual space (e.g. the surface of a sphere attached to a plane) is considered. The light-ray trajectories in a physical space then correspond to geodesics in virtual space.

Indeed, we can think of our setups in a similar way: the surface of the polyhedron P can be regarded as a non-Euclidean virtual space, whereas the respective quotient space fitted with SC wedges corresponds to a physical-space structure. The curvature of otherwise flat physical space is concentrated at the vertices of the quotient space; identifying the pairs of edges, which intersect at the vertices, is performed optically using appropriate SC wedges. This introduces a new concept into transformation optics and has a potential to extend its ideas and capabilities.

4.9.2 Negative refraction

SC-wedges using negative refraction assume an existence of non-dispersive, non-absorbing and non-reflective materials with a refractive index equal to minus one for all wavelengths (at least within the visible range). This is, in fact, also one of the toughest barriers to overcome on the path leading to an experimental realisation. At present, such a “transparent” negative-refractive-index material for a visible light remains undiscovered.

A material provides a negative refractive index if both electric permittivity ε and magnetic permeability μ are negative [103]. A natural question arises: do such materials exist? Although it sounds unlikely, it is not so difficult to find materials with negative values of both ε and μ . For example, metals such as silver, gold and aluminium exhibit negative ε ; negative μ include resonant ferromagnetic or antiferromagnetic systems [104]. Unfortunately, all these materials exhibit a strong dispersion; the condition $\varepsilon < 0, \mu < 0$ is realised only over a narrow bandwidth around the resonance frequency ω_0 of the material. This phenomenon can be explained, for example, by Drude-Lorentz model of a material, in which the atoms are conceptually replaced by a set of harmonically bound electron oscillators resonant at frequency ω_0 .

Alternatively, a medium with negative refractive index can be realised by a suitable metamaterial [104] designed to have a strong response to an applied electromagnetic field. Such metamaterials exist and several experiments have been performed [105–107]. All these experiments showed negative refraction due to the metamaterial. Negative refraction can be also achieved by photonic crystals [108–111]. Six years after the first demonstration of negative refraction [105], negative-index metamaterials have been brought from microwave frequencies [105–107, 112, 113] toward the visible light [114] (wavelength 780

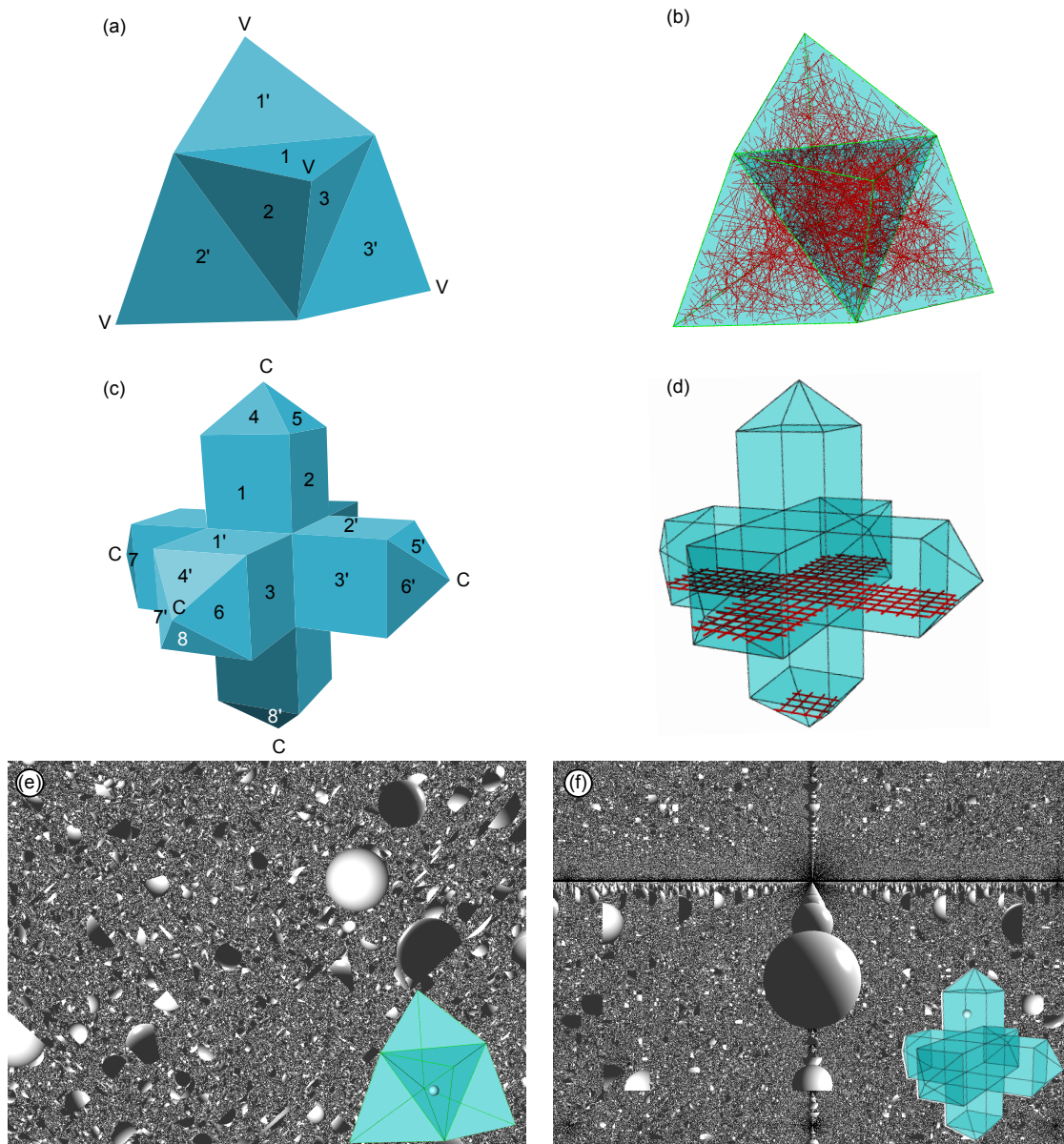


Figure 4.11: Raytracing simulations of the 3D hypersurface of (a) a 5-cell and (c) of a hypercube. The gluing instructions are represented with numbers: faces with the same numbers are identified (e.g. faces 1 and 1' are identified, some faces are unnumbered since the identified face is not visible.) (a) After unfolding, the fifth vertex of the 5-cell V splits into the 4 outermost vertices. On the other hand, the four outermost vertices of the net of the hypercube (c), all labelled C , represent the centre of the eighth cubic cell of the hypercube. Panel (b) shows one light-ray trajectory as seen from the outside of the net of a 5-cell. The view from the inside of such hypersurface is shown in (e), where a white sphere has been placed into the net as shown in the bottom left corner of panel (e). (d, f) Similar simulations, performed in Dr TIM [1], have also been performed for the hypercube.

nm and $n = -0.6$). However, losses of energy still need to be eliminated, for example by using crystalline metals and/or by introducing optically amplifying materials [115]. Moreover, the discrete nature of all designs mentioned above adversely affects transmission. For applications to come within reach, isotropic designs, and ways of mass production of large-area structures needs to be achieved. With emerging techniques such as micro-contact printing, nanoembossing, holographic lithography, and quantum tailoring of large molecules, however, these technical challenges can be successfully met.

In our particular application, we require that the refractive index of the negative-refractive-index wedge equals a negative value of the refractive index of the surrounding medium. In vacuum (air), this is not satisfied for most of the designs mentioned above ($n=-2.7$ [105], $n=-0.35$ [106], $n=-1.05$ [107], $n=-0.3$ [112] and $n=-0.6$ [114]). However, for $|n| > 1$ this issue can be treated by choosing an appropriate surrounding medium as it is easier to find a material with a certain value of positive refractive index rather than with the negative one.

Another device, which changes a light-ray direction in the same manner as a negative-refraction interface, is a sheet composed of very tiny dove prisms [116]. Hence in principal, we can replace the negative refraction wedges by two such sheets. However, the optical path length of a light ray passing through this system of two dove prism sheets is greater than zero. This is not a problem for light-ray simulations, when we are only interested in the change of light-ray direction. A problem appears when we want to simulate wave optics since the optical path length through the "non-existing" space is not equal to zero, which might cause unwanted interference patterns. Another obvious limitation is the discrete character of dove-prism sheets, which negatively affects a transmission of a light beam through the sheet.

4.9.3 General relativity

Without any doubt, the most famous and most exciting field of research where one can come across with curved spaces and curved space-times is the General Theory of Relativity formulated in 1916 by Albert Einstein [61]. The beauty of this theory is that it provides fantastic and well-tested predictions at the same time, for example space-time singularities from which even the light can not escape: black holes. Although most of the predictions of General Relativity have been astronomically observed, some effects remain undetected. Again, the most famous example is Hawking radiation where a black hole spontaneously emits virtual particles or photons emergent from the vacuum [68]. The main reason why Hawking radiation is still unseen is that its temperature is supposed to be much lower than the cosmic microwave background; thus, the signal is within the noise of cosmic microwave background. However, creating tabletop optical analogues of black holes is a new and promising approach [19,20] that may hold the key to the elucidation of phenomena that are extremely difficult to study through direct astronomical observations. These experiments employed the fact that ultrashort high-intensity laser pulses create moving refractive index perturbations that optically mimic the conditions at the black hole's event horizon.

We presented another way of simulating curved spaces, based on finite element methods. The obvious limitation of our method is that so far we can build only time-independent manifolds. In other words, we can simulate only curved spaces, no space-times. This restriction makes observing of phenomena like Hawking radiation and gravitational blue shift impossible. However, we can still simulate cosmic strings, another exciting prediction of General Relativity [117].

4.9.4 Wave optics

Even more interesting than studying light rays might be examination of electromagnetic waves travelling in a curved space. Several experiments mimicking curved space-times have been done.

In 2013, Sheng, Chong *et al.* performed an experiment in which a gravitational lensing was simulated on a surface of an integrated photonic chip [118]. A thin layer of polymethylmethacrylate on the chip acted as a waveguide, confining light to the chip's surface. The plastic layer was then heated and polystyrene microspheres were added before the plastic cooled. The surface tension of the sphere embedded in the slab made the plastic thickness vary in a continuous way. This mimicked a variation in the plastic's refractive index, and thus simulated the curved space.

In 2010, Ulf Peschel *et al.* realised a beam interference in a negatively curved space [119]. In their experiment, glass solids have been fabricated and the beam was then guided inside the glass tangent to the surface by total internal reflection. A camera was rotated around the sample to detect the scattered light.

And recently, in 2018, Patsyk *et al.* presented the first experimental observation of accelerating wave packets in curved space [120]. More specifically, they demonstrated, experimentally and theoretically, shape-preserving accelerating beams propagating on spherical surfaces: closed-form solutions of the wave equation manifesting non-geodesic self-similar evolution. Unlike accelerating beams in flat space, these wave packets change their acceleration trajectory due to the interplay between interference effects and the space curvature, and they focus and defocus periodically due to the spatial curvature of the medium in which they propagate.

However, all these experiments are two-dimensional, i.e. always a wave in a two-dimensional curved manifold is simulated. Our design allows us, in principle, to mimic beam propagation in a three-dimensional curved space. To preserve border conditions of the wavefunction, the phase and amplitude distributions on faces which are identified with each other must be identical. That implies the optical path length is equal to zero and there are no energy losses in a "non-existing space". So far this is the main limitation of experimental realisation of our ideas as there are no "transparent" negative-refractive-index materials.

4.9.5 Negative curvature

In this thesis, we simulated curved spaces with a positive curvature, i.e. the deficit angle ε around any single bone is less than 2π . This was done by "cancelling" a wedge of space with an angle ε at the tip. However, there are a lot of examples of curved spaces with a negative curvature, e.g. a torus. A natural question then arises: can one apply our strategy to simulate spaces with negative curvature?

So far, we have not found a way to optically simulate a manifold with negative deficiency. The reason for this is following: It is clear that if positive curvature was achieved by "cancelling" a space, a negative deficit angle corresponds to "adding" a wedge of space to the bone. If such a negative-deficiency simplicial complex is unfolded, an area of overlay of two spaces will appear: one rotated by angle $-\varepsilon$ with respect to each other. In fact, a light-ray trajectory is not unique inside this overlay, which implies a non-linear optical medium. Due to this fact, a negative deficiency remains very challenging to be mimicked optically.

4.10 Conclusions

In this chapter, we have presented a new approach for the optical simulation of curved spaces, which is based on triangulation and unfolding the curved spaces. We demonstrated our method for both 2D and 3D curved spaces, namely the triangulations of a sphere (surface of a tetrahedron and a cube) and of a hypersphere (hypersurface of a 5-cell and of a hypercube).

The key ingredient of our simulations is the space-cancelling wedge, an optical device which maps its faces onto each other and thus optically identifies the edges or faces to be glued. Space-cancelling wedges can be built in several ways, using wedges of negative refractive index (or ray-optical approximations thereof), or a combination of absolute optical instruments modified by the methods of transformation optics, using a combination of three ideal lenses or employing the light-field transfer. Our approach thus simplifies the optical simulations by omitting manufacturing the actual, “glued” curved spaces.

Our work can potentially open new possibilities in the exciting fields of research, such as transformation optics, negative refraction, geodesic lenses, absolute optical instruments, general relativity, and quantum gravity. Inspired by this research, we have started to investigate wave optics and quantum motion on the compact surfaces, presented in the following chapter.

Chapter 5

Wave optics and quantum motion on compact manifolds

5.1 Introduction

In the previous chapters, we have presented various aspects of geometrical and transformation optics. Starting with description of imaging due to combinations of tilted lenses, we then showed how to build transformation-optics devices from these and finally we have provided a novel approach in transformation optics to simulate light propagation in curved spaces. In this chapter, we will show how our method of optical simulation of curved spaces can be applied to solve the wave equation on some specific compact surfaces, including tetrahedron, Klein bottle, Möbius strip and others.

The propagation of light on curved surfaces has recently attracted interest in connection with so-called geodesic lenses [121, 122]. These lenses are able to shape light by purely geometrical means, and are finding applications in communications technology [123], but also in fields like population biology [124]. In a geodesic lens, the wave propagates freely on a two-dimensional (2D) surface. The light-ray trajectories then follow the geodesics of the surface, and for specific surface shapes (such as e.g. a portion of a sphere), a diffraction limited focus can be achieved [122].

Although geodesic lenses are often open surfaces, one can equally consider the propagation of waves on a closed surface such as a sphere or ellipsoid. This can be realized in acoustics or electromagnetism by, for example, trapping the wave within a thin gap between two solid materials [125, 126]. The problem of finding the wavefunction on a closed surface in a constant potential appears also in quantum mechanics. In this context, one can investigate aspects such as whether we can expect a quantum state revival [127, 128], an effect that is known to be closely related to the Talbot effect in optics [129–132].

The wavefunction ψ on a closed surface is given by the solutions of the Helmholtz equation,

$$\Delta\psi = -k^2\psi, \quad (5.1)$$

where $k \in \mathbb{R}$ is a wavenumber and Δ is the Laplacian defined via the appropriate metric g_{ij}

$$\Delta\psi = \frac{1}{\sqrt{g}} \frac{\partial}{\partial x^i} \left(\sqrt{g} g^{ij} \frac{\partial \psi}{\partial x^j} \right), \quad (5.2)$$

where g^{ij} is the inverse of metric g_{ij} and $g = |\det(g_{ij})|$ is the absolute value of a determinant of g_{ij} . The eigenmodes and eigenvalues in Eq. (5.1) can be found exactly for some special open surfaces, e.g. the well known solutions [133, 134] for rectangular, cylindrical and triangular [135, 136] surfaces. There are many applications for these exact solutions;

determining for example the response of electromagnetic and acoustic cavities [137], the approximate spectrum of a quantum dot [138], the modes of a wave guide with a given cross section [139], and the sound of simple musical instruments [140].

An example of a closed surface, whose modes can be solved analytically, is the surface of a sphere of radius R , where the eigenvalues $k_n = \sqrt{n(n+1)}/R$ are known as Schumann resonances [141]. These resonances determine the low frequency electromagnetic response of the atmosphere, where the region between the ground and the ionosphere acts as an effective waveguide. Related to this is propagation through the planar graded index profile known as the Maxwell Fish Eye lens, where the wave can be understood as the stereographic projection of propagation on the surface of a two-sphere [24, 142]. Although there seem to be just few other exact solutions for propagation on a closed surface, there do exist many results [143, 144] concerning the dependence on the topology of the surface of the eigenvalues and eigenfunctions of the Laplacian.

In this chapter, we will give the solution for the eigenmodes and eigenfrequencies of waves on several closed surfaces, including a tetrahedron, Klein bottle, Möbius strip, real projective plane and infinite potential well. Instead of solving the Helmholtz equation on the surface S itself, our method employs the respective quotient space σ , i.e. the original surface S unfolded and equipped with appropriate gluing instructions.

The quotient spaces of all presented surfaces have the following property: the entire Euclidean plane \mathbb{R}^2 can be tessellated with copies of the quotient space σ without any overlaps or gaps, with gluing instructions satisfied everywhere. We will then apply the results to Schrödinger equation, whose time-independent form is equivalent to the Helmholtz equation. We will show that propagation of a quantum particle, described by a wavefunction $\psi_0(\mathbf{x})$, on any of the presented surfaces is equivalent to the diffraction of light from a grating, whose transmission function $\phi(\mathbf{x})$ corresponds to the tessellation of the plane \mathbb{R}^2 with copies of function $\psi_0(\mathbf{x})$, defined on σ . This demonstrates an interesting equivalence between the Talbot revivals [132, 145] and the quantum wave-packet revivals predicted for a Schrödinger wave evolving on the closed surface S . Last but not least, our method provides a rather simple potential experimental realisation for wave propagation on compact surfaces.

5.1.1 Contributions

The work carried out in this chapter stems from a collaboration between myself, Prof. Tomáš Tyc and Dr Simon Horsley.

5.2 Solving the Helmholtz equation on a manifold and on its quotient space

Consider a compact manifold S . Provided a zero potential, the Hamiltonian of a quantum particle of mass μ living on S is simply $\hat{H} = -\frac{\hbar^2}{2\mu} \Delta$, where Δ is the Laplacian, defined by Eq. (5.1). The Schrödinger equation

$$i\hbar \frac{\partial \psi}{\partial t} = \hat{H}\psi = -\frac{\hbar^2}{2\mu} \Delta \psi \quad (5.3)$$

can be solved applying the ansatz $\psi_n(\mathbf{r}, t) = \psi_n(\mathbf{r}) \exp(-iE_n t/\hbar)$, where the stationary states $\psi_n(\mathbf{r})$ are given as solutions of the Helmholtz equation

$$\Delta \psi_n + k_n^2 \psi_n = 0, \quad (5.4)$$

where k_n is the wavenumber. The corresponding energy eigenvalues are $E_n = \hbar^2 k_n^2 / (2\mu)$.

One can find solving the Eq. (5.4) challenging for a general closed surface S . The Helmholtz equation, however, can be equivalently solved on the unfolded net of the manifold S , equipped with “gluing instructions”, i.e. the rules defining how the edges of the unfolded net are identified. We refer to the unfolded net of S , fitted with appropriate gluing instructions, as the *quotient space* or σ . Although this simplifies the problem of solving the Helmholtz equation on closed surfaces significantly, finding the modes for many quotient spaces is still complicated. However, solving the Helmholtz equation on the quotient space σ becomes much simpler if the entire Euclidean plane \mathbb{R}^2 can be filled with the copies of σ , without gaps or overlaps, and with the gluing instructions satisfied even at the boundaries between the neighbouring copies of σ . In such cases, the Helmholtz equation can be solved in the entire plane \mathbb{R}^2 rather than on σ , provided that the wavefunction has the same values on all the copies of the quotient space. This restriction implies certain constraints on the symmetries of the wavefunction, and leads to discrete modes.

5.3 Tessellating the plane with copies of quotient space

In this section, we will formulate the rules for tessellating the Euclidean plane \mathbb{R}^2 with the copies of the quotient space σ and establish the connection between waves on a respective manifold S and the waves in \mathbb{R}^2 . These tessellation rules will be then employed to obtain the modes on the manifold.

Consider a manifold S which can be unfolded to a quotient space σ . Assume that the entire plane \mathbb{R}^2 can be tiled with copies of σ , with the gluing instructions satisfied everywhere in \mathbb{R}^2 , i.e. the identified edges of different copies of σ are connected with the correct orientation.

Now, given a function $\psi_0(x, y)$ as a solution of the Helmholtz equation (5.4) on the quotient space σ with a single value of wavenumber k , and which also satisfies the gluing instructions on σ . We will refer to such a function as a *mode* on the manifold. Our goal is to define the equivalent mode $\phi(x, y)$ on the whole plane \mathbb{R}^2 . We will generate it from the function $\psi_0(x, y)$ by the tessellation of \mathbb{R}^2 with copies of $\psi_0(x, y)$. Of course, we require $\phi(x, y)$ to satisfy the Helmholtz equation in the whole plane, which implies that the function $\phi(x, y)$ should be continuous and smooth (first derivatives are also continuous) everywhere in \mathbb{R}^2 .

To obtain a general guide for tessellating the plane \mathbb{R}^2 with copies of $\psi_0(x, y)$, we need to distinguish between two classes of manifolds: the first class consists of manifolds without hard boundaries, i.e., without lines on which the wavefunction has to vanish. Surfaces of polyhedra, the torus, the Klein bottle belong to this class. The other class contains manifolds with hard boundaries on which the wavefunction equals to zero, for example polygons with hard walls, the Möbius strip etc.

5.3.1 Manifolds without hard boundaries

Let us first discuss the tessellation rules for the manifolds without hard boundaries. For these, the transition from the function $\psi_0(x, y)$, defined on the quotient space σ , to the equivalent function $\phi(x, y)$, defined in the whole plane \mathbb{R}^2 , is given by what we call the **Tessellation rule no. 1**: the copies of $\psi_0(x, y)$ are simply arranged such that the identified edges between two neighbouring copies are attached to each other with the same orientation. This is illustrated in Fig. 5.1(b) for the case of a torus: the respective quotient space coincides with a rectangle with sides a and b , and the pairs of opposite sides

are identified. The tessellation rule no. 1 then yields a periodic rectangular structure with periods a and b in the x and y directions respectively. The function $\phi(x, y)$ is then also periodic, with the same periods.

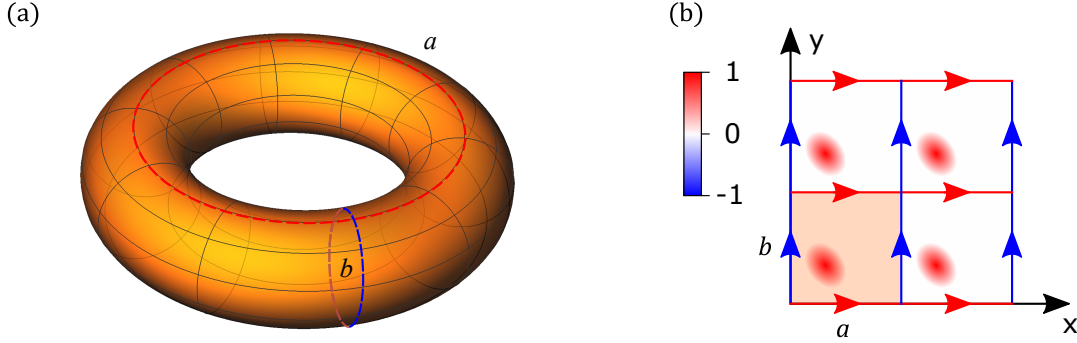


Figure 5.1: (a) A torus is an example of a manifold without hard boundaries; (b) The quotient space of a torus is equivalent to a rectangle of sides a and b , with the opposite sides being identified by relations $(0, y) \sim (a, y)$ and $(x, 0) \sim (x, b)$, indicated with red and blue arrows. The Tessellation rule no. 1 then yields a periodic function $\phi(x, y)$, whose unit cell (red-shaded area) coincides with the function $\psi_0(x, y)$, defined on the quotient space.

5.3.2 Manifolds with hard boundaries

If the regraded manifold contains hard boundaries, the tessellation of the plane \mathbb{R}^2 with copies of $\psi_0(x, y)$, defined on σ , needs to be performed carefully. Let us denote l one of the straight lines forming the hard boundary in the quotient space σ , i.e. that the function $\psi_0(x, y)$ equals to zero on l . Now we aim to derive a rule how to connect two copies of $\psi_0(x, y)$ around l , such that the resulting function $\phi(x, y)$ is the solution of the Helmholtz equation in the whole plane \mathbb{R}^2 (which also means that $\phi(x, y)$ is continuous, including its first derivatives). A natural way how to satisfy this requirement is the following: to the “zero line” l on a given tile (i.e., on a copy of $\psi_0(x, y)$) we attach another tile such that these tiles meeting at l are mirror images of each other with respect to l . To ensure that the derivative of $\phi(x, y)$ normal to l is continuous when going from one tile to the other, one of these two tiles will be “negative”, i.e. multiplied by a factor -1 . For example, consider a function $\psi_0(x, y)$ on σ , with “zero line” l coinciding with y -axis. The tile attached to this line then equals to $-\psi_0(-x, y)$. We can summarize these requirements to the **Tessellation rule no. 2**: two tiles adjacent at the hard boundary l are mirror-symmetric to each other with respect to l and one of them is multiplied by -1 .

This rule is illustrated on an example of a rectangle with hard boundaries along its sides (equivalent to an infinitely deep rectangular potential well), shown in Fig. 5.2. Due to alternating positive and negative tiles, the function $\phi(x, y)$ in the plane \mathbb{R}^2 has periodicity $2a$ and $2b$ respectively.

5.3.3 Transiting from the quotient space to the entire plane

The extension of the function $\psi_0(x, y)$, defined on σ , to the whole plane, resulting in the function $\phi(x, y)$, can be expressed mathematically as the following integral over the

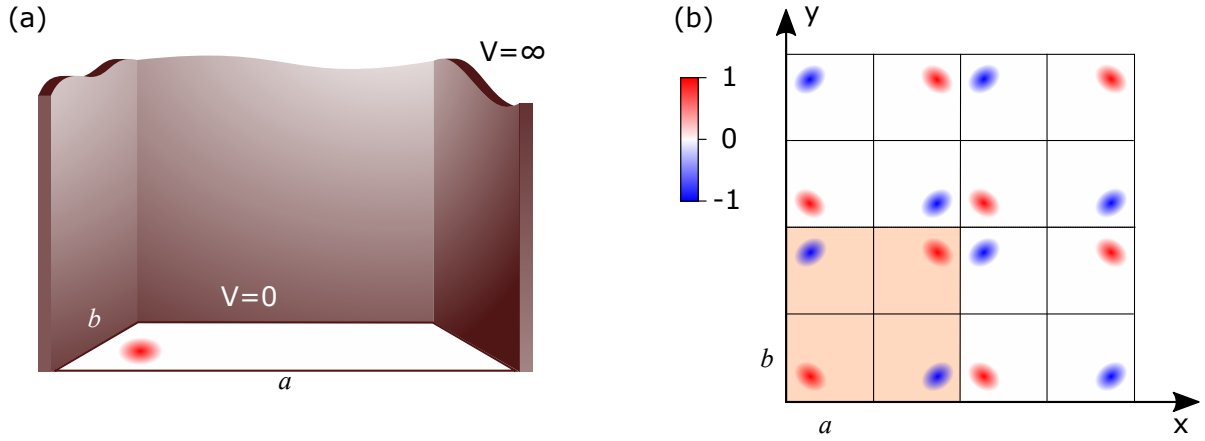


Figure 5.2: (a) An infinite potential well is an example of a manifold with hard boundaries. (b) Employing the Tessellation rule no. 2 leads to the periodic function $\phi(x, y)$, whose unit cell consists of four copies of the function $\psi_0(x, y)$; black lines represent the hard boundaries of the quotient space σ and blue spots represent the “negative” tiles.

quotient space:

$$\phi(x, y) = \iint_{\sigma} \psi_0(x', y') \Psi(x, y, x', y') dx' dy', \quad (5.5)$$

where $\Psi(x, y, x', y')$ is a comb of Dirac δ -functions such that for a given point $(x', y') \in \sigma$, there is a single δ -peak at each tile, whose position corresponds to the position (x', y') on that tile. If the tessellation rules require a tile to be negative, then the corresponding δ -peak is multiplied by a factor -1 . For example, the comb for the torus has the form

$$\Psi_{\text{torus}}(x, y, x', y') = \sum_{m, n=-\infty}^{\infty} \delta(x - x' - ma) \delta(y - y' - nb). \quad (5.6)$$

Note that, as defined, the comb $\Psi(x, y, x', y')$ is a real function, i.e. $\Psi^*(x, y, x', y') = \Psi(x, y, x', y')$ and $\Psi(x, y, x', y') = \delta(x - x')\delta(y - y')$ for $(x, y), (x', y') \in \sigma$. In the following section, we will establish the relation of the function $\Psi(x, y, x', y')$ to the modes of the manifold.

5.4 The mode structure of the quotient space

In this section, we will show the equivalence of the quantum motion on the manifold S (more precisely, on the respective quotient space σ), and in the plane \mathbb{R}^2 , paved by the copies of the corresponding wavefunction $\psi_0(x, y)$ defined on σ . In detail, we will show that the modes ψ_n on σ can be extended to \mathbb{R}^2 , using the tessellation rules defined above. Finally, we will show that functions ϕ_n , created by such tessellation, form a basis in \mathbb{R}^2 , which coincides with the basis ψ_n within the area of σ .

Following the tessellation rules on the function $\psi_0(x, y)$ defined on σ yields a function $\phi(x, y)$ defined on \mathbb{R}^2 . Since there is a finite amount of symmetry operations allowed for the tessellation (translation, rotation, mirroring, multiplying by a factor -1) and there are no overlaps or gaps between the tiles, function $\phi(x, y)$ is periodic. Therefore, the Fourier transform $\tilde{\psi}(k_x, k_y)$ of function $\phi(x, y)$,

$$\tilde{\psi}(k_x, k_y) = \frac{1}{2\pi} \iint_{\mathbb{R}^2} \phi(x, y) e^{-i(k_x x + k_y y)} dx dy, \quad (5.7)$$

is nonzero only on a discrete comb of points in the plane (k_x, k_y) . Furthermore, if the function $\phi(x, y)$ is created by tessellating the plane with the mode ψ_n on σ (i.e., there is only one value of the wavenumber k_n corresponding to ψ_n), the function $\tilde{\psi}(k_x, k_y)$ is nonzero only on the circle $k_x^2 + k_y^2 = k_n^2$. From these two observations, one can deduce that the function $\tilde{\psi}(k_x, k_y)$ is nonzero only on a finite number of discrete points in the (k_x, k_y) plane. This means that each of the modes ψ_n is a superposition of a finite number of plane waves. In Sec. 5.6, we will show that the form of this superposition can be deduced from the symmetries of the function $\phi(x, y)$.

The modes ψ_n are very closely related to the comb $\Psi(x, y, x', y')$ from Eq. (5.5). This can be seen from the fact that the modes form a complete set on the quotient space σ , which means that any function $\psi_0(x, y)$ can be expressed in terms of the modes ψ_n ,

$$\psi_0(x, y) = \sum_n \frac{(\psi_n, \psi_0)}{(\psi_n, \psi_n)} \psi_n(x, y), \quad (5.8)$$

where (f, g) denotes the scalar product of functions f and g . Using the L^2 scalar product with the integral taken over the area of the quotient space and assuming that $(\psi_n, \psi_n) = 1$, Eq. (5.8) can be rewritten into the following form

$$\psi_0(x, y) = \iint_{\sigma} \psi_0(x', y') \left[\sum_n \psi_n^*(x', y') \psi_n(x, y) \right] dx' dy'. \quad (5.9)$$

This equation is satisfied only if the sum inside the square bracket is equal to $\delta(x - x')\delta(y - y')$. Now consider an *extended mode* ϕ_n , defined in the whole plane \mathbb{R}^2 , created by tessellating the plane with copies of the mode ψ_n , defined solely on σ , i.e.

$$\phi_n(x, y) := \iint_{\sigma} \psi_n(x', y') \Psi(x, y, x', y') dx' dy'. \quad (5.10)$$

Assuming that $(x', y') \in \sigma$, one can calculate a sum similar to that in Eq. (5.9), with modes ψ_n replaced with the extended modes ϕ_n

$$\begin{aligned} \sum_n \phi_n^*(x', y') \phi_n(x, y) &= \\ &= \iint_{\sigma} dx'' dy'' \iint_{\sigma} dx''' dy''' \sum_n \psi_n^*(x''', y''') \psi_n(x'', y'') \Psi(x, y, x'', y'') \Psi(x', y', x''', y''') \\ &= \iint_{\sigma} dx'' dy'' \Psi(x, y, x'', y'') \Psi(x', y', x'', y'') = \Psi(x, y, x', y'). \end{aligned} \quad (5.11)$$

In our manipulations, we employed the fact that $\Psi^*(x', y', x''', y''') = \Psi(x', y', x''', y''')$, $\sum_n \psi_n^*(x''', y''') \psi_n(x'', y'') = \delta(x''' - x'')\delta(y''' - y'')$ and $\Psi(x', y', x'', y'') = \delta(x' - x'')\delta(y' - y'')$ for $(x', y'), (x'', y'') \in \sigma$. Finally, we can write the definition of the comb $\Psi(x, y, x', y')$ in terms of the modes as the following

$$\Psi(x, y, x', y') := \sum_n \phi_n^*(x', y') \phi_n(x, y), \quad (x, y), (x', y') \in \mathbb{R}^2. \quad (5.12)$$

More precisely, the domains for which this equation holds should be $(x, y) \in \mathbb{R}^2$ and $(x', y') \in \sigma$. In the practical calculations, however, the domain of points (x', y') is restricted by the area of the quotient space σ and thus the domain of (x', y') is not necessary to be limited in the definition of the comb $\Psi(x, y, x', y')$. Therefore, the requirement

$(x', y') \in \sigma$ can be relaxed, so (x', y') can be an arbitrary point from the plane \mathbb{R}^2 . One can say that the extended modes ϕ_n form a basis in a space of functions $\phi(x, y)$ defined in whole plane \mathbb{R}^2 , which are created by the tessellation with copies of $\psi_0(x, y)$ defined solely on σ since Eq. (5.5), defining the extension from $\psi_0(x, y)$ to $\phi(x, y)$, can be written in the form, which is very similar to the expression of the function $\phi(x, y)$ in terms of basis functions $\phi_n(x, y)$,

$$\phi(x, y) = \iint_{\sigma} \psi_0(x', y') \sum_n \phi_n^*(x', y') \phi_n(x, y) dx' dy'. \quad (5.13)$$

5.5 Connection to the diffraction theory

Once we have presented the general procedure for solving the Schrödinger equation on a quotient space σ , corresponding to a manifold S , we will examine the connection of a quantum motion on S with a classical scalar diffraction theory. Indeed, a time evolution of a free quantum particle in a 2D plane is equivalent to the paraxial propagation of a monochromatic scalar wave in a 3D space along the z axis. This can be seen by comparing the 2D Schrödinger equation with the paraxial Helmholtz equation in free space [146]

$$ik_0 \frac{\partial \psi}{\partial z} = -\frac{1}{2} \Delta_{\text{T}} \psi \quad (5.14)$$

where $\Delta_{\text{T}} = \partial^2/\partial x^2 + \partial^2/\partial y^2$ is the 2D Laplace operator, and k_0 is the respective wavenumber of the wave. A 2D Schrödinger equation can be obtained from Eq. (5.14) by a substitution $z = \hbar k_0 t / \mu$. This connection between Schrödinger equation, describing a quantum motion, and the paraxial Helmholtz equation yields an interesting way how to optically simulate an evolution of a free quantum particle in a plane with a diffraction experiment: given a collimated beam incident on a grating placed in the plane $z = 0$ whose complex transmission function corresponds to the wavefunction $\psi_0(x, y)$, describing the initial state of the quantum particle. The time evolution of the quantum particle is then equivalent to the light wave, created by a diffraction of the collimated beam on the grating, propagating along the z -axis.

In Section 5.4, we showed that quantum motion of a particle living on manifold S (whose quotient space σ can tessellate the the whole plane \mathbb{R}^2 with the gluing instructions satisfied everywhere) is equivalent to its propagation in the plane \mathbb{R}^2 , paved by the copies of the respective wavefunction $\psi_0(x, y)$ defined solely on σ . Combining this idea with the equivalence between the quantum motion and the paraxial diffraction, we obtain an interesting result: the time evolution of a quantum particle on the manifold S is equivalent to diffraction on a grating with complex transmission function $\phi(x, y)$, created by an appropriate tessellation of the plane \mathbb{R}^2 with copies of a function $\psi_0(x, y)$, describing the particle at time $t = 0$ in the respective quotient space σ . This observation provides a simple way of simulating the quantum motion on the manifold S , using a simple diffraction experiment.

Note that the Talbot effect can be observed in the diffraction experiment [129, 130, 132, 147, 148] on a grating with periods p_x and p_y such that the ratio p_x^2/p_y^2 is equal to a rational number, i.e. $p_x^2/p_y^2 = A/B$, where A and B are coprime integers. The Talbot length z_T is then given by a formula $z_T = 2g^2AB/\lambda$ (derivation of this formula is provided in Appendix E), where λ is the wavelength of the incident light beam and g^2 is the common factor of the periods p_x and p_y squared, i.e. $p_x^2 = g^2A$ and $p_y^2 = g^2B$. This implies that the quantum particle living on a compact manifold S performs quantum state revivals if the respective function $\phi(x, y)$ (created by an appropriate tessellation of the

plane with copies of the initial-state function $\psi_0(x, y)$ defined solely on the quotient space σ) provides the Talbot effect. The revival time T can be then calculated using the formula $T = z_T \mu / (\hbar k_0)$. Furthermore, the connection between the quantum motion on S and the Talbot effect yields an analytical expression of the wavefunction $\phi(x, y, t = T P/Q)$ at the rational multiple of the revival time T , using the formula for the fractional Talbot effect (derivation is provided in Appendix F)

$$\phi(x, y, t = T P/Q) = \frac{1}{Q} \sum_{i,j=0}^{Q-1} G(BP, Q, i) G(AP, Q, j) \phi\left(x - i\frac{P_x}{Q}, y - j\frac{P_y}{Q}\right), \quad (5.15)$$

where

$$G(P, Q, j) = \frac{1}{\sqrt{Q}} \sum_{l=0}^{Q-1} \exp\left\{i\frac{2\pi P}{Q} \left(\frac{j}{P}l - l^2\right)\right\} \quad (5.16)$$

is the generalized quadratic Gauss sum [149]. Eq. (5.15) has a straightforward physical interpretation: in each time $t = T P/Q$ the wavefunction $\phi(x, y, t = T P/Q)$ corresponds to a superposition of Q^2 images of the original grating, spatially shifted in the x and y directions with respect to each other and modulated by the product of sums $G(BP, Q, i) G(AP, Q, j)$. Explicit values of these sums have been published in many publications, e.g. in [149]. An important property of the sums $G(P, Q, j)$ is the following: provided that $QP + j$ is an even number [149], they are periodic in both P and j with the period Q , i.e.

$$G(P, Q, j) = G(P + Q, Q, j) = G(P, Q, j + Q). \quad (5.17)$$

Applying this property in Eq. (5.15) yields that the wavefunction $\phi(x, y, t)$ is periodic in time, which leads to the quantum revivals.

5.6 Eigenmodes and eigenvalues on different manifolds

In this section, we will present a number of examples of manifolds, on which the quantum motion can be simulated by a diffraction on an appropriate grating. Following the tessellation rules, we first graphically pave the plane \mathbb{R}^2 with the copies of function $\psi_0(x, y)$, which is depicted as a Gaussian spot in the attached figures. From the symmetries of the tessellation, we will obtain the extended modes $\phi_n(x, y)$; these locally coincide with the eigenmodes $\psi_n(x, y)$ on σ . Then we will derive formulas for the respective quantum eigenenergies. Using Eq. (5.12), we prove that the extended modes obtained in this way yield the expected comb $\Psi(x, y, x', y')$. This calculation will be shown in detail only for the torus and for the infinite potential well since for the other manifolds the calculations can be preformed in an analogous manner. Finally, we will show that any wavefunction on σ exhibits perfect wavefunction revivals for a suitable choice of geometric parameters of σ and we will estate the shortest revival time T for each discussed manifold.

5.6.1 Torus

We start our collection of manifolds by a flat torus. By “flat” we mean that the torus has no intrinsic curvature, so we are not attempting to embed it in a 3D Euclidean space, which would require curvature. The quotient space of such a torus is a rectangle with dimensions a and b , with pairs of opposite sides identified, which can be expressed as

$(0, y) \sim (a, y)$ and $(x, 0) \sim (x, b)$, see Fig. 5.1. Following the tessellation rule no. 1, the plane \mathbb{R}^2 is simply paved by translating the function $\psi_0(x, y)$ by multiples of a and b in the x and y directions, respectively. The resulting wavefunction $\phi(x, y)$ defined by Eq. (5.5) is then periodic in x and y with periods a and b , respectively, which yields the allowed values of the wavevector components $k_x = m2\pi/a$ and $k_y = n2\pi/b$, where $m, n \in \mathbb{Z}$. The (normalised) modes are then

$$\phi_{mn}(x, y) = \frac{1}{\sqrt{ab}} \exp \left[i2\pi \left(m\frac{x}{a} + n\frac{y}{b} \right) \right]. \quad (5.18)$$

Inserting these modes to Eq. (5.12) and using the identity for Fourier series of the Dirac comb

$$\sum_{M=-\infty}^{\infty} \exp \left[i\frac{2\pi}{a} M(x - x') \right] = a \sum_{M=-\infty}^{\infty} \delta(x - x' - Ma), \quad (5.19)$$

we obtain the correct comb $\Psi_{\text{Torus}}(x, y, x', y')$, presented in Eq. (5.6). The corresponding energy spectrum is $E_{mn} = 2\pi^2\hbar^2(m^2/a^2 + n^2/b^2)/\mu$ and the revival time for $a = b$ is $T = \mu a^2/(\pi\hbar)$.

5.6.2 Infinite potential well

Probably the most famous problem of quantum mechanics is an infinite potential well. This corresponds to a rectangle with sides a and b with hard walls, so the particle is “trapped” in the area of the rectangle. Since the quotient space σ contains only hard boundaries, we will follow the tessellation rule no. 2 and attach copies of the function $\psi_0(x, y)$ next to each other, each such tile being the mirror image of the adjacent one, and the signs of the tiles alternating between plus and minus. Fig. 5.2(b) then shows a function $\phi(x, y)$ created in this way. The red-shaded area represents the unit cell of $\phi(x, y)$, which is defined as the smallest unit such that we can reconstruct the entire grating through repeated translation of the cell. As defined, the unit cell is topologically equivalent to a torus and thus we can deduce the allowed components of the wavevector $k_x = m\pi/a$ and $k_y = n\pi/b$. In addition, the unit cell has a symmetry $\phi(x, y) = \phi(-x, -y) = -\phi(x, -y) = \phi(-x, y)$. To form a basis in a space of functions with this symmetry, the extended modes $\phi_{mn}(x, y)$ are required to have the same symmetry and thus $\phi_{mn}(x, y)$ correspond to the following superposition of the “torus modes”

$$\begin{aligned} \phi_{mn}(x, y) &= -\frac{N_{mn}}{4} \left\{ \exp \left[i\pi \left(m\frac{x}{a} + n\frac{y}{b} \right) \right] + \exp \left[-i\pi \left(m\frac{x}{a} + n\frac{y}{b} \right) \right] \right. \\ &\quad \left. - \exp \left[i\pi \left(m\frac{x}{a} - n\frac{y}{b} \right) \right] - \exp \left[-i\pi \left(m\frac{x}{a} - n\frac{y}{b} \right) \right] \right\} \\ &= N_{mn} \sin \left(\frac{\pi mx}{a} \right) \sin \left(\frac{\pi ny}{b} \right), \end{aligned} \quad (5.20)$$

which is indeed the correct result, provided that $N_{mn} = 2/\sqrt{ab}$ and $m, n \in \mathbb{N}$. Inserting modes $\phi_{mn}(x, y)$ to Eq. (5.12) then leads to a comb $\Psi_{\text{well}}(x, y, x', y')$, with the same structure as depicted in Fig. 5.2(b)

$$\begin{aligned}
\Psi_{\text{well}}(x, y, x', y') &= \frac{4}{ab} \sum_{m,n=1}^{\infty} \sin\left(\frac{\pi mx}{a}\right) \sin\left(\frac{\pi ny}{b}\right) \sin\left(\frac{\pi mx'}{a}\right) \sin\left(\frac{\pi ny'}{b}\right) \\
&= \frac{1}{4ab} \sum_{m,n=1}^{\infty} \sum_{\alpha,\beta=0}^1 \left\{ \exp i\pi \left((-1)^\alpha m \frac{x-x'}{a} + (-1)^\beta n \frac{y-y'}{b} \right) \right. \\
&\quad + \exp i\pi \left((-1)^\alpha m \frac{x+x'}{a} + (-1)^\beta n \frac{y+y'}{b} \right) - \exp i\pi \left((-1)^\alpha m \frac{x+x'}{a} + (-1)^\beta n \frac{y-y'}{b} \right) \\
&\quad \left. - \exp i\pi \left((-1)^\alpha m \frac{x-x'}{a} + (-1)^\beta n \frac{y+y'}{b} \right) \right\} \\
&= \frac{1}{4ab} \sum_{m,n=-\infty}^{\infty} \left\{ \exp i\pi \left(m \frac{x-x'}{a} + n \frac{y-y'}{b} \right) + \exp i\pi \left(m \frac{x+x'}{a} + n \frac{y+y'}{b} \right) \right. \\
&\quad \left. - \exp i\pi \left(m \frac{x+x'}{a} + n \frac{y-y'}{b} \right) - \exp i\pi \left(m \frac{x-x'}{a} + n \frac{y+y'}{b} \right) \right\} \\
&= \sum_{m,n=-\infty}^{\infty} [\delta(x-x'-2ma) \delta(y-y'-2nb) + \delta(x+x'-2ma) \delta(y+y'-2nb) \\
&\quad - \delta(x+x'-2ma) \delta(y-y'-2nb) - \delta(x-x'-2ma) \delta(y+y'-2nb)].
\end{aligned} \tag{5.21}$$

The respective eigenenergies are $E_{mn} = \pi^2 \hbar^2 (m^2/a^2 + n^2/b^2)/(2\mu)$ and the revival time for $a = b$ is $T = 4\mu a^2/(\pi \hbar)$.

5.6.3 Cylinder with hard edges

Maybe not so exciting but one example of a surface which can be unitary unfolded to a plane is a cylinder with hard boundaries. The quotient space σ of a cylinder is a rectangle of sides a and b whose opposite sides of length a are identified by relations $(x, 0) \sim (x, b)$ (see Fig. 5.3). The other two sides then represent the hard edges, where the wavefunction is required to be zero. When paving the plane with copies of $\psi_0(x, y)$, both tessellation rules 1 and 2 are employed. Fig. 5.3(b) shows the resulting function $\phi(x, y)$, whose unit cell consists of two copies of $\psi_0(x, y)$. The symmetry $\phi(x, y) = -\phi(-x, y)$ of the unit cell then leads to modes

$$\phi_{mn} = \sqrt{\frac{2}{ab}} \sin\left(\frac{\pi mx}{a}\right) \exp\left(\frac{2\pi i ny}{b}\right), \tag{5.22}$$

with $m \in \mathbb{N}, n \in \mathbb{Z}$. Inserting these modes to Eq. (5.12) again yields the expected comb

$$\Psi_{\text{cylinder}}(x, y, x', y') = \sum_{m,n=-\infty}^{\infty} [\delta(x-x'-2ma) \delta(y-y'-nb) - \delta(x+x'-2ma) \delta(y-y'-nb)] \tag{5.23}$$

The energy spectrum is $E_{mn} = \pi^2 \hbar^2 (m^2/a^2 + 4n^2/b^2)/(2\mu)$ and the revival time for $a = b$ is $T = 4\mu a^2/(\pi \hbar)$.

5.6.4 Möbius Strip

Examining quantum motion inside an infinite potential well and on a cylinder, we showed that quantum motion on surfaces with hard boundaries can be simulated with a diffraction on a grating. Encouraged by this observation, we will find the modes of a Möbius

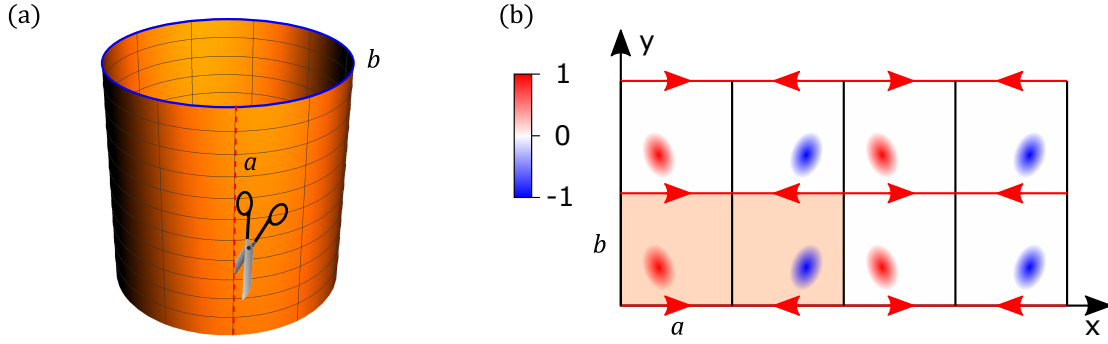


Figure 5.3: (a) Cylinder, when cut and unfolded to a plane, is equivalent to a rectangle of sides a and b , with hard boundaries on sides b , whereas the sides a are identified according to gluing instruction $(x, 0) \sim (x, b)$. (b) Tessellation of the plane with copies of $\psi_0(x, y)$ defined on the quotient space σ yields a periodic function $\phi(x, y)$, whose unit cell consists of two copies of $\psi_0(x, y)$.

strip, which is a non-orientable surface; the Möbius strip has only one boundary. Its quotient space corresponds to a rectangle of sides a and b , whose top and bottom sides are identified by a relation $(x, 0) \sim (a - x, b)$ (see Fig. 5.4). The tessellation rules then yield a periodic function $\phi(x, y)$, whose unit cell has a symmetry $\phi(x, y) = -\phi(x + a, y + b) = \phi(-x, y) = -\phi(a - x, y + b)$ (see Fig. 5.4(b)). Applying this symmetry on a “torus mode” $\exp i\pi(mx/a + ny/b)$ yields the modes ϕ_{mn}

$$\phi_{mn}(x, y) = \sqrt{\frac{2}{ab}} \sin\left(\frac{m\pi x}{a}\right) \exp\left(\frac{i\pi ny}{b}\right) \quad (5.24)$$

with $m \in \mathbb{N}, n \in \mathbb{Z}$ and $m+n$ must be an odd number. The respective comb $\Psi_{\text{Möbius}}(x, y, x', y')$ can be fearlessly calculated using Eq. (5.12)

$$\begin{aligned} \Psi_{\text{Möbius}}(x, y, x', y') = & \sum_{m, n=-\infty}^{\infty} [\delta(x - x' - 2ma) \delta(y - y' - 2nb) - \delta(x + x' - 2ma) \delta(y - y' - 2nb) \\ & - \delta(x - x' - (2m + 1)a) \delta(y - y' - (2n + 1)b) + \delta(x + x' - (2m + 1)a) \delta(y - y' - (2n + 1)b)]. \end{aligned} \quad (5.25)$$

One can check easily that comb $\Psi_{\text{Möbius}}(x, y, x', y')$ has the desired structure, implied by the tessellation rules (see Fig. 5.4(b)). The energy spectrum is $E_{mn} = \pi^2 \hbar^2 (m^2/a^2 + n^2/b^2)/(2\mu)$ and the revival time for $a = b$ is $T = 4\mu a^2/(\pi \hbar)$.

5.6.5 Klein Bottle

By gluing the edges of Möbius strip together one will get a Klein bottle, another example of a non-orientable surface, which cannot be embedded in a 3D Euclidean space without intersecting itself, see Fig. 5.5(a). However, the quotient space of Klein bottle is again a rectangle whose opposite sides of lengths a are identified in the opposite direction, $(x, 0) \sim (a - x, b)$, whereas the opposite sides of lengths b are identified in the same direction, $(0, y) \sim (a, y)$. Fig. 5.5(b) then depicts how the plane is paved with copies of $\psi_0(x, y)$: the unit cell of resulting function $\phi(x, y)$ has a symmetry $\phi(x, y) = \phi(-x, y + b)$. This results in the modes

$$\phi_{mn}(x, y) = N_{mn} \cos\left[\pi\left(\frac{2mx}{a} - \frac{n}{2}\right)\right] \exp\left(\frac{i\pi ny}{b}\right), \quad (5.26)$$

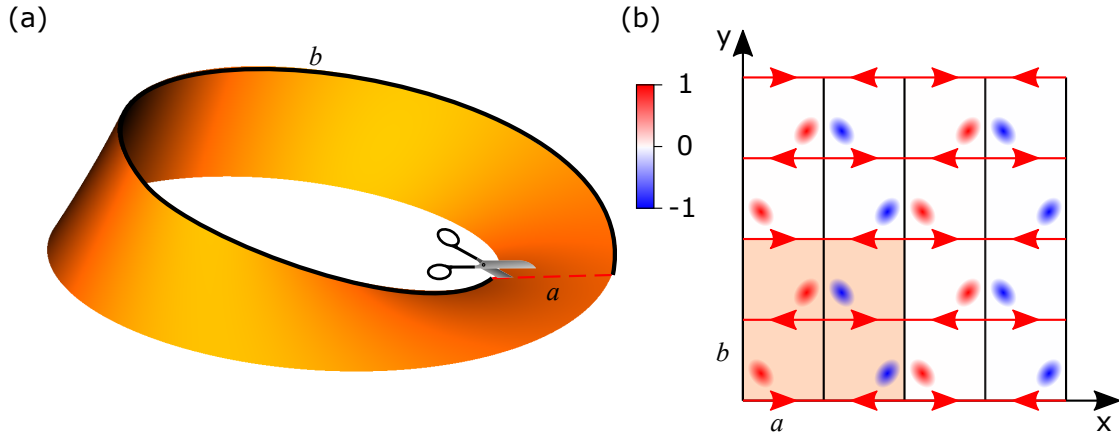


Figure 5.4: (a) Möbius strip, when cut and unfolded to a plane, is equivalent to a rectangle of sides a and b , with hard boundaries on sides b and with a gluing instruction $(x, 0) \sim (a - x, b)$ on sides a . (b) The tessellation $\phi(x, y)$ with copies of a function $\psi_0(x, y)$ defined on the quotient space σ . A unit cell of $\phi(x, y)$ consists of four copies of $\psi_0(x, y)$.

where $N_{mn} = [ab(1 + \delta_{0m})/2]^{-\frac{1}{2}}$ are normalization constants, and the allowed combinations of m and n are $(m \in \mathbb{N}, n \in \mathbb{Z})$ and $(m = 0, n \text{ an even integer})$. Again, the respective comb $\Psi_{\text{Klein}}(x, y, x', y')$ can be calculated using Eq. (5.12)

$$\Psi_{\text{Klein}}(x, y, x', y') = \sum_{m, n = -\infty}^{\infty} [\delta(x - x' - ma) \delta(y - y' - 2nb) + \delta(x + x' - ma) \delta(y - y' - b - 2nb)] \quad (5.27)$$

Since comb $\Psi_{\text{Klein}}(x, y, x', y')$ has the desired structure (indicated in Fig. 5.5(b)), functions given by Eq. (5.26) indeed form a basis in the quotient space of Klein bottle. The energy spectrum is $E_{mn} = \pi^2 \hbar^2 (4m^2/a^2 + n^2/b^2)/(2\mu)$ and the revival time for $a = b$ is $T = 4\mu a^2/(\pi \hbar)$.

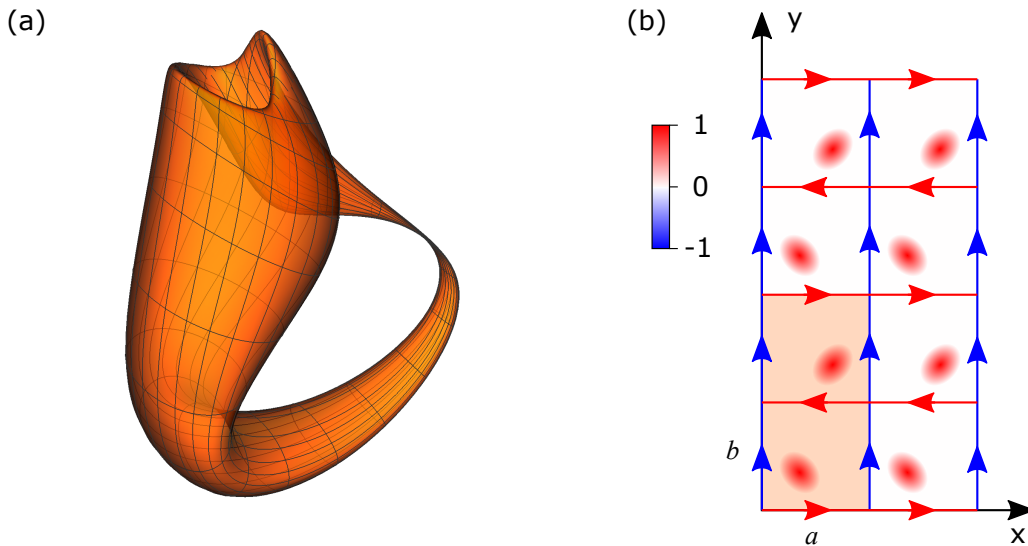


Figure 5.5: (a) A two-dimensional representation of the Klein bottle immersed in three-dimensional space; (b) (b) the quotient space σ of Klein bottle is a rectangle of sides a and b with identification $(0, y) \sim (a, y)$ and $(x, 0) \sim (a - x, b)$. Applying the tessellation rule no. 1 then yields a function $\phi(x, y)$, whose unit cell consists of two copies of function $\psi_0(x, y)$ defined on σ .

5.6.6 Real projective plane

The last example of a compact non-orientable two-dimensional manifold we discuss is a real projective plane; it cannot be embedded in standard three-dimensional space without intersecting itself. It can be thought of as a Euclidean plane equipped with additional "points at infinity" where parallel lines intersect. Therefore, any two distinct lines intersect in one and only one point in a projective plane. The quotient space of a projective plane is a rectangle with sides a and b , whose opposite sides are identified by relations $(0, y) \sim (a, b - y)$ and $(x, 0) \sim (a - x, b)$ (see Fig. 5.6). Tessellation of a plane \mathbb{R}^2 with copies of a function $\psi_0(x, y)$ defined on this quotient space leads to a periodic function, whose unit cell contains four copies of $\psi_0(x, y)$ and has a symmetry $\phi(x, y) = \phi(-x, -y) = \phi(a + x, b - y) = \phi(a - x, b + y)$ (see Fig. 5.6(b)). Applying these symmetries (similarly as in the previous cases), extended modes $\phi_{mn}(x, y)$ of a real projective plane can be found

$$\phi_{mn}(x, y) = N_{mn} \cos \pi \left(m \frac{x}{a} + \frac{m+n}{2} \right) \cos \pi \left(n \frac{y}{b} + \frac{m+n}{2} \right), \quad (5.28)$$

with $N_{mn} = [ab(1 + \delta_{m0})(1 + \delta_{n0})/4]^{-\frac{1}{2}}$ and $m, n \in \mathbb{N}_0$ except the cases when one of the numbers m, n is zero and the other one is odd. Again, these modes yield a correct comb $\Psi_{\text{Projective}}(x, y, x', y')$ (defined by Eq. (5.12))

$$\begin{aligned} \Psi_{\text{Projective}}(x, y, x', y') = & \\ & \sum_{m, n=-\infty}^{\infty} \{ \delta(x - x' - 2ma) \delta(y - y' - 2nb) + \delta(x + x' - 2ma) \delta(y + y' - 2nb) + \\ & + \delta(x - x' - a - 2ma) \delta(y + y' - b - 2nb) + \delta(x + x' - a - 2ma) \delta(y - y' - b - 2nb) \}. \end{aligned} \quad (5.29)$$

The energy spectrum is $E_{mn} = \pi^2 \hbar^2 (m^2/a^2 + n^2/b^2)/(2\mu)$ and the revival time for $a = b$ is $T = 4\mu a^2/(\pi \hbar)$.

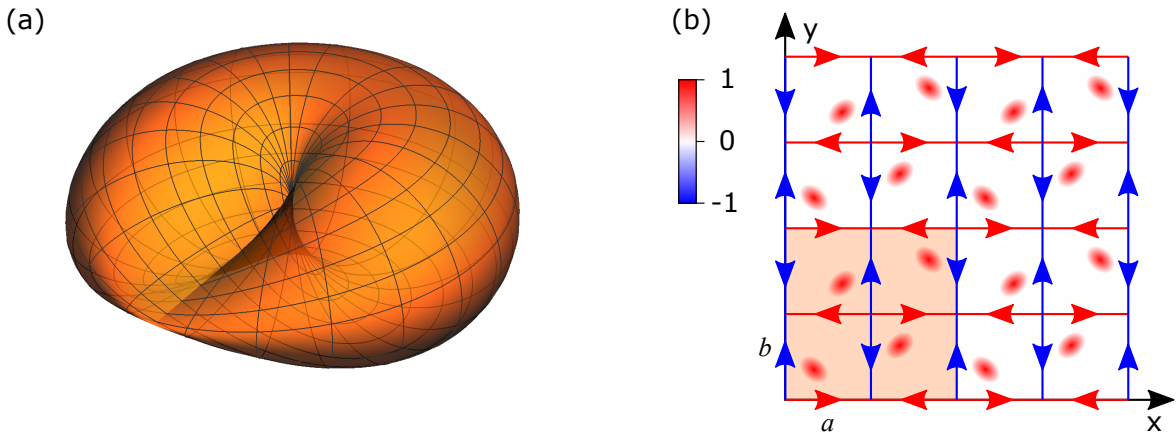


Figure 5.6: (a) Cross-capped disk, a two-dimensional visualization of a real projective plane embedded in a three-dimensional flat space. (b) Tessellation $\phi(x, y)$ of a plane with copies of a function $\psi_0(x, y)$ defined on the quotient space σ . The quotient space σ corresponds to a rectangle of sides a and b , whose opposite sides are identified by gluing instructions $(x, 0) \sim (a - x, b)$ and $(0, y) \sim (a, b - y)$. The unit cell of the function $\phi(x, y)$ then consists of four copies of σ .

5.6.7 Tetrahedron

Probably the most frequently presented example of a two-dimensional curved space is a sphere. In the following sections, we will provide a full analytical solution of Helmholtz equation on three surfaces, topologically equivalent to a sphere: surface of a tetrahedron, double-sided square and a double-sided triangle. Regarding the triangulations of curved spaces, discussed in Sec. 4.5, one could say that the surface of a tetrahedron represents the simplest triangulation of a sphere. Therefore, the quantum movement on the surface of a tetrahedron can be considered as the “first approximation” of the quantum movement on a sphere.

The quotient space σ of a regular tetrahedron with sides of length a corresponds to an equilateral triangle with side lengths $2a$. The gluing instructions defined on the edges of σ are depicted in Fig. 5.7(b); edges labelled with the same colour (for example 1 and 1') are identified. Since there are no hard boundaries on σ , the plane \mathbb{R}^2 can be tiled with copies of function $\psi_0(x, y)$, defined solely on σ , using the tessellation rule no. 1. An example of function $\phi(x, y)$, created by such tessellation, is shown in Fig. 5.7(b). The periodicity of $\phi(x, y)$ implies the allowed components of the wavevector to be $k_x = m\pi/a$ and $k_y = n\pi/a\sqrt{3}$. Additionally, the quantity $m + n$ is required to be equal to an even number since function $\phi(x, y)$ must remain unchanged when we move not only by a vector $(m2a, n2a\sqrt{3})$ but also by a vector $(2ma + a, 2na\sqrt{3} + a\sqrt{3})$. Regarding the symmetry $\phi(x, y) = \phi(-x, -y)$ finally yields the modes

$$\phi_{mn}(x, y) = N_{mn} \cos \pi \left(m \frac{x}{a} + n \frac{y}{a\sqrt{3}} \right), \quad (5.30)$$

where $N_{mn} = (1/a) 2^{1/2} 3^{-1/4} (1 + \delta_{m0}\delta_{n0})^{-1/2}$ is the normalizing constant and the domain \mathcal{D} of indices m, n is chosen to be $\mathcal{D} = \{(m, n); m \in \mathbb{Z}, n \in \mathbb{N}, m + n \text{ even}\} \cup \{(2m, 0); m \in \mathbb{N}_0\}$. This choice takes into account that ϕ_{mn} and $\phi_{-m, -n}$ are actually the same function. Using Eq. 5.12, modes ϕ_{mn} provide again the expected comb $\Psi_{\text{Tetrahedron}}(x, y, x', y')$

$$\Psi_{\text{Tetrahedron}}(x, y, x', y') = \sum_{m, n=-\infty}^{\infty} \left[\delta(x - x' - (2m + n)a) \delta(y - y' - na\sqrt{3}) + \delta(x + x' - (2m + n)a) \delta(y + y' - na\sqrt{3}) \right]. \quad (5.31)$$

The energy spectrum is $E_{mn} = \pi^2 \hbar^2 (3m^2 + n^2) / (6\mu a^2)$ and the revival time is $T = 3a^2 \mu / \pi \hbar$.

5.6.8 Double-sided square

In this section, we will find the solution of Helmholtz equation on a double-sided square. It is a square, on which the wavefunction is defined on both its sides. Although such manifold looks unusual, it is used for Peirce quincuncial projection of a sphere [150]. The quotient space of the double-sided square is a square of side a , with gluing instructions $(a/2 + x, 0) \sim (a/2 - x, 0)$, $(a/2 + x, a) \sim (a/2 - x, a)$, $(0, a/2 + y) \sim (0, a/2 - y)$ and $(a, a/2 + y) \sim (a, a/2 - y)$ (see Fig. 5.8(b)). As in the previous cases, a real plane \mathbb{R}^2 can be tiled with copies of a function $\psi_0(x, y)$ defined solely on that quotient space. The unit cell of a resulting function $\phi(x, y)$ has a symmetry $\phi(x, y) = \phi(x + a, y + b) = \phi(-x, a - y) = \phi(a - x, -y)$, which leads to the modes $\phi_{mn}(x, y)$

$$\phi_{mn}(x, y) = N_{mn} \cos \left[(m + n) \frac{\pi}{a} x + (m - n) \frac{\pi}{a} \left(y - \frac{a}{2} \right) \right] \quad (5.32)$$

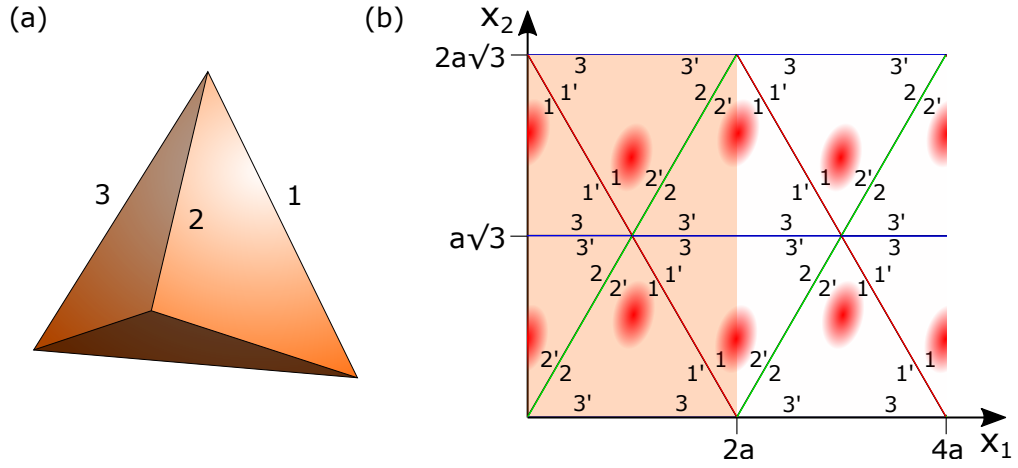


Figure 5.7: (a) A regular tetrahedron of side length a ; (b) To obtain a corresponding quotient space, edges 1, 2, 3 depicted in panel (a) need to be cut and then equipped with appropriate gluing instructions, i.e. edges labelled with the same colour (e.g. 1 and 1') are identified. The tessellation rule no. 1 then yields a periodic function $\phi(x, y)$, with a structure analogous to one presented in panel (b) (red shaded area represents the unit cell).

with $m, n \in \mathbb{N}_0$ and the normalizing constants $N_{mn} = (1/a)[(1 + \delta_{m0}\delta_{n0})/2]^{-1/2}$. As in the previous cases, these modes yield a correct comb $\Psi_{\text{square}}(x, x', y, y')$

$$\begin{aligned} \Psi_{\text{square}}(x, x', y, y') = & \\ \sum_{m,n} \{ & \delta(x - x' - 2ma) \delta(y - y' - 2na) + \delta(x - x' - a - 2ma) \delta(y - y' - a - 2na) \\ & + \delta(x + x' - a - 2ma) \delta(y + y' - 2na) + \delta(x + x' - 2ma) \delta(y + y' - a - 2na) \} \end{aligned} \quad (5.33)$$

The energy spectrum is $E_{mn} = \pi^2 \hbar^2 (m^2 + n^2) / (\mu a^2)$ and the revival time is $T = 2\mu a^2 / (\pi \hbar)$.

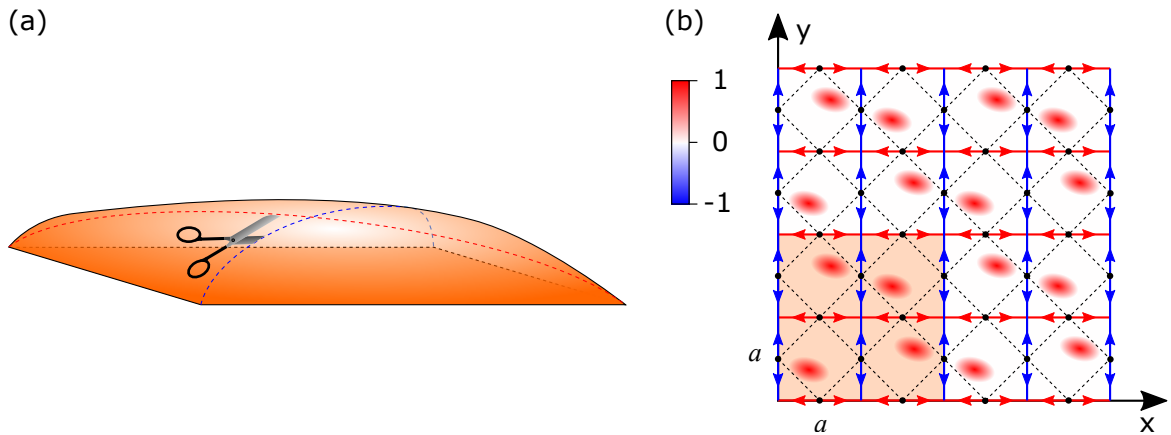


Figure 5.8: (a) A folded square of a side $a/\sqrt{2}$, where a is a length of its diagonal; (b) The quotient space is equivalent to square of side a , created by cutting the diagonals on one of its sides (e.g., the upper side as indicated in panel (a)). The sides of the original folded square are indicated with black dashed lines and black dots indicate its corners. Panel (b) shows a function $\phi(x, y)$, created by the tessellation with copies of $\psi_0(x, y)$ defined solely on σ .

5.6.9 Double-sided triangle

The last manifold we will discuss is a double-sided equilateral triangle of side a . As shown in Fig. 5.9(a), the respective quotient space is created by cutting one of the faces from the centre of mass towards the corners of the triangle. When unfolded, this results in a regular hexagon with gluing instructions as these visualised in Fig. 5.9(b) (edges labelled with the same colour, e.g. 1 and 1', are identified). Fig. 5.9(b) shows the plane \mathbb{R}^2 tiled with copies of function $\psi_0(x, y)$ defined on σ , using the tessellation rule no. 1. The unit cell of the resulting function $\phi(x, y)$ corresponds to a rectangle with sides $3a$ and $a\sqrt{3}$. This yields the allowed components of the wavevector to be $k_x = 2m\pi/3a$ and $k_y = 2n\pi/a\sqrt{3}$. However, function $\phi(x, y)$ remains unchanged when we move by a vector $(3ma, na\sqrt{3})$ as well as we move along a vector $(3ma + 3a/2, na\sqrt{3} + a\sqrt{3}/2)$. This requires the sum $m + n$ to be equal to an even integer. Finally, the unit cell has a three-fold rotational symmetry and thus the modes $\phi_{mn}(x, y)$ coincide with superpositions of three plane waves with their wavevectors mutually rotated by angle $\pm 2\pi/3$

$$\psi_{mn}(x, y) = N_{mn} \left\{ \exp \left[\frac{i\pi}{a} \left(\frac{2m}{3} x + \frac{2n}{\sqrt{3}} y \right) \right] + \exp \left[\frac{i\pi}{a} \left(\frac{-m + 3n}{3} x - \frac{m + n}{\sqrt{3}} y \right) \right] + \exp \left[\frac{i\pi}{a} \left(-\frac{m + 3n}{3} x + \frac{m - n}{\sqrt{3}} y \right) \right] \right\}, \quad (5.34)$$

with normalisation constants $N_{mn} = (3\sqrt{3}a^2(1 + 2\delta_{m0}\delta_{n0})/2)^{-\frac{1}{2}}$ and the domain \mathcal{D} for the indices m, n can be expressed as $\mathcal{D} = \{(m, n) = (0, 0)\} \cup (\{(m, n); m \in \mathbb{Z}, n \in \mathbb{N}_0, m + n \text{ even}\} \cap \{(m, n); m, n \in \mathbb{Z}, n > -m, m + n \text{ even}\})$. Indeed, these modes yield the correct comb $\Psi_{\text{Triangle}}(x, y, x', y')$

$$\begin{aligned} \Psi_{\text{Triangle}}(x, y, x', y') = \sum_{m, n} & \left[\delta \left(x - x' - \left(m + \frac{n}{2} \right) 3a \right) \delta \left(y - y' - na \frac{\sqrt{3}}{2} \right) \right. \\ & + \delta \left(x + \frac{x' - y'\sqrt{3}}{2} - \left(m + \frac{n}{2} \right) 3a \right) \delta \left(y + \frac{y' + x'\sqrt{3}}{2} - na \frac{\sqrt{3}}{2} \right) \\ & \left. + \delta \left(x + \frac{x' + y'\sqrt{3}}{2} - \left(m + \frac{n}{2} \right) 3a \right) \delta \left(y + \frac{y' - x'\sqrt{3}}{2} - na \frac{\sqrt{3}}{2} \right) \right]. \end{aligned} \quad (5.35)$$

The energy spectrum is $E_{mn} = 2\pi^2\hbar^2(m^2 + 3n^2)/(9\mu a^2)$ and the revival time is $T = 9\mu a^2/(4\pi\hbar)$.

5.7 Obtaining the topology of the manifold from its modes

Once we have derived the modes, we can employ these to investigate the topologies of the corresponding manifolds. For this aim, we will apply the Poincaré-Hopf Theorem [151]: Let \mathbf{v} be a vector field with isolated zero points, defined on a manifold S , where S is without boundary. Then the sum of the indices of the zeros of the vector field \mathbf{v} is then equal to the Euler characteristic of the manifold. This can be written mathematically in the following way

$$\sum_n \text{index}_{x_n}(\mathbf{v}) = \chi_S, \quad (5.36)$$

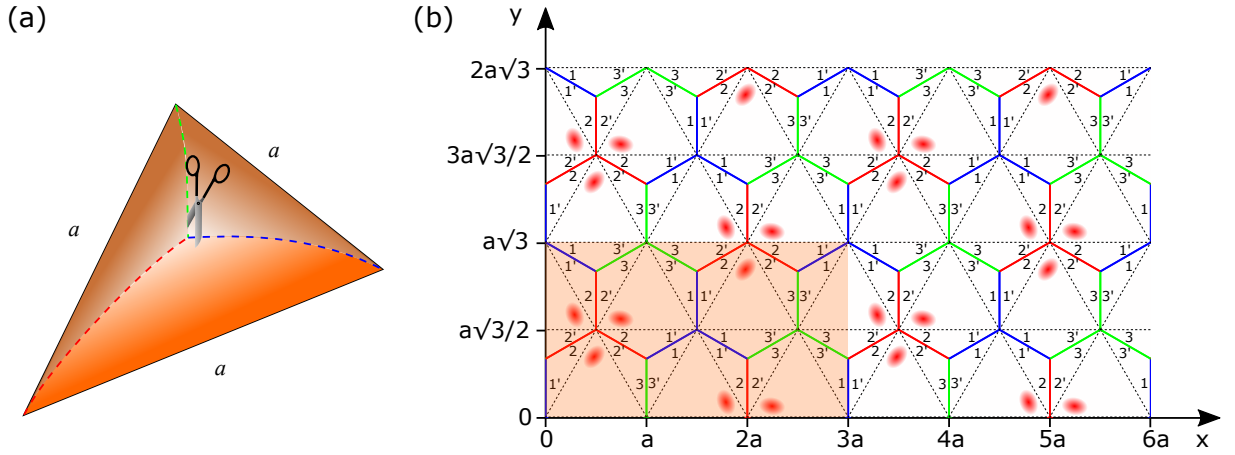


Figure 5.9: (a) A both-sided regular triangle of a side a ; (b) The quotient space is equivalent to a regular hexagon, created by cutting one of the faces from the centre of mass towards the corners of the triangle (e.g., the upper side as indicated in panel (a)). The unit cell (red-shaded rectangle) consists of six copies of the quotient space. One copy is just shifted by vector $(3a/2, a\sqrt{3}/2)$ with respect to the original quotient space. Two other copies are shifted by vectors $(a, 0)$ and $(0, a\sqrt{3}/2)$ respectively and rotated by angle $2\pi/3$ with respect to the original quotient space. The two remaining copies are then rotated by angle $4\pi/3$ and shifted by vectors $(2a, 0)$ and $(a/2, a\sqrt{3}/2)$ respectively. The gluing instructions are visualised with red, green and blue colours of identified edges, e.g. blue edges labelled 1 and 1' are identified.

where χ_S is the Euler characteristic of S and x_n are the zero points of the vector field \mathbf{v} on S . The index of the vector field \mathbf{v} at each of its zero points x_n is calculated by moving a point P along a closed loop γ around x_n and recording how many times the vector $\mathbf{v}(P)$ rotates as we move around the loop: n anticlockwise rotations of \mathbf{v} corresponds to an index of $+n$, and an index of $-n$ corresponds to n clockwise rotations.

In Sec. 5.6, we solved the Helmholtz equation on quotient spaces of six manifolds without a boundary: torus, Klein bottle, real projective plane, tetrahedron, double-sided square and the double sided triangle. Provided a vector field \mathbf{v} on each of these manifolds, their Euler characteristics can be calculated using the Poincaré-Hopf theorem. In our calculations, we will choose the vector field $\mathbf{v} = \text{grad } \psi$ to be the gradient of a scalar function $\psi(x, y)$, defined on the respective quotient space σ . Given the modes on σ , we choose the function $\psi(x, y)$ to be either the mode on σ or the superposition of degenerate modes (i.e., with the same value of the wavenumber $k = \sqrt{k_x^2 + k_y^2}$) such that the resulting vector field \mathbf{v} contains only isolated zero points. The zero points of vector field \mathbf{v} , of course, correspond to the critical points of function $\psi(x, y)$. The index of \mathbf{v} is equal to $+1$ at every maximum or minimum of $\psi(x, y)$ and -1 at the saddle points of $\psi(x, y)$.

Examples of such functions $\psi(x, y)$ for each considered manifold S are presented in Fig. 5.10 in their respective quotient spaces σ . The isolated zero points of $\mathbf{v} = \text{grad } \psi$ are marked with dark-yellow and grey dots respectively: dark-yellow dots represent the extreme points of $\psi(x, y)$, whereas grey dots correspond to saddle points of $\psi(x, y)$. After being unfolded and flattened to σ , some zero points of \mathbf{v} on S become split into N zero points on the edges of σ , which are identified by the gluing instructions defined on σ . For example, four maxima at the corners of the quotient space of the torus (see Fig. 5.10(a)) correspond to a single maximum on the folded surface. We therefore count these zero points on the edges of σ multiplied by a factor $1/N$ (for example, the four maxima located at the corners of the quotient space of the torus are counted each with a factor $1/4$). Table 5.1 shows the values of Euler characteristics χ for each manifold obtained by

| Manifold | χ |
|-----------------------|--------|
| Torus | 0 |
| Klein bottle | 0 |
| Real projective plane | 1 |
| Tetrahedron | 2 |
| Double-sided square | 2 |
| Double-sided triangle | 2 |

Table 5.1: Euler characteristics χ for different manifolds S , obtained by summing the indices of zero points of a vector field $\mathbf{v} = \text{grad } \phi$ (scalar function ϕ is presented in Fig. 5.10 for each manifold) defined on the respective quotient spaces σ .

our method. All presented values are equal to those presented in literature, for example in [152, 153] (torus, Klein bottle and the real projective plane). For the tetrahedron, double-sided square and the double-sided triangle, the value of Euler characteristic is $\chi = 2$, which indicates that these manifolds are topological spheres since the Euler characteristic of a sphere is also equal to 2.

5.8 Simulations

In this section, we present numerical simulations of quantum motion on a selection of the manifolds discussed in Sec. 5.6. We set $a = b$ wherever the quotient space is a rectangle with sides a and b . Except for the tetrahedron, all presented figures show a portion of the plane, containing four copies of the quotient space. The plots show the probability density $|\phi(x, y, t)|^2$ at different rational multiples of the revival time T . All the simulations were performed using MATLAB.

Fig. 5.11 shows the quantum motion of a particle on the Klein bottle. In our simulations, the initial state $\psi_0(x, y)$ is constant on a circle and continuously becomes zero on the edge of the circle. An interesting phenomenon can be observed: whereas the resulting pattern at time $T/8$ has a rectangular symmetry, the probability density at time $T/6$ exhibits an almost hexagonal symmetry. This is caused by the configurations of the fractional Talbot images at the corresponding times. A similar initial state $\psi_0(x, y)$ was employed to visualise the quantum motion of a particle on the Möbius strip, presented in Fig. 5.12. Note that the diffraction pattern, simulating the probability density, remains always zero at lines $x = ma$, corresponding to the hard boundaries of the copies of the quotient space σ .

Figs. 5.13 and 5.14 visualise quantum motion of a particle on the tetrahedron and the double-sided square, respectively. In both cases, the initial state is chosen to be a map of the globe, conformally projected on the respective quotient space, which in Fig. 5.13 coincides with the Peirce quincuncial projection.

5.9 Discussion and conclusions

We have found fully analytic solutions of Schrödinger equation for a number of compact manifolds. Each presented manifold can be unfolded and flattened to the respective quotient space σ , equipped with the gluing instructions such that the function $\psi_0(x, y)$ defined solely on σ can pave the whole plane, without gaps or overlaps, and with the gluing instructions defined on σ satisfied everywhere. Thanks to the tessellation rules formulated

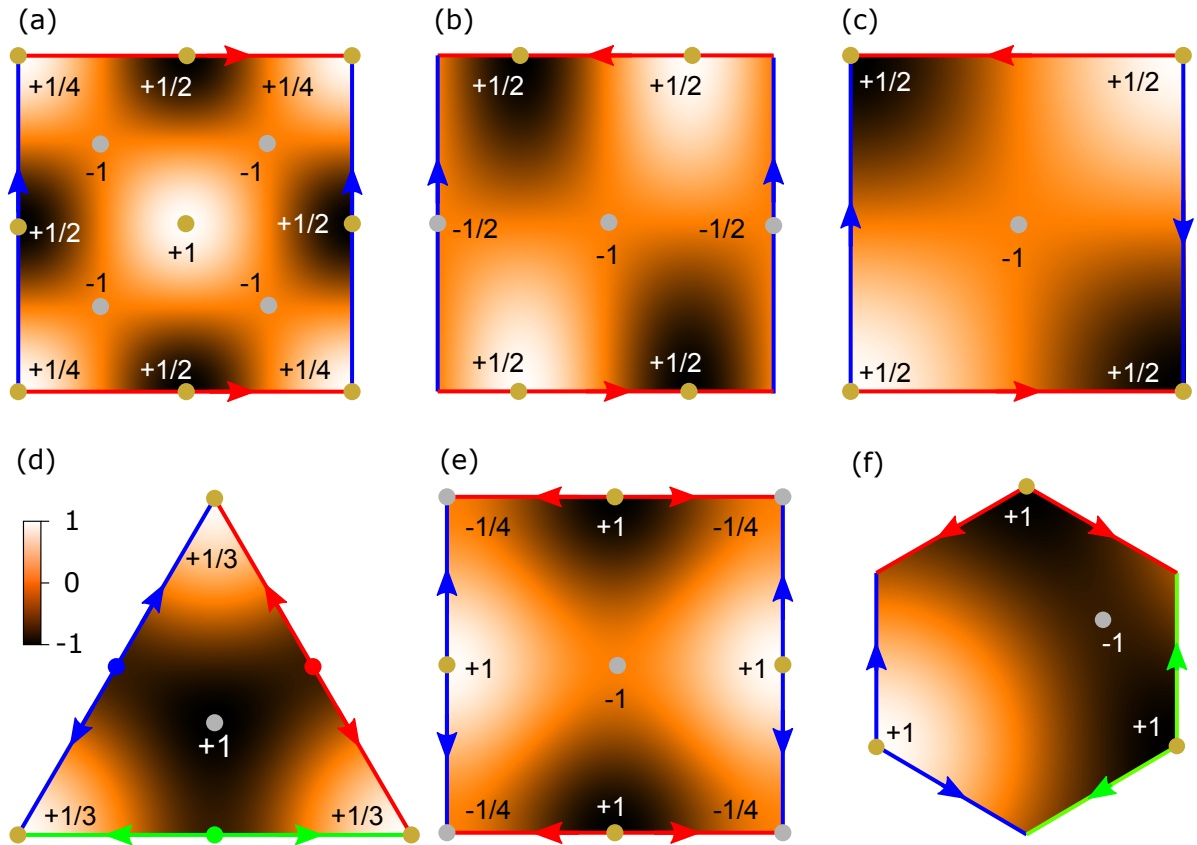


Figure 5.10: (a) Torus with the mode $\psi = \phi_{1,1} + \phi_{-1,1} + \phi_{1,-1} + \phi_{-1,-1}$. (b) Klein bottle with $\psi = \phi_{1,1} + \phi_{1,-1}$. (c) Real projective plane with the mode $\psi = \phi_{1,1}$. (d) Tetrahedron with $\psi = \phi_{1,1} + \phi_{1,-1} + \phi_{0,2}$ (e) Double-sided square with $\psi = \phi_{1,1} + \phi_{1,-1}$. (f) Double-sided triangle with $\psi = \phi_{1,1} + \phi_{-1,-1}$. Maxima/minima are labelled with dark-yellow dots, whereas saddle points are marked with grey dots. Some critical points on the edges are actually identified due to the gluing instructions (e.g. all three maxima in the corners of the quotient space of a tetrahedron in panel (d) actually correspond to a single point on the folded surface). Their indices are therefore multiplied by a factor (1/3 in the case of a tetrahedron), so their sum yields the correct single-point index value on the respective folded surface.

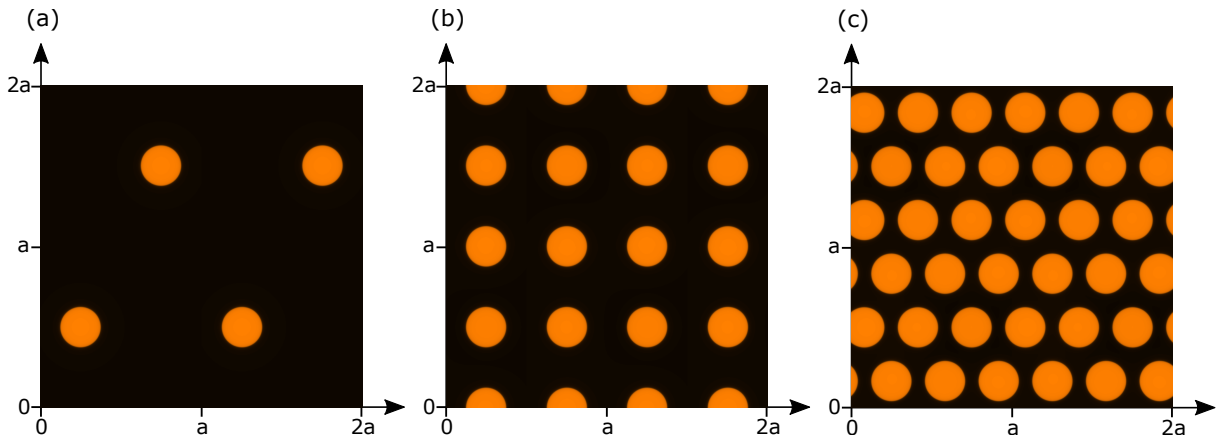


Figure 5.11: Evolution of the state on the Klein bottle shown at (a) $t = 0$ (initial state), (b) $t = T/8$ and (c) $t = T/6$. Note that in (b) the probability density exhibits a rectangular symmetry while in (c) its symmetry is almost hexagonal.

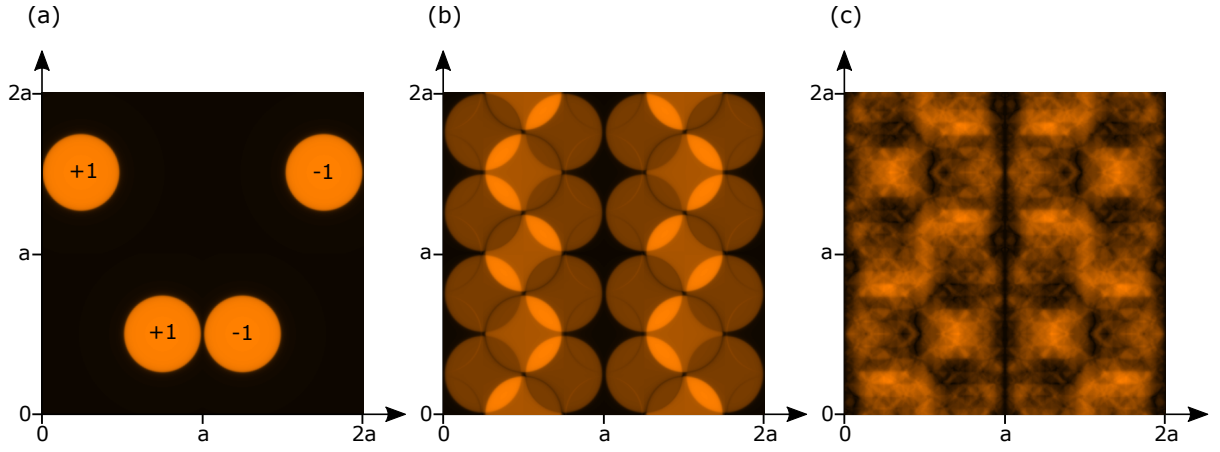


Figure 5.12: Evolution of the state on the Möbius strip shown at (a) $t = 0$ (initial state), (b) $t = T/4$ and (c) $t = 5T/13$. In (a) the signs of the initial wavefunction at different copies of the quotient space are marked.

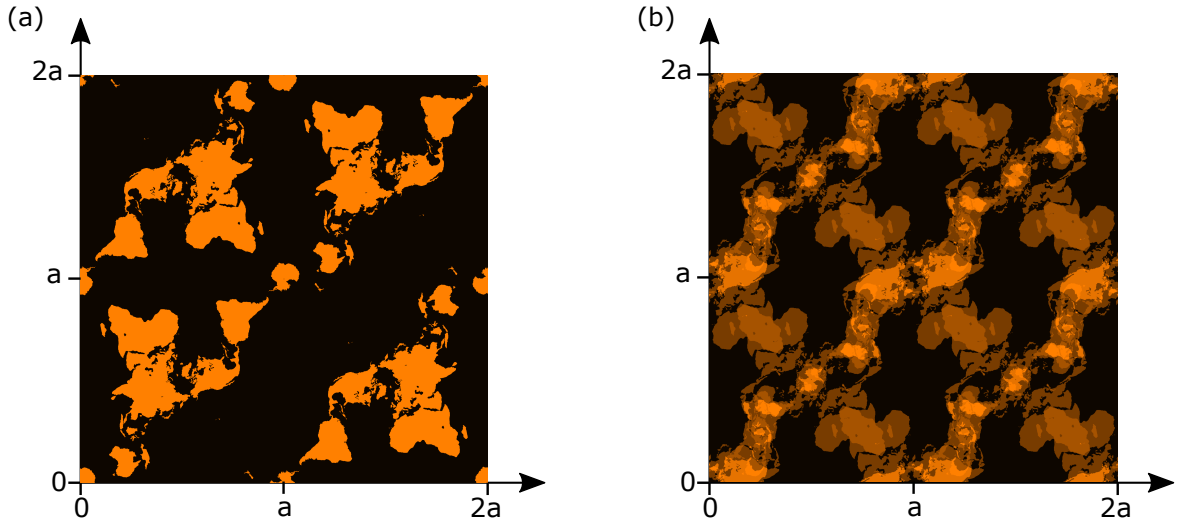


Figure 5.13: “Quantum motion of the continents” – evolution of the state on the double-sided square shown at (a) $t = 0$ (initial state in the form of the Earth surface conformally projected on the square quotient space, using Peirce quincuncial projection), (b) at $t = T/4$, we see four overlapping copies of the original map of the world.

in Sec. 5.3, the function $\phi(x, y)$ created by such tiling is a solution of Schrödinger equation in the quotient space σ and the whole plane \mathbb{R}^2 at the same time. The symmetries of function $\phi(x, y)$ were then employed to derive the analytic expressions of the eigenmodes and eigenenergies of Schrödinger equation for each discussed manifold. Finally, the equivalence between the quantum motion on a compact manifold and in the plane with certain symmetries have been applied to show that time evolution of the wavefunction $\psi_0(x, y)$ defined solely on σ is equivalent to diffraction on a grating with transmission function $\phi(x, y)$, created by tiling the plane with copies of $\psi_0(x, y)$.

Interestingly, any periodic pattern can be classified by one of the seventeen planar crystallographic groups, also known as wallpaper groups [154]. Wallpaper group can be defined as a group of isometries (translations, rotation, reflections, glide reflections), acting on a two-dimensional repeating pattern [154–156]. The smallest repeat unit of a two-dimensional pattern can be represented with an orbifold [157], which is a generalization of the notion of manifold as well as of that of quotient space of a manifold with respect to a properly discontinuous group of transformations [158]. Our work is therefore closely

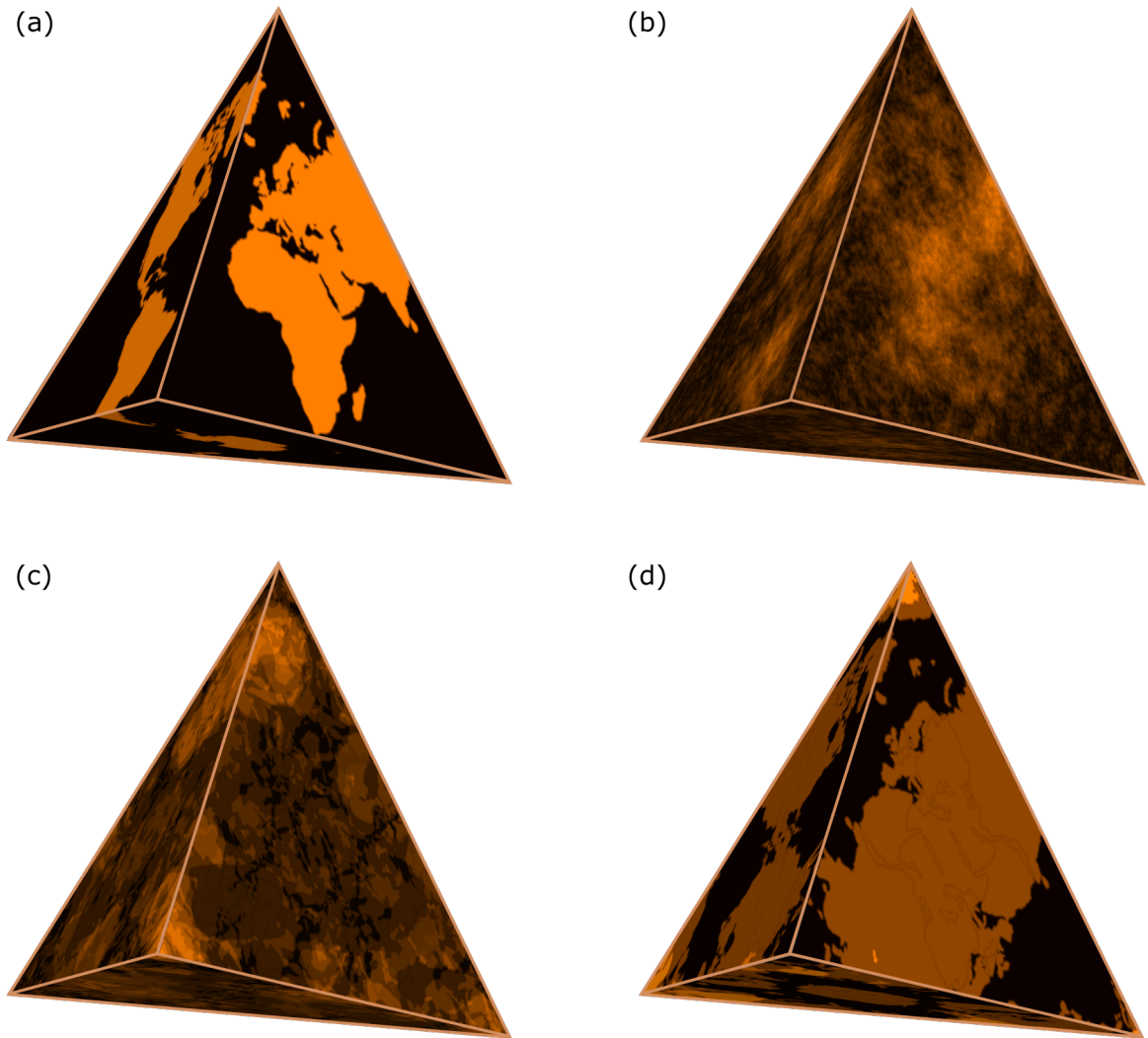


Figure 5.14: “Quantum motion of the continents”, projected on the surface of a tetrahedron – the initial state in the form of the map of the Earth conformally projected on a tetrahedron; evolution of this state is presented at time (a) $t = 0$, (b) $t = T/128$, (c) $t = T/6$, and (d) $t = T/3$.

connected to the theory of orbifolds, appearing in topology, geometry, geometric group theory [155] and in the string theory [159, 160].

Furthermore, the presented relation of diffraction and the lattice symmetry is closely related to several other areas of research, e.g. so-called glide and twist symmetries [161, 162]. Regarding glide and twist symmetries, a typical structure is periodic along one axis and has symmetry such that the smallest repeat unit fills the whole space with a combination of translation and inversion operations [163–165]. These symmetries have been recently applied to reduce the dispersion of guided modes, which provides an opportunity for the development of new kinds of leaky-wave antennas based on an accurate control of the non-dispersive refractive index [162].

To best of our knowledge, the possibility of exploring the quantum mechanics on folded surfaces with simple diffraction experiments does not seem to be appreciated yet. We therefore believe that our method may potentially become a standard tool in areas of research, where diffraction from some gratings can be understood in terms of motion of waves on closed surfaces.

Chapter 6

Conclusions and future work

This thesis aimed to propose new methods of designing omnidirectional optical devices, including invisibility cloaks and setups simulating the optics of curved spaces, using simple and well-known optical elements.

To meet this objective, we first investigated the imaging properties of systems of tilted lenses in Chapter 2. We have found a simple and elegant description of imaging by a pair of skew lenses as a single lens, whose object and image spaces are sheared. We then defined the lens-imaging coordinates, in which the imaging due to a pair of skew lenses can be described as standard single-lens imaging. We showed how to construct the optical axis, the directions of object-sided and image-sided transverse planes, and how to find all cardinal points of a general two-lens system. Our construction is remarkably simple and has the potential to be applied for designing and understanding novel optical devices. As an example of such a novel device, we have proposed a combination of three skew lenses, which performs an image rotation by an arbitrary angle $\Delta\alpha$ around the axis V of common intersection of all three included lenses.

In the future we would like to develop an analogous description of imaging due to systems of more than two tilted lenses. Another natural extension of this work would be to perform an experimental demonstration. Due to the fact the conventional lenses are well-optimised for imaging of an object lying on its optical axis, they are poorly optimised for off-axis imaging and therefore such an experimental demonstration would require designing and manufacturing novel types of lenses which is currently a highly active field of research and is capable of yielding impressive outcomes, e.g. metalenses [32–34]. These metalenses seem to overcome the aberrations of conventional lenses and thus have the potential to become real-life implementations of ideal thin lenses. This leads us to believe that systems of tilted lenses might be experimentally demonstrated in a near future, using metalenses. Finally, the proposed three-lens image rotator can be upgraded if the included lenses of the rotator are replaced by corresponding omnidirectional lenses, discussed in Chapter 3. Any observer inside such an omnidirectional lens is completely surrounded by the lens, and sees the image of the outside in all directions. If the three omnidirectional lenses are gradually nested inside each other, an observer inside the innermost omnidirectional lens is completely surrounded by all three lenses, and sees the image of the outside in all directions as mapped by the three lenses, namely rotated around the line V . However, just like the field of view of a combination of three thin ideal lenses is limited, analogous field-of-view limitations can be expected.

In Chapter 3, we then presented a “virtuoso geometrical optics with lenses” in sense that we have stretched the possibilities of that field by designing a number of omnidirectional devices purely from ideal thin lenses. To guarantee a unique mapping, we have derived two conditions on such ideal-lens devices: loop-imaging and the edge-imaging

condition. The edge-imaging condition was then applied on simple intersections of several lenses to get the conditions on their principal-point positions and their focal lengths. These lens combinations have been consequently employed as building blocks of a TO device, which we have called the Structure S. We showed that the Structure S can be interpreted as an omnidirectional lens, i.e. any object inside the Structure S is imaged to the outside like due to an ideal lens in all viewing directions. If the inside object is imaged to the outside with magnification approaching zero, Structure S can be interpreted as an almost-invisibility cloak as the object will become barely recognizable when seen from the outside. To achieve a perfect invisibility, one can tune the parameters of the Structure S such that the object P inside the device is imaged to a point P', lying outside the device. When observed from a direction such that P' is not in line with any part of the Structure S, image P' (and thus object P itself) are invisible. We have call this configuration an abyss cloak. The perfect invisibility cloak for all viewing directions – the bi-abyss cloak – then consists two nested abyss cloaks, which are perpendicular to each other.

In the future work we aim to study the properties of nested omnidirectional lenses even further. So far, we have shown that nested omnidirectional lenses can work as the omnidirectional image rotator and the perfect invisibility cloak. However, we believe that even more interesting devices can be obtained from nested omnidirectional lenses, for example the optical analog of a wormhole, similar to the device presented in Ref. [74]. When designing devices with nested omnidirectional lenses, field-of-view limitations can be expected just like the field of view of a standard lens is. The future work should therefore include finding ways how the field of view of nested omnidirectional lenses can be optimised. The other natural extension of this project is the experimental demonstration of the proposed devices. Although standard lenses are not expected to work well, the structure S can be built using either metalenses [32–34] or appropriate lens holograms [43, 44, 53–55].

In Chapter 4, we have presented a new method of the optical simulation of curved spaces, which is based on triangulation and unfolding the curved spaces. Our method can be employed to mimic both 2D and 3D curved spaces, namely the triangulations of a sphere (surface of a tetrahedron and a cube) and of a hypersphere (3D hypersurface of a 5-cell and of a hypercube). The building block of our simulations is the space-cancelling (SC) wedge, an optical device which maps its faces onto each other and thus optically identifies the edges or faces to be glued. We have discussed several way how the space-cancelling wedges can be built: using wedges of negative refractive index (or ray-optical approximations thereof), or a combination of absolute optical instruments modified by the methods of transformation optics, using a combination of three ideal lenses, and employing the light-field transfer. Our approach thus simplifies the optical simulations by omitting manufacturing the actual, “glued” curved spaces. Our work connects exciting fields of research, such as transformation optics, negative refraction, geodesic lenses, absolute optical instruments, general relativity, and quantum gravity.

In the future, we therefore intend to explore the possible applications of our method in these branches of knowledge. This will include finding ways how to mimic manifolds with a negative curvature; although SC wedges using light-field transfer appear to be appropriate for simulating two-dimensional spaces with negative curvature, the method of simulating analogous three-dimensional spaces still needs to be worked out. Another natural extension of our work is to upgrade our method for simulating a curved space-time, which requires building suitable time-dependent configurations of the SC wedges. Finally, experimental verification of our method would be also desirable in the future work: recently, a concept of a “spaceplate”, which effectively propagates light for a length that can be considerably longer than the plate thickness, had been presented [166]. Be believe

that if the material properties are tuned such that the effective propagation distance of light passing through the spaceplate will become shorter than the plate thickness (ideally zero), these spaceplates can also work as SC wedges. Together with the rapid development of materials with negative refractive index [105–107, 112–114] and coherent fibre bundles [93, 95–102], this leads us to believe that SC wedges will be possible to manufacture in a near future.

In Chapter 5, we studied the wave mechanics and found full analytical solutions of Schrödinger equation on several two-dimensional compact surfaces including the Klein bottle, Möbius strip and projective plane. Each presented manifold can be unfolded and flattened to the respective quotient space σ , equipped with the gluing instructions such that the function $\psi_0(x, y)$ defined solely on σ can pave the whole plane, without gaps or overlaps, and with the gluing instructions defined on σ satisfied everywhere. We then showed that solving the Schrödinger equation on σ is equivalent to solving it in the whole plane \mathbb{R}^2 , provided that the wavefunction has the same values on all the copies of the quotient space σ . A universal guide of tiling the plane with copies of function $\psi_0(x, y)$ defined solely on σ has been provided by formulating the tessellation rules. The symmetries of function $\phi(x, y)$ created by such tiling were then employed to derive the analytical expressions of the eigenmodes and eigenenergies of Schrödinger equation for each discussed manifold. Finally, we have shown that time evolution of the wavefunction $\psi_0(x, y)$ defined solely on σ is equivalent to diffraction on a grating with transmission function $\phi(x, y)$, created by tiling the plane with copies of $\psi_0(x, y)$.

In the future we intend to investigate the wave motion on surfaces, whose respective quotient spaces cannot pave the plane \mathbb{R}^2 without gaps or overlaps and with the gluing instructions satisfied everywhere. For example, if one attempts to tessellate the plane with unfolded nets of a cube, an array of empty squares will be created in which the wavefunction is not defined. Because of these regions of “non-existing optical space”, the modes ψ_n of a cube are expected to be in form of functions other than plane waves, which might lead to interesting wave-propagation phenomena. Another natural extension of this project is studying the wave motion in three-dimensional compact manifolds. We have already made an effort to solve the Helmholtz equation on a 3D hypersurface of a hypercube and found a solution in terms of plane waves. However, these plane waves do not form a basis, i.e. there are functions defined on the hypersurface of a hypercube which cannot be expressed in terms of plane waves. We therefore intend to further investigate the wave motion in three-dimensional curved spaces in future work. We would also like to further explore the relation of our work with the theory of orbifolds, which might open the connections to other exciting research fields such as topology, geometric group theory [155] and string theory [159, 160]. Finally, we can see a natural extension of our work by exploring potential applications of the presented entanglement of diffraction and the lattice symmetry, which is closely related to several other areas of research, e.g. so-called glide and twist symmetries [161, 162]. As these symmetries have been successfully employed to reduce the dispersion of guided modes, research in this field promises an opportunity for the development of new kinds of leaky-wave antennas based on an accurate control of the non-dispersive refractive index [162].

Appendix A

Derivation of the formula for intersection point w_i

In this section, we will derive the intersection point w_i of the two-lens optical axis with a plane through line V of the common intersection of lenses L_1 and L_2 and the line I of the intersection of the image-sided focal plane L_1 and the object-sided focal plane of L_2 . In our calculations, we will employ the following definitions, all expressed in a Cartesian coordinate system defined in Fig. 2.8: plane of lens L_1

$$x = -z \cot \varphi_1, \quad (\text{A.1})$$

plane of L_2

$$x = -(z - d \cos \beta) \cot \varphi_2, \quad (\text{A.2})$$

image-sided focal plane of L_1

$$x = -(z - g_1 \cos \beta) \cot \varphi_1, \quad (\text{A.3})$$

and the object-sided focal plane of L_2

$$x = -[z - (d - g_2) \cos \beta] \cot \varphi_2. \quad (\text{A.4})$$

The intersection line V of lenses L_1 and L_2 can be then parametrized as following

$$V \equiv (V_x, t, V_z) = \left(d \cos \beta \frac{\cot \varphi_1 \cot \varphi_2}{\cot \varphi_2 - \cot \varphi_1}, t, -d \cos \beta \frac{\cot \varphi_2}{\cot \varphi_2 - \cot \varphi_1} \right), \quad t \in \mathbb{R} \quad (\text{A.5})$$

Similarly, one can parametrize the intersection line I of the image-sided focal plane of lens L_1 and the object-sided focal plane of lens L_2

$$I \equiv (I_x, s, I_z) = \left(-\cos \beta \frac{(d - g_1 - g_2) \cot \varphi_1 \cot \varphi_2}{\cot \varphi_2 - \cot \varphi_1}, s, \cos \beta \frac{(d - g_2) \cot \varphi_2 - g_1 \cot \varphi_1}{\cot \varphi_2 - \cot \varphi_1} \right), \quad (\text{A.6})$$

where $s \in \mathbb{R}$ is a real parameter. Lines V and I define a plane, which satisfies the equation

$$x - V_x = \frac{I_x - V_x}{I_z - V_z} (z - V_z). \quad (\text{A.7})$$

Using this expression, we will finally calculate intersection point $W_{\text{im}} = (0, w_{\text{im}} \sin \beta, w_{\text{im}} \cos \beta)$ of this plane with the w axis. Substituting $x = 0$, $z = w_{\text{im}} \cos \beta$ and the definitions of V_x , V_z , I_x and I_z finally yields the formula for w_{im} presented in Sec. 2.3.8,

$$w_{\text{im}} = \frac{dg_1}{g_1 + g_2}. \quad (\text{A.8})$$

Appendix B

Derivation of the formulas for slopes $\cot \alpha$ and $\cot \alpha'$ of two-lens object-sided and image-sided transverse planes

In this section, we will derive formulas for the slopes $-\cot \alpha$ and $-\cot \alpha'$ of the two-lens object-sided and image-sided transverse planes. Namely, we will show how the slope $-\cot \alpha$ can be calculated; slope $-\cot \alpha'$ can be calculated analogously. We will use the parametrization of the line $V = (V_x, t, V_z)$, given by Eq. (A.5).

As defined, \mathcal{P} is a plane through both point $P = (0, P_w \sin \beta, P_w \cos \beta)$ (where P_w is given by Eq. (2.19)) and the line V . A vector $\mathbf{n}_{\mathcal{P}}$, normal to such plane, can be calculated as a cross product of two arbitrary vectors $\mathbf{a} \times \mathbf{b}$, lying in \mathcal{P} . Let us choose $\mathbf{a} = (-V_x, 0, P_w \cos \beta - V_z)$ and $\mathbf{b} = (0, 1, 0)$. Thus, $\mathbf{n}_{\mathcal{P}} = \mathbf{a} \times \mathbf{b} = (-P_w \cos \beta + V_z, 0, -V_x)$. As defined, α is an angle between the plane \mathcal{P} and x axis (see Fig. 2.8). Therefore, one can deduce that

$$\cot \alpha = \frac{V_x}{P_w \cos \beta - V_z}, \quad (\text{B.1})$$

and inserting the definitions of V_x , V_z and P_w finally yields

$$\cot \alpha = \cot \varphi_1 \frac{d - g_1 - g_2}{d - g_2 - g_1 \cot \varphi_1 / \cot \varphi_2}. \quad (\text{B.2})$$

Repeating this procedure for the image-sided principal plane \mathcal{P}' then leads to the following formula for $\cot \alpha'$

$$\cot \alpha' = \cot \varphi_2 \frac{d - g_1 - g_2}{d - g_1 - g_2 \cot \varphi_2 / \cot \varphi_1}. \quad (\text{B.3})$$

Appendix C

Parameters of the three-lens image-rotation system

In Section 2.6, we showed that an appropriate combination of three skew lenses provides an image rotation of the entire object space. However, a relationship between the parameters of the system T and the inclination angle $\Delta\alpha = \alpha' - \alpha$ remains unrevealed. We will settle this debt in this section. Let us start with a system D = L₁ + L₂ of two skew lenses of focal lengths f_1 and f_2 . According to the theory of imaging with two skew lenses presented in Sec. 2.4, the object-sided transverse planes make an angle α with the x -axis, which is related to the parameters of the system D by the Eq. (2.35)

$$-\cot \alpha = -\cot \varphi_1 \frac{d - g_1 - g_2}{d - g_2 - g_1 \cot \varphi_1 / \cot \varphi_2}, \quad (\text{C.1})$$

where g_i are the projected focal lengths of included lenses and d is the separation between the principal points of the lenses. In the same section, we also presented a similar formula for the angle α' between the x -axis and the image-sided transverse planes:

$$-\cot \alpha' = -\cot \varphi_2 \frac{d - g_1 - g_2}{d - g_1 - g_2 \cot \varphi_2 / \cot \varphi_1}. \quad (\text{C.2})$$

As shown in section 2.6.1, for the system D to be a part of an image rotator, the angles α and α' must satisfy the condition $\alpha + \alpha' = 0$. This implies a constraint on the parameters of the system D. Specifically, summing Eqs. (C.1) and (C.2) with $\alpha = -\alpha'$ yields the following relation:

$$\cot \varphi_1 (d - 2g_1) = -\cot \varphi_2 (d - 2g_2). \quad (\text{C.3})$$

If Eq. (C.3) is satisfied, the following simple expressions can be derived for $\cot \alpha$ and $\cot \alpha'$ respectively:

$$\cot \alpha = \cot \varphi_1 \left(1 - \frac{2g_1}{d} \right), \quad (\text{C.4})$$

$$\cot \alpha' = -\cot \alpha = -\cot \varphi_1 \left(1 - \frac{2g_1}{d} \right). \quad (\text{C.5})$$

For a given rotation angle $\Delta\alpha = \alpha' - \alpha = 2\alpha'$, Eq. (C.5) can be solved for the focal length f_1 to give

$$f_1 = \frac{d}{2} \left(\cos \varphi_1 + \cot \frac{\Delta\alpha}{2} \sin \varphi_1 \right), \quad (\text{C.6})$$

where we have denoted $\cot \alpha' \equiv \cot \frac{\Delta\alpha}{2}$. A formula for the focal length $f_2 = g_2 \cos \varphi_2$ of lens L_2 can be obtained from Eq. (C.3):

$$f_2 = \frac{\sin \varphi_2}{2} \left(d \cot \varphi_1 - 2 \frac{f_1}{\sin \varphi_1} \right) + \frac{d \cos \varphi_2}{2}. \quad (\text{C.7})$$

Finally, the third lens L_3 needs to be added to the system D to complete the image rotator. The plane of the lens L_3 coincides with the image-sided principal plane \mathcal{P}' of the system D. From Eq. (2.49), the position of the principal point of lens L_3 , expressed in lens-imaging coordinates, is $(u, w) = (u', w') = (-f_D \sin \Delta\alpha, 0)$. Here, of course, f_D denotes the effective focal length of system D, given by Eq. (2.18). Given $\beta = 0$, the position (L_x, L_y, L_z) of the principal point of lens L_3 , expressed in global Cartesian coordinates, can be found using the transition matrix T_i^{-1} (given by Eq. (eqn:Ti-1)) to be

$$\begin{pmatrix} L_x \\ L_y \\ L_z - P'_w \end{pmatrix} = \begin{pmatrix} 1 & 0 & 0 \\ 0 & 1 & 0 \\ -\tan \frac{\Delta\alpha}{2} & 0 & 1 \end{pmatrix} \begin{pmatrix} -f_D \sin \Delta\alpha \\ 0 \\ 0 \end{pmatrix} = \begin{pmatrix} f_D \sin \Delta\alpha \\ 0 \\ 2f_D \sin^2 \frac{\Delta\alpha}{2} \end{pmatrix}. \quad (\text{C.8})$$

The projected focal length g_3 of lens L_3 equals $-f_D$ and thus the actual focal length f_3 is

$$f_3 = -f_D \cos \frac{\Delta\alpha}{2}. \quad (\text{C.9})$$

Appendix D

Calculation leading to focal lengths of an asymmetric four-lens intersection, which satisfies the edge-imaging condition

In this section, we will derive formulas for focal lengths of an asymmetric four-lens intersection, which satisfies the edge-imaging condition, presented in Eqn. (3.12). The idea of our computation follows naturally from the edge-imaging condition: consider an object Q located in the cell between lenses L_2 and L_3 (see Fig. D.1). If this object is imaged successively by lenses L_2 and L_1 , the image due to these two lenses (call it $Q_{2,1}$) must coincide with an image $Q_{3,4}$ due to lenses L_3 and L_4 . The corresponding equation $Q_{2,1} = Q_{3,4}$ then yields certain conditions on the focal lengths f_1, f_2, f_3 and f_4 . In the next step, we will employ the same argument to a point W in the cell between lenses L_1 and L_2 , i.e. its image $W_{2,3,4}$ by lenses L_2, L_3 and L_4 must coincide with the image W_1 by lens L_1 . This yields additional conditions for the focal lengths.

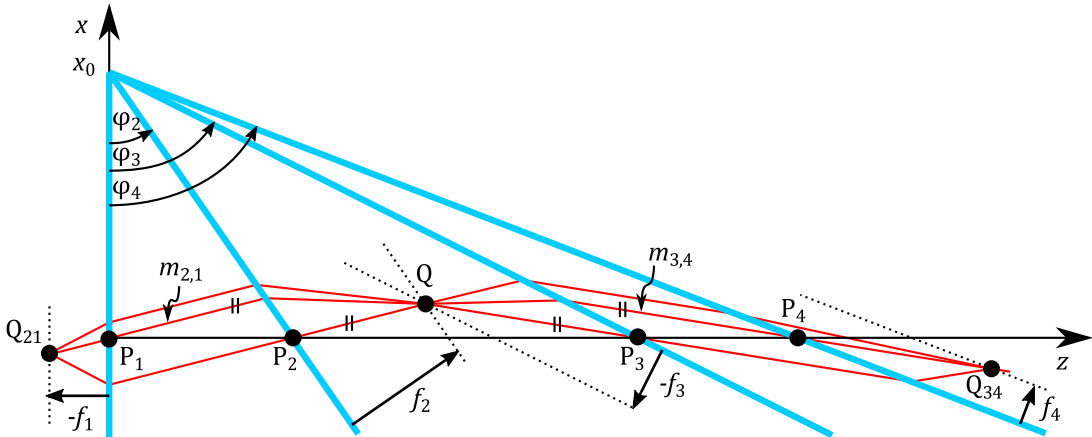


Figure D.1: To explain the calculations of focal lengths of lenses included in an asymmetric four-lens intersection.

For the purpose of our calculations, we will choose the point Q lying at the intersection $l_{2,3}$ of the focal planes of lenses L_2 and L_3 . Since Q lies in both of these focal planes, light rays emerging from Q become parallel after being transmitted through L_2 , the same is true for light rays being transmitted through L_3 . The image $Q_{3,4}$ then lies in the focal plane of lens L_4 since it is a result of focusing of a parallel bundle. To find the precise

position within this plane, we will employ a ray $m_{3,4}$ from the above mentioned parallel bundle between lenses L_3 and L_4 that passes through the principal point P_4 of lens L_4 . Since this ray is not deflected by L_4 , the image $Q_{3,4}$ lies at the intersection of this ray and the focal plane of L_4 . Later, we will find the position of a point $Q_{2,1}$ in a similar way.

Before transforming our ideas into equations, we will write down several general formulas that will be useful. First such a formula is a parametrization of an axis of a lens L_i (which is in fact perpendicular to the plane $z = x \tan \varphi_i$)

$$(x, y, z) = (t \sin \varphi_i, 0, P_i + t \cos \varphi_i), \quad (\text{D.1})$$

where $t \in \mathbb{R}$ is a real parameter. Now, both object- and image-sided focal points can be found easily by substituting $t = \pm f_i$ in Eq. (D.1) (the upper and lower sign corresponds to the image- and object-sided focal points, respectively). Then, the focal planes can then be parametrized as

$$(x, y, z) = (\pm f_i \sin \varphi_i - t \cos \varphi_i, s, P_i \pm f_i \cos \varphi_i + t \sin \varphi_i),$$

(where $t, s \in \mathbb{R}$) or equivalently

$$z = (x_0 - x) \tan \varphi_i \pm F_i, \quad (\text{D.2})$$

where we have denoted $F_i \equiv \frac{f_i}{\cos \varphi_i}$. Now, we place point A at the intersection of an image-sided focal plane of L_2 and an object-sided focal plane of L_3 . Writing Eq. (D.2) for lenses L_2 and L_3 with the appropriate signs in front of the focal lengths F_2 and F_3 and equating them, we obtain the parametric equations of the line $l_{2,3}$ in a following form

$$\begin{aligned} x &= x_0 + \frac{F_2 + F_3}{\tan \varphi_2 - \tan \varphi_3} \equiv x_{2,3}, \\ y &= t, \\ z &= \frac{F_3 \tan \varphi_2 + F_2 \tan \varphi_3}{\tan \varphi_3 - \tan \varphi_2} \equiv z_{2,3}. \end{aligned} \quad (\text{D.3})$$

Since point A can be any point lying on the line $l_{2,3}$, we can fix the value of parameter t to y_0 to get the coordinates of $A = (x_{2,3}, y_0, z_{2,3})$. The ray travelling from A towards the principal point of lens L_3 will not change its direction after being transmitted through the lens, so the direction of this ray determines the direction of the parallel bundle in the cell between lenses L_3 and L_4 . It is obvious that the line passing through both points Q and P_3 can be parametrized in the following way:

$$\begin{aligned} x &= x_{2,3}(1 - t) \\ y &= y_0(1 + t) \\ z &= z_{2,3} + t(P_3 - z_{2,3}). \end{aligned} \quad (\text{D.4})$$

The light ray $m_{3,4}$ mentioned above (a ray from the parallel bundle between lenses L_3 and L_4 that passes through the principal point P_4 of lens L_4) can be obtained by parallel shifting the line parametrized by Eq. (D.4) such that it passes through the principal point P_4 . Doing this, we get the equations of the line $m_{3,4}$ as

$$\begin{aligned} x &= -x_{2,3}t \\ y &= y_0(1 + t) \\ z &= P_4 + t(P_3 - z_{2,3}). \end{aligned} \quad (\text{D.5})$$

Similarly, we can find the line $m_{2,1}$ on which the image $A_{2,1}$ of point A due to lenses L_2 and L_1 must be located:

$$\begin{aligned}x &= -x_{2,3}s \\y &= y_0(1 + s) \\z &= P_1 + s(P_2 - z_{2,3}).\end{aligned}\tag{D.6}$$

For $A_{2,1}$ and $A_{3,4}$ to coincide, the lines $m_{2,1}$ and $m_{2,4}$ must intersect and their intersection. At the same time, point $A_{2,1} = A_{3,4}$, must lie at the intersection of object-sided focal plane of lens L_1 and image-sided focal plane of lens L_4 . Equating Eqs. (D.5) and (D.6), we can easily verify that they are compatible, i.e. the straight lines $m_{6,5}$ and $m_{7,8}$ indeed do intersect. Denoting $x_{1,4}$ and $z_{1,4}$ the x and z coordinates of their intersection point $A_{2,1} = A_{3,4}$ (we will not need the coordinate y), we finally get

$$\begin{aligned}x_{1,4} &= -x_0 \frac{P_1 - P_4}{P_3 - P_2} + x_0 \frac{(P_1 - P_4)(F_2 + F_3)}{(P_3 - P_2)^2}, \\z_{1,4} &= \frac{P_3 P_1 - P_4 P_2}{P_3 - P_2} - \frac{F_3 P_2 + F_2 P_3}{(P_3 - P_2)^2},\end{aligned}\tag{D.7}$$

where we employed $\tan \varphi_i = P_i/x_0$. As mentioned, this intersection point must lie in both the object-sided focal planes of L_1 and image-sided focal plane of L_4 . Applying the same procedure as for the intersection line of focal planes of lenses L_2 and L_3 (see Eq. (D.3)), we find the following expression for the coordinates $x_{1,4}$ and $z_{1,4}$

$$\begin{aligned}x_{1,4} &= x_0 + \frac{F_1 + F_4}{\tan \varphi_4 - \tan \varphi_1} = x_0 + x_0 \frac{F_1 + F_4}{P_4 - P_1} \\z_{1,4} &= \frac{F_4 P_1 + F_1 P_4}{P_1 - P_4}.\end{aligned}\tag{D.8}$$

Equating Eqs. (D.7) and (D.8) gives two conditions for the parameters F_1, F_2, F_3, F_4

$$\begin{aligned}\frac{F_1 + F_4}{P_1 - P_4} &= \frac{P_1 - P_2 + P_3 - P_4}{P_3 - P_2} + \frac{(P_4 - P_1)(F_2 + F_3)}{(P_3 - P_2)^2}, \\ \frac{F_4 P_1 + F_1 P_4}{P_1 - P_4} &= \frac{P_3 P_1 - P_4 P_2}{P_3 - P_2} - \frac{F_3 P_2 + F_2 P_3}{(P_3 - P_2)^2}.\end{aligned}\tag{D.9}$$

Writing these equations, we have again employed the fact that $x_0 \tan \varphi_i = P_i$. The analogous procedure can be performed with a point W, lying at the intersection of the image-sided focal plane of L_1 and the object-sided focal plane of lens L_2 . This yields two additional equations for the parameters F_1, F_2, F_3, F_4 :

$$\begin{aligned}\frac{F_4 + F_3}{P_4 - P_3} &= \frac{P_4 - P_1 + P_2 - P_3}{P_2 - P_1} + \frac{(P_3 - P_4)(F_1 + F_2)}{(P_2 - P_1)^2}, \\ \frac{F_3 P_4 + F_4 P_3}{P_4 - P_3} &= \frac{P_2 P_4 - P_3 P_1}{P_2 - P_1} - \frac{F_2 P_1 + F_1 P_2}{(P_2 - P_1)^2}.\end{aligned}\tag{D.10}$$

Eqs. (D.9) and (D.10) form a set of four linear inhomogeneous equations for F_1, F_2, F_3, F_4 . Solving these equations (using *Mathematica*) revealed that the equations are actually linearly dependent. Thus we can choose one of the parameters (e.g. F_1) arbitrarily and express the other three in terms of it. When this is done and the actual focal lengths f_2, f_3, f_4 and f_1 are expressed, we obtain Eqn. (3.12).

Appendix E

Derivation of the formula for Talbot length

In this section, we will derive the formula for the distance z_T behind the infinite periodic lattice where the image of the lattice is retrieved — the *Talbot length*. Before we derive the expression for the Talbot length z_T , we will briefly discuss the Fourier spectrum propagation method, which will be employed not only for the derivation of the Talbot length z_T , but also for a derivation of the formula of a fractional Talbot effect in Sec. F. Consider a two-dimensional grating, described by a transmission function $t(x, y)$, with periods p_x and p_y in x and y direction respectively. Let us choose a Cartesian coordinate system such that the grating lies in a plane $z = 0$. Now consider a collimated light beam of wavelength λ incident perpendicular to the grating. The wavefunction $\psi(x, y; z = 0)$ is then equal to the transmission function $t(x, y)$ of the grating. To obtain an expression for the wavefunction $\psi(x, y; z)$ at an arbitrary distance z behind the grating, we will first decompose the wavefunction $\psi(x, y; 0) = t(x, y)$ into plane waves, using the Fourier series

$$\psi(x, y; 0) = \sum_{m,n} c_{mn} \exp i2\pi \left(\frac{m}{p_x} x + \frac{n}{p_y} y \right) \quad (\text{E.1})$$

where coefficients c_{mn} are given by the integral

$$c_{mn} = \frac{1}{p_x p_y} \int_0^{p_x} dx' \int_0^{p_y} dy' t(x', y') \exp -i2\pi \left(\frac{m}{p_x} x' + \frac{n}{p_y} y' \right). \quad (\text{E.2})$$

Now the wavefunction $\psi(x, y; z)$ can be obtained by multiplying the plane waves on the right-hand side of Eq. (E.1) by appropriate phase factors $\exp ik_z z$, where the wavevector component k_z for each plane wave is given by the following formula

$$k_z = \sqrt{k_0^2 - (2\pi)^2 \left(\frac{m^2}{p_x^2} + \frac{n^2}{p_y^2} \right)} \approx k_0 - \frac{(2\pi)^2 \left(\frac{m^2}{p_x^2} + \frac{n^2}{p_y^2} \right)}{2k_0} = k_0 - \pi \lambda \left(\frac{m^2}{p_x^2} + \frac{n^2}{p_y^2} \right), \quad (\text{E.3})$$

where $k_0 = 2\pi/\lambda$ is the wavenumber of the beam. Combining Eqs. (E.1) and (E.2), and multiplying the resulting expression on the right-hand side by the factors $\exp ik_z z$, where k_z is given by Eq. (E.3), yields the desired wavefunction $\psi(x, y; z)$

$$\begin{aligned} \psi(x, y; z) &= \frac{\exp ik_0 z}{p_x p_y} \int_0^{p_x} dx' \int_0^{p_y} dy' t(x', y') \\ &\times \sum_{m,n} \exp i2\pi \left[m \frac{x - x'}{p_x} + n \frac{y - y'}{p_y} - \frac{\lambda z}{2} \left(\frac{m^2}{p_x^2} + \frac{n^2}{p_y^2} \right) \right]. \end{aligned} \quad (\text{E.4})$$

To derive the formula for the Talbot length, let us assume that the ratio p_x^2/p_y^2 is equal to a rational number, i.e. $p_x^2/p_y^2 = A/B$, where A and B are coprime integers. Then we can denote $p_x^2 = g^2 A$ and $p_y^2 = g^2 B$. Inserting these expressions to Eq. (E.4) yields

$$\begin{aligned} \psi(x, y; z) = & \frac{\exp i k_0 z}{p_x p_y} \int_0^{p_x} dx' \int_0^{p_y} dy' t(x', y') \\ & \times \sum_{m,n} \exp i 2\pi \left[m \frac{x - x'}{p_x} + n \frac{y - y'}{p_y} - \frac{\lambda z}{2g^2 AB} (Bm^2 + An^2) \right]. \end{aligned} \quad (\text{E.5})$$

Now if one chooses the propagation distance z_T such that the fraction $\lambda z_T / (2g^2 AB)$ in Eq. (E.5) is equal to an integer, the wavefunction $\psi(x, y; z_T)$ is equal to the wavefunction $\psi(x, y; 0)$, up to the global phase $\exp i k_0 z_T$. Therefore, one can say that the wavefunction $\psi(x, y; 0)$ is retrieved at distance z_T . The smallest non-zero integer value of the fraction $\lambda z_T / (2g^2 AB)$, unity, then corresponds to the Talbot length, for which we get the expression

$$z_T = \frac{2g^2 AB}{\lambda}, \quad (\text{E.6})$$

presented in Sec. 5.5.

Appendix F

Derivation of the formula for the fractional Talbot effect

In this section, we will derive the formula for the fractional Talbot effect, presented in Sec. 5.5. We will consider the same initial conditions as in the previous section, i.e. a plane wave illumination is incident perpendicular to the grating with a transmission function $t(x, y)$ and periods p_x and p_y such that $p_x^2/p_y^2 = A/B$, where A and B are coprimes. Then, the wavefunction $\psi(x, y; z)$ can be calculated with Eq. (E.5). Now assume that the propagation distance is chosen to be the rational multiple of the Talbot distance z_T , i.e. $z/z_T = P/Q$, where P and Q are coprimes. This simplifies the Eq. (E.5) into the following form (in the following calculations, we will ignore the unnecessary global phase $\exp ik_0 z$)

$$\begin{aligned} \psi(x, y; z_T P/Q) &= \frac{1}{p_x p_y} \int_0^{p_x} dx' \int_0^{p_y} dy' t(x', y') \\ &\times \sum_{m,n} \exp i2\pi \left[m \frac{x-x'}{p_x} + n \frac{y-y'}{p_y} - \frac{P}{Q} (Bm^2 + An^2) \right]. \end{aligned} \quad (\text{F.1})$$

both sums over m and n in Eq. (F.1) can be rewritten in terms of Q sums given by remainders after division of m and n respectively by number Q , i.e. $m = MQ + j$ and $n = NQ + l$

$$\sum_{m=-\infty}^{\infty} [\dots] \times \sum_{n=-\infty}^{\infty} [\dots] \rightarrow \sum_{M=-\infty}^{\infty} \sum_{j=0}^{Q-1} [\dots] \times \sum_{N=-\infty}^{\infty} \sum_{l=0}^{Q-1} [\dots]. \quad (\text{F.2})$$

Employing the fact that the exponential factors $\exp(i2\pi APQM^2)$, $\exp(i4\pi APMj)$, $\exp(i2\pi BPQN^2)$ and $\exp(i4\pi BPNl)$ that appear during the calculation are all equal to unity, we can evaluate the sums in Eq. (F.1)

$$\begin{aligned} &\sum_{m,n} \exp i2\pi \left[m \frac{x-x'}{p_x} + n \frac{y-y'}{p_y} - \frac{P}{Q} (Bm^2 + An^2) \right] = \\ &= \sum_{M,N} \exp i2\pi \left[M \frac{Q(x-x')}{p_x} + N \frac{Q(y-y')}{p_y} \right] \sum_{j,l=0}^{Q-1} \exp i2\pi \left[j \frac{x-x'}{p_x} + l \frac{y-y'}{p_y} - \frac{P}{Q} (Bj^2 + Al^2) \right]. \end{aligned} \quad (\text{F.3})$$

Sums over M and N in Eq. (F.3) can be evaluated using the Poisson summation formula, presented in Eq. (5.19)

$$\begin{aligned} & \sum_{M,N} \exp i2\pi \left[M \frac{Q(x-x')}{p_x} + N \frac{Q(y-y')}{p_y} \right] \sum_{j,l=0}^{Q-1} \exp i2\pi \left[j \frac{x-x'}{p_x} + l \frac{y-y'}{p_y} - \frac{P}{Q} (Bj^2 + Al^2) \right] \\ &= \frac{p_x p_y}{Q} \sum_{m,n} \delta \left(x - x' - m \frac{p_x}{Q} \right) \delta \left(y - y' - n \frac{p_y}{Q} \right) G(BP, Q, m) G(AP, Q, n), \end{aligned} \quad (\text{F.4})$$

where

$$G(P, Q, j) = \frac{1}{\sqrt{Q}} \sum_{l=0}^{Q-1} \exp \left\{ i \frac{2\pi P}{Q} \left(\frac{j}{P} l - l^2 \right) \right\} \quad (\text{F.5})$$

is the generalized quadratic Gauss sum [149]. Inserting the sum in the second line of Eq. (F.4) to Eq. (F.1) yields the analytical formula for the wavefunction $\psi(x, y; z_T P/Q)$. The resulting expression, however, can be further simplified if the sums over m and n in Eq. (F.4) are rewritten again in terms of Q sums given by remainders after division of m and n by number Q , i.e. $m = MQ + i$ and $n = NQ + j$. Employing the periodicity of both the transmission function $t(x', y')$ (which appears in Eq. (F.1)) and the Gauss sums, i.e. $t(x' - Mp_x, y' - Np_y) = t(x', y')$ and $G(P, Q, j) = G(P, Q, j + NQ)$, we obtain the final result

$$\psi(x, y; z_T P/Q) = \frac{1}{Q} \sum_{i,j=0}^{Q-1} G(BP, Q, i) G(AP, Q, j) t \left(x - i \frac{p_x}{Q}, y - j \frac{p_y}{Q} \right). \quad (\text{F.6})$$

This is the general formula for the diffraction pattern at distance $z = z_T P/Q$ from a grating described by a transmission function $t(x, y)$. Due to the equivalence of quantum movement on a compact manifold S and the diffraction on a periodic grating (presented in Sec. 5.5), the wavefunction $\phi(x, y, t = T P/Q)$ describing the quantum particle on S at some rational multiple of the revival time T (see Eq. (5.15)) can be obtained easily by substituting $z_T \rightarrow T$, $\psi(x, y; z_T P/Q) \rightarrow \phi(x, y, T P/Q)$ and $t(x, y) \rightarrow \phi(x, y)$ into Eq. (F.6).

Bibliography

- [1] Stephen Oxburgh, Tomáš Tyc, and Johannes Courtial. Dr tim: Ray-tracer tim, with additional specialist scientific capabilities. *Computer Physics Communications*, 185(3):1027–1037, 2014.
- [2] J. B. Pendry, D. Schurig, and D. R. Smith. Controlling Electromagnetic Fields. *Science*, 312:1780, 2006.
- [3] Ulf Leonhardt and Tomáš Tyc. Broadband invisibility by non-euclidean cloaking. *Science*, 323(5910):110–112, 2009.
- [4] University of Rochester. Rochester cloak to fit all sizes. <https://phys.org/news/2016-05-digital-rochester-cloak-sizes.html>.
- [5] John B Pendry, David Schurig, and David R Smith. Controlling electromagnetic fields. *Science*, 312(5781):1780–1782, 2006.
- [6] <https://www.subpng.com/png-evywr1/>.
- [7] <https://developers.arcgis.com/java/10-2/sample-code/geodesic-geometries/>.
- [8] Ulf Leonhardt. Optical conformal mapping. *Science*, 312(5781):1777–1780, 2006.
- [9] Robert Schittny, Muamer Kadic, Sebastien Guenneau, and Martin Wegener. Experiments on transformation thermodynamics: molding the flow of heat. *Physical review letters*, 110(19):195901, 2013.
- [10] Run Hu, Xuli Wei, Jinyan Hu, and Xiaobing Luo. Local heating realization by reverse thermal cloak. *Scientific reports*, 4:3600, 2014.
- [11] Bogdan-Ioan Popa, Lucian Zigoneanu, and Steven A Cummer. Experimental acoustic ground cloak in air. *Physical review letters*, 106(25):253901, 2011.
- [12] Nicolas Stenger, Manfred Wilhelm, and Martin Wegener. Experiments on elastic cloaking in thin plates. *Physical Review Letters*, 108(1):014301, 2012.
- [13] Stéphane Brûlé, EH Javelaud, Stefan Enoch, and Sébastien Guenneau. Experiments on seismic metamaterials: Molding surface waves. *Physical review letters*, 112(13):133901, 2014.
- [14] Francesco Monticone and Andrea Alù. Invisibility exposed: physical bounds on passive cloaking. *Optica*, 3(7):718–724, 2016.
- [15] Joseph S Choi and John C Howell. Paraxial ray optics cloaking. *Optics express*, 22(24):29465–29478, 2014.

- [16] Tomáš Tyc, Stephen Oxburgh, Euan N Cowie, Gregory J Chaplain, Gavin Macauley, Chris D White, and Johannes Courtial. Omnidirectional transformation-optics cloak made from lenses and glenses. *JOSA A*, 33(6):1032–1040, 2016.
- [17] Stephen Oxburgh, Chris D White, Georgios Antoniou, Ejobbokoghene Orife, and Johannes Courtial. Transformation optics with windows. In *SPIE Optical Engineering+ Applications*, pages 91931E–91931E. International Society for Optics and Photonics, 2014.
- [18] Alasdair C Hamilton and Johannes Courtial. Imaging with parallel ray-rotation sheets. *Optics express*, 16(25):20826–20833, 2008.
- [19] Thomas G Philbin, Chris Kuklewicz, Scott Robertson, Stephen Hill, Friedrich König, and Ulf Leonhardt. Fiber-optical analog of the event horizon. *Science*, 319(5868):1367–1370, 2008.
- [20] F Belgiorno, SL Cacciatori, M Clerici, V Gorini, G Ortenzi, L Rizzi, E Rubino, VG Sala, and D Faccio. Hawking radiation from ultrashort laser pulse filaments. *Physical review letters*, 105(20):203901, 2010.
- [21] Max Born and Emil Wolf. *Principles of Optics*. Cambridge University Press, 7th edition, 1999.
- [22] Warren J Smith. *Modern optical engineering*. Tata McGraw-Hill Education, 2000.
- [23] John E Greivenkamp. *Field guide to geometrical optics*, volume 1. SPIE press Bellingham, WA, 2004.
- [24] U. Leonhardt and T. G. Philbin. *Geometry and Light: The Science of Invisibility*. Dover, 2012.
- [25] Gregory J Chaplain, Gavin Macauley, Jakub Bělin, Tomáš Tyc, Euan N Cowie, and Johannes Courtial. Ray optics of generalized lenses. *JOSA A*, 33(5):962–969, 2016.
- [26] Jean Gallier. *Geometric Methods and Applications for Computer Science and Engineering*. Springer, 2nd edition, 2011.
- [27] John Bryant and Penelope Kirby. Course notes for mad 2104 discrete mathematics i. *Florida State University*, 2011.
- [28] Bill Cherowitzo. Central collineations. <http://math.ucdenver.edu/~wcherowi/courses/m6221/pglc3a.html>, 2009.
- [29] Richard Alfred Buchroeder. *Tilted component optical systems*. PhD thesis, The University of Arizona, 1976.
- [30] Max Born and Emil Wolf. *Principles of Optics*, chapter 4.3.1. Cambridge University Press, 7th edition edition, 1999.
- [31] Jakub Bělin and Johannes Courtial. Mathematica notebooks related to imaging with two skew ideal lenses. figshare (2018) [accessed 11 October 2018], <http://doi.org/10.6084/m9.figshare.7195760>.
- [32] Mohammadreza Khorasaninejad and Federico Capasso. Metalenses: Versatile multifunctional photonic components. *Science*, 358(6367):eaam8100, 2017.

- [33] E. Arbabi, A. Arbabi, S. M. Kamali, Y. Horie, and A. Faraon. Multiwavelength polarization-insensitive lenses based on dielectric metasurfaces with metamolecules. *Optica*, 3:628, 2016.
- [34] Wei Ting Chen, Alexander Y. Zhu, Vyshakh Sanjeev, Mohammadreza Khorasaninejad, Zhujun Shi, Eric Lee, and Federico Capasso. A broadband achromatic metalens for focusing and imaging in the visible. *Nature Nanotechnology*, 13(3):220–226, 2018.
- [35] Cornelius Hahlweg, Wenjing Zhao, and Hendrik Rothe. Fourier planes vs. Scheimpflug principle in microscopic and scatterometric devices. *Proc. SPIE*, 8127:8127 – 8127–7, 2011.
- [36] Pablo Gimenez-Benitez, Juan Carlos Miñano, José Blen, Rubén Mohedano Arroyo, Júlio Chaves, Oliver Dross, Maikel Hernández, and Waqidi Falicoff. Simultaneous multiple surface optical design method in three dimensions. *Optical Engineering*, 43(7):1489–1503, 2004.
- [37] M. Khorasaninejad, F. Aieta, P. Kanhaiya, M. A. Kats, P. Genevet, D. Rousso, and F. Capasso. Achromatic metasurface lens at telecommunication wavelengths. *Nano Lett.*, 15:5358–5362, 2015.
- [38] Mohammadreza Khorasaninejad, Wei Ting Chen, Robert C. Devlin, Jaewon Oh, Alexander Y. Zhu, and Federico Capasso. Metalenses at visible wavelengths: Diffraction-limited focusing and subwavelength resolution imaging. *Science*, 352:1190–1194, 2016.
- [39] Nanfang Yu, Patrice Genevet, Mikhail A Kats, Francesco Aieta, Jean-Philippe Tetienne, Federico Capasso, and Zeno Gaburro. Light propagation with phase discontinuities: generalized laws of reflection and refraction. *science*, 334(6054):333–337, 2011.
- [40] Xingjie Ni, Alexander V Kildishev, and Vladimir M Shalaev. Metasurface holograms for visible light. *Nature communications*, 4:2807, 2013.
- [41] Nanfang Yu and Federico Capasso. Flat optics with designer metasurfaces. *Nature materials*, 13(2):139, 2014.
- [42] Guoxing Zheng, Holger Mühlenbernd, Mitchell Kenney, Guixin Li, Thomas Zentgraf, and Shuang Zhang. Metasurface holograms reaching 80% efficiency. *Nature nanotechnology*, 10(4):308, 2015.
- [43] Lei Wang, Sergey Kruk, Hanzhi Tang, Tao Li, Ivan Kravchenko, Dragomir N Neshev, and Yuri S Kivshar. Grayscale transparent metasurface holograms. *Optica*, 3(12):1504–1505, 2016.
- [44] Patrice Genevet, Federico Capasso, Francesco Aieta, Mohammadreza Khorasaninejad, and Robert Devlin. Recent advances in planar optics: from plasmonic to dielectric metasurfaces. *Optica*, 4(1):139–152, 2017.
- [45] Francesco Aieta, Mikhail A Kats, Patrice Genevet, and Federico Capasso. Multiwavelength achromatic metasurfaces by dispersive phase compensation. *Science*, 347(6228):1342–1345, 2015.

- [46] Mohammadreza Khorasaninejad, Antonio Ambrosio, Pritpal Kanhaiya, and Federico Capasso. Broadband and chiral binary dielectric meta-holograms. *Science Advances*, 2(5):e1501258, 2016.
- [47] Hou-Tong Chen, Antoinette J Taylor, and Nanfang Yu. A review of metasurfaces: physics and applications. *Rep. Prog. Phys.*, 79(7):076401, 2016.
- [48] U. Leonhardt and T. G. Philbin. General Relativity in Electrical Engineering. *New J. Phys.*, 8:247, 2006.
- [49] Hossein Eskandari and Tomáš Tyc. Controlling refractive index of transformation-optics devices via optical path rescaling. *Scientific Reports*, 9(1):1–12, 2019.
- [50] Christophe Caloz and Tatsuo Itoh. *Electromagnetic metamaterials: transmission line theory and microwave applications*. John Wiley & Sons, 2005.
- [51] Juan C Miñano. Perfect imaging in a homogeneous three-dimensional region. *Optics express*, 14(21):9627–9635, 2006.
- [52] Awatif Hendi, Julian Henn, and Ulf Leonhardt. Ambiguities in the scattering tomography for central potentials. *Physical review letters*, 97(7):073902, 2006.
- [53] Mohammadreza Khorasaninejad, Wei Ting Chen, Robert C Devlin, Jaewon Oh, Alexander Y Zhu, and Federico Capasso. Metalenses at visible wavelengths: Diffraction-limited focusing and subwavelength resolution imaging. *Science*, 352(6290):1190–1194, 2016.
- [54] Sajjan Shrestha, Adam C Overvig, Ming Lu, Aaron Stein, and Nanfang Yu. Broadband achromatic dielectric metalenses. *Light: Science & Applications*, 7(1):1–11, 2018.
- [55] Wei Ting Chen, Alexander Y Zhu, Vyshakh Sanjeev, Mohammadreza Khorasaninejad, Zhujun Shi, Eric Lee, and Federico Capasso. A broadband achromatic metalens for focusing and imaging in the visible. *Nature nanotechnology*, 13(3):220–226, 2018.
- [56] Stefan Hell and Ernst HK Stelzer. Properties of a 4pi confocal fluorescence microscope. *JOSA A*, 9(12):2159–2166, 1992.
- [57] Parth Rajesh Desai, Pooja Nikhil Desai, Komal Deepak Ajmera, and Khushbu Mehta. A review paper on oculus rift-a virtual reality headset. *arXiv preprint arXiv:1408.1173*, 2014.
- [58] Peter Rubin. Oculus rift. *Wired*, 22(6):78–95, 2014.
- [59] E3 12: John Carmack’s VR Presentation. Rochester cloak to fit all sizes. <https://www.youtube.com/watch?v=kW-DlWw1XHo>.
- [60] Juan C Miñano, Pablo Benitez, Dejan Grabovičkić, Pablo Zamora, Marina Buljan, and Bharathwaj Narasimhan. Time multiplexing for increased fov and resolution in virtual reality. In *Digital Optical Technologies 2017*, volume 10335, page 1033504. International Society for Optics and Photonics, 2017.
- [61] A Einstein. The foundation of the general theory of relativity. *Annalen Phys.*, 49:769–822, 1916.

- [62] Albert Einstein. Lens-like action of a star by the deviation of light in the gravitational field. *Science*, 84(2188):506–507, 1936.
- [63] Karl Schwarzschild. Über das gravitationsfeld einer kugel aus inkompressibler flüssigkeit nach der einsteinschen theorie. In *Sitzungsberichte der Königlich Preussischen Akademie der Wissenschaften zu Berlin, Phys.-Math. Klasse, 424-434 (1916)*, 1916.
- [64] Albert Einstein and Nathan Rosen. On gravitational waves. In *Albert Einsteins Relativitätstheorie*, pages 304–316. Springer, 1937.
- [65] Dennis Walsh, Robert F Carswell, and Ray J Weymann. 0957+ 561 a, b: twin quasistellar objects or gravitational lens? *Nature*, 279(5712):381–384, 1979.
- [66] Charles Thomas Bolton. Identification of cygnus x-1 with hde 226868. *Nature*, 235(5336):271–273, 1972.
- [67] Benjamin P Abbott, Richard Abbott, TD Abbott, MR Abernathy, Fausto Acernese, Kendall Ackley, Carl Adams, Thomas Adams, Paolo Addesso, RX Adhikari, et al. Observation of gravitational waves from a binary black hole merger. *Physical review letters*, 116(6):061102, 2016.
- [68] Stephen W Hawking. Black hole explosions? *Nature*, 248(5443):30, 1974.
- [69] William G Unruh. Notes on black-hole evaporation. *Physical Review D*, 14(4):870, 1976.
- [70] Carlos Barceló, Stefano Liberati, and Matt Visser. Probing semiclassical analog gravity in bose-einstein condensates with widely tunable interactions. *Physical Review A*, 68(5):053613, 2003.
- [71] Nader Engheta and Richard W Ziolkowski. *Metamaterials: physics and engineering explorations*. John Wiley & Sons, 2006.
- [72] IE Tamm. Crystal-optics of the theory of relativity pertinent to the geometry of a biquadratic form. *J. Russ. Phys. Chem. Soc*, 57(1), 1925.
- [73] Jingjing Yang, Ming Huang, Chengfu Yang, Zhe Xiao, and Jinhui Peng. Metamaterial electromagnetic concentrators with arbitrary geometries. *Optics Express*, 17(22):19656–19661, 2009.
- [74] Allan Greenleaf, Yaroslav Kurylev, Matti Lassas, and Gunther Uhlmann. Electromagnetic wormholes and virtual magnetic monopoles from metamaterials. *Physical Review Letters*, 99(18):183901, 2007.
- [75] Do-Hoon Kwon and Douglas H Werner. Polarization splitter and polarization rotator designs based on transformation optics. *Optics Express*, 16(23):18731–18738, 2008.
- [76] Do-Hoon Kwon and Douglas H Werner. Transformation optical designs for wave collimators, flat lenses and right-angle bends. *New Journal of Physics*, 10(11):115023, 2008.
- [77] DA Roberts, N Kundtz, and DR Smith. Optical lens compression via transformation optics. *Optics Express*, 17(19):16535–16542, 2009.

- [78] Yun Gui Ma, CK Ong, Tomáš Tyc, and Ulf Leonhardt. An omnidirectional retroreflector based on the transmutation of dielectric singularities. *Nature Materials*, 8(8):639–642, 2009.
- [79] Tullio Regge. General relativity without coordinates. *Il Nuovo Cimento (1955-1965)*, 19(3):558–571, 1961.
- [80] Adrian P Gentle. Regge calculus: a unique tool for numerical relativity. *General Relativity and Gravitation*, 34(10):1701–1718, 2002.
- [81] WJ Tropf, ME Thomas, and TJ Harris. Handbook of optics. volume 2. McGraw-Hill New York, 1995.
- [82] Suzuki Michio. Group theory ii, 1986.
- [83] Manfredo P Do Carmo. *Differential geometry of curves and surfaces: revised and updated second edition*. Courier Dover Publications, 2016.
- [84] Sean M Carroll. *Spacetime and geometry*. Cambridge University Press, 2019.
- [85] Chris J Isham. *Modern differential geometry for physicists*, volume 61. World Scientific, 1999.
- [86] Mikio Nakahara. *Geometry, topology and physics*. CRC Press, 2003.
- [87] Jim Wheeler. Lecture notes on geodesics. <http://www.physics.usu.edu/Wheeler/GenRel2013/Notes/Geodesics.pdf>, 2013.
- [88] Robert Messer and Philip Straffin. *Topology now!*, volume 42. American Mathematical Soc., 2018.
- [89] James R Munkres. *Elements of algebraic topology*. CRC Press, 2018.
- [90] Herbert Edelsbrunner and Nimish R Shah. Triangulating topological spaces. In *Proceedings of the tenth annual symposium on Computational geometry*, pages 285–292, 1994.
- [91] Tomáš Tyc and Aaron J Danner. Absolute optical instruments, classical superintegrability, and separability of the hamilton-jacobi equation. *Physical Review A*, 96(5):053838, 2017.
- [92] Aaron J Danner, HL Dao, and Tomáš Tyc. The lissajous lens: a three-dimensional absolute optical instrument without spherical symmetry. *Optics express*, 23(5):5716–5722, 2015.
- [93] Edward H Adelson and John Y. A. Wang. Single lens stereo with a plenoptic camera. *IEEE Transactions on Pattern Analysis & Machine Intelligence*, (2):99–106, 1992.
- [94] Adolf W Lohmann, Rainer G Dorsch, David Mendlovic, Zeev Zalevsky, and Carlos Ferreira. Space–bandwidth product of optical signals and systems. *JOSA A*, 13(3):470–473, 1996.
- [95] Jason Geng. Three-dimensional display technologies. *Advances in optics and photonics*, 5(4):456–535, 2013.
- [96] Roland V Shack. Production and use of a lecticular hartmann screen. *J. Opt. Soc. Am.*, 61:656–661, 1971.

- [97] Gabriel Lippmann. Epreuves reversibles photographies integrals. *Comptes-Rendus Academie des Sciences*, 146:446–451, 1908.
- [98] RF Stevens and TG Harvey. Lens arrays for a three-dimensional imaging system. *Journal of Optics A: Pure and Applied Optics*, 4(4):S17, 2002.
- [99] Alasdair C Hamilton and Johannes Courtial. Generalized refraction using lenslet arrays. *Journal of Optics A: Pure and Applied Optics*, 11(6):065502, mar 2009.
- [100] M C Hutley, R Hunt, R F Stevens, and P Savander. The moire magnifier. *Pure and Applied Optics: Journal of the European Optical Society Part A*, 3(2):133–142, mar 1994.
- [101] C Hembd-Sölner, R F Stevens, and M C Hutley. Imaging properties of the gabor superlens. *Journal of Optics A: Pure and Applied Optics*, 1(1):94–102, jan 1999.
- [102] Joseph S. Choi and John C. Howell. Digital integral cloaking. *Optica*, 3(5):536–540, May 2016.
- [103] Viktor G Veselago. The electrodynamics of substances with simultaneously negative values of ε and μ . *Soviet physics uspekhi*, 10(4):509, 1968.
- [104] John B Pendry and David R Smith. Reversing light with negative refraction. *Physics today*, 57:37–43, 2004.
- [105] Richard A Shelby, David R Smith, and Seldon Schultz. Experimental verification of a negative index of refraction. *Science*, 292(5514):77–79, 2001.
- [106] Andrew A Houck, Jeffrey B Brock, and Isaac L Chuang. Experimental observations of a left-handed material that obeys snell’s law. *Physical Review Letters*, 90(13):137401, 2003.
- [107] CG Parazzoli, RB Greigor, K. Li, BEC Koltenbah, and M Tanielian. Experimental verification and simulation of negative index of refraction using snell’s law. *Physical Review Letters*, 90(10):107401, 2003.
- [108] M Notomi. Theory of light propagation in strongly modulated photonic crystals: Refractionlike behavior in the vicinity of the photonic band gap. *Physical Review B*, 62(16):10696, 2000.
- [109] Chiyang Luo, Steven G Johnson, JD Joannopoulos, and JB Pendry. Subwavelength imaging in photonic crystals. *Physical Review B*, 68(4):045115, 2003.
- [110] Patanjali V Parimi, Wentao T Lu, Plarenta Vodo, and Srinivas Sridhar. Photonic crystals: Imaging by flat lens using negative refraction. *Nature*, 426(6965):404, 2003.
- [111] Ertugrul Cubukcu, Koray Aydin, Ekmel Ozbay, Stavroula Foteinopoulou, and Costas M Soukoulis. Electromagnetic waves: Negative refraction by photonic crystals. *Nature*, 423(6940):604, 2003.
- [112] Vladimir M Shalaev, Wenshan Cai, Uday K Chettiar, Hsiao-Kuan Yuan, Andrey K Sarychev, Vladimir P Drachev, and Alexander V Kildishev. Negative index of refraction in optical metamaterials. *Optics letters*, 30(24):3356–3358, 2005.

- [113] Gunnar Dolling, Christian Enkrich, Martin Wegener, Costas M Soukoulis, and Stefan Linden. Simultaneous negative phase and group velocity of light in a metamaterial. *Science*, 312(5775):892–894, 2006.
- [114] Gunnar Dolling, Martin Wegener, Costas M Soukoulis, and Stefan Linden. Negative-index metamaterial at 780 nm wavelength. *Optics letters*, 32(1):53–55, 2007.
- [115] Costas M Soukoulis, Stefan Linden, and Martin Wegener. Negative refractive index at optical wavelengths. *Science*, 315(5808):47–49, 2007.
- [116] Johannes Courtial and John Nelson. Ray-optical negative refraction and pseudoscopic imaging with dove-prism arrays. *New Journal of Physics*, 10(2):023028, 2008.
- [117] Alexander Vilenkin and E Paul S Shellard. *Cosmic strings and other topological defects*. Cambridge University Press, 2000.
- [118] Chong Sheng, Hui Liu, Yi Wang, SN Zhu, and DA Genov. Trapping light by mimicking gravitational lensing. *Nature Photonics*, 7(11):902, 2013.
- [119] Vincent H Schultheiss, Sascha Batz, Alexander Szameit, Felix Dreisow, Stefan Nolte, Andreas Tünnermann, Stefano Longhi, and Ulf Peschel. Optics in curved space. *Physical review letters*, 105(14):143901, 2010.
- [120] Anatoly Patsyk, Miguel A Bandres, Rivka Bekenstein, and Mordechai Segev. Observation of accelerating wave packets in curved space. *Physical Review X*, 8(1):011001, 2018.
- [121] RF Rinehart. A Solution of the Problem of Rapid Scanning for Radar Antennae. *Journal of Applied Physics*, 19(9):860–862, 1948.
- [122] Martin Šarbort and Tomáš Tyc. Spherical media and geodesic lenses in geometrical optics. *Journal of Optics*, 14(7):075705, 2012.
- [123] Q Liao, NJG Fonseca, and O Quevedo-Teruel. Compact Multibeam Fully Metallic Geodesic Luneburg Lens Antenna Based on Non-Euclidean Transformation Optics. *IEEE Transactions on Antennas and Propagation*, 66(12):7383–7388, 2018.
- [124] D. A. Beller, K. M. J. Alards, F. Tesser, R. A. Mosna, F. Toschi, and W. Möbius. Evolution of Populations Expanding on Curved Surfaces. 123:58005, 2018.
- [125] Juan C Miñano, Pablo Benítez, and Juan C González. Perfect imaging with geodesic waveguides. *New Journal of Physics*, 12(12):123023, 2010.
- [126] Dietrich Marcuse. *Theory of dielectric optical waveguides*. Elsevier, 2013.
- [127] Richard W Robinett. Quantum wave packet revivals. *Physics Reports*, 392(1-2):1–119, 2004.
- [128] Michael Berry, Irene Marzoli, and Wolfgang Schleich. Quantum carpets, carpets of light. *Physics World*, 14(6):39, 2001.
- [129] Henry Fox Talbot. Lxxvi. facts relating to optical science. no. iv. *The London, Edinburgh, and Dublin Philosophical Magazine and Journal of Science*, 9(56):401–407, 1836.

- [130] Jianming Wen, Yong Zhang, and Min Xiao. The Talbot Effect: Recent Advances in Classical Optics, Nonlinear Optics, and Quantum Optics. *Advances in Optics and Photonics*, 5(1):83–130, 2013.
- [131] Tingge Gao, E Estrecho, G Li, Oleg A Egorov, X Ma, Karol Winkler, Martin Kamp, C Schneider, Sven Hoefling, AG Truscott, et al. Talbot Effect for Exciton Polaritons. *Physical Review Letters*, 117(9):097403, 2016.
- [132] M. V. Berry and S. Klein. *J. Mod. Opt.*, 43(10):2139, 1996.
- [133] P. M. Morse and H. Feshbach. *Methods of Theoretical Physics (Part 1)*. McGraw Hill, 1953.
- [134] W. C. Elmore and M. A Heald. *Physics of Waves*. Dover, 1985.
- [135] M. G. Lamé. *Le Cons sur la Théorie Mathématique de L'élasticité des Corps Solides*. Bachelier, Paris, 1852.
- [136] W.-K. Li and S. M. Blinder. *J. Math Phys.*, 26:2784, 1985.
- [137] D. A. Hill. *Electromagnetic Fields in Cavities: Deterministic and Statistical Theories*. John Wiley & Sons, 2009.
- [138] D. Bimberg, M. Grundmann, and N. N. Ledentsov. *Quantum Dot Heterostructures*. John Wiley & Sons, 1999.
- [139] L. D. Landau and E. M. Lifshitz. *Electrodynamics of Continuous Media*. Butterworth-Heinemann, 2004.
- [140] N. H. Fletcher and T. D. Rossing. *The Physics of Musical Instruments*. Springer, 2013.
- [141] A. P. Nickolaenko and M. Hayakawa. *Resonances in the Earth-Ionosphere Cavity*. Springer, 2002.
- [142] J. C. Miñano, P. Benítez, and J. C. González. *New J. Phys.*, 12:123023, 2010.
- [143] P. C. Yang and S.-T. Yau. *Annali della Scuola Normale Superiore di Pisa - Classe di Scienze*, 7:55, 1980.
- [144] S. Rosenberg. *The Laplacian on a Riemannian Manifold: An Introduction to Analysis on Manifolds*. Cambridge University Press, 1997.
- [145] M. Mansuripur. *Classical Optics and Its Applications*. Cambridge University Press, 2002.
- [146] Joseph W Goodman. *Introduction to Fourier optics*. Roberts and Company Publishers, 2005.
- [147] Lord Rayleigh. Xxv. on copying diffraction-gratings, and on some phenomena connected therewith. *The London, Edinburgh, and Dublin Philosophical Magazine and Journal of Science*, 11(67):196–205, 1881.
- [148] Jakub Bělín and Tomáš Tyc. Talbot Effect for Gratings with Diagonal Symmetry. *Journal of Optics*, 20(2):025604, 2018.

- [149] JH Hannay and Michael V Berry. Quantization of Linear Maps on a Torus-Fresnel Diffraction by a Periodic Grating. *Physica D: Nonlinear Phenomena*, 1(3):267–290, 1980.
- [150] Charles S Peirce. A quincuncial projection of the sphere. *American Journal of Mathematics*, 2(4):394–396, 1879.
- [151] Jonathan Libgober. The euler characteristic, poincaré-hopf theorem and applications. *Uchicago math REU*, 17(6), 2012.
- [152] William S Massey. *A basic course in algebraic topology*, volume 127. Springer, 2019.
- [153] Christopher T Dodson, Phillip E Parker, and PE Parker. *A user’s guide to algebraic topology*, volume 387. Springer Science & Business Media, 1997.
- [154] Heinrich Walter Guggenheimer. *Plane geometry and its groups*. Holden-Day, 1967.
- [155] Mark A Armstrong. *Groups and symmetry*. Springer Science & Business Media, 2013.
- [156] Maxwell Levine. Plane symmetry groups. *University of Chicago*, 2008.
- [157] J.H. Conway, H. Burgiel, and C. Goodman-Strauss. *The Symmetries of Things*. Taylor & Francis, 2008.
- [158] Ichirô Satake. On a generalization of the notion of manifold. *Proceedings of the National Academy of Sciences of the United States of America*, 42(6):359, 1956.
- [159] Lance Dixon, Jeffrey A Harvey, Cumrun Vafa, and Edward Witten. Strings on orbifolds. *Nuclear Physics B*, 261:678–686, 1985.
- [160] Shamit Kachru and Eva Silverstein. 4d conformal field theories and strings on orbifolds. *Physical Review Letters*, 80(22):4855, 1998.
- [161] Ling Lu, Chen Fang, Liang Fu, Steven G Johnson, John D Joannopoulos, and Marin Soljačić. Symmetry-protected topological photonic crystal in three dimensions. *Nature Physics*, 12(4):337, 2016.
- [162] O Dahlberg, RC Mitchell-Thomas, and Oscar Quevedo-Teruel. Reducing the dispersion of periodic structures with twist and polar glide symmetries. *Scientific reports*, 7(1):10136, 2017.
- [163] Christian Lytle, Thomas J McManus, and Mark Haas. A model of na-k-2cl co-transport based on ordered ion binding and glide symmetry. *American Journal of Physiology-Cell Physiology*, 274(2):C299–C309, 1998.
- [164] Miguel Camacho, Rhiannon C Mitchell-Thomas, Alastair P Hibbins, J Roy Sambles, and Oscar Quevedo-Teruel. Mimicking glide symmetry dispersion with coupled slot metasurfaces. *Applied Physics Letters*, 111(12):121603, 2017.
- [165] G. Valerio, Z. Sipus, A. Grbic, and O. Quevedo-Teruel. Accurate equivalent-circuit descriptions of thin glide-symmetric corrugated metasurfaces. *IEEE Transactions on Antennas and Propagation*, 65(5):2695–2700, 2017.
- [166] Orad Reshef, Michael P DelMastro, Katherine KM Bearne, Ali H Alhulaymi, Lambert Giner, Robert W Boyd, and Jeff S Lundeen. Towards ultra-thin imaging systems: an optic that replaces space. *arXiv preprint arXiv:2002.06791*, 2020.